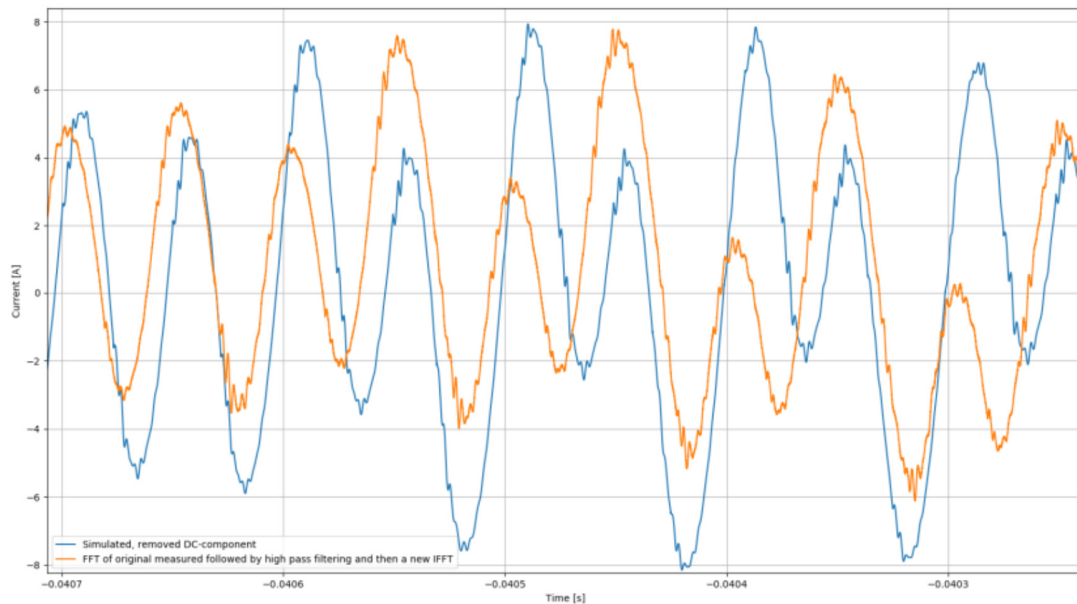# RIFEL

Ripple and Electromagnetic Fields in Electric Vehicles

Idm time domain, RIFEL-07

Authors: Anders Bergqvist, Andreas Henriksson, Johan Lektenius, John Simonsson,
                Per Jacobsson, Peter Ankarson, Shemsedin Salih Nursebo, Torbjörn
                Thiringer, Urban Lundgren

Date   2018-04-30

Department of Electrical Engineering,

Chalmers University of Technology

Göteborg, Sweden, 2018

Ripple and Electromagnetic Fields in Electric Vehicles

Anders Bergqvist, Andreas Henriksson, Johan Lektenius, John Simonsson, Per Jacobsson, Peter Ankarson, Shemsedin Salih Nursebo, Torbjörn Thiringer, Urban Lundgren

Ripple and Electromagnetic Fields in Electric Vehicles

Anders Bergqvist, Andreas Henriksson, Johan Lektenius, John Simonsson, Per Jacobsson, Peter Ankarson, Shemsedin Salih Nursebo, Torbjörn Thiringer, Urban Lundgren

Content

1 Summary

The electrical system in an electrified vehicle consists of high voltage (HV) components interacting in a complex way. The switching interaction in the power electronics results in ripple causing electromagnetic fields, disturbing other electronics and degradation of components. An overview of this can first be obtained when a physical system is built which could lead to unintentional over- or under dimensioning of HV components. This lack of information within the electrical system can lead to late verifications in the project causing substantial cost if changes are needed.

This project aims at improving early evaluation of new concepts, create tools and build the necessary competence for a virtual system model that includes the key HV components: battery, electrical motor and power electronics, a simple load along with cable and connectors. This virtual model shall be able to simulate voltage and current ripple generated by the power electronics, initially in a frequency range up to 100 kHz. Results from the simulations shall be presented both in time and frequency domain as well as be expressed in RMS values for easier comparison to measured results.

Some of the more important findings are briefly summarised below;
For the high voltage battery, the electrical characteristics up to a frequency of roughly 1000 Hz was well determined using an impedance spectroscopy instrument at cell level and then multiplied by the numbers of cells. However for finding the impedance behaviour for frequencies above 1000 Hz, the determination must be done on the battery pack level since bus bars and other component in the complete battery pack will be dominating in this frequency range.

From measurements of differential mode impedance in high voltage cables it is found that it is important that the mutual inductance between the centre conductor and shield is included in the model to describe cable impedance below 10 kHz properly.

The control of the inverter is very important for the overall behaviour and in this project SVM was used which has been shown to give the lowest current and voltage ripple of the traditional switching schemes. And for the machine model, the temperature variations must be taken into account since the machine parameters has been found to vary with ~20 % over the specified temperature range.

The system model is found to agree well with rig measurements well up to 1 MHz with regards to both currents and voltages at the DC and AC sides. Furthermore, measurements in a real car match those in the rig. For time domain simulations, it was decided to use Ansys Simplorer since it can handle the inverter and the electrical machine simulations very well and for frequency domain simulations, it was decided to use LTspice since it is freeware, has support for AC-sweeps, improved switching compared to other SPICE-simulators, and is easy to use.

Magnetic field simulations have been calculated and compared to measurements in the driveline rig at Chalmers. It was a good match across the investigated frequency range 10 Hz to 100 kHz.

In this project, only internally developed component models were considered. To expand the functionality of the system modelling tool, international interface standards such as the Functional Mockup Interface (FMI) need to be investigated. Consequently, it would be a good idea to include additional automotive OEMs as well as suppliers and software vendors in future research collaborations.

2 Sammanfattning på svenska

Det elektriska högvoltssystemet i ett elektrifierat fordon består av flertalet komponenter som samverkar på ett komplext sätt. Switchningar i elektroniken ger upphov till ström- och spänningsrippel som kan störa annan elektronik på grund av externa elektromagnetiska fält samt degradera ingående komponenter såsom kondensatorer. Det är också svårt att få en överblick över ripplet innan det fysiska systemet är byggt och fullt ut förstå konsekvenserna för de egenskaper som ska uppnås vilket kan leda till oavsiktlig över eller underdimensionering av komponenter. Denna brist på tidig information om det elektriska systemets funktion kan leda till ofullständig eller sen utvärdering av nya elektrifieringskoncept samt sena ändringar i projekt vilket för med sig stora kostnader.

Detta projekt syftar till att förbättra tidiga konceptutvärderingar, skapa verktyg och bygga nödvändig kompetens genom att ta fram en virtuell modell på systemnivå bestående av de viktigaste högspänningskomponenterna: HV batteri, elmaskin med tillhörande kraftelektronik, enklare laster samt kablage och kontaktdon. Den virtuella modellen skall klara av att simulera spännings och strömrippel genererat från kraftelektroniken, initialt i ett frekvensområde som sträcker sig upp till 100 kHz. Simuleringsresultat skall visas dels i tids och frekvensdomänen men även som RMS värden för att mer överskådligt kunna jämföras med verifieringar i fysisk rigg.

Projektet är uppdelat i fem arbetspaket (AP) och med tre olika intressenter. Arbetspaket 1 (AP1) leds av Volvo Cars och hanterar projektledning samt resultatspridning och de övriga hanterar respektive delsystem. Arbetspaket 2 (AP2) leds av Volvo Cars och fokuserar på högfrekvent modellering och validering av HV batteriet, arbetspaket 3 (AP3) leds av Chalmers och undersöker simuleringsmodeller för olika kraftelektroniska enheter och elektriska maskiner i systemet och arbetspaket 4 (AP4) leds av RISE och fokuserar på kablagemodellering samt dess inverkan på systemnivå. Resultaten från dessa arbetspaket kommer sedan att kopplas samman till en systemmodell i arbetspaket 5 (AP5), som leds av Volvo Cars, för att skapa en fungerande modell med hög detaljgrad. Systemfokus är projektets kärna och för att för att tidigt kunna definiera sammankopplingen och vilka interface som kommer att användas genom projektet kommer arbetspaket 2 till 4 att ha tidiga leveranser till systemmodellen. Projektet har definierade milstolpar där bland annat 3 offentliga seminarier samt ett antal publikationer och presentationer ingår, dessa kan ses i kapitel 13.

Några av de mer intressanta resultaten beskrivs kort nedan;

För högvoltsbatteriet räcker det att karakterisera cell nivå impedansen och sedan beräkna det totala resultaten för antalet celler i batteriet för frekvenser under 1 kHz. För att göra liknande beräkningar för frekvenser över 1 kHz måste hela packnivån inkluderas, främst för att bus bars och andra komponenter kommer bli dominerade i detta frekvensområde.

Genom mätningar av differential mode impedans i högvoltskablarna framkom att det är viktigt att den gemensamma induktansen mellan ledare och skärm är inkluderad i modellerna för att beskriva kabelimpedansen korrekt vid frekvenser under 10 kHz.

Hur omriktaren kontrolleras är väldigt viktigt för de generella rippel resultaten och i detta projekt användes SVM som anses ge de lägsta rippelnivåerna av de mer traditionella switchningsstrategierna. Elmaskinens temperatur måste tas med i beräkningarna för att få ett bra resultat då vitala parametrar kan variera upp till 20 % vid olika temperaturer vilket påverkar resultatet.

Systemmodellen stämmer överens med mätningar i rig upp till 1MHz vad gäller både ström och spänningsrippel, både på DC och AC sidan. Verkliga mätningar i bil stämmer också överens med riggmätningar i samma mätpunkter.

Ansys simplorer användes för att göra simuleringar i tidsdomänen eftersom programmet bland annat har stöd för omriktare och elmaskiner. För simuleringar i frekvensdomänen användes istället LTspice eftersom det är gratis, har support för AC svep, har bättre stöd för omslagsmodeller än andra SPICE simulatorer och att det är enkelt att använda.

Magnetiska fält beräknades och jämfördes med mätningar i den elektriska drivline riggen på Chalmers och visade sig stämma bra i det uppmätta frekvensområden 10 Hz till 100 kHz.

I detta projekt användes bara internt framtagna modeller av högvoltssystemet. För att utvidga systemmodelleringsarbetet och dess funktion hade internationella interface standarder, till exempel Functional Mockup Interface (FMI) kunnat använts. Det hade också varit fördelaktigt att inkludera andra OEM:er, leverantörer och mjukvaruutvecklare i framtida forskning inom detta område.

Projektet har även bidragit till FFI genom stödja följande programmål:

- Teknologier som möjliggör reducering av fossilberoendet

Projektet har fokuserat helt på elektrifierade fordon och förbättringar av deras design och utvecklingsprocess. Genom att minska ledtider och utvecklingskostnader samt att förbättra kvalitén kommer användningen av elektrifierade fordon att öka och därmed kommer CO_2 emissionen i fordonsflottan att minska.

- Främja den svenska fordonsindustrins konkurrenskraft

Kortare ledtider är en nyckelfaktor i att bibehålla och öka svensk fordonsindustrins konkurrenskraft. Detta projekt har bidragit direkt till detta genom att tillhandahålla virtuella och validerade systemmodeller i tidiga faser och därmed minska utvecklingsledtiderna.

- Stärka forsknings- och innovationskapaciteten i Sverige

De utvecklade systemmodellerna och den kompetens som byggt upp i projektet kommer utgöra viktiga verktyg för både industri (Volvo) och akademi (Chalmers och RISE) efter

projektets slut. Modelleringskunskapen kommer att bidra till målet att stärka forskning och innovation genom att ge möjliggöra snabb återkoppling på nya koncept innan hårdvara finns tillgänglig.

- Främja samverkan mellan industri och akademi

Projektet har utförts i samarbete med Volvo, Chalmers och RISE. Kunskapen har också att delgivits genom en seminarieserie där även andra parter såsom Volvo AB, Scania, BorgWarner, CEVT med flera har medverkat i. Från tidigare erfarenheter vet vi att samarbete mellan akademi och industri ger en bra grogrund för innovationer och ökar den gemensamma kunskapsnivån på en nationell nivå.

Projektet syftar även till att ge nya verktyg för att bygga kompetens och brygga ett kunskapsgap inom programmet för "Elektronik, Mjukvara och Kommunikation". Inriktningen är huvudsakligen programbeskrivningen med syftet att "Utveckla nödvändig basteknologi för att realisera funktioner. …" och "Etablera världsledande metoder och verktyg för fordonsutveckling".

Utveckla nödvändig basteknologi för realisering av "green functions" innebär i detta projekt att frekvensområdet mellan 1 kHz till 1 MHz studeras extra noga eftersom modellerna blir betydligt mer komplicerade här då många olika mekanismer samverkar. Det finns ett kunskapsgap inom systemmodellering eftersom det krävs validerade högfrekventa komponentmodeller samt tydliga gränssnitt när olika komponenter skall kopplas samman i ett system. Även om projektet från början skulle leverera verifierade modeller upp till 100 kHz så har mätningar visat att systemmodellen klarar att leverera valida resultat i ett högre frekvensområde, upp till 1MHz.

Projektet möter också Verification/Validation i programmet genom att öka den virtuella förmågan till att inkludera HV DC-systemets elektriska miljö med fokus på högfrekvent rippel och störningar. Virtuella metoderhar skapats som i ett tidigt utvecklingsskede kan analysera nya koncept eller nya kravställningar i befintliga konstruktioner vilket i sin tur kan leda till minskad utvecklingsledtid, ökad flexibilitet samt högre kvalité.

3 Preface, Objective and Project realisation

Ever since Volvo cars started to discuss voltage and current ripple in hybrid vehicles, the major question has focused on requirement levels and unwanted effects caused by ripple. The lack of knowledge in this area lead Volvo Cars into the idea to start a separate project, including both industry and academy to gain maximum results. It was decided to apply for an FFI (fordonsstrategisk forskning och innovation) project with Chalmers and RISE as partners with the aim to develop a virtual model of the HV system that should be able to simulate voltage and current ripple. Without the support from Vinnova, it is very unlikely that this project had ever started since the resources needed for this type of investigation could be hard to secure, since the ripple issue was not causing immediate problems.

The project lasted for a little bit more than 2 years during which it evolved from being a theoretical idea to a verified prototype that can be used for multiple purposes. Numerous meetings and workshops has been performed, some very creative and some more confusing. In the end, this system model prototype performs much better than ever could be thought at project start.

Numerous people has contributed to this project, the list of all involved would be too long to fit in this short summary. However, a few has made contributions that would be dishonest not mentioning here.

First of all we would like to thank Vinnova for making this project possible via your contribution for FFI, it is very important that these kind of support is available for the industry.

A very special thanks to the project core team, including people that for one reason or another was not participating during the complete project time. You have made this project possible and also contributed to major parts of this report.

Dr. Alexandra Nafari who was the creator of RIFEL and the project leader for the first year of the project. Without your initial effort this project would never have started.

Robert Ericsson, Torbjörn Thiringer and Jan Welinder for the support and guidance as project steering members.

Worth mentioning are the master thesis students who contributed with input to this project:

Navya Kundaranahalli Renukaiah and Premkumar Ayyadurai for their master thesis work; Battery modelling for large current pulses.

Anton Holm for his master thesis work; SiC converter for electrical vehicle – DC-link ripple.

Daniel Heinerås and Daniel Fahlgren for their master thesis work; Analysis and optimization of high power cable design alternatives for electrical vehicles.

Apart from these persons numerous colleagues, workshops and external experts has contributed, a humble thanks to all these people.

3.1 Project Structure

The overall project target was to systematically build a system model with relevant HV components models from an electrified vehicle. This was managed by dividing the project in to 5 work packages with the following content:

Work Package 1	Project and results
Lead	Volvo Cars
Method	Continuous follow up via project meetings, coordination of workshops, follow up in steering committee, internal presentations at Volvo, seminary etc.
Content	Project follow-up 3 Seminary during the projects with invited parties 3 Thesis works within the field of simulations/ripple Publications and knowledge sharing Administrative reporting and follow up
Deliverables	One publication per Work package 3 master thesis 3 Seminaries Final report

Work Package 2	High voltage battery modelling and validation
Lead	Volvo Cars
Method	Modelling of Li-Ion battery for higher frequencies (<100kHz) which was verified with measurements. Static methods for parameterisations and sensitivity analysis.
Content	Development of a verified battery model on cell-level including relevant inductive, capacitive and resistive parts. Analysis of cell integration into the HV battery module and pack level. Parameterisations and sensitivity analysis on both cell, module and pack level.
Deliverables	M1: Development of a battery model on cell-level which included relevant inductive and capacitive elements for frequencies up to ~1Hz.

	M2: Battery model on Module level with relevant inductive and capacitive elements for frequencies up to ~1kHz. This model was verified with measurements.
	M3: Battery model on pack level with capacitive, inductive and resistive elements for frequencies above 10kHz. Analysis of the validity for higher frequencies was also done.

Work Package 3	Inverter and electrical machine modelling and validation
Lead	Chalmers
Method	Analyse of electrical machines with simplified models. Modelling and verification of relevant switching circuitry with matching control algorithms.
Content	Use of electromagnetic field simulations of electric machines in order to investigate potential as well as verify and ensure concept design. Analysis of computationally heavy models on FEM level to develop simplified models with shorter simulation time but with sufficient level of detail to capture all relevant effects. Parameter study and sensitivity analysis of models for inverter and electrical machines including capacitors and other system components.
Deliverables	M1: Equation based model of the electrical machine with matching inverter for frequencies up to 1kHz, including capacitive, inductive and resistive elements. M2: Combined FEM-model simulation for electrical machine and electrical circuitry simulation with matching inverter for frequencies up to 10kHz. Model to be validated on subsystem level. M3: Combined FEM-model simulation for electrical machine and electrical circuitry simulation with matching inverter for frequencies above 10kHz. Analysis of the validity for higher frequencies shall also be done. M4: Analysis of simplified models in the system. These models was verified through measurements.

Work Package 4	Magnetic field and cable modelling and validation
Lead	RISE
Method	Modelling of cables with two purposes: 1. To include the cable effect in the system simulations and 2. Calculate the magnetic field in the vehicle. Cables were modelled with circuit based models which was integrated in the system model.

	Magnetic field calculations was bases on modelled current in the other WP as well as surrounding vehicle body (sheet metal).
Content	Analyze field sources and possible measures to reduce fields. The analysis was done with measurements before the start of the simulation work. Development of circuit model and analytical cable model for frequencies up to at least 1 kHz. Fine-tuning and validation of cable models as well as determination of limitations in frequency, impact of connectors and other factors up to 10 kHz. Analysis of higher frequencies (>> 10 kHz) in the electrical system. Reflections and resonances can create serious high voltage spikes and resonances in cables.
Deliverables	M1: Analyse which electromagnetic fields exist in a modern electrified vehicle and that are relevant to analyse in the project. Analytical cable model valid for frequencies up to at least 1 kHz. M2: Validate the cable model for use in system modelling (WP5). Builds further on the models that appeared in M1. Method to determine relevant cable parameters in cases where they are not available from the supplier. M3: High frequency model of cables for studying resonances in cables and cables resulting surge and disturbances. Analysis of the possibilities of include the results in system models. M4: Calculation of resulting electromagnetic fields based on input data from other work packages. Field image must be validated within a relevant frequency range, in addition, its dependence on external parameters (such as screen effect) shall be described.

Work Package 5	System modelling and validation
Lead	Volvo Cars
Method	Merging of the models presented in work packages 2, 3 and 4. The merged system was verified by measurements in a complete systems rig. A virtual prototype was proposed for product development.
Content	Combine updated models for battery, electric machine, inverters as well as cabling. Validation of model at vehicle level. Investigation of how the different subsystems affects the resulting ripple on the DC bus. Parameter studies and sensitivity analysis of the incoming systems. The parameters that was investigated include those within the electric machine, inverters and cables.

	Verify the complexity level of the models that have been developed in WP 2, 3 and 4. If required, further details must be included in order to determine the high-frequency behaviour adequately. Analyse and verify current and voltage ripple on the DC bus at different operating points.
Deliverables	M1: Develop a system model valid for frequency up to 1kHz which included capacitive, inductive and resistive elements. M2: Combined FEM-model simulation for electrical machine and electrical circuitry simulation with matching inverter, high voltage battery and cables for frequencies up to 10kHz. M3: Combined FEM-model simulation for electrical machine and electrical circuitry simulation with matching inverter, high voltage battery and cables for frequencies above 10kHz. Validate this model towards measurement in the system rig. M4: Suggest a virtual system model prototype

Figure 3.1 describes the Work packages from a Hardware point, whereas WP2-4 support WP5 with models which are then merged into the system model in WP5.
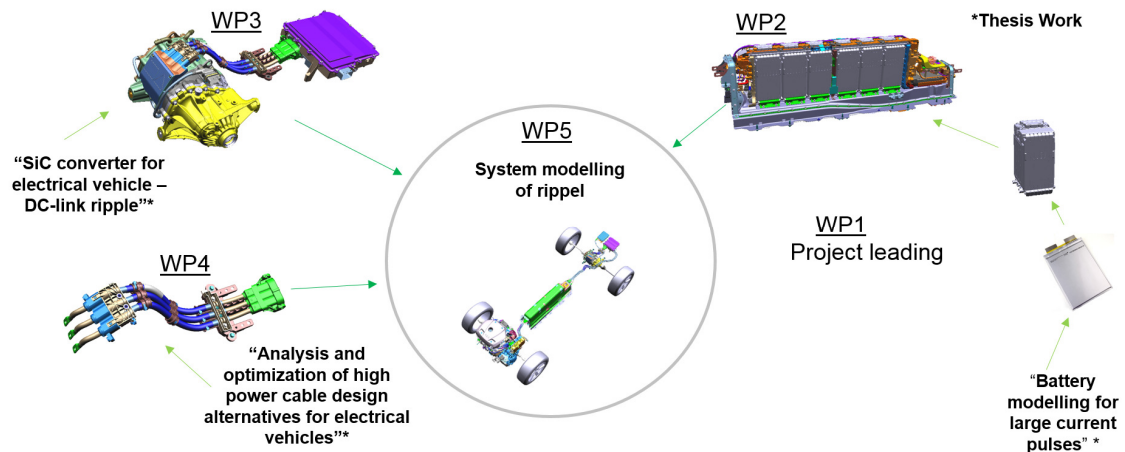

Figure 3.1 – Workpackage illustration in the RIFEL project

The initial time plan, which can be seen in Figure 3.2, was changed once during the project phase, leading to a 3-month extension of the project due to resource limitations and parental leave. However, the budget remain the same throughout the entire project.

AP		2016				2017			
		Q1	Q2	Q3	Q4	Q1	Q2	Q3	Q4
AP1	Projektledning och resultatspridning		Seminarie 1				Seminarie 2		Seminarie 3
AP2	HF batterimodellering och validering	M1		M2		M3			
AP3	HF modellering och validering av Kraftelektronik och Elmaskiner	M1		M2		M3		M4	
AP4	Magnetfält och HF Kabelmodellering och validering	M1		M2		M3		M4	
AP5	HF systemmodellering och validering		M1		M2		M3		M4

Figure 3.2 – Initial time plan for the RIFEL project

The initial steering group can be seen in Figure 3.3. Also in this group, changes were made throughout the project.

Figure 3.3 – Initial steering group for the RIFEL project

The overall plan described in this chapter was successfully implemented although some changes were made on the time plan, steering group, content and deliverables.

4 Background

4.1 Problem background

The increasing demand to lower CO_2 emissions together with a decreasing cost for high-voltage (HV) batteries has led to a large interest in electrification of vehicles within the automotive industry. There is also an increasing customer demand for electric and hybrid vehicles, which drives the interest in electrification further. This has led to a beginning shift in technology, from traditional internal combustion engines (ICE) towards electrified powertrains, where one or more electric machines are introduced, alone or in combination with an ICE. In addition to the technology shift, there is also an ambition to develop more of the control software in-house, as well as a constant aim to shorten time to market. For the automotive industry, the coming decade will be a very exciting as well as uncertain time. The introduction of new technology, more complex control software, and the shorter time to market will, maybe more than ever, require accurate, flexible, and validated methods for virtual testing and verification of vehicle systems and subsystems. An effect of Volvo Car Corporation's commitment to electrification is that there will be some kind of electric powertrain in all vehicles in the near future. Issues that need to be addressed in this aspect include verification of system functions, electromagnetic compatibility (EMC) and possible health hazards related to radiated electromagnetic fields, and the increasing amount of software code.

When it comes to verifying the system functions, it is important that this can be done in every phase in the product development process. To achieve this, there is a need for virtual methods that are flexible so that they can be adapted to different development phases, as well as to different configurations of the electric powertrain. There might, e.g., be alternative configurations of number of electric machines, placement of components or battery size depending on the size of the vehicle or price segment. Normalization of electric powertrains will lead to a modularized way of working when it comes to hardware. This must be mirrored for the virtual engineering in order to make sure that there are reliable simulation models at each phase in the product development process.

The HV system, here defined by HV battery, power inverter, electric machine, and electric wiring, is an expensive part of electric and hybrid vehicles and there is a need for methods to efficiently dimension the system. Furthermore, the introduction of a HV system in a vehicle increases the risk of disturbances in the form of high-frequency current and voltage ripple. This could lead to degradation and performance loss for the HV components. In addition, this could also affect other critical components in the vehicle or the environment surrounding the vehicle, leading to bad electromagnetic compatibility (EMC) performance. In this regard, Volvo Car Corporation has initiated the research project RIFEL (Ripple and Electromagnetic Fields in Electric Vehicles) in order to investigate virtual methods for analysing the HV system.

The main goal of the project is to model voltage and current ripple in the HV system. This is important in order to understand the effect of ripple on EMC, dimensioning aspects, and components in an early phase of the product development process, where there is no hardware available.

4.2 Previous work

The work done in this project builds on the knowledge from the previous FFI-sponsored project xEVCO (2009-04836). The xEVCO project laid a foundation for how to apply model-based design for the electric powertrain in the automotive industry by means of experimental data, physical models, framework, and modelling languages. From xEVCO and previous work performed at the involved project partners, models at component level for the HV battery, electric machine, and power electronics valid at lower frequencies existed. They are used as input and starting point for the modelling in the RIFEL project.

When it comes to previous work in battery modelling, the literature is extensive, however most of the modelling focuses on cell level modelling [20]–[25]. Among these some researchers [21]–[23] have worked with impedance spectroscopy of the cell, but the frequency range of interest low compared what is analyzed in the RIFEL project. Reference [26] deals with the high frequency model of a battery cell starting from the structure of the battery cell. The aim is to use the model of the battery cell when building the battery pack impedance. However, as will be discussed in the subsequent sections, the inductance behavior of the battery pack cannot be obtained from the inductance of the battery cell by applying circuit theory calculations. The authors in [27] have investigated the impedance behavior a battery pack using different measurement setups. They have also tried to calculate the equivalent impedance model of the battery using the structure of the battery pack and Ansys Q3D tool. However, such approach requires knowledge of cell and battery pack structure and it is also unnecessarily complex as it requires the model of each cell within the pack. To the authors' knowledge there is almost no research work that provides a circuit equivalent model for a battery pack while comparing the impedance behavior of battery cell, module, and pack within a large frequency range (from 10 Hz to 1 MHz).

System models of electric drives have been proposed in a number of publications, often focusing on EMI [14]–[19]. Works differ in what frequency ranges are concerned, the level of fidelity and whether modelling is done in the time domain or the frequency domain. Refs [14]–[16] discuss and compare both approaches and list some advantages and disadvantages. In general, it can be said that frequency domain models are often considered more computationally efficient, especially for high frequencies. However, modelling of a switched power converter in the frequency domain poses certain challenges since they are not time invariant systems. Both approaches have been studied in this project.

Measurement of the magnetic fields inside the compartment of Volvo hybrid vehicle when driving at a speed of 50 km/h have been done by VCC. From the measurements a weighted "Body average" magnetic field value was calculated for different areas. In a project called "Safe hybrid", magnetic field measurements and common mode currents on cables between battery and inverter on real hybrid vehicles were measured at 40 and 20 km/h, respectively. In another project called "Deliver", measurements of common mode currents between battery and inverter on an electric delivery vehicle was used as input to an electromagnetic simulation software to compute a coarse prediction of the magnetic field. The car metal plates were modeled as perfect electric conductors, which is not true for low frequencies. In literature [8]–[11], measurements of common mode currents and sometimes also

magnetic field has been performed. The currents were measured between battery and inverter, or between inverter and electric machine.

Cables can conveniently be modelled by using transmission line models. The requirement for using these models is that the extent of the cable cross-section should be small in comparison with the wavelength at the highest frequency of interest. If this requirement is not met, we cannot guarantee the assumed TEM mode of propagation and more advanced models need to be used, i.e., we need to solve the full Maxwell's equations. Inherent in the transmission line models is also that radiation losses are neglected. It should however be pointed out that once we have computed the current distribution along the length of the cable, we can compute the radiated field, so this is in practice no limitation.

5 Purpose, research questions and method

5.1 Purpose & Research questions

The power quality of an electric grid is an area that has attracted enormous research interest throughout the years. However, the focus for this issue has almost completely been on the 50/60 Hz grids. As DC-grids become more and more common where one important example is the electrification of vehicles, more knowledge has to be developed also for this area. While the AC-grids have a large number of standards describing the power quality issue, the standardization work regarding dc-grids has reached the stationary voltage levels. However, the transient and dynamic frequency ranges still awaits to be covered in standards. The goal is to design a power system where the chain 'generation-propagation-component immunity' reaches its 'best combination'. With 'best' is here meant that the cost function of the various components, as well as efficiency, robustness, cost of EMI, etc., reaches a favourable combination. In order to design such a complex system with a virtual tool, adequate modelling both on component and system level is needed. The models needs to be sufficiently accurate in detail but still be computationally efficient so that an analysis can be done in a reasonable time. The method of how such a model can be extracted is also of interest to investigate; the model shall preferably be possible to develop early in the project phase, i.e. based on virtual tools, but also possible to validate by measurements on a subsystem level as an individual component.

A very high research value would be to study how a DC power system in a plug-in hybrid electrical vehicle could be designed, based on a physical-based modelling approach. The dynamic electrical environment needs to be determined on a system level where the main DC-link is the focus of this investigation. In order to perform this task, the components needs to be modelled accurately and their interaction with the system has to be investigated. Accordingly, the high voltage battery, inverter, electric machine as well as the connecting cables need to be incorporated in the system simulation model. Of extreme importance is that the theory behind each subsystem model must be verified with measurements in order to ensure that not only the main component but also the parasitic components have been accounted for since they can affect the results to a very large extent.

5.2 Model architecture

In order for the model to be useful in the project and for future investigations, it is important that it is flexible both in terms of fidelity and modularity. If there are different levels of fidelity for each component model and the system model is flexible in terms of choosing between the components models, the system model can be tailored to the right overall fidelity level for a certain purpose. Furthermore, in order to make the system model reusable in future projects, it needs to be flexible in terms of which components are included and how they are connected. This leads to a modelling approach that mirrors a modular approach to product development.

When it comes to the technical details of the model, it should be defined in time domain and use an acasual modelling approach to effectively model transient physical behaviour in the electric powertrain. The transient properties of the model are, e.g., important to capture the behaviour of the switching of the IGBTs in the inverter in order to correctly simulate the high-frequency behaviour of the system. When it comes to using a casual (e.g. Simulink) or acasual (e.g. Dymola or Ansys Simplorer) modelling approach, acasual modelling has a lot of advantages when it comes to simulating physical systems. One of the main reasons is that it is relatively easy to change the model in response to a topology change in the physical system when using an acasual modelling approach. For casual modelling, the entire system model might have to be recreated in order to reflect the change in the physical system.

However, it is important to be able to couple the acasual physical plant model to controller software. In this project, the focus is on modelling the physical system, but in order to run simulations, the actual controller software needs to be represented in the model. In addition, for future use of the model, it might also be relevant to use the plant model for virtual software testing, and then it is crucial that the controller software can be coupled to the plant model in an easy manner. Since controller software is inherently casual and physical models are acasual, the model architecture needs to support coupling of casual and acasual models

In order to fulfil the demands on the model architecture, an investigation of different software tools for physical modelling was conducted in the beginning of the project. For a more detailed description of the software tool investigation, see Sec. 7. Properties that affected the choice of software tool were, among others, ability for fidelity flexibility, predefined models of components, coupling to 3D models, and coupling to controller software. Another important issue to consider is the use of the system model in a larger context. There is a general ambition in the automotive industry to simulate complex systems and in order for the model in this project to fit into a larger picture, it is important to consider interfaces to external models. An example could be to use software tools that adhere to international standards of model interfaces, such as the Functional Mockup Interface (FMI).

6 Description of Time domain and frequency domain analysis

6.1 Time and Frequency Domain Analysis

Each electric signal in the analyzed system will consist of a range of frequency components and can be represented in either time domain or in frequency domain, see Figure 6.1. Consequently, an electric circuit in general can therefore also be modeled in either the electric domain or in the frequency domain, Figure 6.2.

Time domain is the analysis of signals or time series with respect to time. An oscilloscope is a tool commonly used to visualize real-world signals in the time domain. A time-domain graph shows how a signal changes with time. For a time domain model, a transient simulation is performed where e.g. currents and voltages are solved for discrete time steps. If fast events are to be modeled (e.g. switching of an IGBT), a small time-step need to be implemented which increases the simulation time.

For the frequency domain representation, the behavior of the circuit is analyzed for each frequency. A frequency-domain graph shows how much of the signal lies within each given frequency band over a range of frequencies. Since the circuit behavior is only solved for a given range of frequencies, this type of simulation will in general take shorter time to solve.
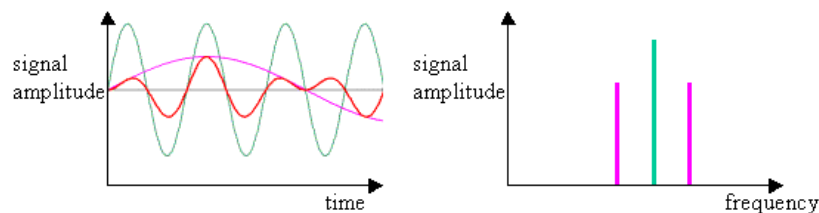
Figure 6.1 – Illustration of the frequency content in an arbitrary signal

a) Time Domain RC Circuit   b) Frequency Domain RC Circuit

$$H(\omega) = \frac{V_o(\omega)}{V_s(\omega)} = \frac{\dfrac{1}{j\omega C}}{R + \dfrac{1}{j\omega C}} = \frac{1}{1 + j\omega RC} \quad \text{Transfer Function}$$
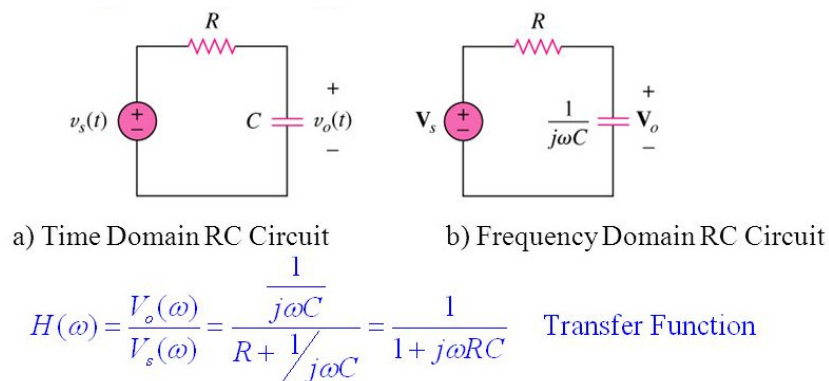
Figure 6.2 – Illustration of time domain and frequency domain representation for a simple RC-circuit.

If the circuit in Figure 6.2 is solved in both time domain and in frequency domain, the resulting responses can be seen in Figure 6.3.
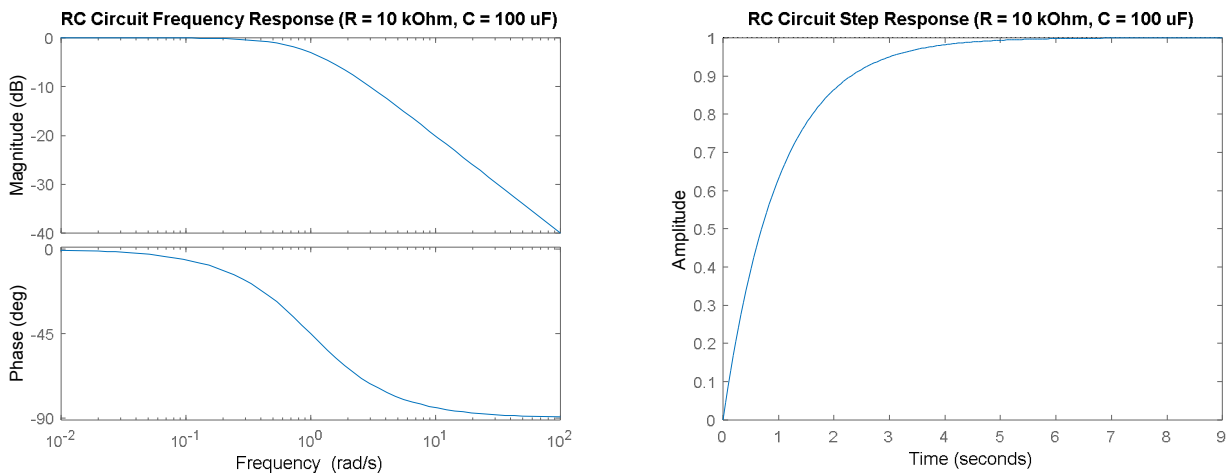
Figure 6.3 – Frequency response (left) and step response (right) of a simple RC-circuit.

6.2 Frequency Content and Sampling Time

For a given highest frequency, the lower bound of the sampling frequency is twice the frequency or Nyquist rate. For instance: for a signal whose maximum frequency is 16kHz, we need a 32kHz sampling rate. If a lower sampling rate is used, the original singal can be mixed up with other frequency components, see Figure 6.4.
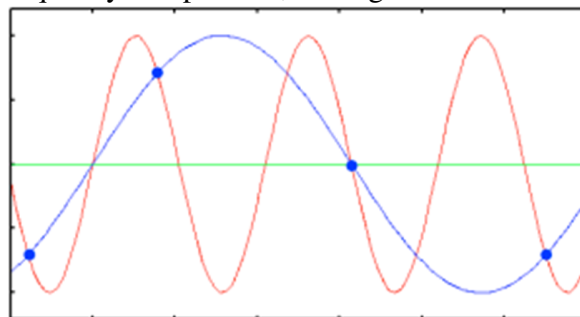

Figure 6.4 – Illustration of signal aliasing due to low sampling rate

When a signal is sampled, its contents is reduced from real numbers to integer numbers. If a signal is sampled with 32kHz sampling rate, any frequency components above 16kHz (the Nyquist frequency) will create an aliasing. Any frequency component above this frequency is indistinguishable from a lower-frequency component, called an alias, associated with one of the copies. The Fourier transform of the signal creates a symmetrical image where the energy above the Nyquist frequency is transferred below this frequency. If the signal is insufficiently bandlimited, the overlapping edges are adding and creating a spectrum, see Figure 6.5.
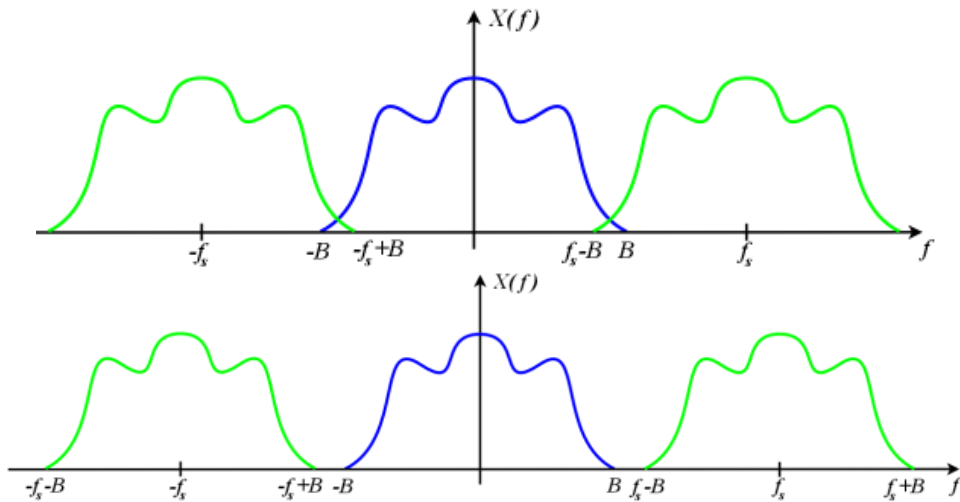
Figure 6.5 – Spectrum of an arbitrary signal with too low sampling rate (upper graph)
and proper sampling rate (lower graph)

6.3   Time Domain Modelling of the Drive train

The time domain simulation model developed in this project is shown in Figure 6.6. All signals (e.g. currents and voltages) in the circuit are solved for discrete time steps. It consists of subcircuits which all consist of RLC-circuits derived from measurements.
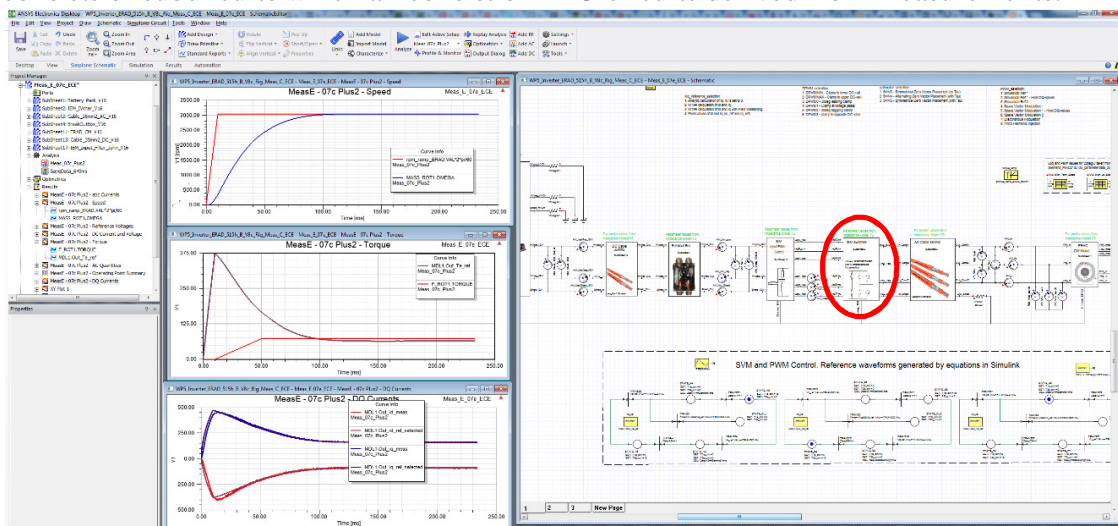
Figure 6.6 – Time domain system simulation model in Ansys Simplorer

The system is always initiated at standstill (0 rpm and 0 torque) due to difficulties to find the correct operating point of the controller and the mechanical system at the start of a simulation. The model is simulated for 600ms which is sufficient for the mechanical system to reach steady state. For the initial transient solution (0ms<t<650ms), a large time step (Hmin=2500μs) can be used which reduces the overall simulation time. If a more detailed result is needed, the minimum time step can be reduced as steady state has been reached.

The switching stage of the time domain simulation model consist of actual switches with varying complexity. Since each switching event is considered, the time step needs to be relatively small in order to capture all necessary events.

The electric machine is modeled with an equivalent circuit which means that the resulting rotational speed and electromagnetic torque is calculated for each time step.

6.4   Frequency Domain Modelling of the Drive Train

The frequency domain simulation model developed in this project is shown in Figure 6.7. As for the time domain simulation model, it consists of several subcircuits which all consist of RLC-circuits derived from measurements.

The frequency response of the circuit is solved for a discrete frequency range (typically 10Hz 10 10MHz). The result is the impedance as seen from an injected current or voltage source at one point in the model. Also, the transfer function from one quantity can be derived by the model, an example can be the transfer function from an injected current to the resulting current ripple at the DC-link.
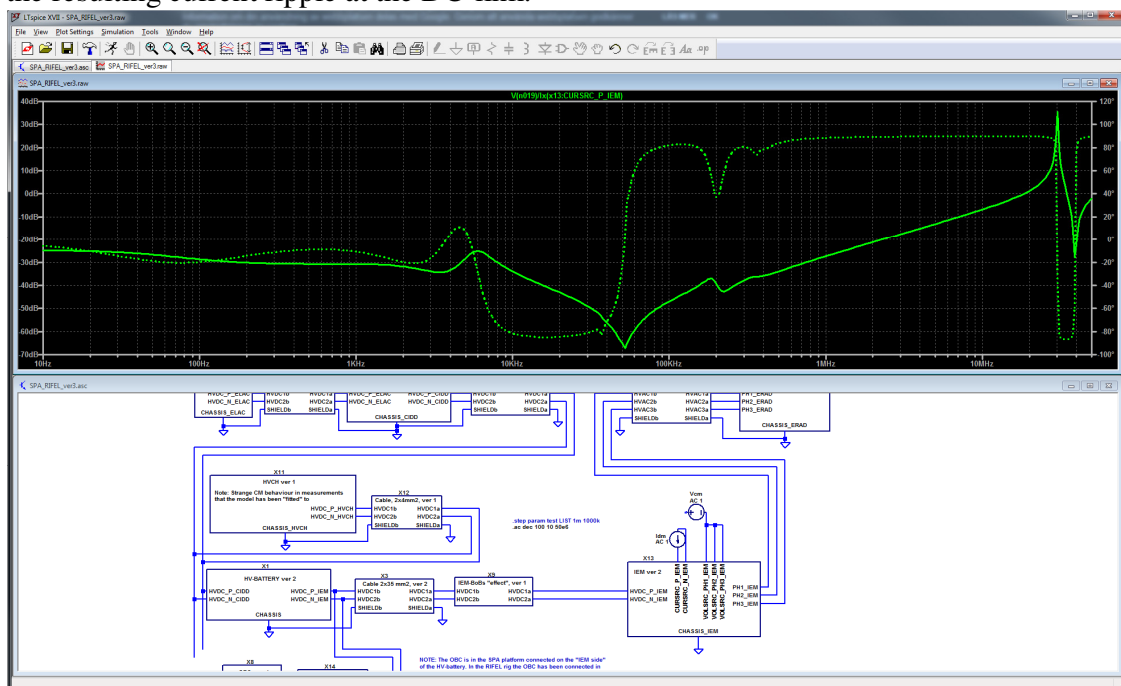
Figure 6.7 – Frequency domain system simulation model in LTspice

In the frequency domain simulation model, the actual swtiches of the switching stage are not implemented. The input to the system therefore needs to be defined externally by the user (e.g. a pulsed current generated by the inverter). However, the CM-coupling in the switching stage is included which is necessary for correct CM estimation.

The electric machine is modeled with an equivalent RLC-circuit and only considers the CM-coupling. The rotational speed and electromagnetic torque is not accounted for and as previously mentioned, the pulsed currents generated by the inverter that are the source of the current and voltage ripple in the system, needs to be calculated externally.

7 Evaluation of Simulation Tools

The project requires a software tool for performing simulations of electric circuits. A large number of such tools exists on the market. The selection of a suitable tool for this work has involved a number of criteria:

- Component libraries: Pre-defined models for important components such as battery and electric motor
- Compatibility: How the tools supports standards such as FMI; modelling languages such as VHDL-AMS, SPICE and Modelica; and linking to other relevant simulation tools such as Mathworks Simulink and ANSYS Maxwell.
- Productivity tools: Scripting environment, support for parametric studies, import of tabular data from files, etc.
- Performance: Switched power systems involve nonlinearities and many events and can be quite challenging from a numerical point of view. Significant differences exist with regards to solution speed, robustness, and accuracy.
- Existing competence an availability: Some tools are already used by the project partners.

It was not possible to perform an exhaustive analysis of all possible alternatives. Below the candidates that appeared most interesting are briefly described.

7.1 Mathworks Simscape

Simscape is built on top of MATLAB Simulink which is widely used for control systems. Whereas Simulink is causal, making it suitable for modelling of control systems and process flow, Simscape is acausal, rendering it more useful for modelling physical systems, see Figure 7.1 for an example of an implementation of an electric drive system.

With Simscape, physical component models are built based on physical connections that can be integrated with block diagrams of e.g. control systems. You model systems such as electric motors, bridge rectifiers and hydraulic actuators. Simscape add-ons such as Electronics can provide more detailed component models and analysis capabilities.
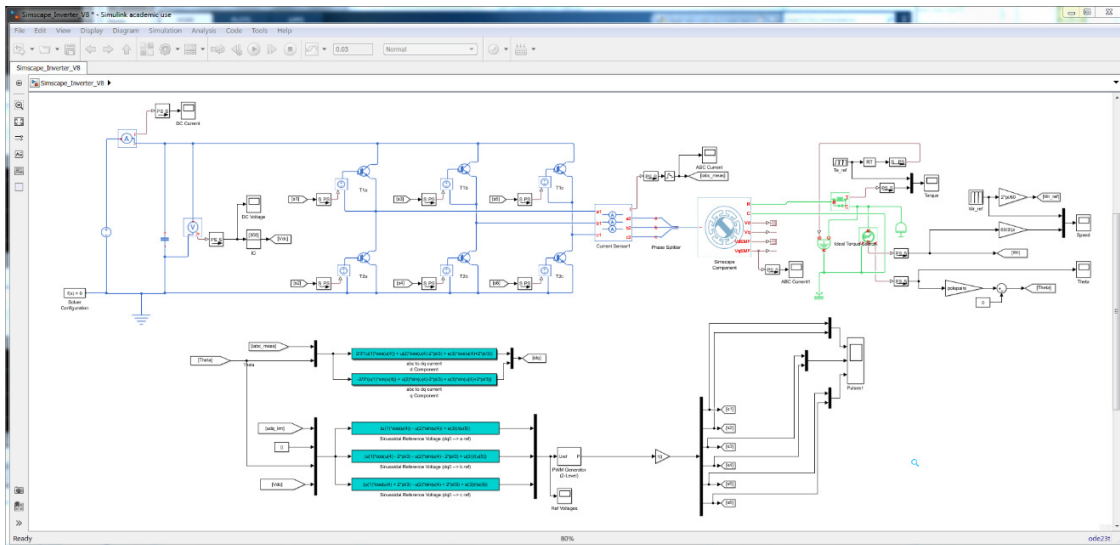
Figure 7.1 – Screenshot from Mathworks SimScape

7.2 ANSYS Simplorer

Simplorer is a tool from ANSYS originally developed for simulating electronic circuits, see Figure 7.2. It incorporates solver techniques tailored for systems featuring switching circuits and support other physical domains such as mechanical and magnetic domains. Support for the Modelica language has been implemented recently, although with certain limitations. It supports co-simulation with ANSYS Maxwell, which is used for finite element simulations of electric motors at VCC. Custom components can be defined on an equation level using the modelling language VHDL-AMS.
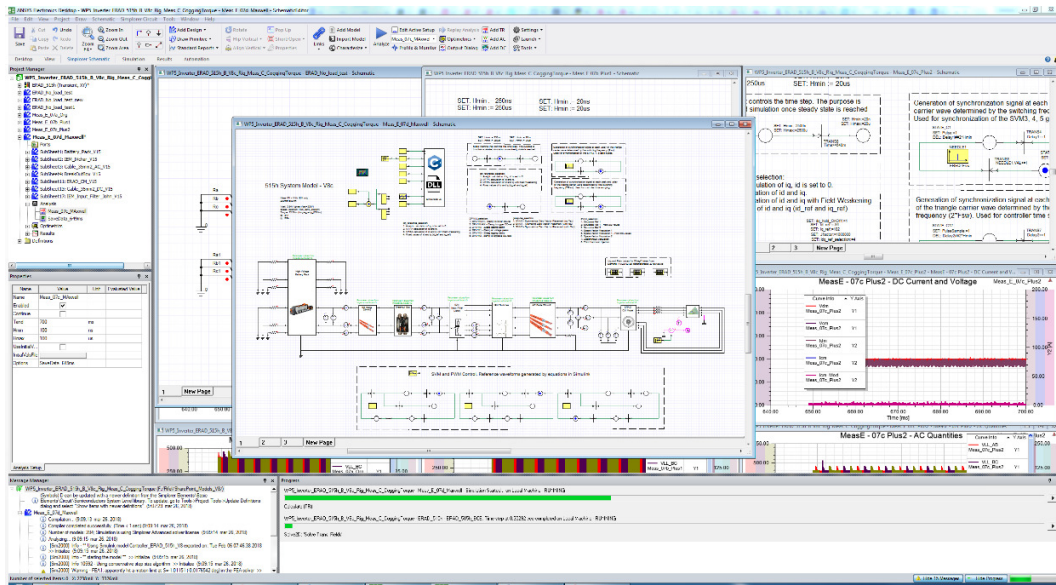
Figure 7.2 – Screenshot from Ansys Simplorer

7.3 Dymola and OpenModelica

Modelica is a domain specific programming language targeting simulation of systems of ordinary differential equations. A number of simulation tools based on Modelica exist on the market. These include the commercial tool Dymola, owned by Dassault, and used at VCC for some mechanical simulations, and the open source tool OpenModelica, see Figure 7.3. Dymola and OpenModelica have much in common and models developed in one tool can in most cases be used directly in the other. Advantages of Dymola compared to OpenModelica include a faster GUI, support for replacable components and productivity tools such as parametric sweeps. Tests also showed that its solver is more robust.
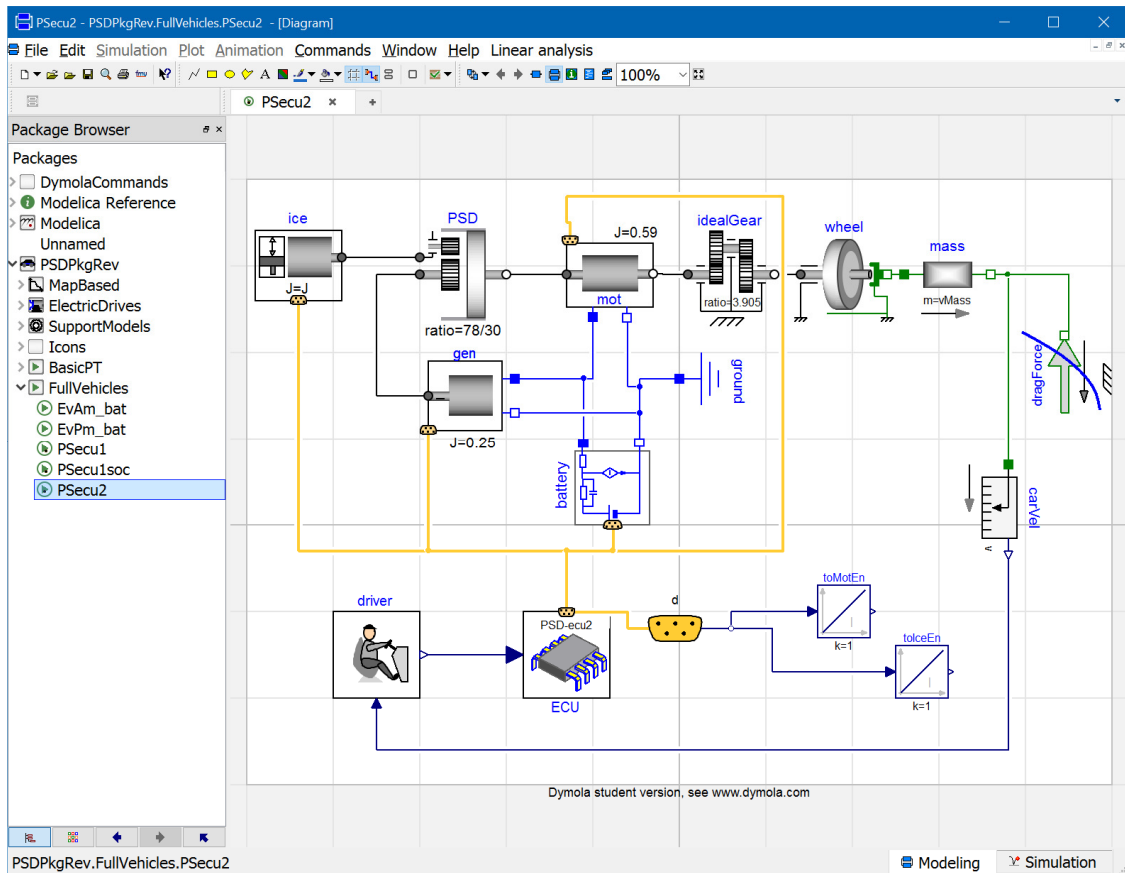
Figure 7.3 – Screenshot from OpenModelica

7.4 Synopsys SABER

Synopsys Saber is a simulation tool for mixed-signal, mixed-domain, power electronics and mechatronic systems, see Figure 7.4 for screenshot. In its appearance it is very similar to e.g. Simplorer but has previously been experienced as less robust and user friendly. Saber has not previously been by any project participants. Features of the tool include:

- Native support for standard languages VHDL-AMS & MAST.
- Ensure accuracy by accessing a library of 30,000+ component models.
- Create models quickly with data import and model characterization tools.
- Protect intellectual property with model encryption (MAST & VHDL-AMS).
- Verify hardware/software interaction with co-simulation.
- Grid computing support for expedited simulation of thousands of virtual prototypes.
- Integration with JMAG RT for simulation of electric machines
- Co-simulation with Matlab Simulink.
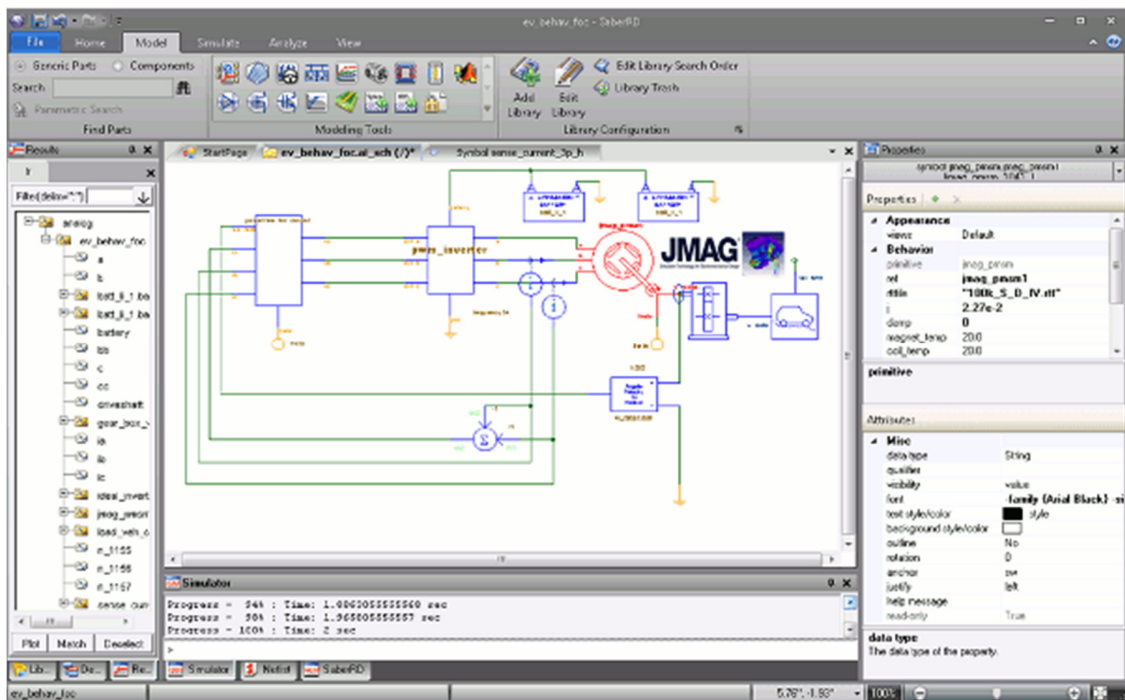
Figure 7.4 – Screenshot from Synopsys Saber

7.5 LTspice

SPICE is a widely used modelling language primarily for analogue electric circuits and has been implemented in a number of tools, both commercial and free. LTspice is one such tool that is freely available and as such has become widely used, see Figure 7.5 for screenshot It is a high performance SPICE simulator, schematic capture and waveform viewer mainly for power supply design. LTspice adds enhancements and models to SPICE, significantly reducing simulation time compared to typical SPICE simulators. LTspice is node-unlimited and third-party models can be imported. Circuit simulations based on transient, AC, noise and DC analysis can be plotted as well as Fourier analysis. Heat dissipation of components can be calculated and efficiency reports can also be generated.
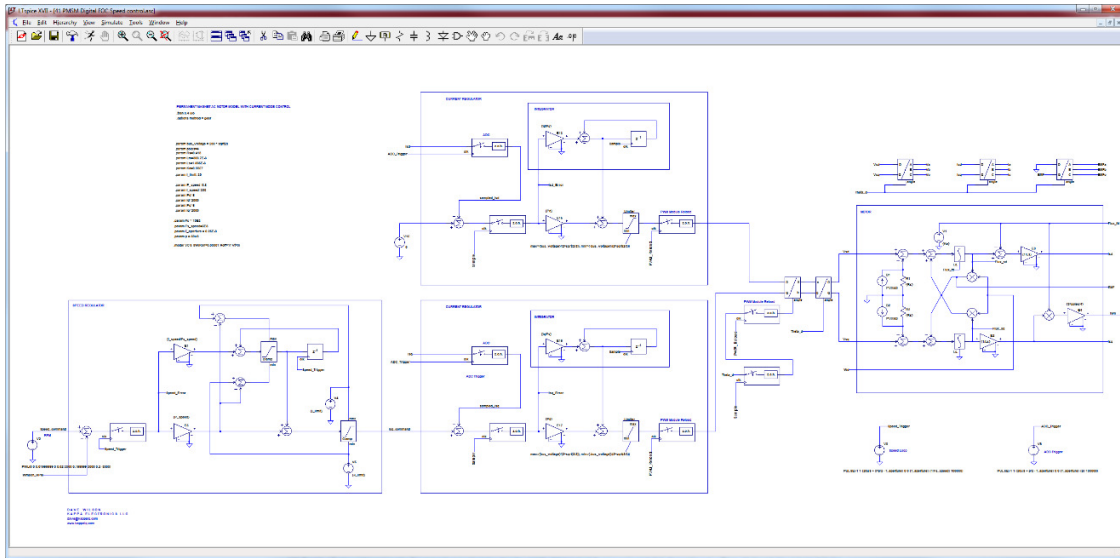
Figure 7.5 – Screenshot from LTspice

7.6 Psim

Psim is a simulation tool from Powersim which is aimed for time domain simulations of power electronics and electric drive systems, see Figure 7.6 for screenshot. The software feature add-on modules, third-party software integration and hardware target support. No project partn

- PSIM-SPICE engine
- Running LTspice from PSIM
- Motor Drive module with electric machine models, mechanical load models and control blocks of FOC and SVM.
- Motor Control Design Suite
- MagCoupler with dynamic link for PSIM and JMAG co-simulation
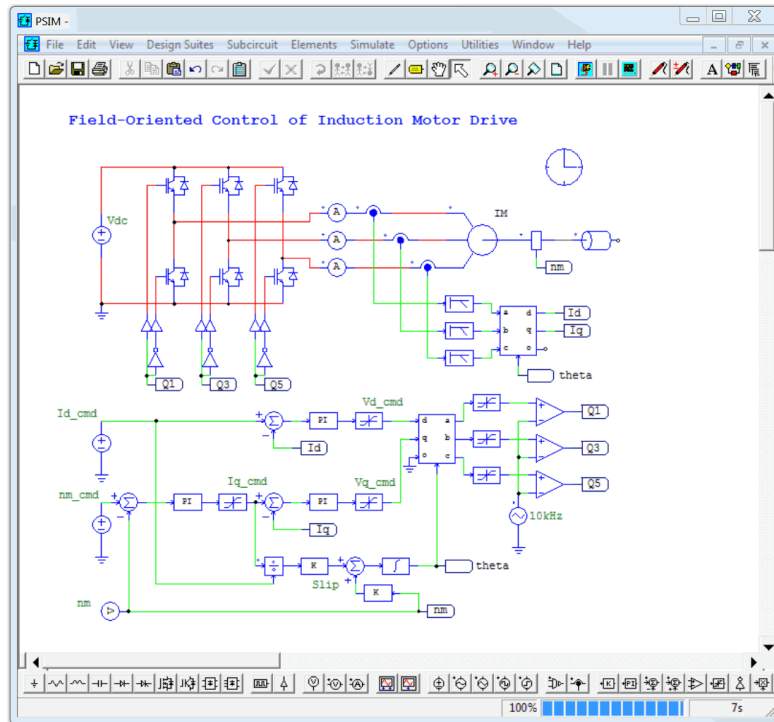
Figure 7.6 – Screenshot from Psim

7.7 Program selection

Simplorer was chosen as the main tool of development largely due to its strong solver performance and features for electric drives and its links to other ANSYS tools in use. Meanwhile, LTspie was found to be useful when pursuing an alternative track of frequency domain modelling, particularly with regards to development of impedance models for specific components that were matched to measurements and then implemented in the Simplorer system. A summary of pros and cons of the different tools that were evaluated in the project can be seen in Table 7.1.

Some work was also done to develop time domain models in Dymola/OpenModelica, however while these tools are satisfactory in many ways, it was observed that getting a converged solution could be a significant hurdle when more detailed component models were implemented, especially with OpenModelica.

Table 7.1 – Pros and cons of the different simulation tools evaluated in the project.

		Simscape	Simplorer	Dymola	SaberRD	SPICE	PSIM
Component modeling	Battery	4	4	4	4	4	4
	Inverter	4	5	4	5	2	5
	Motor	4	5	4	5	2	4
	Cables	4	4	4	5	4	4
	Control	5	4	4	4	1	4

Compatibility	Maxwell	No	Co-sim and ROM	No	No	No	No
	Simulink	Yes	Yes	Add-on	Yes	No	Yes
	Modelica	No	Yes	Yes	No	No	No
	FMI	No	Yes	Yes	No	No	No
	SPICE compo.	No	Yes	Partial	Yes	Yes	No
	Lookup tables	Yes	Yes	Yes	Yes	No	Yes
Productivity	Optimization/ statistics	Yes (via MATLAB)	Yes	MATLAB add-on	Yes	No	No?
	Scripted comps	Yes	Yes	Yes	Yes	No	No
Current availability		VCC,CTH	CTH	VCC	VCC	CTH	-

8 Cable model. Description, modelling, measurements & verification

8.1 Background

Cables can conveniently be modelled by using transmission line models. The requirement for using these models is that the extent of the cable cross-section should be small in comparison with the wavelength at the highest frequency of interest. If this requirement is not met, we cannot guarantee the assumed TEM mode of propagation and more advanced models need to be used, i.e., we need to solve the full Maxwell's equations. Inherent in the transmission line models is also that radiation losses are neglected. It should however be pointed out that once we have computed the current distribution along the length of the cable, we can compute the radiated field, so this is in practice no limitation.

8.1.1 Transmission line equations

Transmission lines and in particular multi-conductor transmission lines are very useful in cable modelling in automotive applications. The per unit-length parameters of multi-conductor transmission lines, i.e., a cable with more than two lines including the reference, will be represented by matrices. For a vehicle, one of the lines (preferably treated as reference) is the chassis of the car.

The transmission line equations in the frequency domain (the Telegrapher's equations) are given by:

$$\begin{cases} \dfrac{d}{dz}[V] = -[Z][I] \\ \dfrac{d}{dz}[I] = -[Y][V] \end{cases} \text{where} \begin{cases} [Z] = [R] + j\omega[L] \\ [Y] = [G] + j\omega[C] \end{cases} \tag{1}$$

In order to describe the multi conductor transmission line we use the so called per unit-length parameters R, L,C and G (resistance, inductance, capacitance and conductance).

It is possible to find analytic solutions to the coupled differential equations but we instead use circuit equivalent models. The attractive properties of circuit equivalent models include that circuit equivalent models can be used in many simulation programs and can be used in both time and frequency domain.

The per unit-length parameters of a transmission line are needed to setup the circuit equivalent model. The per unit-length parameters are determined by the physical dimensions of the cross section, and the material properties. If the cross section varies along the length of the cable, the cable is divided into sections with constant cross sections and the resulting circuit equivalent models are cascaded. For low frequencies it is sufficient to

consider only the per unit-length inductance and capacitance matrices. Losses can be incorporated by adding the per unit-length resistance, the conductance can often be neglected.

8.1.2   Calculation of per unit-length parameters

The assumed TEM mode in the multi conductor transmission line has a field pattern that looks the same as the electrostatic field pattern. We can therefore determine the per unit-length capacitances and inductances by solving the electrostatic case. The per unit-length parameters, the capacitances and the inductances, for a multi conductor transmission line can be determined by solving the two-dimensional electrostatic field problem for the cross section geometry. When the electrostatic field problem is solved, i.e., the electric field pattern in the cross section of the transmission line is known, the capacitances can be calculated by the use of Gauss' law. If the medium in the cross section is free space the inductance matrix can easily be determined as, [1]: $[L] = \mu_0 \varepsilon_0 [C_0]^{-1}$ where $[C_0]$ is the capacitance matrix.

If the medium in the cross section is not free space we have to calculate the capacitance matrix taking the dielectric materials into account and also calculate the capacitance matrix for the case when all material is free space. The latter has to be calculated in order to calculate the inductance matrix. In order to solve the electrostatic field problem for a two-dimensional region in the xy-plane that contains no free charges, we start with the following Maxwell equations:

$$
\begin{cases}
\mathbf{D} = \varepsilon \mathbf{E} \\
\mathbf{E} = -\nabla V \\
\nabla \cdot \mathbf{D} = 0
\end{cases}
\tag{2}
$$

where ε is the permittivity and V is the electrostatic potential.

Insertion of the first and second relation into the last relation in (2) gives for the homogeneous case:

$$
\nabla \cdot (\varepsilon \nabla V) = \nabla \cdot \left(\hat{x} \varepsilon \frac{\partial V}{\partial x} + \hat{y} \varepsilon \frac{\partial V}{\partial y} \right) = \varepsilon \left[\frac{\partial^2 V}{\partial x^2} + \frac{\partial^2 V}{\partial y^2} \right] = 0
\tag{3}
$$

In order to solve (3) numerically on a computer we approximate the derivatives by finite differences.

The field distribution for the electrostatic case satisfies the Laplace equation in two dimensions, which accordingly has to be solved. In order to solve the Laplace equation the choice in this document is to use an iterative finite difference procedure. The computer program solves the Laplace equation by an iterative finite difference method and, when

this is done in the program, integrates around the conductors in order to compute the enclosed charges, and thereby the capacitances. The introduction of a relaxation factor is speeding up the time to convergence of the code. Finally the inductance matrix is computed by inverting the free space capacitance matrix. The details of how the program works can be found in [2] and [3].

Now, when the electric potential distribution in the region can be computed with the method discussed above, the question is how to use the method in order to calculate the capacitance and inductance matrices. The capacitance matrix is a symmetric matrix, i.e., $C_{ij} = C_{ji}$. The elements in the capacitance matrix are defined by,[3]: $C_{ij} = \left. \dfrac{Q_i}{V_j} \right|_{V_m = 0, m \neq j}$

where Q_i is the total charge on conductor i due to the voltage on conductor j. The elements in the capacitance matrix satisfy the following relations:

$$\begin{cases} C_{ii} \geq 0 \\ C_{ij} \leq 0 \text{ for } i \neq j \\ C_{ij} = C_{ji} \end{cases} \qquad (4)$$

The total charge enclosed by a closed surface can be computed by Gauss' law, [4]. For the two-dimensional case, as treated here, the charge is the charge per unit-length and the surface integral is reduced to a line integral. Thus, $Q_i = -\oint_{l_i} \varepsilon \nabla V \cdot \hat{n} dl_i$ where l_i is a closed line around conductor $i, \hat{n}$ is an outward directed unit vector and V is the potential distribution. Thus, in order to calculate all elements in the capacitance matrix for a configuration with N conductors, we have to compute the potential distribution $V(x, y)$ N times (with different boundary conditions) and perform the integration according to Gauss' law $N + (N-1) + ... + 1$ times. As an example, the procedure for the configuration in Figure 8.1 will be as follows:

1. Compute the potential distribution when the potential on conductor 1 is unity and zero on conductor 2.
2. Compute the charges on conductor 1 and 2.
3. Compute the capacitances C_{11}, $C_{12} = C_{21}$
4. Compute the potential distribution when the potential on conductor 1 is zero and unity on conductor 2.
5. Compute the charge on conductor 2.
6. Compute the capacitance C_{22}

Figure 8.1 - Two conductors over a reference.

In order to describe the multi conductor transmission line we use the so called per unit-length parameters R, L,C and G (resistance, inductance, capacitance and conductance). In the following we ignore the conductance. For all cases except for the 1-line these parameters are matrices. The diagonal elements in the matrices are associated with self-terms and the off-diagonal elements with mutual terms. As an example a short section of a 2-line and the per unit-length matrices are shown in

Figure 8.2.
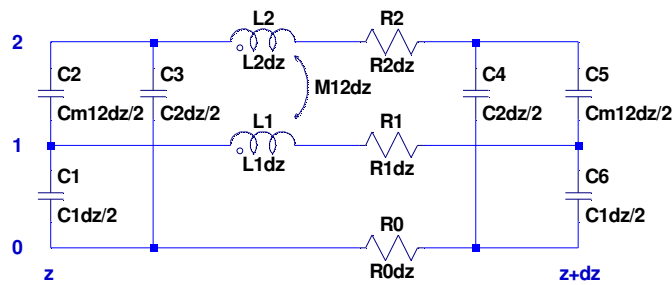
$$[R]=\begin{bmatrix} R1+R0 & R0 \\ R0 & R2+R0 \end{bmatrix} [L]=\begin{bmatrix} L1 & M12 \\ M12 & L2 \end{bmatrix} [C]=\begin{bmatrix} C1+Cm12 & -Cm12 \\ -Cm12 & C2+Cm12 \end{bmatrix}$$

Figure 8.2 - Short section of a 2-line and the per unit length matrices.

The relations between the elements in the per unit-length matrices and the individual components in the short lumped section can seem to be strange at first, especially the negative entries in the capacitance matrix. However, if Kirchoff's voltage and currents laws are applied to the lumped section in

Figure 8.2 and the equations for the voltages and the currents are written in matrix form (equation 1), the relations can be understood.

The model for the short section shown in

Figure 8.2 is called a pi-section. This model is not the only one possible, other models can be used but the parameters are the same. For lossless lines the resistance, R, and the conductance, G, are both equal to zero. The assumption of a lossless line is often used and is usually a very good approximation for real cases. If losses should be taken into account this is usually done by assuming some resistance and still letting the conductance be equal to zero. The resistance for the conductors are in general frequency dependent, through the

skin depth, but the DC-approximation often provides a sufficient accuracy. The resistance, R, represents losses in the conductors while the conductance, G, represents losses in the medium between the conductors (dielectric losses).

8.1.3   Per unit-length parameters to circuit equivalent model

The strategy for computing the per unit-length capacitances and inductances discussed in chapter 8.1.2 was incorporated in a computer program FD2D [5] that can be used on an ordinary PC. The executable windows program can be downloaded from the website www.sp.se/en/index/research/emc/Sidor/FD2D.aspx.

In Figure 8.3, the cross-section of two wires over ground has been modelled and the capacitance and inductance per unit-length matrices have been computed. For generation of a SPICE circuit file (*.cir) the length of the transmission line, number of pi-sections and start numbering of nodes have to be specified, see Figure 8.4. The inductance and capacitance values are then converted into a pi-section structure. Depending on the electrical length of the transmission line, more than one pi-section might be needed. As a rule of thumb, each section should have an electrical length not exceeding 1/10 of the wavelength at the highest frequency of interest.
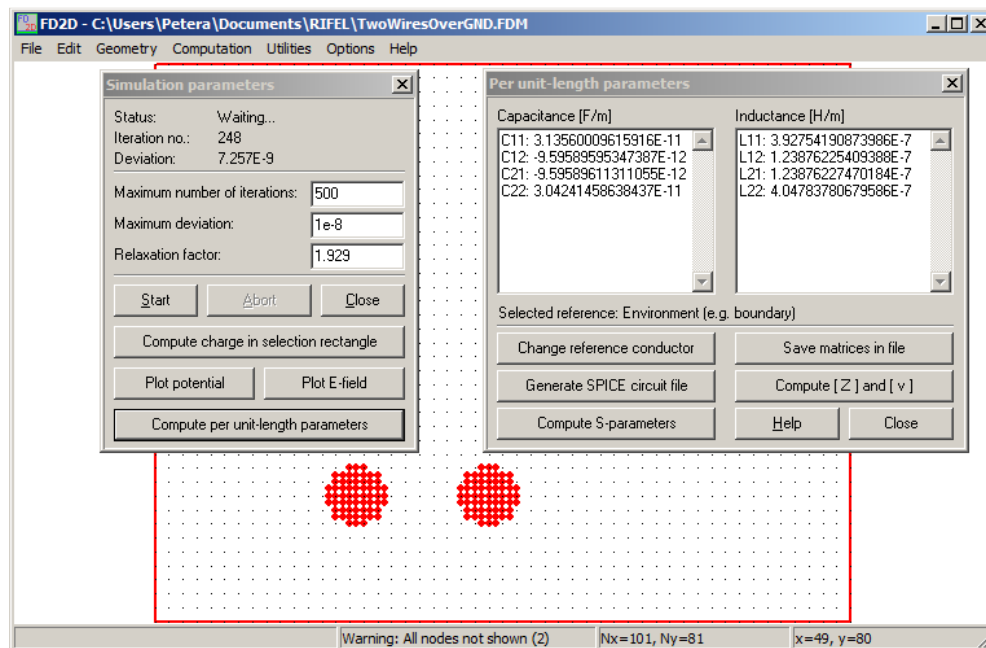
Figure 8.3 - User-interface of the finite difference program, FD2D, for determination of the per-unit length parameters. In the figure two wires over a ground plane is analyzed.
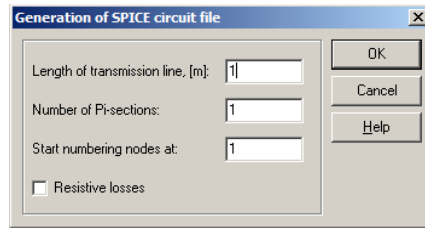
Figure 8.4 - Generation of a SPICE circuit file after the computation of L and C matrices.

Below is shown the generated SPICE circuit file (netlist) for the 2-wire transmission line shown in Figure 8.3, where the length has been set to 1m. In Figure 8.5 the components in the pi-section structure together with additional source and loads are shown.

```
* Lumped section number 1
* TL Two wires over GND
C0 2 1 1.08801e-11
C1 3 1 1.04141e-11
C2 3 2 4.79795e-12
L1 2 4 3.92754e-07
L2 3 5 4.04784e-07
K0 L1 L2 0.310682
C3 4 1 1.08801e-11
C4 5 1 1.04141e-11
C5 5 4 4.79795e-12
```
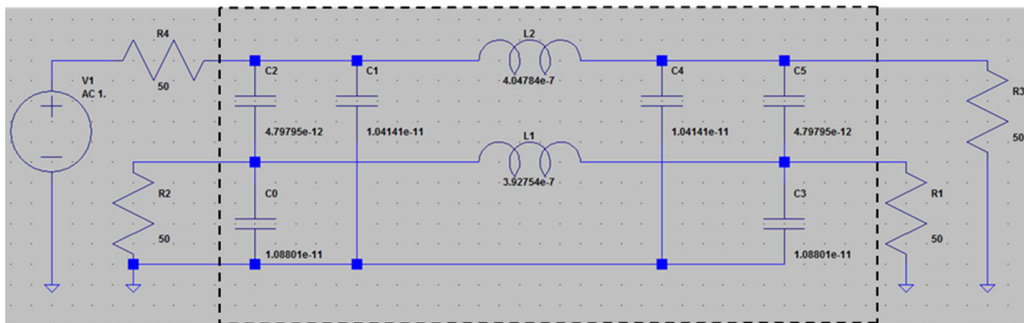

Figure 8.5 - Circuit equivalent for two wires over ground modelled using one pi-section(inside dashed rectangle) and additional source and loads.

8.1.4   Sub-circuit model from SPICE circuit file

With a SPICE circuit file (*.cir) as input, the file is converted into a sub-circuit library file (*.lib) for making it easier to use in a circuit analysis program. This is done by adding the commands *.subckt* at the beginning and *.ends* at the end of the netlist, see below. The *.subckt* statement is followed by the name of the sub-circuit followed by the ports (e.g. .subckt Twowire 1 2 3 4 5). The sub-circuit is ended with the *.ends* statement. The netlist

is saved as *filename*.lib, the name does not have to be the same as the name of the sub-circuit.

The .param command is used to pass parameters to the sub-circuit, in this case Length which represents the physical length of the transmission line. In this way any length can be passed to the transmission line model, see chapter 8.1.5.

Note! For the intended use of the parameter Length, the length of the transmission line has to be set to 1 m in "Generation of SPICE circuit file", see Figure 8.4.

```
* Lumped circuit representation of a MTL
* generated by FD2D (c) Jan Carlsson, SP
* Input nodes of the MTL:
*   Reference: Node 1
*   Line 1: Node 2
*   Line 2: Node 3
* Output nodes of the MTL:
*   Reference: Node 1
*   Line 1: Node 4
*   Line 2: Node 5
* Lumped section number 1
* TL Two wires over GND
*                Ref In1 In2 Out1 Out2
.subckt TwoWire  1   2   3   4    5
C0 2 1 {1.08801e-11*Length}
C1 3 1 {1.04141e-11*Length}
C2 3 2 {4.79795e-12*Length}
L1 2 4 {3.92754e-07*Length}
L2 3 5 {4.04784e-07*Length}
K0 L1 L2 0.310682
C3 4 1 {1.08801e-11*Length}
C4 5 1 {1.04141e-11*Length}
C5 5 4 {4.79795e-12*Length}
.param Length={1}
.ends TwoWire
```

8.1.5   Graphical symbols linked to a sub-circuit

In LTspice [6], a graphical symbol representing a device can be linked to a sub-circuit. In Figure 8.6 is shown a user-defined graphical symbol of a 2-wire transmission line model. The symbol is drawn using lines, rectangles, circles etc in LTspice Symbol Editor. Ports are placed in connection to the symbol. The order of the ports corresponds to the order of the ports in the sub-circuit. The port's function relates to the connection specified in the sub-circuit netlist. A label can be inserted, but has nothing to do with the function of the port. In the example below, for a 2-wire transmission line model, the labels Ref, In_1, In_2,

Out_1 and Out_2 correspond to port 1, 2, 3, 4 and 5, respectively (see netlist numbers in chapter 8.1.4).
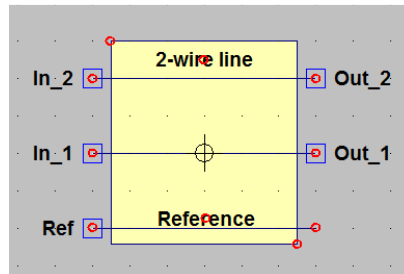
Figure 8.6 - User-defined graphical symbol of a 2-wire over ground transmission line model.

In the Symbol Attribute Editor (Edit -> Attributes -> Edit Attributes), see Figure 8.7, the 'Prefix' set to X tells LTspice that this is a sub-circuit. 'Value' is the name of the sub-circuit that the symbol will be linked to and SpiceLine is used to pass parameters (.param) to the sub-circuit. The user-defined parameter Length may be set to a value corresponding to the physical length of the transmission line. (The .param command is used to pass parameters to the sub-circuit. In this case the parameter Length is the length of the transmission line). In this example the graphical symbol in Figure 8.6 is equivalent to the transmission line model in Figure 8.5.
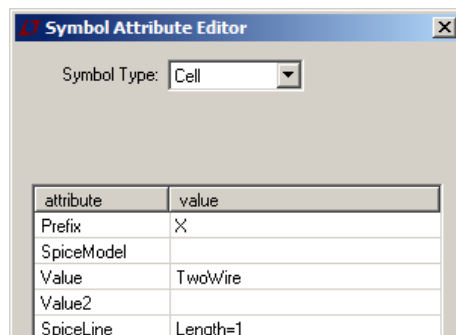
Figure 8.7 - Symbol Attribute Editor.

8.1.6 Use of graphical symbol in the circuit diagram

In Figure 8.8 an example using the user-defined symbol of the 2-wire over ground transmission line model is shown, see Figure 8.6. In the circuit diagram the sub-circuit is used together with additional components such as a voltage source and resistive loads. The circuit in Figure 8.8 is equivalent to the circuit shown in Figure 8.5. To be able to run the simulation in LTspice, a SPICE Directive has to be included in the schematic with the path of the sub-circuit file (e.g. .lib C:\Users…\TwoWire.lib).
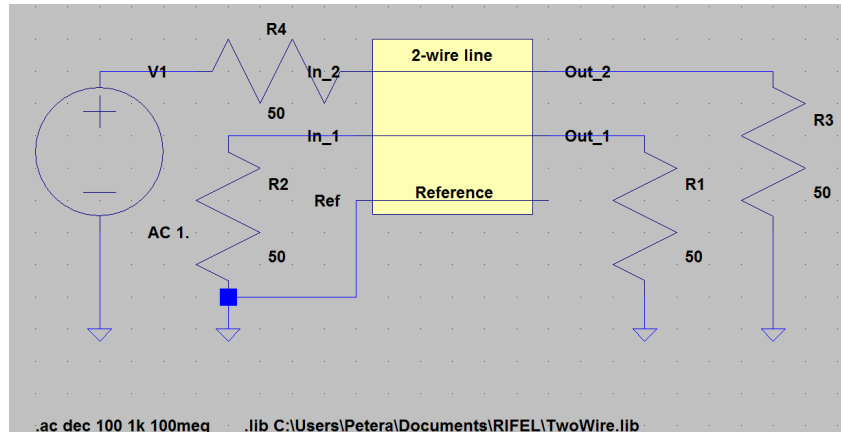
Figure 8.8 - User-defined 2-wire line model including one pi section (yellow box) and additional source and loads.

8.1.7   More than one pi-section in SPICE circuit

In the generation of the SPICE circuit file, see Figure 8.4, the number of pi-sections for the transmission line is set so that the electrical length is not exceeding 1/10 of the wavelength at the highest frequency of interest. In Figure 8.9 is shown the same example as above but with three instead of one pi-section for modelling the transmission line.

In Figure 8.10 a circuit diagram with a user-defined 2-wire line model including 3 pi sections and additional source and loads is shown. The graphical symbol and corresponding sub-circuit has been created in the same way as in 8.1.4.
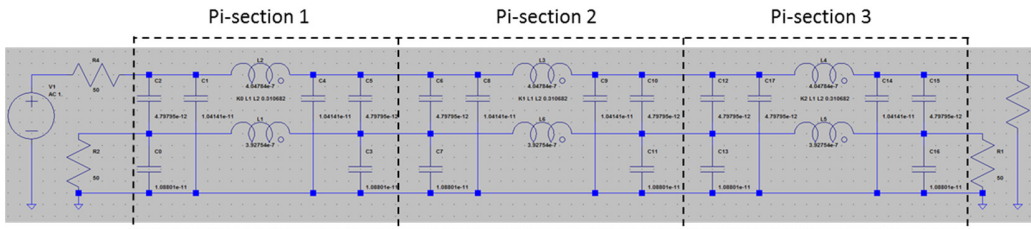
Figure 8.9 - Transmission line model l for a three pi-section model (inside dashed rectangle) and additional source and loads.
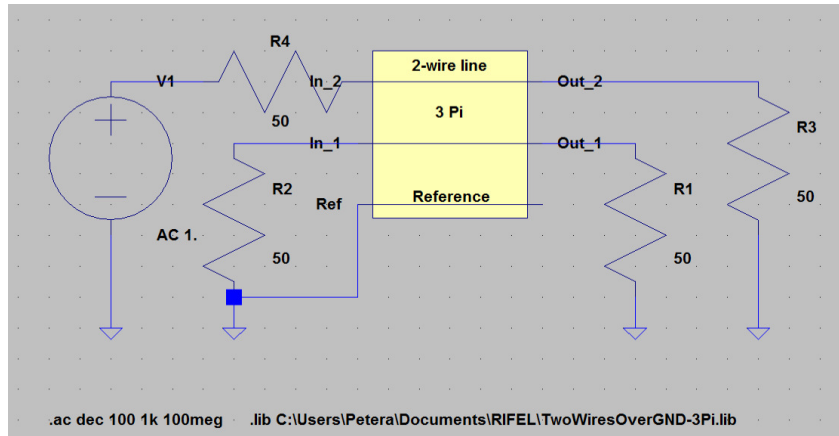
Figure 8.10 - Circuit diagram with user-defined 2-wire line model including 3 pi sections (yellow box) and additional source and loads.

8.1.8   Comparison of one and three pi-section circuit model

We will make a comparison of the result using a one and a three pi-section 2-wire transmission model. We will use the same models as in Figure 8.8 and Figure 8.10. The computed quantity is the voltage at Out_1, the exciting voltage source is set to 1 volt. The length of the transmission line is set to 0.3 m which means that each pi-section in the three pi-section model is set to 0.1 m. As can be seen, in Figure 8.11, the voltage at Out_1 is the same for both cases in the frequency interval 1 kHz to 100 MHz. This means it is sufficient with one pi-section transmission model for frequencies below 100 MHz, for the considered length of the transmission line.
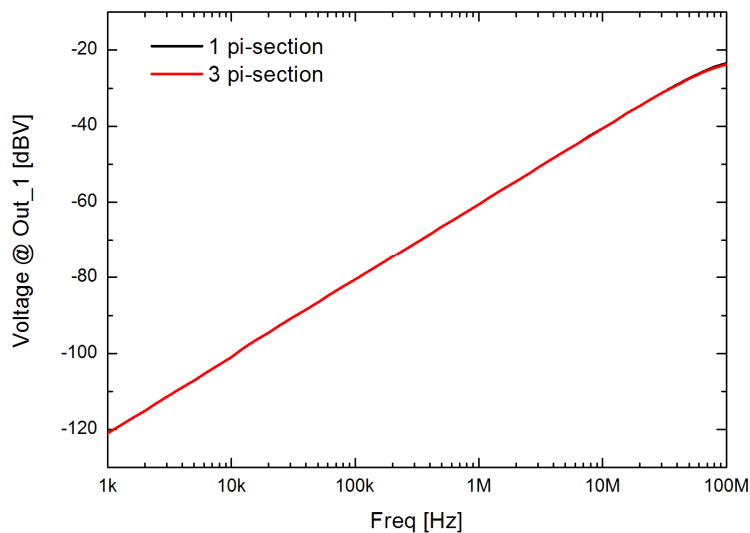
Figure 8.11 - The voltage at Out_1 for a one and three pi-section model of a 2-wire transmission line, respectively. The excitation was 1 volt and the transmission line length was 0.3m.

8.1.9 Many sub-circuits cascade coupled

In a vehicle the cross-section geometry of the cable will vary along the length of the cable. For such a case we need to create sub-circuits for each section with a constant cross-section and cascade these circuits in order to model the whole length of the cable. In Figure 8.12 is shown an example of three cascaded sub-circuits. In this particular case, the sub-circuit of the 2-wire model in 8.1.7 is re-used but the length of each sub-circuit consisting of one pi-section is set to 0.1 m. Thus, the total length of the transmission line is 0.3 m.

We will make a comparison of this model including three sub-circuits and the models described in chapter 8.1.4, and once again consider the voltage at Out_1. As can be seen in Figure 8.13, the voltage at Out_1 is the same for all models in the frequency interval 1 kHz to 100 MHz. Thus, the sub-circuits can be cascade coupled after each other without loss of accuracy. This also implies that we can approximate two single wires along a car chassis with a varying cross-section (e.g. varying distance to the chassis along the length) as a number of cascaded sub-circuits.
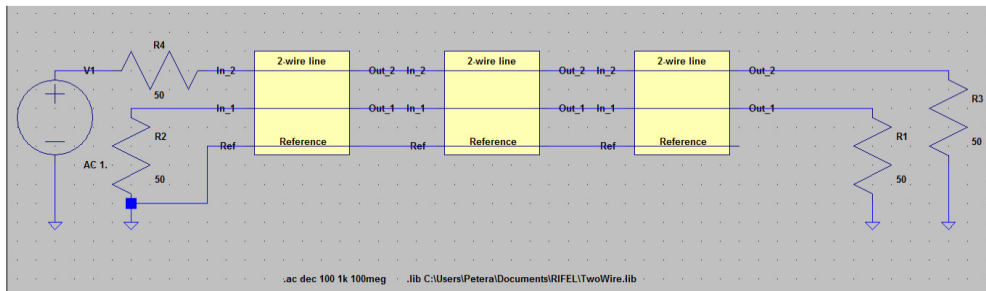
Figure 8.12 - Circuit diagram with three user-defined 2-wire line transmission models, each including 1 pi section (yellow box) and additional source and loads.
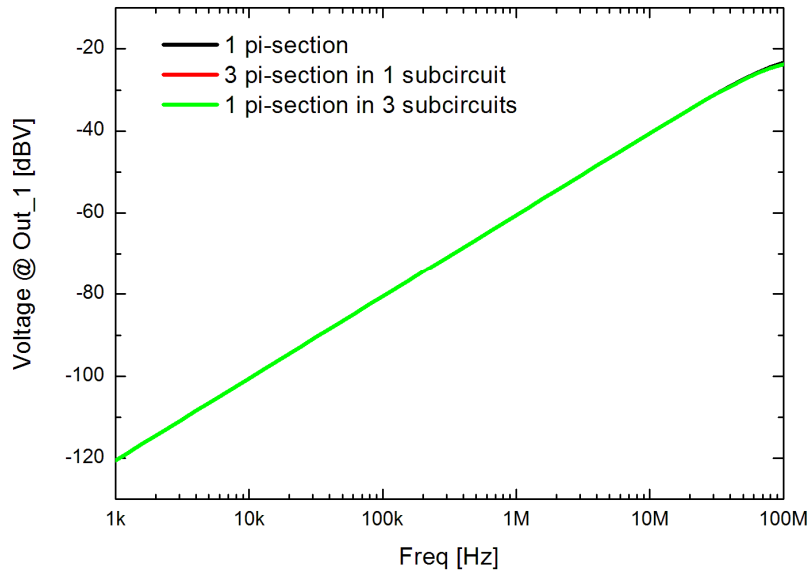
Figure 8.13 - The voltage at Out_1 for a one pi-section, three pi-section models and three sub-circuits each with a pi-section, respectively, for a 2-wire transmission line. The excitation was 1 volt and the total transmission line length was 0.3m.

8.2 Cable modelling strategy

Based on the discussions in the previous section, the cable modelling strategy can be summarized in the following steps;

- Determine the cable cross-section including the material properties
    - If the cross-section varies along the length, divide the cable in sections with uniform cross-sections
- Compute the per unit-length matrices for each uniform section, use, e.g., FD2D
- From the per unit-length matrices, create circuit equivalent models, one for each uniform section
    - If a section is longer than one tenth of the wavelength at the highest frequency of interest, use more than one pi-section
- Make a sub-circuit that is more conveniently use in a circuit simulation program such as LTSpice or Ansys Simplorer

These steps are visualized in Figure 8.14.
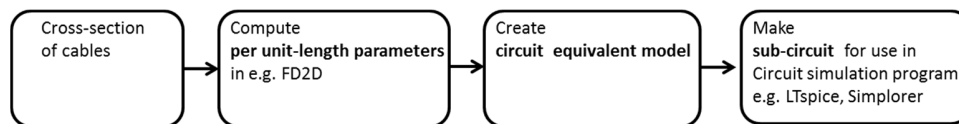
Figure 8.14 - Cable modelling strategy.

For shielded cables, such as high voltage cables in vehicles, the problem has to be divided into two parts, one inner problem and one outer. The cross-section for the inner problem is then defined as the area between the conductors inside the shield and the shield itself, and the cross-section for the outer problem is defined as the area on the outside of the shield. The reference for the inner problem is the shield, and for the outer the chassis of the vehicle. Often can the shield be considered to be ideal, especially for low frequencies and high quality shields. For this case the coupling between the inner and outer problems takes place only at the ends of the cable. For non-ideal shields the coupling along the cable can be modelled with the transfer impedance of the shield. In general is the transfer impedance complex but for low frequencies it is purely resistive, simply given as the DC-resistance which easily can be computed, or measured. Coupling through the transfer impedance can be taken into account by the use of a current controlled voltage source.

8.3 Measurement of resistance for cables and connectors

In this chapter we measure the DC resistance of the cables and connectors in the chain from the battery housing/chassis via the inverter to the electric machine. This includes the DC- and AC-cables, inner-conductors and shield, the connectors and part of the housing for battery and inverter.

The main components of the electric powertrain are the battery, DC-cable, inverter, AC-cable and electric machine. In Figure 8.15, the DC-cable, AC-cable with attached connectors and part of the housing for the battery and inverter can be seen.
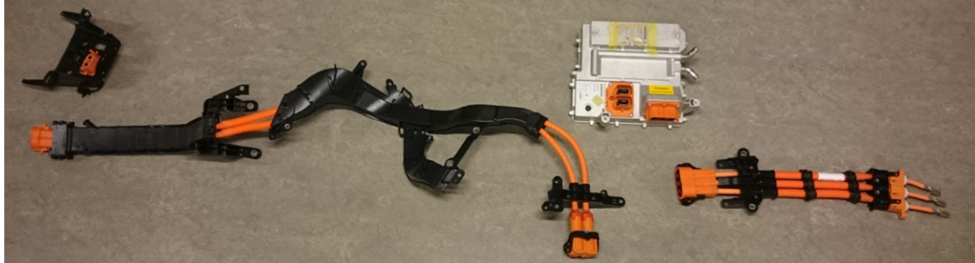
Figure 8.15 - The DC-cable, AC-cable with attached connectors and part of the housing for the battery and inverter.

The instrument used for measuring DC low ohm resistance is an Agilent 34420A micro ohm meter.
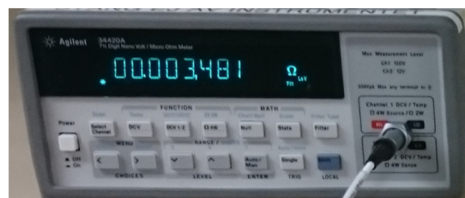
Figure 8.16 - Micro ohm meter.

8.3.2   Copper cable

In this report copper cables with a length of 1 m and a radius of 1 mm are used for measuring the coupling between cables that are used in the test rig, see chapter 2.
We use the DC micro ohm meter to measure the resistance on a 1 m long copper cable. The measured resistance was 5.47 mΩ.

Figure 8.17 - Copper cable with a diameter of 2 mm and length of 1 m.

Theoretically the resistance of the cable is $R = \rho \cdot l / A$. For copper the electrical resistivity ρ is $1.68 \cdot 10^{-8}$ $(\Omega \cdot m)$. The cross-sectional area is $A = \pi \cdot r^2$ (m^2). For a 1 m long copper cable with a radius of 1 mm the theoretical calculated resistance is 5.34 mΩ. This is quite close to the measured resistance of 5.47 mΩ.

8.3.3 DC cable with attached connector at inverter

According to data specifications of the high voltage cable, used for the DC-cable and AC-cable, the resistance of the inner conductor and shielding is at DC 0.527 mΩ/m and 3.5 mΩ/m, respectively. The DC-cable, connectors with unknown resistance are attached to both ends of the cable. The DC-cable is almost 2 m.

In the measurement setup, see Figure 8.18, the DC-cable with connectors and part of the inverter housing can be seen.
-   The measured DC resistance between the shield at one connector and the inverter housing at the other end is about 7.6 mΩ. This includes the resistance of the almost 2 m long shield, two connectors and part of the inverter housing.

-   The measured DC resistance between the inner conductor at connector 1 and the inner conductor at connector 2 is about 1.2 mΩ. This includes the resistance of the almost 2 m long conductor and two connectors.
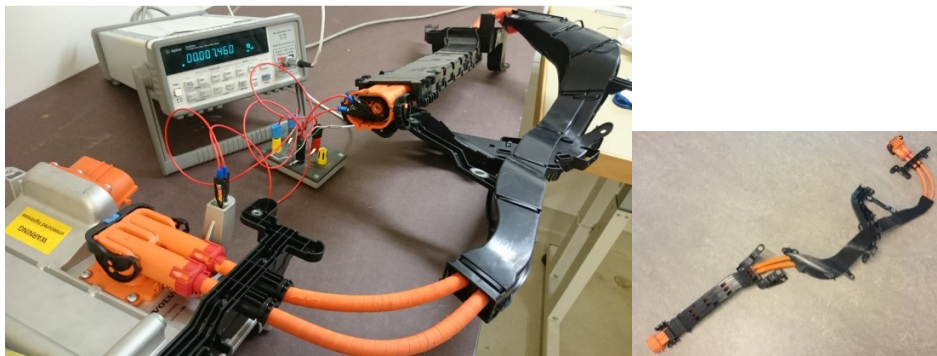
Figure 8.18 - DC cable with connectors at both ends.

8.3.4 DC connector on battery housing

The DC connector consists of the inner conductors and the screens. The inner conductors are of compactly packed stranded metal wires. However, the connector's screens are on the backside split into metal "tongues" that should get in contact with the metal housing/chassis of the battery, see Figure 8.19.

The first measurements of the DC resistance between screens and battery housing/chassis showed a big difference in resistance between the screens and chassis, see below. Therefore, the DC connector and battery housing were separated and reassembled. But the measured DC resistances discrepancy was even higher. After a new modification the resistances changed once again. So, it seems that the current design of the mating surfaces on the battery for the DC-cable connector gives poor repeatability and big difference between screen 1 and screen 2.

First measurement:

Screen 1 to chassis: 4.2 mΩ
Screen 2 to chassis: 2.4 mΩ
Screen 1 to screen 2: 6.3 mΩ
After modification 1
Screen 1 to chassis: 12.0 mΩ
Screen 2 to chassis: 1.92 mΩ
Screen 1 to screen 2: 14.0 mΩ
After modification 2
Screen 1 to chassis: 2.8 mΩ
Screen 2 to chassis: 5.8 mΩ
Screen 1 to screen 2: 9.0 mΩ
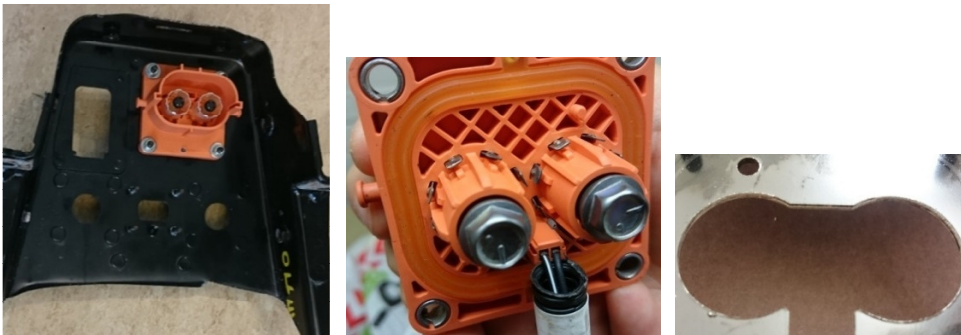
Figure 8.19 - Left – DC cable connector (outside battery) on part of battery housing (outside). Middle –Battery connector with metal "tongues", Right – Battery housing (inside battery) where DC connector "tongues"(Middle) get in contact with battery housing.

Figure 8.20 - Measurement of resistance between housing/chassis for battery and screen on DC connector.

8.3.5   DC connector on inverter housing

The DC connector, see Figure 8.21, consists of the inner conductors and the screens. The measured DC resistance between screens and inverter battery/chassis of the DC connector is equal to or below 7.5 mΩ, see below.

Screen 1 to chassis: 7.5 mΩ
Screen 2 to chassis: 7.4 mΩ
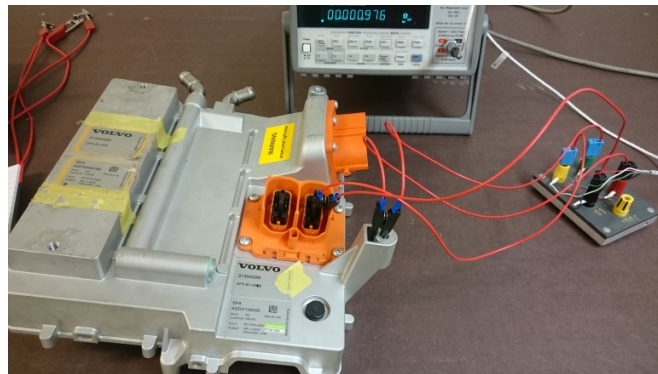
Figure 8.21 - Measurement of the resistance between shields in the DC connector and the inverter housing.

8.3.6   AC cable

According to data specifications of the high voltage cable, used for the DC-cable and AC-cable, the resistance of the inner conductor and shielding is at DC 0.527 mΩ/m and 3.5 mΩ/m, respectively. For the AC-cable a connector, with unknown resistance, is mounted on the "right" end side of the cable, see Figure 8.22. The AC-cable is about 0.6 m.

The measured resistance from screens at connector to screen on the other side of the AC cable is equal to or below 4.11 mΩ. The measured resistance from conductor at one end to the other end is equal to or less than 0.44 mΩ.

Screen 1: 2.99 mΩ
Screen 2: 4.11 mΩ
Screen 3: 3.33 mΩ

Inner conductor 1: 0.42 mΩ
Inner conductor 2: 0.44 mΩ
Inner conductor 3: 0.42 mΩ
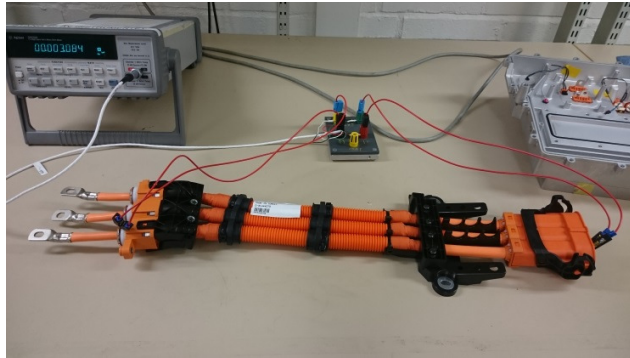
Figure 8.22 - AC cable with connector on the right side and motor connections of inner conductors on the left side.

8.3.7 AC cable with attached connector at inverter

The measured resistance from screens at "left" end to the housing/chassis of the inverter is equal to or below 4.60 mΩ.

Screen 1: 3.12 mΩ
Screen 2: 4.60 mΩ
Screen 3: 3.45 mΩ
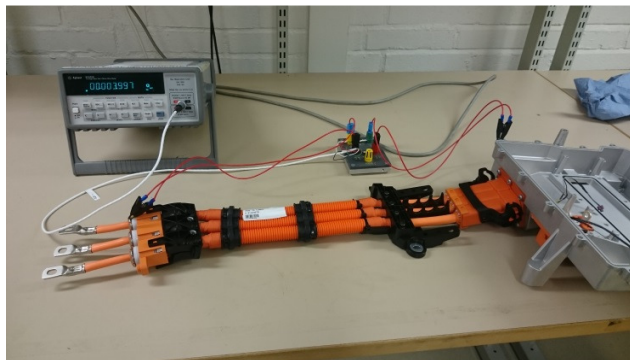
Figure 8.23 - AC cable with inner conductors on the left side and inverter housing/chassis on the right side.

8.3.8 AC connector on inverter housing

The AC connector, see Figure 8.24, consists of the inner conductors and the screens. The measured DC resistance between screens and inverter housing/chassis of the AC connector is equal to or below 0.8 mΩ, see below.

Screen 1 to chassis: 0.6 mΩ
Screen 2 to chassis: 0.8 mΩ
Screen 3 to chassis: 0.4 mΩ
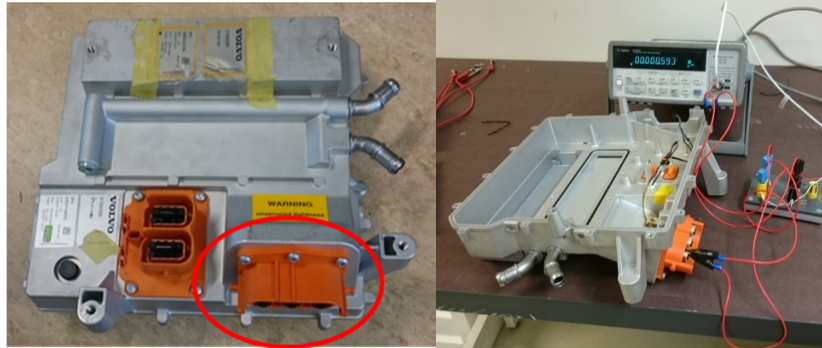
Figure 8.24 - Housing of inverter with AC cable contact (marked red). Measurement of resistance between screen and housing/chassis of inverter.

8.3.9 Between two points on housings

The resistance is measured on two different points on the housing/chassis of the battery and inverter, respectively.

The measured resistance between 2 points on battery housing/chassis: 0.03-0.05 mΩ.

The measured resistance between 2 points on inverter housing/chassis: 0.03-0.05 mΩ
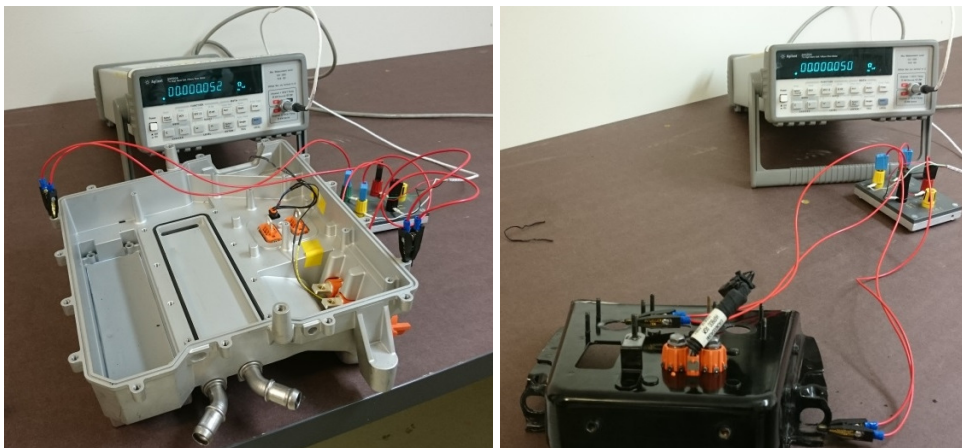
Figure 8.25 - Measurement of resistance between 2 points on housing/chassis for battery and inverter, respectively.

8.4 Measurement of near-end and far-end crosstalk

8.4.1 Measurement equipment and setup

The instrument for measuring S-parameters is a R&S Network Analyzer ZVRE, see Figure 8.26. This instrument has 2 ports and the measurement frequency interval is from 9 kHz to 4 GHz. The output voltage level can be adjusted with the internal amplifier.

Figure 8.26 - Network analyzer ZVRE for measuring S-parameters.

The test rig for cable measurements, see Figure 8.27, consists of an 800x1500 mm copper plane and two adjustable 5 mm thick copper plates each with a "vertical dimension" of 210x300 mm. The plates are separated 1 m from each other. The height over copper plane and distance between the holes in the plate where connectors are attached can be seen in Figure 8.28.

Figure 8.27   Test rig for cable measurements over copper plane. Here two copper cables are attached to the N-connectors on the copper plates and additional loads.
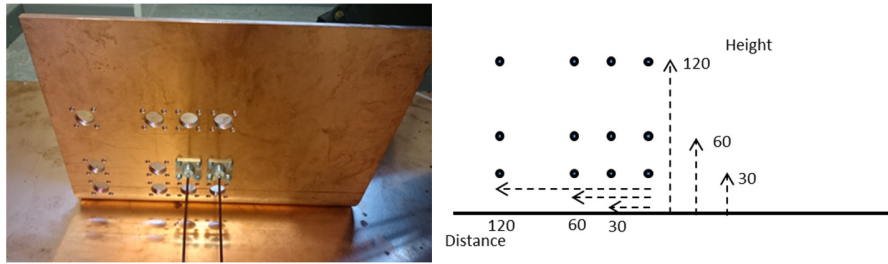
Figure 8.28 - Left figure: Part of test rig consisting of copper plate where N-connectors with copper wires are attached. Right figure: Measure of distance and height between holes for the connectors.

8.4.2   Far-end crosstalk between two cables

In the following, measurements of far-end crosstalk between parallel cables, as function of height over a copper plane, are studied.

Two copper cables, each with a length of 1 m and a diameter of 2 mm, were soldered to a N-connector at both ends, similar to what is shown for RG58 cables in Figure 8.46. The N-connectors, were mounted to the copper plate at each end. In Figure 8.28 is an example showing the cables mounted at a distance of 30 mm between each other at a height of 60 mm.

The output voltage of the network analyzer was set to 1 V. The frequency span was set to 9 - 100 kHz. In Figure 8.29, the schematic for measuring far-end crosstalk (S21), with a network analyzer, of two parallel cables in the test rig with 50 ohm terminations is shown. The distance between the two parallel cables were 30 mm and the height over the copper plane for the cables was varied in the interval 30, 60 and 120 mm, respectively. For each height, the S-parameter S21 was recorded, see Figure 8.30. As can be seen, the far-end crosstalk is increasing as the frequency gets higher. We also see that the crosstalk increases as we move the transmission lines further away from the ground.
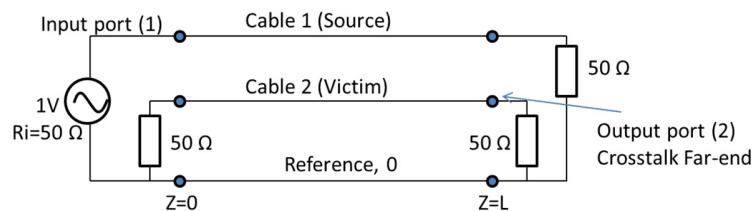
Figure 8.29 - Schematic for measuring far-end crosstalk (S21), with a network analyzer, of two parallel cables in the test rig with 50 ohm terminations.
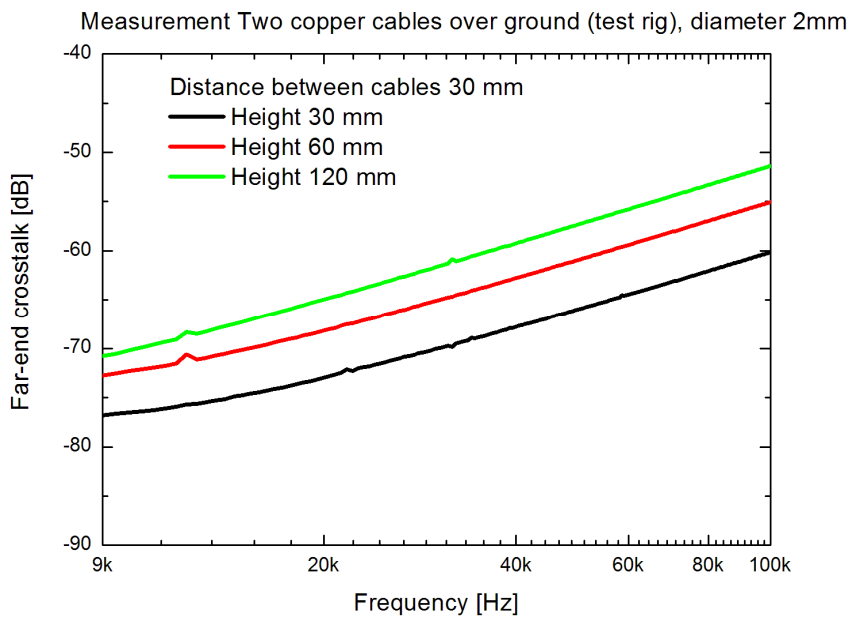
Figure 8.30 - Measured far-end crosstalk for two parallel cables in the test rig with 50 ohm terminations. Three different heights of the parallel cables over the ground were measured.

8.5 Cable modelling and simulation

In this chapter two and three cables over a ground plane are modelled and simulated. The 2-cable model is corresponding to the measurements (far-end crosstalk) on the test rig in chapter 2. The models also take the cable resistances of copper into account.

8.5.1 Two cables over ground

Two parallel copper cables over a ground corresponding to the measurements on the test rig in chapter 2 are modelled and simulated. A general schematic of a 2-cable model with 50 ohms terminations pointing out the far-end crosstalk can be seen in Figure 8.31.
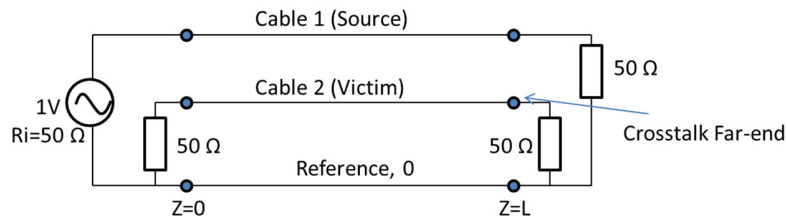
Figure 8.31 - Schematic of two cables over ground with 50 ohm terminations.

The crosstalk can be expressed as the ratio of the induced voltage in the victim line to the source voltage. If a cable of length L has a source voltage at z=0, the far-end crosstalk (

CT_{FE}) is defined as the ratio of the induced voltage in the victim line at z=L to the source voltage.

$$CT_{FE} = \frac{V_{Victim}|_{z=L}}{V_{source}}$$

8.5.2   Computation of the per unit-length parameters

A 2-cable transmission line in has a height over ground of 30 mm, distance between cables 30 mm and a cable diameter of 2 mm. The cross-section of the two cables and the capacitance and inductance per unit-length parameters have been computed in the program FD2D, see Figure 8.32.
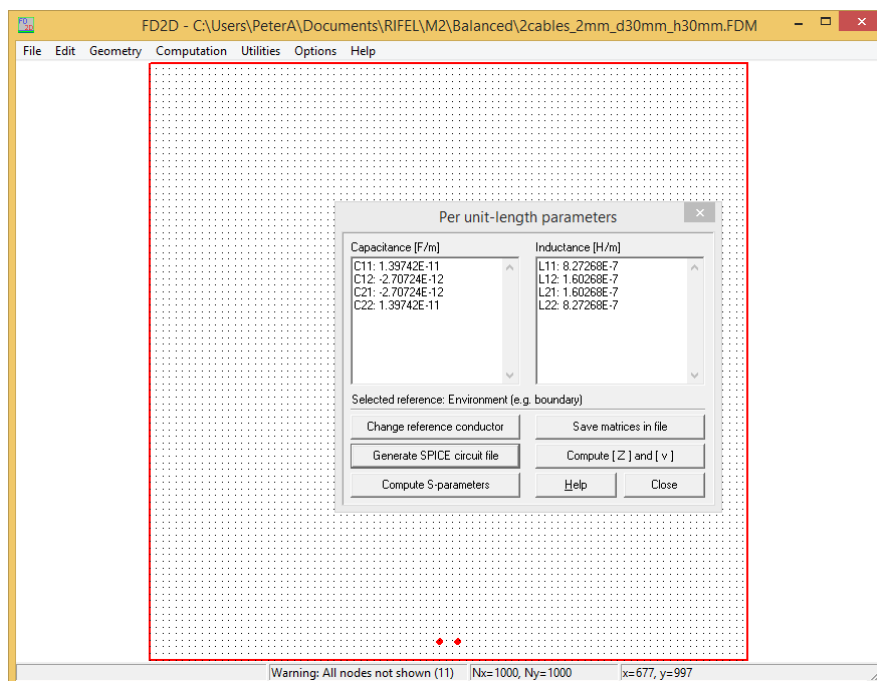
Figure 8.32 - Determination of the per-unit length parameters for two cables (cable diameter 2mm) 30 mm apart and 30 mm over ground.

For the generation of a SPICE circuit file (netlist) the length of the 2-cable transmission line was set to 1 m and one pi-section was used. The inductance and capacitance values are then converted into a pi-section structure. Into the SPICE file the calculated copper cable series resistance for each cable is also taken into account, see chapter 1. With a cable diameter of 2 mm and a length of 1m the copper cable series resistance is 5.47e-3 ohm, see R1 and R2.

Below is shown the generated SPICE circuit file for the 2-cable transmission line in Figure 8.32. In Figure 8.33, the components of the pi-section structure with additional source and loads are shown.

* **Input nodes of the MTL:**
*   Reference: Node 0
*   Line 1: Node 1
*   Line 2: Node 2
* **Output nodes of the MTL:**
*   Reference: Node 5
*   Line 1: Node 6
*   Line 2: Node 7
* Lumped section number 1
*TL Two copper cables diam 2mm, 30mm over GND, separated 3 mm, length 1m

C0 1 0 5.63346e-12
C1 2 0 5.63347e-12
C2 2 1 1.35362e-12
L1 1 3 8.27268e-07
L2 2 4 8.27268e-07
K0 L1 L2 0.193732
R1 3 6 5.47e-3
R2 4 7 5.47e-3
C3 6 5 5.63346e-12
C4 7 5 5.63347e-12
C5 7 6 1.35362e-12
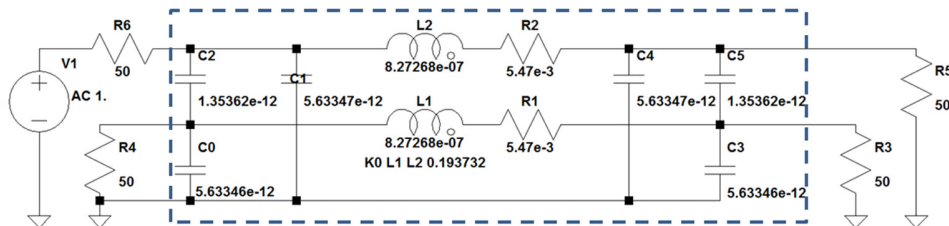
Figure 8.33 - Circuit equivalent for two copper cables each with a diameter of 2 mm and a length of 1 m, 30 mm over ground and with a distance between the cables of 30 mm, modelled using one pi-section(inside dashed rectangle) and additional source and loads.

8.5.3 Far-end crosstalk as function of height

A comparison of the far-end crosstalk for 2-cable transmission lines at the heights 30, 60 and 120 mm over the ground is made. The SPICE circuit file and Circuit equivalent for the 2-cable transmission cable 30 mm over the ground has been done in 8.5.2. The same

procedure is used, for the heights 60 and 120 mm over ground, to get the additional SPICE circuit files and circuit equivalent models.

We use the program LTspice for computations in the frequency interval 9 – 100 kHz. The computed quantity is the voltage at the far-end victim line, the exciting voltage source is set to 1 volt. The far-end crosstalk is calculated according to equation 3.1, i.e. the voltage at the far-end victim line (R3) divided by the voltage at the connection point (R6-C2).

As can be seen in Figure 8.34, the far-end crosstalk is increasing as the frequency gets higher. We also see that the crosstalk increases as we move the transmission line further away from the ground.

Simulation: Two parallel copper cables over ground, diameter 2mm
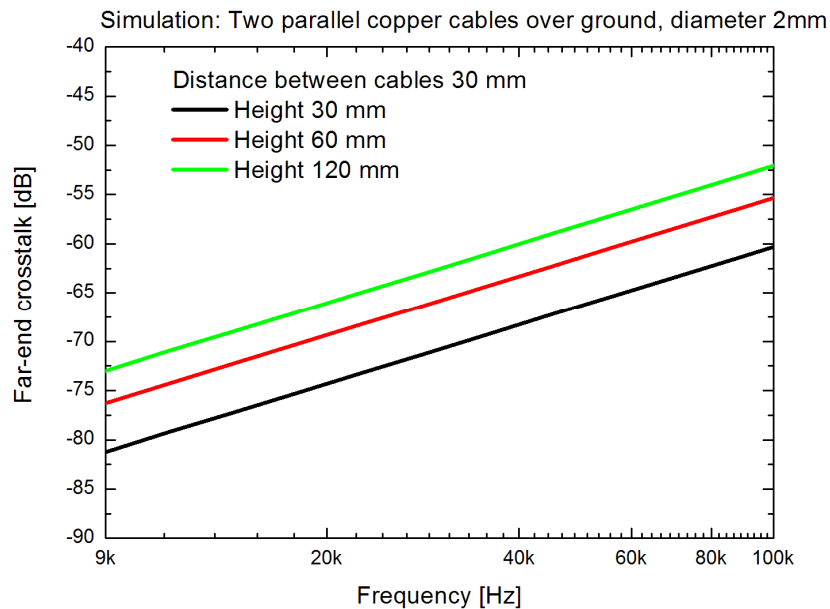
Figure 8.34 - Computed far-end crosstalk for two parallel cables over a ground plane with 50 ohm terminations. Three different heights of the parallel cables over the ground were computed.

8.5.4   Three cables over ground

In Figure 8.35 a general schematic of a 3-cable model over a reference with 50 ohms terminations can be seen.
We model and simulate three 1 m long parallel cables 30 mm over a ground plane. The cable diameter is 2 mm and the distance between each cable is 30 mm.
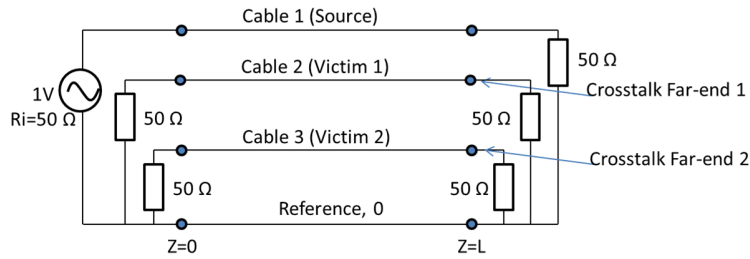
Figure 8.35 - Schematic of three cables with 50 ohm terminations over ground.

8.5.5 Computation of the per unit-length parameters

In Figure 8.36, the cross-section of three cables 30 mm over ground and the capacitance and inductance per unit-length parameters have been computed in the program FD2D.
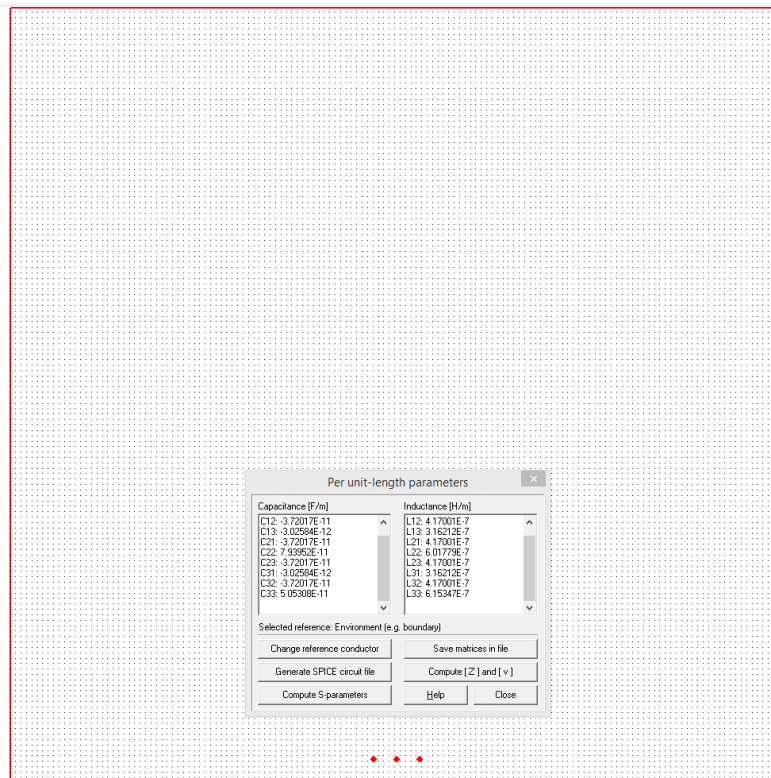
Figure 8.36 - Determination of the per-unit length parameters for three cables (cable diameter 2mm) 30 mm apart from each other and 30 mm over ground.

Below, the generated SPICE circuit file for the 3-cable transmission line is shown. In Figure 8.37, the components of the pi-section structure with additional source and loads are shown. We define the source as being applied on cable 1 (left) and the loads as being applied on cable 2 (middle) and cable 3 (right).

* Input nodes of the MTL:
*   Reference: Node 0
*   Line 1: Node 1
*   Line 2: Node 2
*   Line 3: Node 3

* Output nodes of the MTL:
*   Reference: Node 7
*   Line 1: Node 8
*   Line 2: Node 9
*   Line 3: Node 10

* Lumped section number 1
*TL Three copper cables diam 2mm, 30mm over GND, separated 30mm, length 1m

C0 1 0 5.37898e-12
C1 2 0 4.64232e-12
C2 3 0 5.37899e-12
C3 2 1 1.29218e-12
C4 3 1 3.31753e-13
C5 3 2 1.29218e-12
L1 1 4 8.2724e-07
L2 2 5 8.27115e-07
L3 3 6 8.27237e-07
K0 L1 L2 0.193682
K1 L1 L3 0.0831067
K2 L2 L3 0.19368
R1 4 8 5.47e-3
R2 5 9 5.47e-3
R3 6 10 5.47e-3
C6 8 7 5.37898e-12
C7 9 7 4.64232e-12
C8 10 7 5.37899e-12
C9 9 8 1.29218e-12
C10 10 8 3.31753e-13
C11 10 9 1.29218e-12
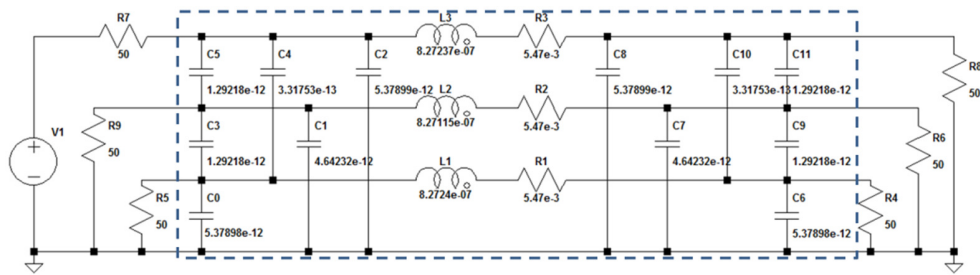
Figure 8.37 - Circuit equivalent for three copper cables with a diameter of 2 mm, length of 1 m, 30 mm over ground and 30 mm apart from each other, modelled using one pi-section(inside dashed rectangle) and additional source and loads.

8.5.6   Far-end crosstalk 1 and 2

We make a comparison of the far-end crosstalk for 3-cable transmission lines between a) source (left) to cable 2 (middle) and b) source (left) to cable 3 (right).

We use the program LTspice for computations in the frequency interval 9 – 100 kHz. The computed quantity is the voltage at the far-end victim line, the exciting voltage source is set to 1 volt. The far-end crosstalk is calculated according to chapter 3.1, i.e. the voltage at the far-end victim line 2 (R6) and far-end victim line 3 (R4), respectively, divided by the voltage at the connection point (R7-C5).

As can be seen in Figure 8.38, the far-end crosstalk is increasing as the frequency increases. We also see that the far-end crosstalk between cable1 (source) and cable2 (30 mm away) is almost the same as the for the 2-cable case (30 mm away) in chapter 3.1.2. The far-end crosstalk between cable1 (source) and cable3 (60 mm away) is 7.5 dB lower compared to cable1 to cable2. The main reason for this is that the distance from source to cable 3 is larger (cable2 may also have a small shielding effect).
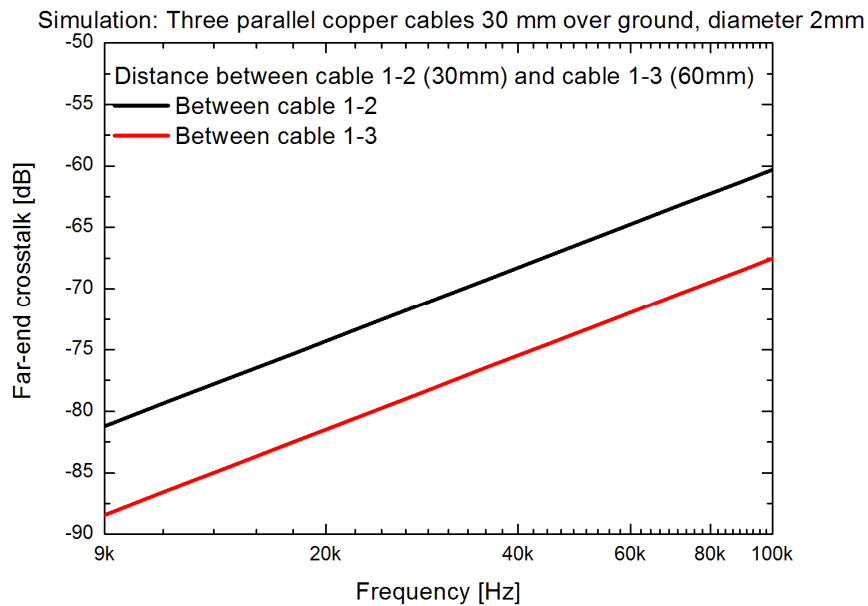
Figure 8.38 - Computed far-end crosstalk for three parallel cables over a ground plane with 50 ohm terminations.

8.5.7 Modelling in Simscape

In the chapters before the pi-sections from the generated SPICE circuit file has been input to the program LTspice. Another possibility is to use the program Simscape [7]. An example using Simscape can be seen in Figure 8.39 where one pi-sections is modelled as one block. If the block is clicked on the pi-section is shown. We have designed a pop-up window so that L and C values of the pi-section can be input as well as the length in meters of the pi-section.
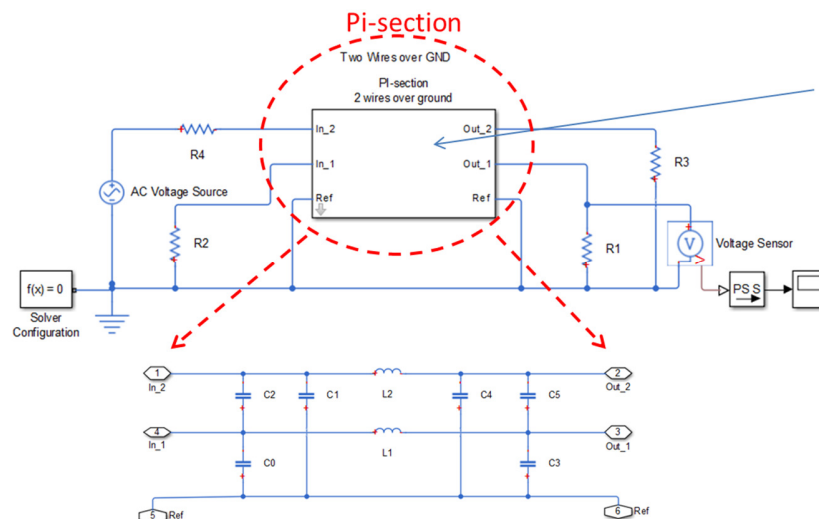
Figure 8.39 - Circuit equivalent for two cables over ground modelled using one pi-section(inside dashed circle) and additional source and loads.
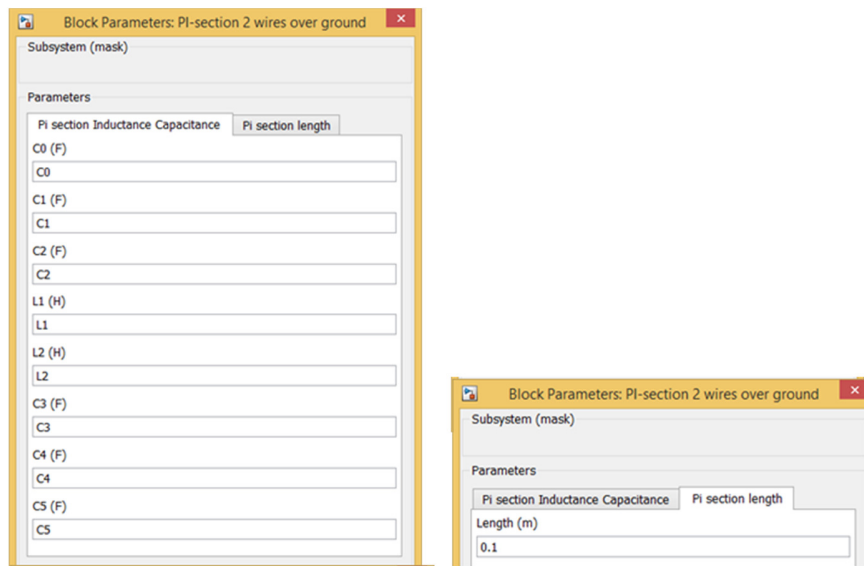
Figure 8.40 - Input of L, C and length of pi-section.

8.5.8 Cables over ground Simulation vs Analytical solution

Analytical solution for n wires over ground plane
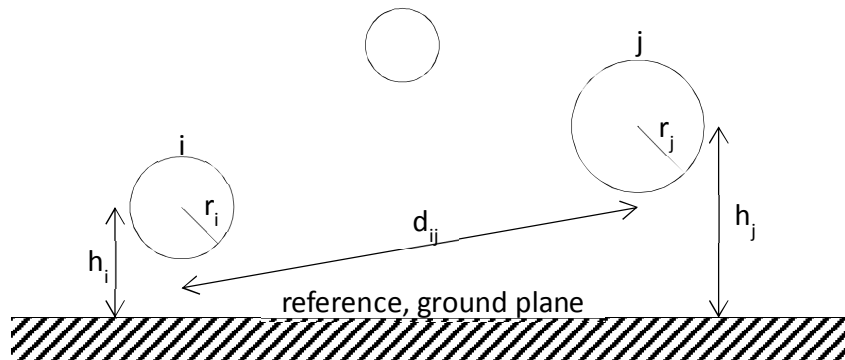
Figure 8.41 - Cross-section of n wires over infinite, ground plane.

If we assume the heights over ground plane to be much larger than each wire radius the inductance matrix is given by:

$$L_{ii} = \frac{\mu}{2\pi} ln\left(\frac{2h_i}{r_i}\right) \text{ [H/m]}$$

$$L_{ij} = \frac{\mu}{4\pi} ln\left(1 + \frac{4h_i h_j}{d_{ij}^2}\right) \text{ [H/m]}$$

The capacitance matrix can be obtained by using
$$C = \mu\varepsilon L^{-1}$$

With $\mu \approx \mu_0 = 4\pi$ *H/m* the inductance matrix is given by:

$$L_{ii} = 2ln\left(\frac{2h_i}{r_i}\right) \text{ [H/m]}$$
$$L_{ij} = ln\left(1 + \frac{4h_ih_j}{d_{ij}^2}\right) \text{ [H/m]}$$
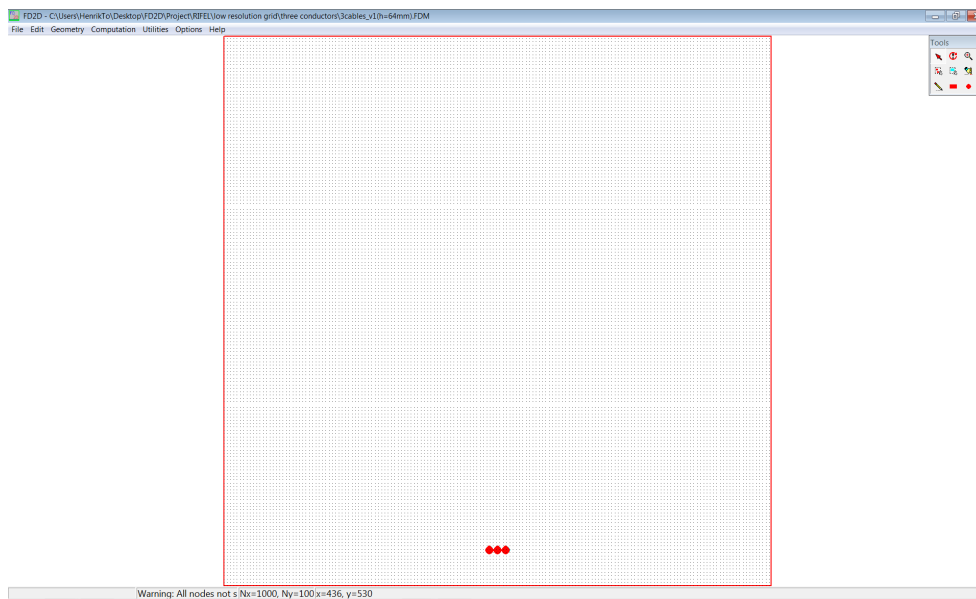
Figure 8.42 - Three conductors bundled in a row parallel to ground. Modelled and simulated in FD2D to calculate the LC matrices.

The LC matrices for three conductors bundled in a row over the ground is calculated analytically for various heights over the ground. The same problem is modelled and simulated in FD2D, see Figure 8.42. In Figure 8.43 and Figure 8.44, the resulting parameters, inductance L11 and mutual inductance M12, from the analytical solution and the FD2D computation are compared. The results agree quite well to each other. The small deviation could be due to e.g. other edges or the insulation being disregarded in the simplified theoretical calculations.

If decided that the agreement of the analytical solution and FD2D simulation of LC matrices are good enough new opportunities will be open. For example, a parameter; Height, representing the height of the cables over ground, may be passed to the transmission line model. In this way the SPICE circuit file may be modified with a variable for the height.
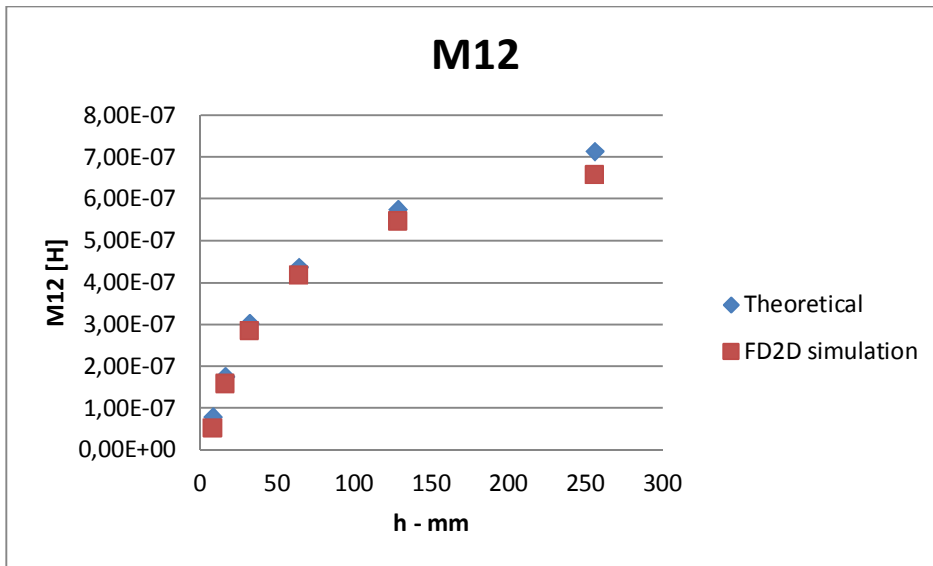
Figure 8.43 - Mutual coupling M12 for three conductors bundled in a row parallel to ground.
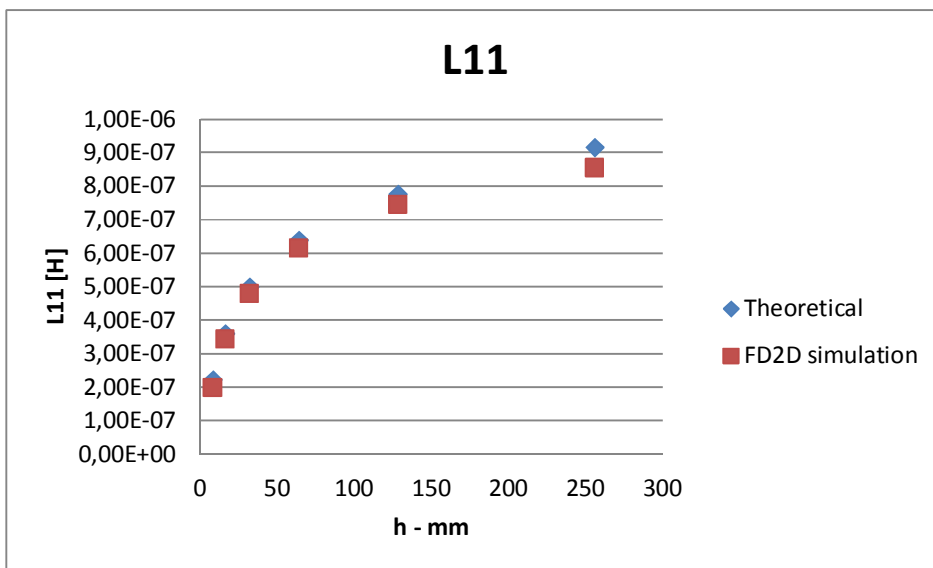
Figure 8.44 - Inductance L11 for three conductors bundled in a row parallel to ground.

8.6   Coaxial cables

In the following, measurements of near-end crosstalk between two parallel RG58 coaxial cables, as function of height over a copper plane, are studied.

Two RG58 coaxial cables (50 ohm, 85 pF/m), each with a length of 1 m and a diameter of approximately 5 mm were soldered to a N-connector at both ends. The N-connectors, were mounted to the copper plate at each end. In Figure 8.45 an example showing the cables mounted at a distance of 60 mm between each other at a height of 30 mm is shown. For each measurement setup all cables were terminated with one of the terminations shown in Figure 8.46.

Figure 8.45 - Cable rig for cable measurements over copper plane. Here two RG58 coaxial cables are attached to the N-connectors on the copper plates and additional loads.
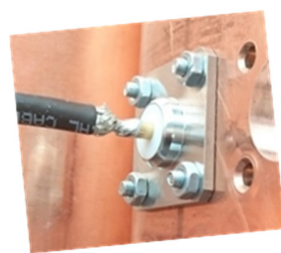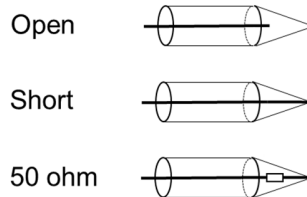
Figure 8.46 - RG58 coaxial cable terminations.

The output voltage of the network analyzer was set to 1 V. The frequency span was set to 9 - 100 kHz. In Figure 8.47, the schematic for measuring near-end crosstalk (S21), with a network analyzer, of two parallel cables in the test rig with 50 ohm terminations is shown. For each configuration, the S-parameter S21 was recorded.
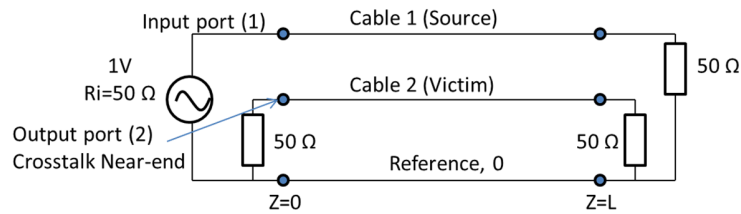
Figure 8.47 - Schematic for measuring near-end crosstalk (S21), with a network analyzer, of two parallel cables in the test rig with 50 ohm terminations.

8.6.1 Near-end coupling between cables with small separation

The distance between the two parallel cables were 30 mm and the height over the copper plane for the cables was 120 mm. All cables were terminated with open terminations. The measured and simulated S-parameter S21 can be seen in Figure 8.48. As can be seen, the near-end crosstalk is increasing as the frequency gets higher. See chapter 8.5.2 for a corresponding simulation model.
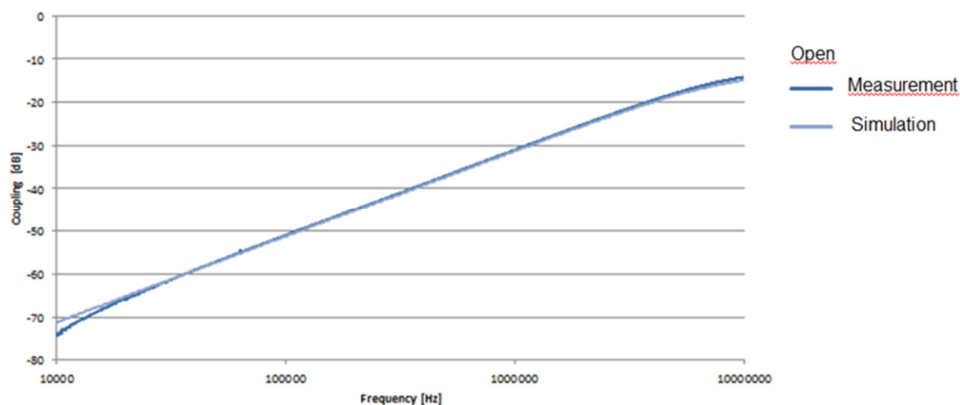
Figure 8.48 - Measured and simulated near-end crosstalk for two parallel cables with small separation in the test rig with 50 ohm terminations.

8.6.2 Near-end coupling between cables close to ground plane

The distance between the two parallel cables were 120 mm and the height over the copper plane for the cables was 30 mm. All cables were terminated with open terminations. The measured and simulated S-parameter S21 can be seen in Figure 8.49. As can be seen, the near-end crosstalk is increasing as the frequency gets higher. We also see that the crosstalk is approximately 30 dB lower compared to the case presented in chapter 8.5.2. This is due to that the crosstalk decreases as we move the transmission lines closer to the ground. See chapter 8.5.2 for a corresponding simulation model.
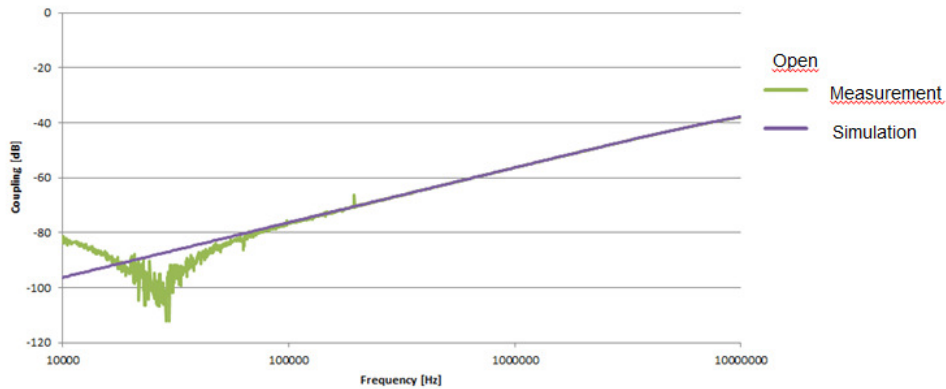
Figure 8.49 - Measured near-end crosstalk for two parallel cables close to ground plane in the test rig with 50 ohm terminations.
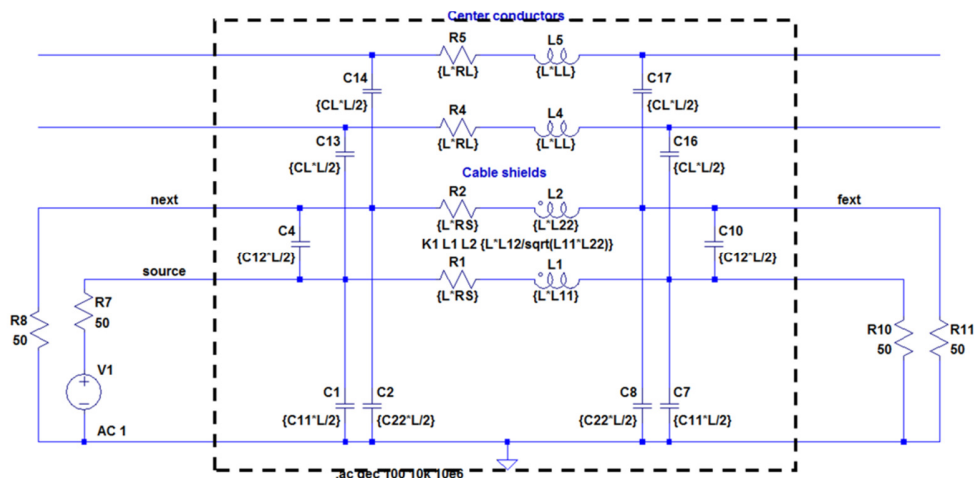
In Figure 8.50 is shown a circuit equivalent for two parallel coaxial cables modelled over a ground plane using one pi-section (inside dashed rectangle) and additional source and 50 ohm loads. Notation next and fext stands for "near-end crosstalk" and "far-end crosstalk", respectively. The values for capacitances and inductances are solved analytically, while the resistances of the cables have been measured.

Figure 8.50 - A circuit equivalent for two coaxial cables over a ground plane modelled using one pi-section (inside dashed rectangle) and additional source and 50 ohm loads.

8.6.3 Effect of skin depth on current distribution and selection of case for comparison

The distance between the two parallel cables were 30 mm and the height over the copper plane for the cables was 120 mm. The cables were terminated with either open, short or matched terminations as shown in Figure 8.46. The measured and simulated S-parameters S21 can be seen in Figure 8.51. As can be seen, the near-end crosstalk is increasing as the frequency gets higher. See chapter 3.1 for a corresponding simulation model.
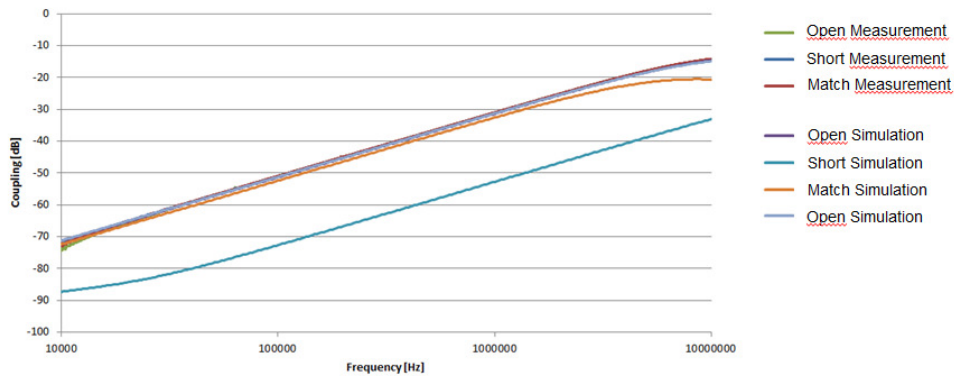
Figure 8.51 - Measured near-end crosstalk for two parallel cables with small separation in the test rig. Termination is open, short or matched (50 ohm).

8.7 Shielded high voltage cables

8.7.1 Measurements of coupling between two shielded high voltage cables

With two one-meter samples of shielded high voltage cables the measurement of near end crosstalk measured and compared with corresponding circuit simulation using the relevant cable model. For these measurements the measurements fixture was positioned against a wall to have the cables hanging in an almost vertical configuration in parallel with the ground plane leaning towards the wall. This way the cable mass did not affect the distance between the cable and the ground plane very much.

Figure 8.52 - Cable coupling measurement fixture with ground plane
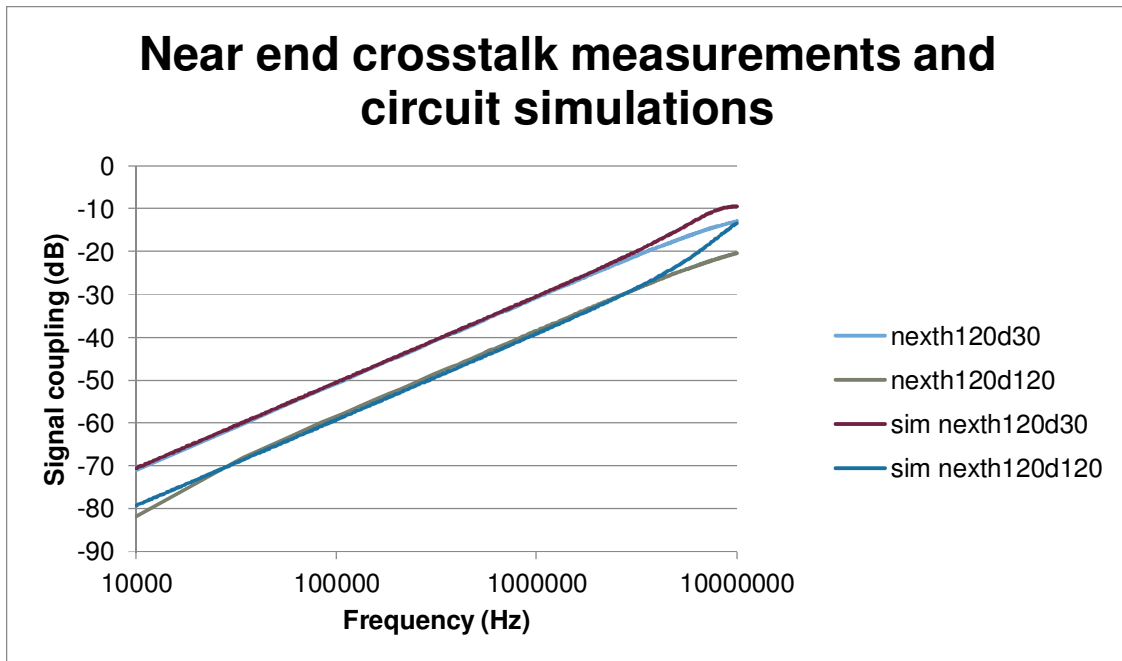
Figure 8.53 - Comparison of measurements and simulations of near end crosstalk with different distances between cables

8.7.2   Preliminary model of high voltage DC cable

The preliminary model for the DC cable has been used in circuit simulation of near end crosstalk and compared with measurements to verify the coupling between cables.
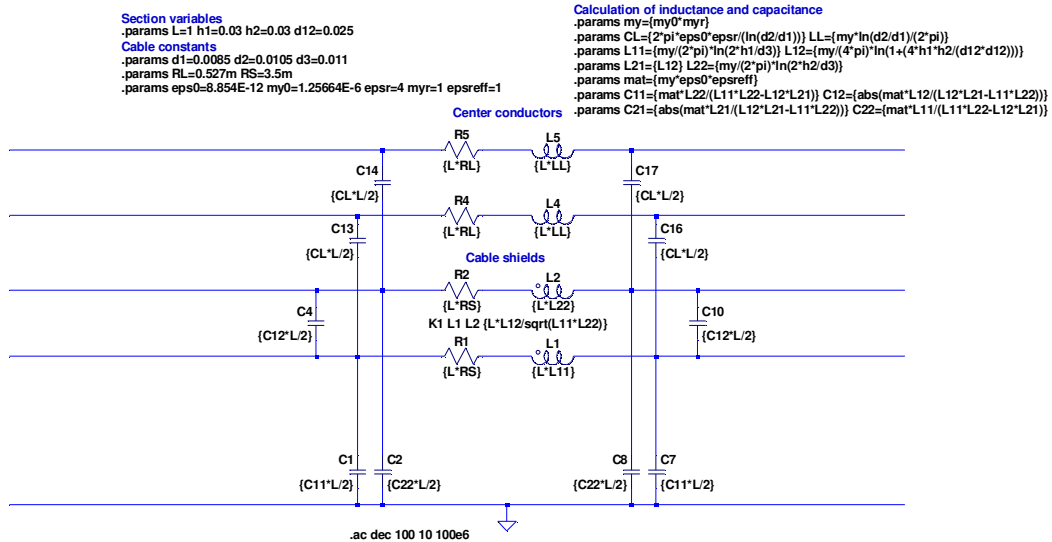

Figure 8.54 - Model of shielded high voltage DC cable based on cable geometry and measured coupling between cables

8.7.3   Preliminary model of high voltage AC cable

A similar model for the AC-cable using same approach as for the DC cable but involving three shielded cables.
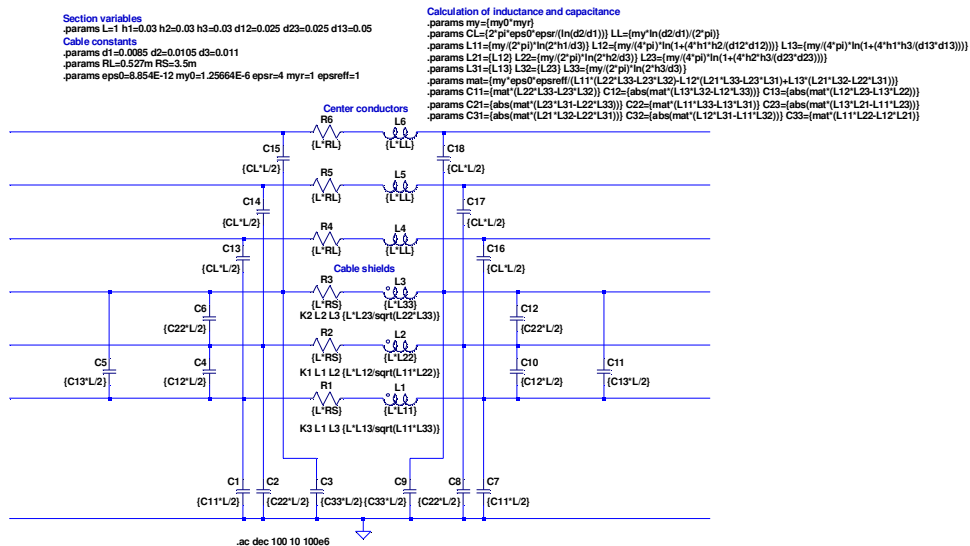
Figure 8.55 - Model of shielded high voltage AC cable based on cable geometry and measured coupling between cables

8.7.4 Measurement of differential mode impedance

To be able to correctly derive the current ripple in cables it is important that the impedance of the cable model have realistic value in the frequency range of interest. From measurements it is shown that the differential mode impedance is affected by induced current in the cable shield in a specific frequency range.
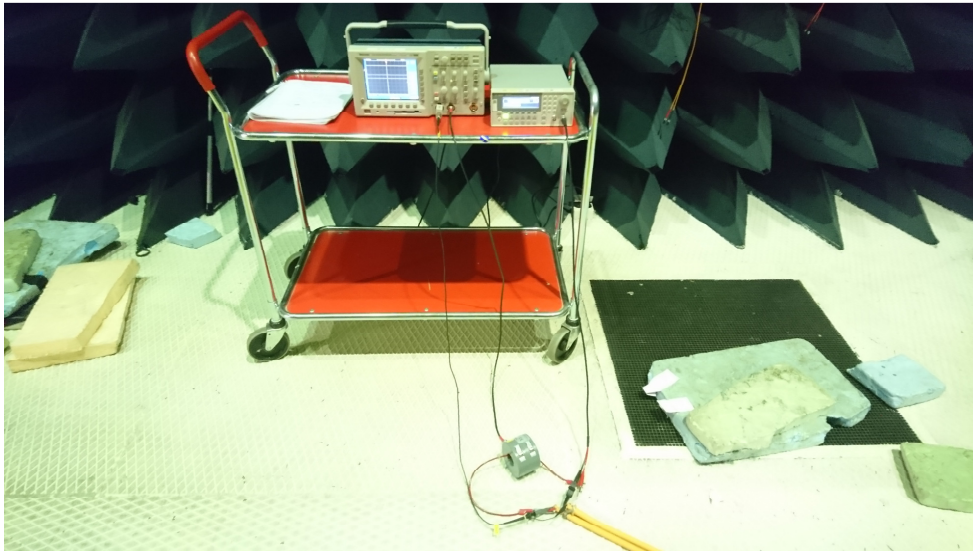

Figure 8.56 - Part of measurement setup for measurement of differential mode impedance of shielded high voltage DC cable.

An AC-signal is fed into the 10 meter long DC-cable driving a AC-current when the DC-cable has a short circuit in the far end. The cable shields are connected to each other in both end as is the case in a real installation.

Figure 8.57 - Conceptual drawing showing measurement setup for measurement of differential mode impedance of shielded high voltage DC cable.

The voltage between the two centre conductors and the current into the cable are recorded at many frequency points from 10 Hz to 1 MHz. The measurements were performed when cables were placed on a conducting ground plane and repeated with a 5 cm airfoam distance between the cables and the ground plane. The distance between the cables was 3 cm.
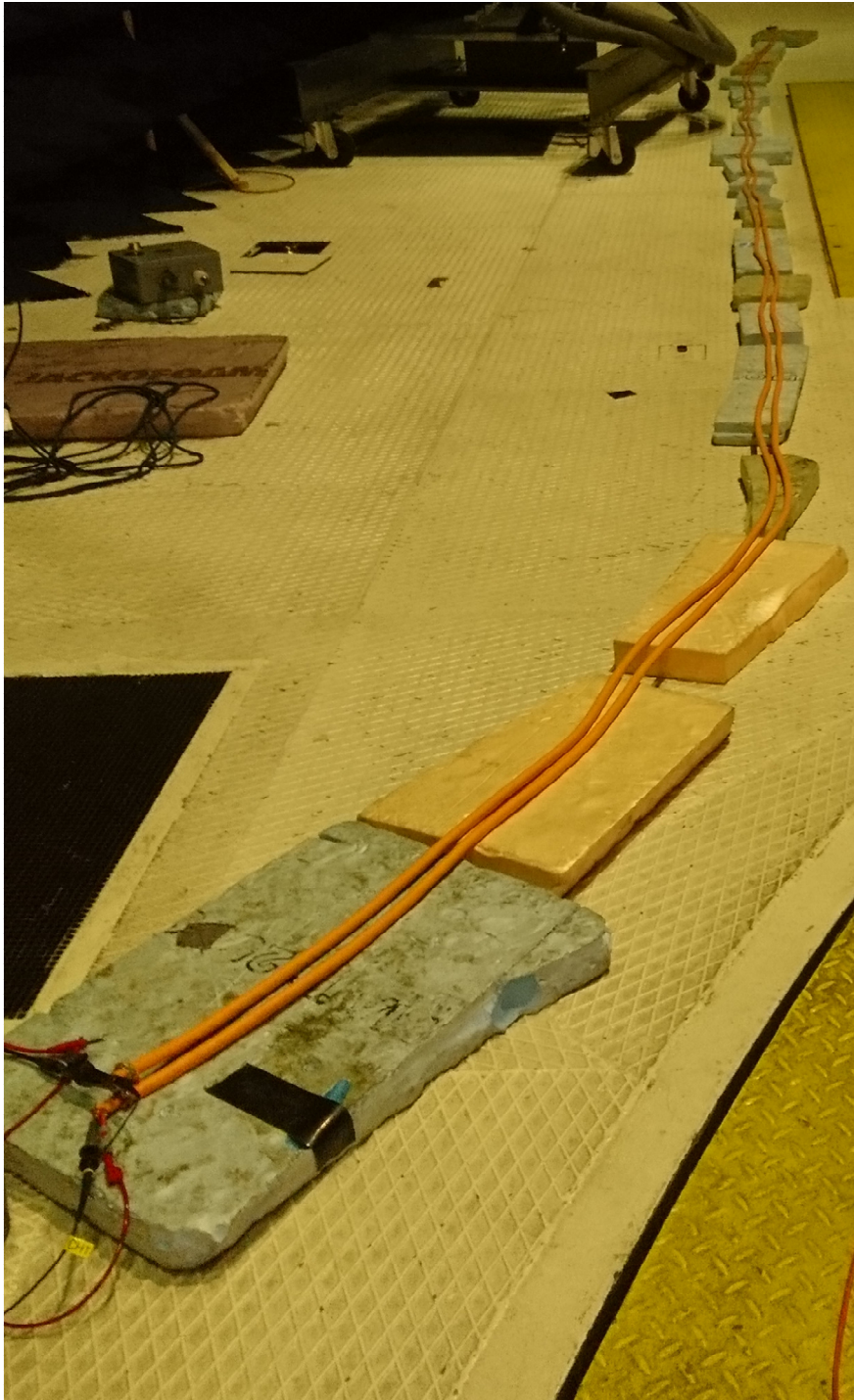
Figure 8.58 - Part of measurement setup for measurement of differential mode impedance of shielded high voltage DC cable.

From the measurements, the differential mode impedance is calculated as $Z_{DM} = \frac{U}{I}$ ohms for each frequency point. There is no significant effect of the height over ground plane.

Using the final version of the DC-cable model, see Figure 8.61, the differential mode impedance can be derived by circuit simulation in LT-SPICE.
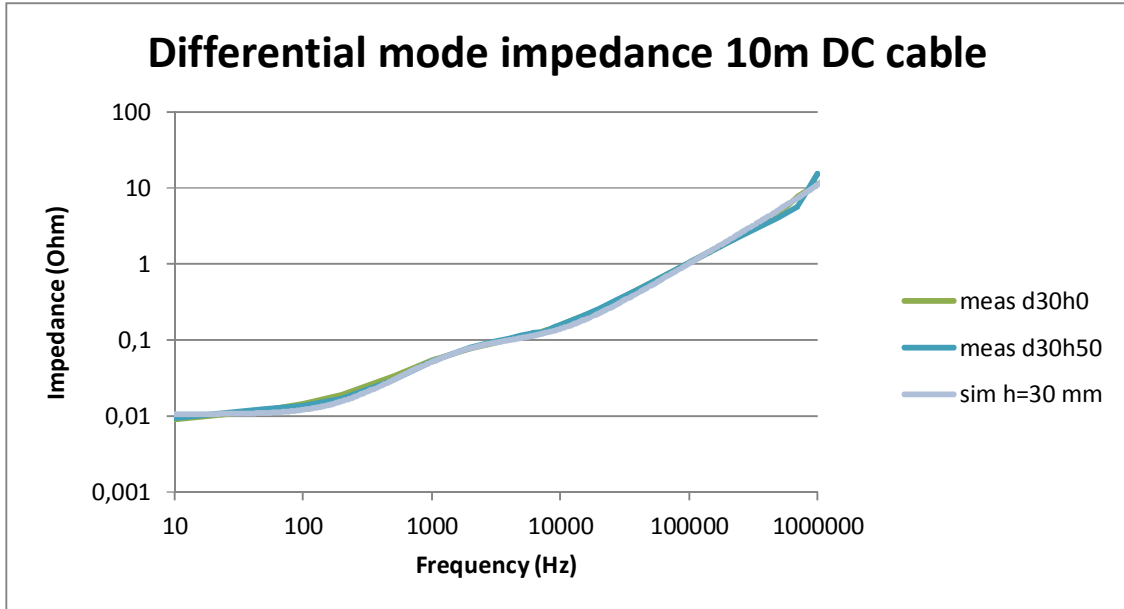

Figure 8.59 - Results from measurement of differential mode impedance of shielded high voltage DC cable compared to circuit simulation results.
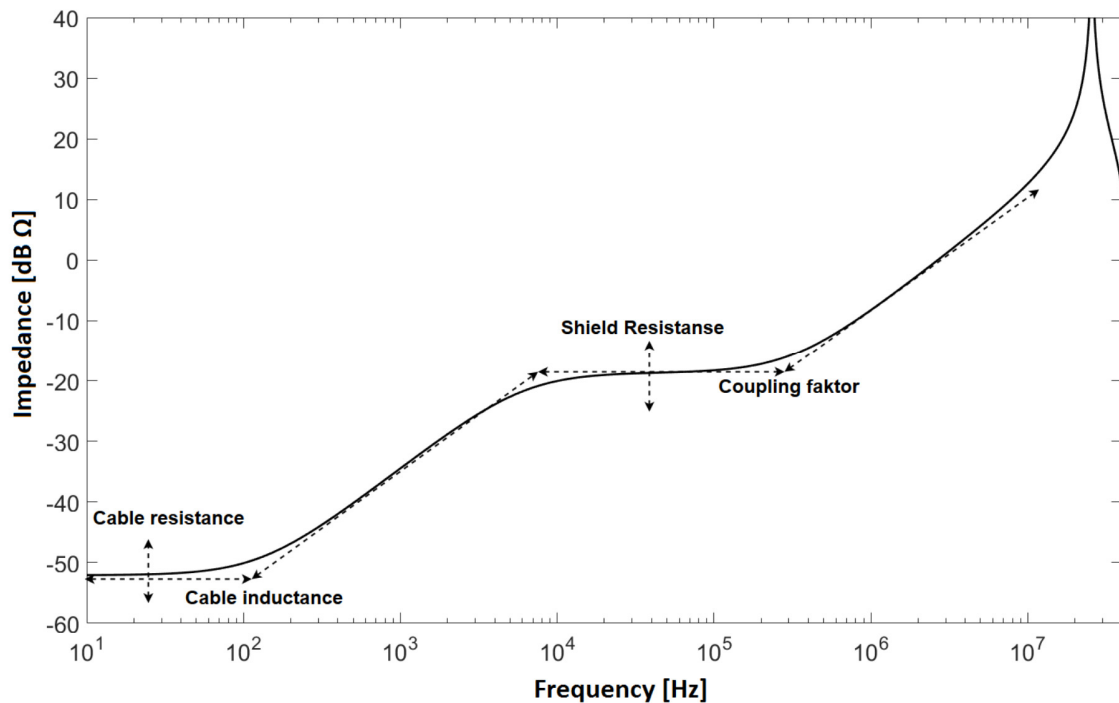
Figure 8.60 - Explanation of parts how the frequency behaviour is depending on physical characteristics.

The current in the centre conductor is due to inductance causing a magnetic field. When the cable shield is connected in both end a highly conductive loop is formed inclosing a part of the magnetic field. The magnetic field is inducing a current in the shield causing a second magnetic field that partly is cancelling the first magnetic field. With proper low resistive connection of shield conductors, the magnitude of the induced shield current can be quite large fraction of the centre conductor current magnitude at frequencies of 1 kHz and higher. At the same time the magnetic field can to a large part be cancelled.

The resistive losses in the cable shield will give the cable a low pass filter characteristic for ripple currents.

The potential high shield currents are because forward and return currents are shielded separately. A configuration with forward and return current conductors with a common shield, the shield current magnitude can be much smaller.

During the measurements above it was verified that the shield current can be more than half of the magnitude of the centre conductor current in frequencies of 1 kHz and higher.

8.7.5 Model of high voltage DC cable

The model of the shielded high voltage DC cable was adjusted to adapt to the measured differential mode impedance frequency variation.
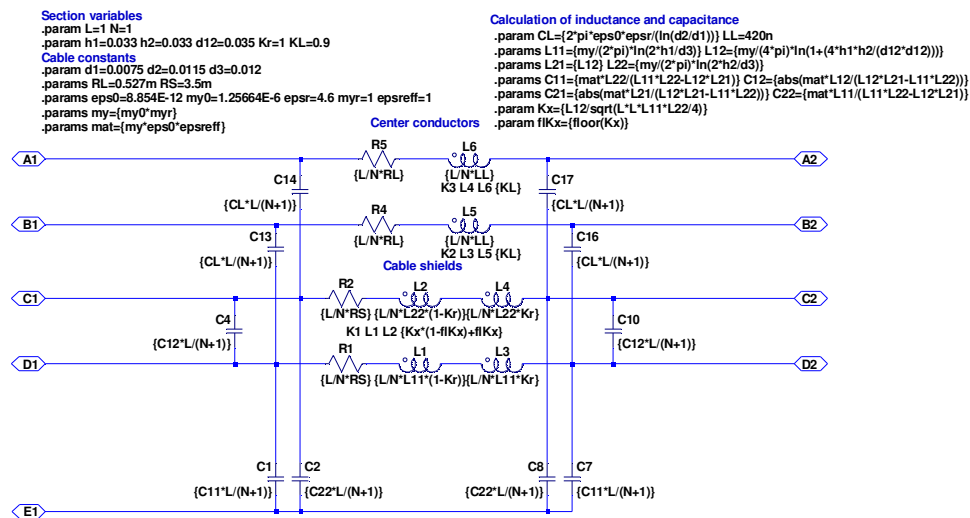

Figure 8.61 - Model of shielded high voltage DC cable based on cable geometry and measured differential mode impedance

8.7.6 Model of high voltage AC cable

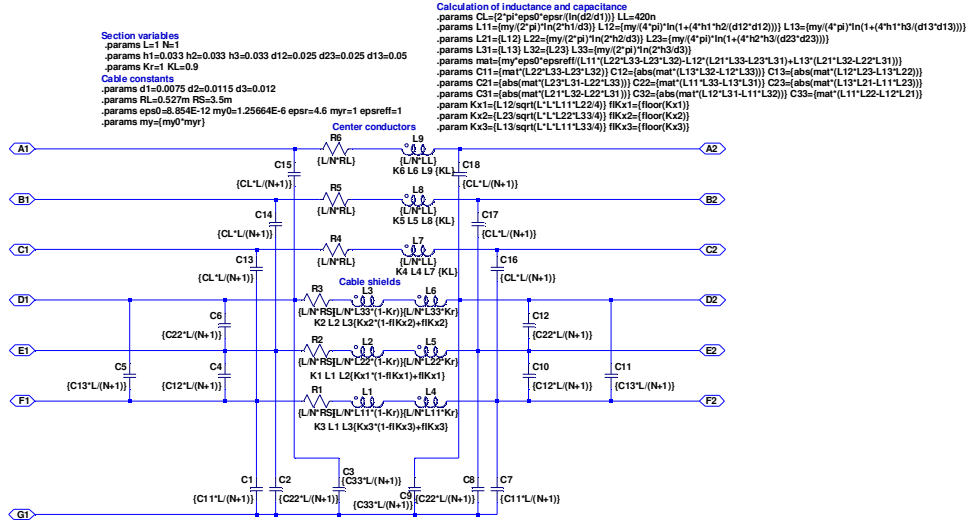Similarly the three phase shielded high voltage AC cable was adjusted accordingly.

Figure 8.62 - Model of shielded high voltage AC cable based on cable geometry and measured differential mode impedance

8.8 Summary and conclusions

For shielded cables, such as high voltage cables in vehicles, the problem has to be divided into two parts, one inner problem and one outer. The cross-section for the inner problem is then defined as the area between the conductors inside the shield and the shield itself, and the cross-section for the outer problem is defined as the area on the outside of the shield. The reference for the inner problem is the shield, and for the outer the chassis of the vehicle. Often the shield can be considered to be ideal, especially for low frequencies and high quality shields. For this case the coupling between the inner and outer problems takes place only at the ends of the cable. For non-ideal shields the coupling along the cable can be modelled with the transfer impedance of the shield. In general, the transfer impedance is complex but for low frequencies it is purely resistive, simply given as the DC-resistance which can easily be computed or measured.

From measurements of differential mode impedance it is found that it is important that the mutual inductance between centre conductor and shield is included in the model to describe cable impedance below 10 kHz properly. The induced current in the cable shield can be quite large if the shield loop impedance is small and depending mainly on contact resistances for the shield connection in the cable ends.

9 HV Battery model from cell to pack

9.1 Background

The main usage of the battery modelling part in the RIFEL project is to obtain a representation of the full battery to predict the electrical environment on the dc-link of the vehicle. The main focus is on the higher frequencies, however, in order to make the modelling versatile, the frequency range all the way from 1 mHz has been considered.

A battery pack consists of 6 modules and each of the modules comprises 16 cells.

9.2 Battery Impedance measurement

9.2.1 Cell Impedance measurements

9.2.1.1 Impedance measurement of an isolated battery cell

A Gamry reference 3000 and a Bode 100 was used for the cell measurements.
First several measurements were done with different layouts of the current feeding cable and the voltage sensing cables, and the results varied, especially for higher frequencies, from case to case. These measurements were performed with the Gamry reference 3000.

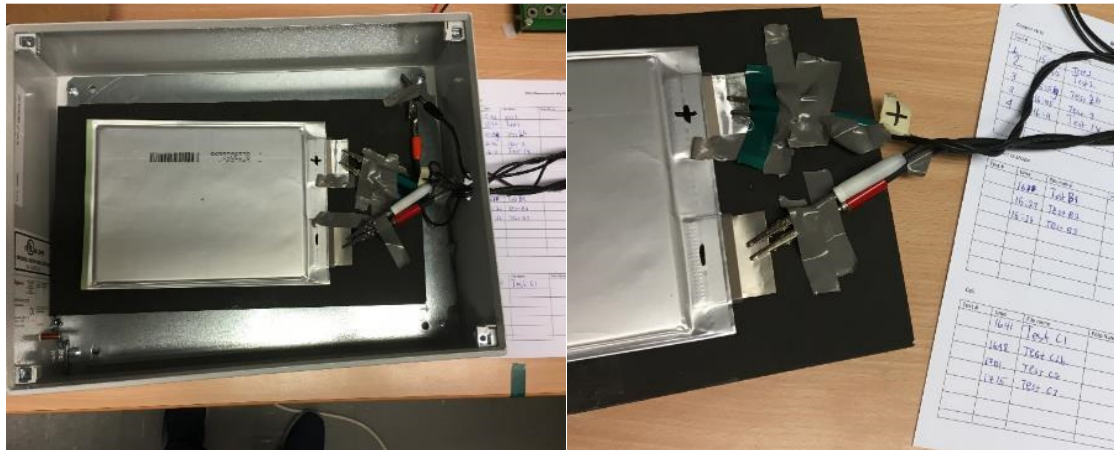A photo of a set-up in a shielded box as well as without a shielded box is shown in Figure 9.1.

Figure 9.1 - Photo of the set-up for the cell measurements, with and without a shielded box.

The results from the measurements are shown in Figure 9.2. First two measurements were made on the set-up in the box to check the repetitively, and then a measurements was done outside the box. The reason for performing the test in the box and outside was to establish the impact of the surrounding environment when conducting the tests.
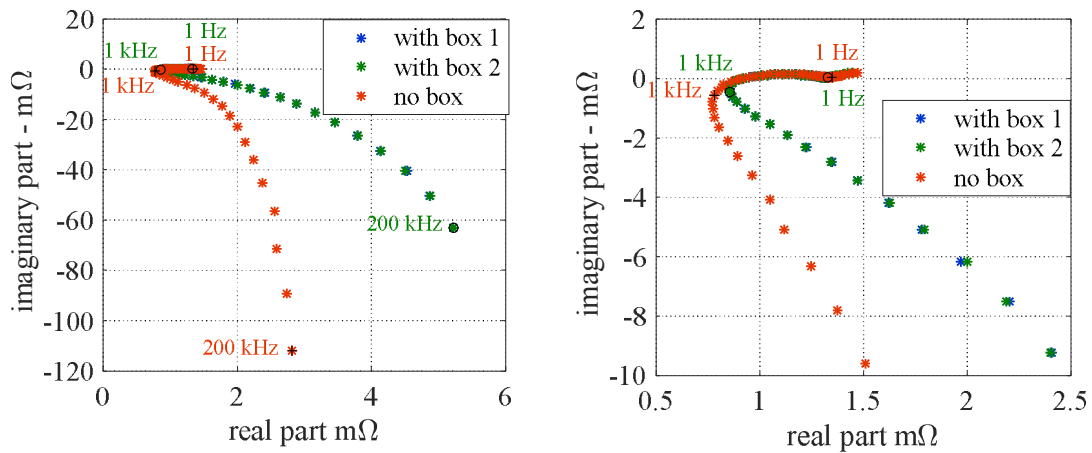

Figure 9.2 - Cell EIS measurement with a shielding box and without

The repetitiveness of the measurements was very good, however, the impact of the shielding box is very strong. This is expected as the shield box affect the inductance of the battery cell, considering the inductance of the battery cell is in the order of nH.

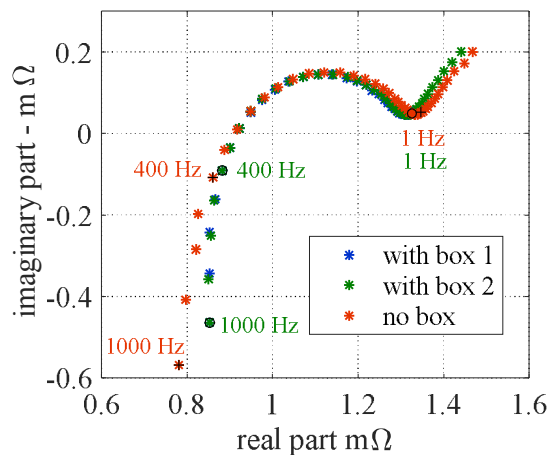The results for frequencies below 1kHz is shown in Figure 9.3.

Figure 9.3 - EIS results for frequencies below 1k Hz.

There are some small discrepancies, however, for the lower frequencies, the results are rather similar. To sum up, it can be stated that the coupling used and the 'environment' has a very large impact

Furthermore, it is worth mentioning that the connection of the current supply cables and the voltage sensing cables played a substantial impact on the results, here a large effort was put on making the connections as tight and twisted as possible following the instructions from the GAMRY manual.

9.2.1.2   Impedance measurement of battery cells in a module

With the knowledge of the problems regarding the cabling, measurements on individual cells in a module was conducted. In Figure 9.4, a part of the module is shown where measurements were made over various numbers of cells.
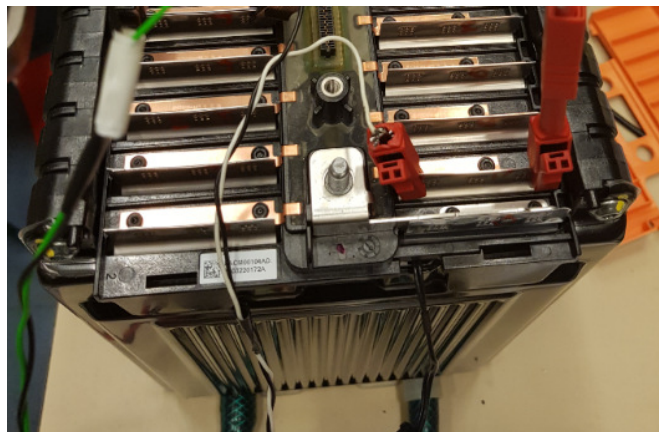

Figure 9.4 - Battery module with the tabs visible for measurements over the cells.

 In addition to using the Gamry instrument, also a Bode 100 instrument was used to determine the frequency characteristics. The Bode 100 set-up is more suited for measurements in the high-frequency region. In Figure 9.5 measurements over the first 3 cells when still located inside a battery module are presented using the Gamry instrument.
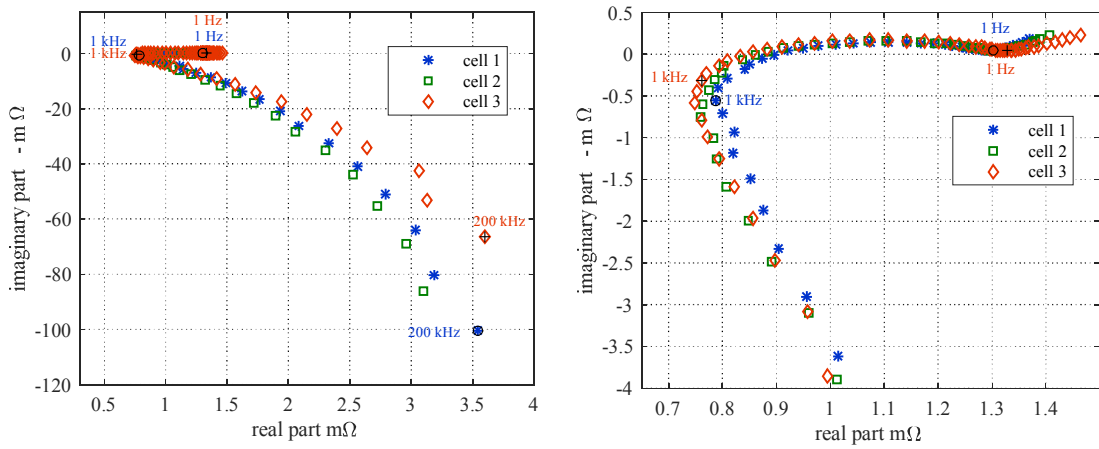
Figure 9.5 - Measured EIS result using the Gamry instrument on individual cells in the battery pack (frequency range 1 Hz to 200 kHz).

The results show a fairly equal result regarding the impedance for lower frequencies, however, the high-frequency results differ a bit more. It can be noted that although there is a metal casing enclosing the module, the cell results from the module measurements are better represented by the measurements on the cell outside the metal box in Figure 9.2.

In Figure 9.6 a comparison between the Bode 100 and Gamry instrument for the three cells in the module is shown up to a frequency of 50 kHz.
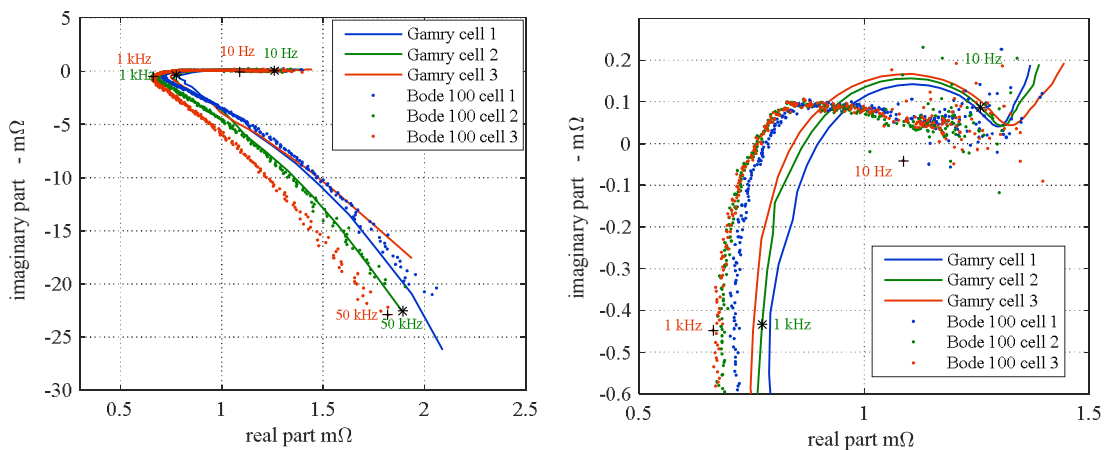

Figure 9.6 - Comparison between the Bode 100 and Gamry instrument for the three cells, up to 50 kHz.

The results are surprisingly equal, providing a good confidence in the results. Obviously for frequencies below 10 Hz, the Gamry outperforms the Bode 100 instrument.

9.2.1.3   Comparison of single cell impedance with multiple cells impedance behavior

Figure 9.7 compares a single cell impedance behavior with a three-cell impedance behavior (converted to single cell equivalent). Both measurements are done on the cells inside the module shown in Figure 9.4.
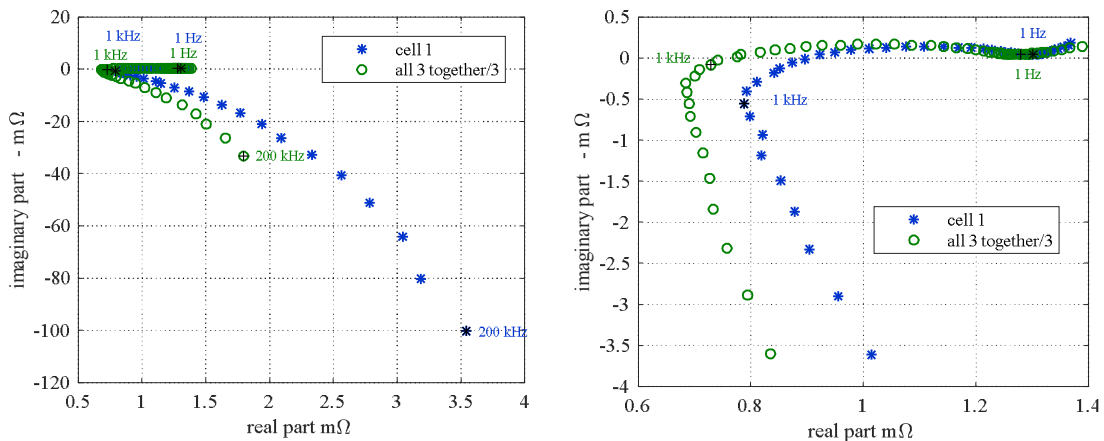

Figure 9.7 - Measured result using the Gamry instrument on one single cell versus the average of 3 cells (frequency range 1 Hz to 200 kHz).

It can be observed that the inductance is very much reduced. This shows that the series connection of individual cells does not result in additive behavior of their inductance. This is highly affected by how they are interconnected and placed in the module.   The lower frequency region is, however, possible to represent using a single cell as this region have mainly capacitive nature.

The results are confirmed by presentations given with the real and imaginary parts as a function of frequency, displayed in Figure 9.8. The figure compares the impedance of three cell in series, module (16 cells in series), and pack (96 cells in series). As shown in the figure, the measured pack/module impedance is converted to single cell equivalent by dividing the impedance by the number of cells involved in the measurement.
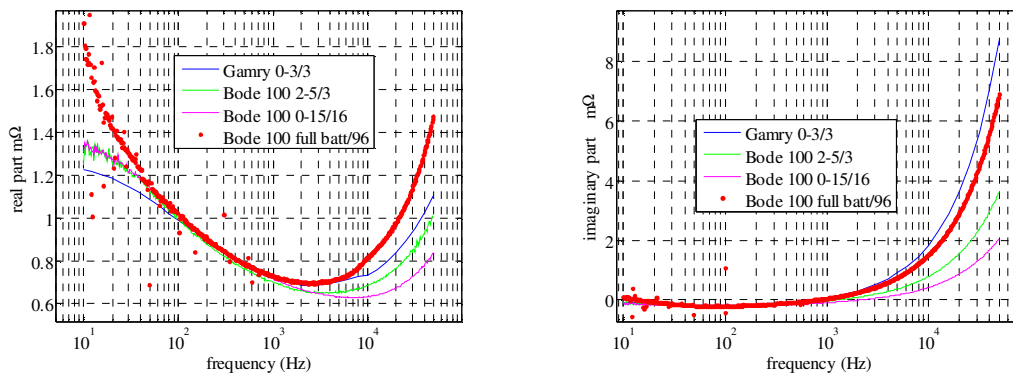
Figure 9.8 - Real and imaginary part, transferred to an equivalent cell, using the Gamry and the Bode instrument.

For the real part excellent results were obtained between 100 and 2000 Hz and for the imaginary part the results between 10 and 2000 Hz are excellent. However, the figure shows that it is not possible to deduce the overall pack impedance behavior through impedance measurement of single or module. This is due to the fact that:

- The cumulative inductance of cells connected in series or parallel cannot be calculated from individual cell inductance using circuit theory as it is affected by how the cells are placed in the module and how are they interconnected.
- Even if one can get a full picture how the cells are interconnected, due to low value of the inductance of the cells, the connecting fixtures and basbars used in the battery pack affect the resulting impedance of the pack. This is even true if one is to calculate the impedance of the pack from impedance of modules in the pack.

On other hand, one can use the cell impedance to capture the impedance behavior packs at low frequency region (<1 kHz). This is actually useful due to the difficulties associated with measuring the low frequency impedance of a battery pack.

9.2.2 Battery pack impedance measurement

Here it is first explained how the battery pack is built up. Thereafter the measurements performed are explained. Most pack level measurement results are shown together with the model predictions in section 9.3.2.

Measurements have been performed on two live battery packs and one inert battery pack. One of the live battery packs was also disassembled so measurements could be performed all the way from pack, to module to cell level on the same cells. These measurements are presented in this chapter

9.2.2.1 Battery pack build up
The battery pack has four connections. One for the HVCH (High Voltage Coolant Heater), one for the OBC (OnBoard Charger), one for the CIDD (Combined Inverter Dc/Dc converter) and one for the IEM (Inverter for Electric Machine). The location of the connectors can be seen in the pictures below. The pictures show an inert battery pack, i.e. the cells have been fully discharged and 56 Ω resistors have been placed over each module to make sure the cell voltages stay low. The 56 Ω resistors did not pose any problems later for measurements on the inert battery pack since the impedances in the inert battery pack is much lower than 6x56 Ω.

Figure 9.9 - Inert battery pack. The side with the CIDD (upper) and HVCH (lower) connector. With and without lid

Figure 9.10 - Inert battery pack. The side with the IEM (right) and OBC (left) connector. Here also the MSD (Manual Safety Disconnect) can be seen. With and without lid

Figure 9.11 - Inert battery pack. The Y-capacitors in each end of the battery. IEM side of the battery to the left and CIDD side to the right
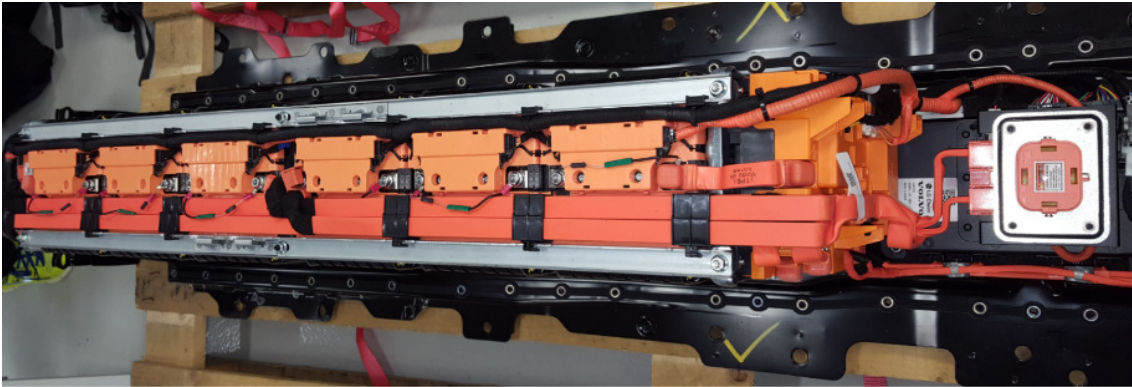
Figure 9.12 - Inert battery pack. Top view showing where the 56 Ω resistors over each of the six modules are located
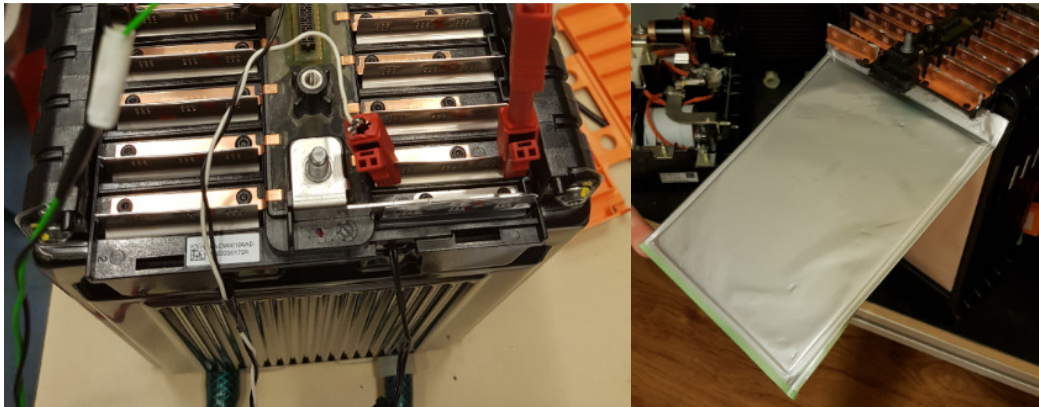

Figure 9.13 - Two modules taken from a live battery pack

Figure 9.14 - Left: A live module where measurements are being performed; Right: An inert cell in a module
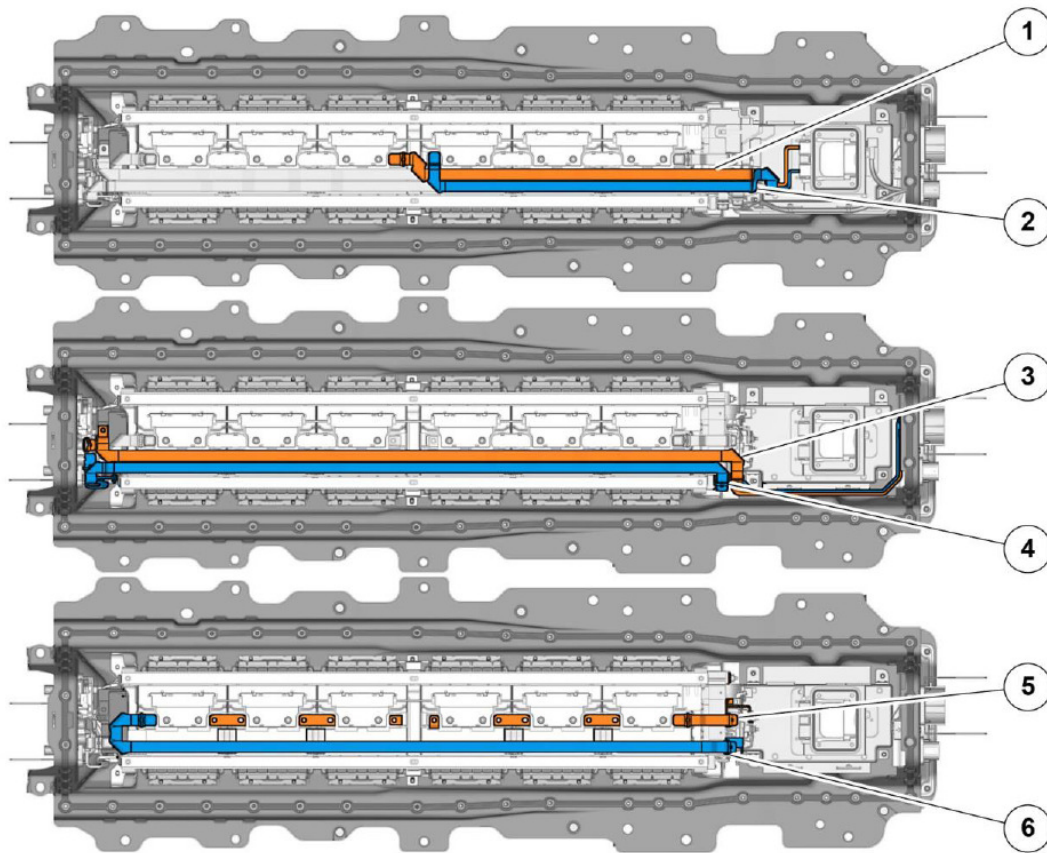
Figure 9.15 - Identification of the bus bars inside the battery pack.
1-2: From the centre of the pack to the MSD
5-6: Bus bars between modules and to "contactor part"
3-4: Bus bars mainly from contactor part to CIDD/HVCH outlets. The bus bars from the contactor part to the
IEM/OBC outlets can also be seen in the right part of the drawing

Measurements have been performed on two live and one inert battery pack.

On live batteries differential mode impedance on the IEM side of the battery was measured. Some "sub-system" measurements were also performed. The differential mode impedance of the following "sub-system" configurations were measured together with one battery:

- HV-battery and "original" IEM-HV-battery cabling

- HV-battery and IEM-HV-battery cabling with 2 Break-out-Boxes integrated on the cabling

- HV-battery with CIDD and OBC connected.
  Note: The OBC was connected in the HVCH outlet

- HV-battery with OBC connected.
  Note: The OBC was connected in the HVCH outlet

- HV-battery with CIDD connected.
  Note: The OBC was connected in the HVCH outlet

It was shown that at frequencies above ~3 kHz the differential impedance of the inert battery was very similar to the impedance of the live batteries. Therefore many measurements were performed on the inert battery that could not or at least could not easily be performed on a live battery pack. The following are a list of the most important measurements performed on the inert battery pack (for all configurations below both differential mode and common mode impedance measurements have been performed):

- Measure in the IEM contact. Status in the CIDD contact:
    - Open circuit
    - Short circuit HVDC+ to HVDC-
    - Short circuit HVDC+ to HVDC- to Chassis

- Measure in the CIDD contact. Status in the IEM contact:
    - Open circuit
    - Short circuit HVDC+ to HVDC-
    - Short circuit HVDC+ to HVDC- to Chassis

- Measure in the IEM and then also in the CIDD contact
    - Y-caps at the CIDD end removed
    - Y-caps in both the CIDD and IEM end removed

- Measurement of the Y-cap impedance

9.2.2.2 Measurements at pack, module and cells from the same battery pack

Measurements have been performed on different number of cells in series all the way up to the complete battery pack. Then the results have been scaled to the number of cells at pack level and compared, i.e. when measuring on 1 cell the result is multiplied by 96 since there are 96 cells in a complete battery pack.
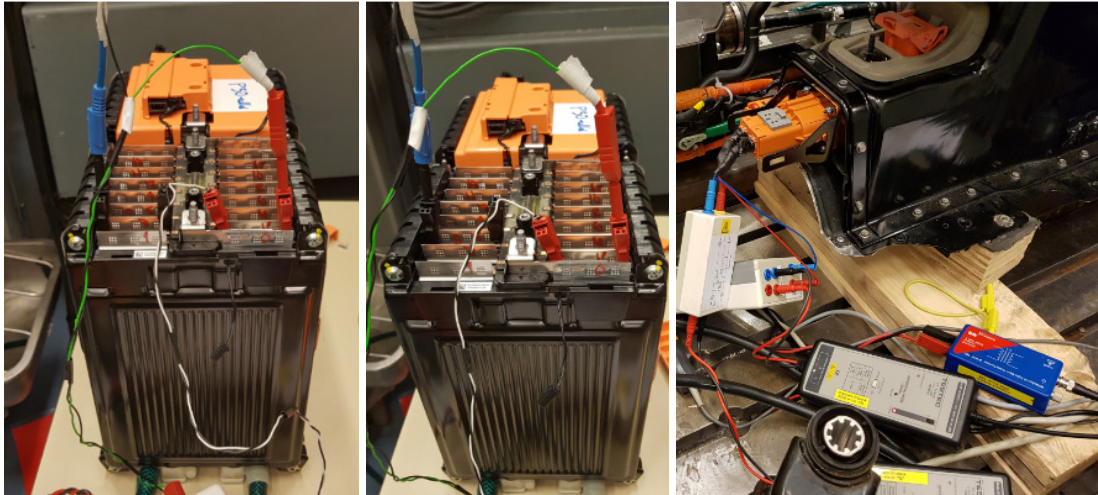

Figure 9.16 - Measurements of 1 cell (left), 3 cells (middle) and a complete battery pack (right)

In Figure 9.17 it can be seen the components are more or less inductive (+20 dB/decade) at 30 kHz. Assuming that the cell(s), module and pack are purely inductive at 30 kHz the inductances, scaled to 96 cells in series, are

1 cell	2.89 µH
3 cell	1.13 µH
5 cell	0.97 µH
7 cell	0.85 µH
Module	0.75 µH
HV-battery pack	2.21 µH

This shows that measuring at one or a few cells gives an overestimated value of the inductance. The result from measuring at 7 cells is not so far from the result obtained when measuring at a complete module (16 cells). The module measurement result is considered to be the most "correct" here when it comes to what should be used when building up the model. In the model this inductance is part of the parameters *Lpack*, *LpackFix* and *RpackFix*. The reason for the higher value when measuring at a complete pack is of course due to all the bus bars inside the pack.

A conclusion from this is that measurements at module level should give a fairly accurate estimation for the inductance/cell and measurements at cell level seems more or less meaningless for frequencies above a few kHz. Measurements at cell level or for a few cells in series should therefore focus on the parameters *RpackA*, *RpackB* and *CpackA* in the model and their variation due to temperature, SOC etc at low frequencies.

In Figure 9.18 the low frequency, non-inductive, behaviour of the measurement results are studied. At 300 Hz, scaled to 96 cells in series, the results are

1 cell	74 mΩ
3 cell	81 mΩ
5 cell	82 mΩ
7 cell	83 mΩ
Module	83 mΩ
HV-battery pack	84 mΩ

The results are very consistent. There is a deviation of ~9 mΩ when measuring on 1 cell scaled to 96 cells compared to when measuring on 7 cells or a module. When measuring on 1 cell the actual impedance measured is only 770 µΩ and the actual deviation is only 94 µΩ. A lower error should not be expected here considering the measurement technique used with a network analyser together with self-built injection boxes.
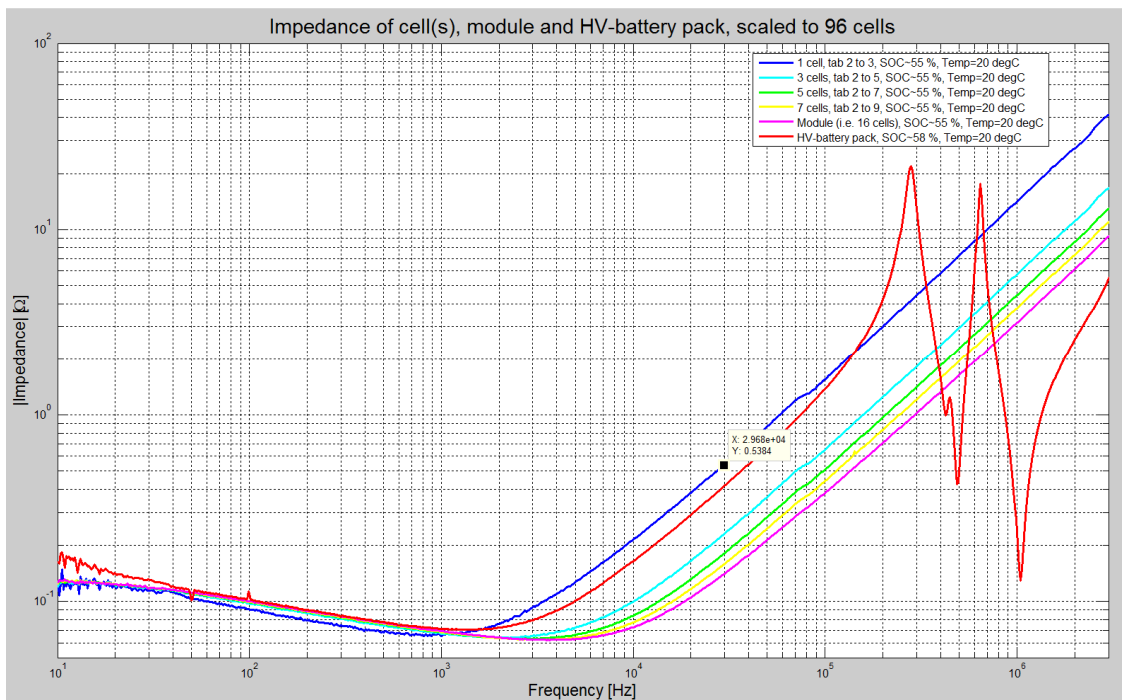
Figure 9.17 - Measurement at cell to pack level with results scaled to pack level
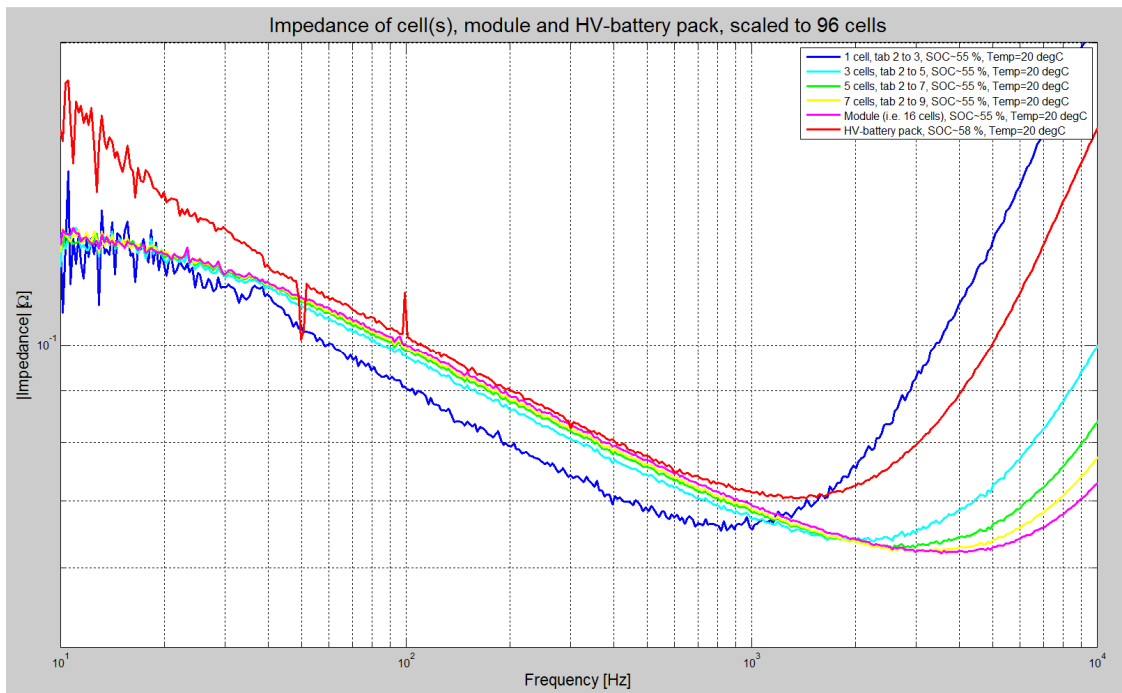

Figure 9.18 - Measurement at cell to pack level with results scaled to pack level. Zoom in on plot in previous figure. Note that there are some measurement problems at low frequencies, e.g. below 50 Hz. Some AC grid disturbances are also seen in the pack level measurements at 50 Hz and 100 Hz.

9.3 Battery Impedance Modelling

9.3.1 Battery cell impedance modelling

The impedance behavior of the battery cell as shown in Figure 9.2 and Figure 9.3 can be captured using a circuit model composed of a series connection of a resistor, an R//C branch, an R//L branch, and an inductor (i.e. R+R//C+R//L+L) as shown in Figure 9.19. This is due to the fact that the aim in this project is to capture the high frequency behavior of the battery cell. If one is interested in capturing mainly the low frequency behavior of the battery cell (in the range 0.1Hz to 1 kHz), it can be useful to add one capacitive branch (i.e. R//C) to capture the very low frequency behavior of the battery and remove the R//L or L branch.
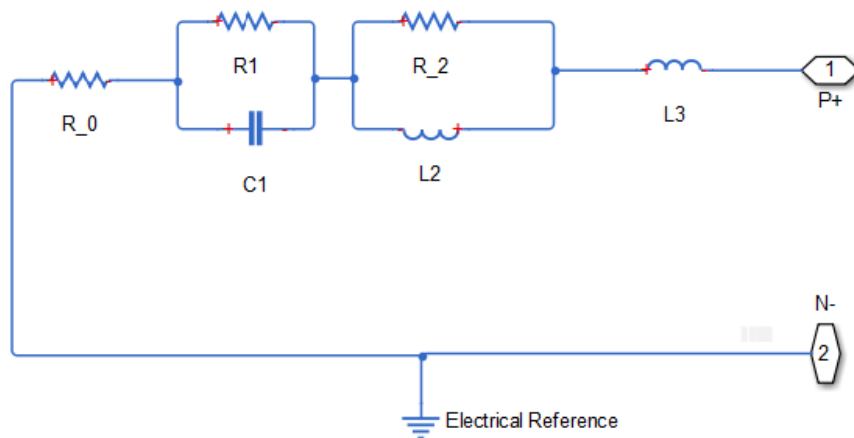

Figure 9.19 - Circuit equivalent impedance model of battery cells

Using some initial guess values for the various parameters, the model parameters are optimized to fit the measurement data which results in the parameter values of Table 9.1.

Table 9.1 - Cell model parameter values of for measurement data shown in Figure 9.2

Model parameters	Values
R0	0.975 mOhm
R1	0.193 mOhm
C1	1.756 F

R2	2.138 mOhm
L2	6.160 nH
L3	68.39 nH

The comparison of the cell impedance measurement and model impedance behavior is shown in Figure 9.20.
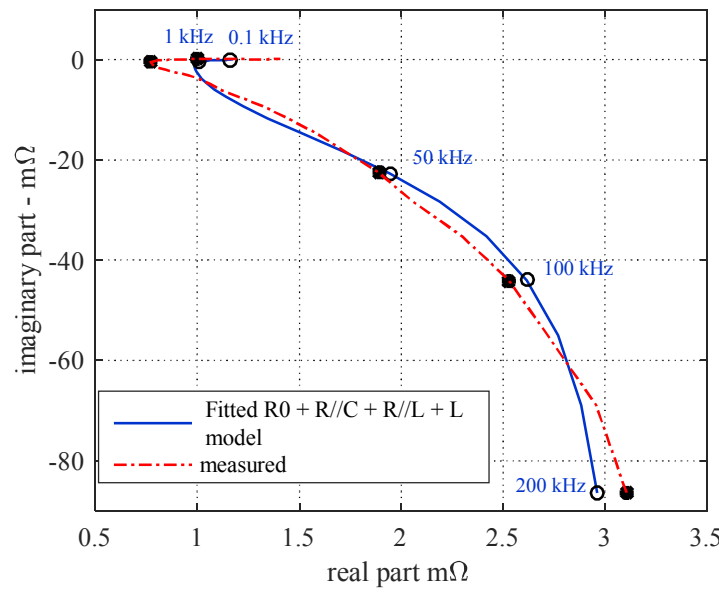

Figure 9.20 - Comparison of cell impedance measurement data and cell circuit equivalent model impedance behaviour

Generally the circuit model chosen here is good enough to the capture the impedance behavior of the battery cell in the frequency range used in this analysis (1 Hz to 200 kHz). However, as discussed at the end of Section 9.2.1, the model parameters calculated here that can be useful in the modelling of the battery pack impedance behavior are only R0, R1, and C1; These are the parameters that model the low frequency behavior of the battery.

9.3.2 Battery pack impedance modelling

9.3.2.1 The model

The model has been obtained by a "semi-manual" process, i.e. some thinking combined with "trial and error". The aim was to get a model that is rather "physical" and not just a model that fits the measurement data. This in order to be able to investigate the effect on the complete system if something inside the battery is modified.

In the model below the following parts can be identified:

- The battery low frequency behavior. This models the dominant differential behavior, i.e. this is the lowest impedance, up to about a few kHz.
  CpackA, RpackA, RpackB

- Y-capacitors in the CIDD and IEM ends
  CY1a, CY1b, CY2a, CY2b, LeslY1a, LeslY1b, LeslY2a, LeslY2b, ReslY1a, ReslY1b, ReslY2a, ReslY2b, Lygnd1, Lygnd2, Rygnd2

- Bus bars a) between the battery modules, b) from the battery modules to the contactor part, c) from the centre of the battery pack to the MSD including effect of the MSD. It also included the inductive effect/contribution inside the cells
  Lpack, LpackFix, RpackFix

- Bus bars on the IEM side between the contactor part and the Y-capacitor connection
  Lbar1a, Lbar1b, LbarFix1a, LbarFix1b, RbarFix1a, RbarFix1b, K1_BAT

- IEM side from the Y-capacitor connection to connector pins in the connectors
  Lbar0a, Lbar0b, K0_BAT

- Bus bars on the CIDD side between the contactor part and the Y-capacitor connection
  Lbar2a, Lbar2b, LbarFix2a, LbarFix2b, RbarFix2a, RbarFix2b, K2_BAT

- CIDD side from the Y-capacitor connection to connector pins in the connectors
  Lbar3a, Lbar3b, K3_BAT

Note 1: The R//L-links, e.g. *LbarFix1a* and *RbarFix1a*, have been included in order to try to account for the skin and proximity effects in the bus bars

Note 2: The *K0_BAT* to *K3_BAT* parameters describes mutual coupling between bus bars. 1 means perfect coupling and 0 means no coupling.
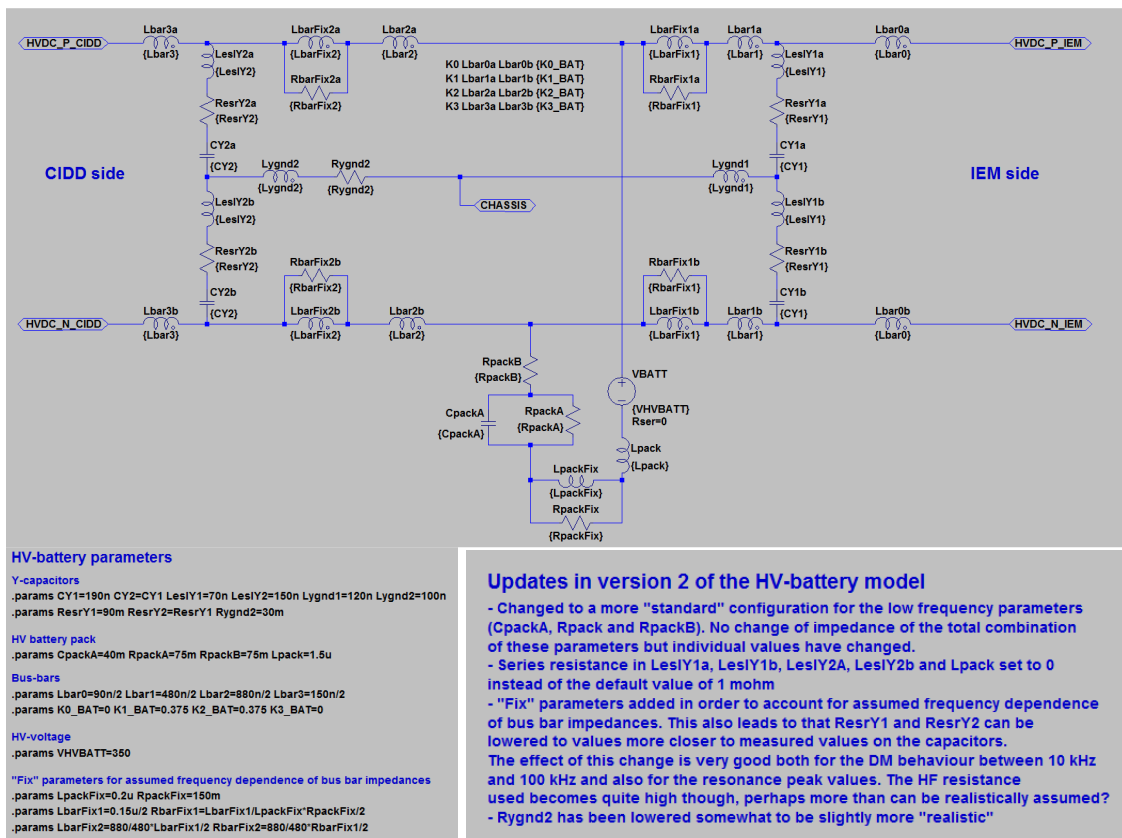
HVDC_P_CIDD — Lbar3a {Lbar3} — LeslY2a {LeslY2} — {ResrY2} ResrY2a — CY2a {CY2}

LbarFix2a {LbarFix2} — RbarFix2a {RbarFix2}

Lbar2a {Lbar2}

K0 Lbar0a Lbar0b {K0_BAT}
K1 Lbar1a Lbar1b {K1_BAT}
K2 Lbar2a Lbar2b {K2_BAT}
K3 Lbar3a Lbar3b {K3_BAT}

LbarFix1a {LbarFix1} — RbarFix1a {RbarFix1}

Lbar1a {Lbar1} — LeslY1a {LeslY1} — ResrY1a {ResrY1} — CY1a {CY1}

Lbar0a {Lbar0} — HVDC_P_IEM

CIDD side

Lygnd2 {Lygnd2} — Rygnd2 {Rygnd2} — CHASSIS

Lygnd1 {Lygnd1}

IEM side

LeslY2b {LeslY2} — ResrY2b {ResrY2} — CY2b {CY2}

LeslY1b {LeslY1} — ResrY1b {ResrY1} — CY1b {CY1}

HVDC_N_CIDD — Lbar3b {Lbar3}

LbarFix2b {LbarFix2} — RbarFix2b {RbarFix2} — LbarFix2b {LbarFix2}

Lbar2b {Lbar2}

RbarFix1b {RbarFix1} — LbarFix1b {LbarFix1}

Lbar1b {Lbar1}

Lbar0b {Lbar0} — HVDC_N_IEM

RpackB {RpackB}

VBATT {VHVBATT} Rser=0

CpackA {CpackA} — RpackA {RpackA}

Lpack {Lpack}

LpackFix {LpackFix} — RpackFix {RpackFix}

HV-battery parameters

Y-capacitors
.params CY1=190n CY2=CY1 LeslY1=70n LeslY2=150n Lygnd1=120n Lygnd2=100n
.params ResrY1=90m ResrY2=ResrY1 Rygnd2=30m

HV battery pack
.params CpackA=40m RpackA=75m RpackB=75m Lpack=1.5u

Bus-bars
.params Lbar0=90n/2 Lbar1=480n/2 Lbar2=880n/2 Lbar3=150n/2
.params K0_BAT=0 K1_BAT=0.375 K2_BAT=0.375 K3_BAT=0

HV-voltage
.params VHVBATT=350

"Fix" parameters for assumed frequency dependence of bus bar impedances
.params LpackFix=0.2u RpackFix=150m
.params LbarFix1=0.15u/2 RbarFix1=LbarFix1/LpackFix*RpackFix/2
.params LbarFix2=880/480*LbarFix1/2 RbarFix2=880/480*RbarFix1/2

Updates in version 2 of the HV-battery model
- Changed to a more "standard" configuration for the low frequency parameters (CpackA, Rpack and RpackB). No change of impedance of the total combination of these parameters but individual values have changed.
- Series resistance in LeslY1a, LeslY1b, LeslY2A, LeslY2b and Lpack set to 0 instead of the default value of 1 mohm
- "Fix" parameters added in order to account for assumed frequency dependence of bus bar impedances. This also leads to that ResrY1 and ResrY2 can be lowered to values more closer to measured values on the capacitors.
The effect of this change is very good both for the DM behaviour between 10 kHz and 100 kHz and also for the resonance peak values. The HF resistance used becomes quite high though, perhaps more than can be realistically assumed?
- Rygnd2 has been lowered somewhat to be slightly more "realistic"

Figure 9.21 - Battery pack model with component values and comments on what is new in version 2 of the model

9.3.2.2 *Model predictions vs measurements results*

Here several different comparisons are made with different battery "configurations".

Figure 9.23 and Figure 9.24 shows differential impedance measurements on
- two different live battery packs by Volvo
- one of the live battery packs above by Rise
- one inert battery pack by Volvo

The figures also shows the battery pack differential impedance predicted by the model.

Some comments about the results seen in Figure 9.23 and Figure 9.24
- The measurement results are generally quite close to the impedance predicted by the model. This is especially true at, the for RIFEL very important frequencies of 1 and 2 times the IEM inverter switching frequency, i.e. 10 kHz and 20 kHz
- The agreement between the measurements by Volvo/RISE on the same battery with slightly different methods were quite good. The biggest deviation was seen in the 1-2 kHz frequency range and was <10 %
- Impedances of inert and live battery only starts to differ below ~3 kHz
- It can be seen that the live measurements by Volvo were not good above a few MHz. This was due to the probes used during the measurements. At another measurement occasion the results coincided with the model and the inert measurements all the way up to 10 MHz.

In Figure 9.25 the measurement results on an inert battery in the IEM contact are compared with model predictions both for differential mode and common mode impedance. Measurements have been performed both with open circuit and short circuit of the battery in the CIDD end. The model predicts the behavior quite well

In Figure 9.26 the measurement results on an inert battery in the IEM contact are compared with model predictions both for differential mode and common mode impedance. Here the Y capacitors are removed, first in the CIDD end and then in both the CIDD and IEM end. The model predicts the behavior quite well when removing the Y-capacitor in the CIDD end. When also removing the capacitor in the IEM end there is no coupling to chassis any longer in the model but in reality there is still a coupling of around 2 nF to the chassis. Note that this is insignificant compared to the almost 800 nF "intentionally" added Y-capacitance in the battery.

A note about the remaining ~2 nF to chassis when removing the Y-caps: There is capacitive coupling from the cells in the battery to the cooling plates. Each cell is located next to one cooling plate and since there are 96 cells in the battery that means a total of 48 cooling plates, see Figure 9.22 below. The cooling plates are only connected to chassis though via the cooling water.

The result from measurements on one inert module from the cooling plate(s) to HVDC-/HVDC+ in the frequency range 10 kHz – 1 MHz assuming it is a pure capacitance was between 7 and 10 nF for the 8 different cooling plates. Since there could have been some coupling between the cooling plates this gives an upper limit for the capacitance in one module of 67 nF to the cooling plate(s) and around 400 nF for the complete pack.

This capacitance should have little effect on the ripple in the SPA platform for frequencies above the IEM inverter switching frequency, 10 kHz, since it is connected in series with the cooling water to chassis. In our tests we had no cooling water in the inert battery and normal "tap" water in the live batteries. Assuming as a worst case that sea water with a resistivity of 0.2 Ωm is used for cooling the battery. The resistance from the closest module to chassis is then estimated to be ~1 kΩ based on the geometry of the cooling hose. At 10 kHz the battery Y-caps impedance is already down at ~20 Ω which is very much lower than 1 kΩ.
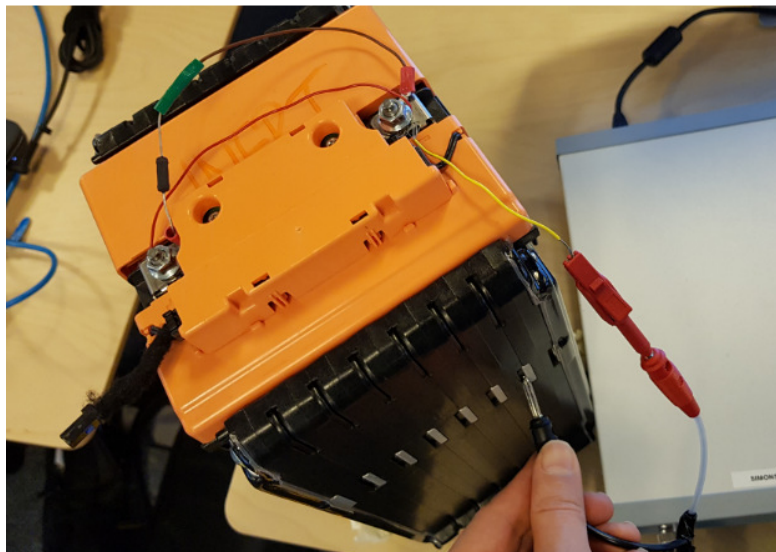
Figure 9.22 - Measuring the capacitive coupling from HVDC+/HVDC- to one of 8 cooling plates in a module (inert)
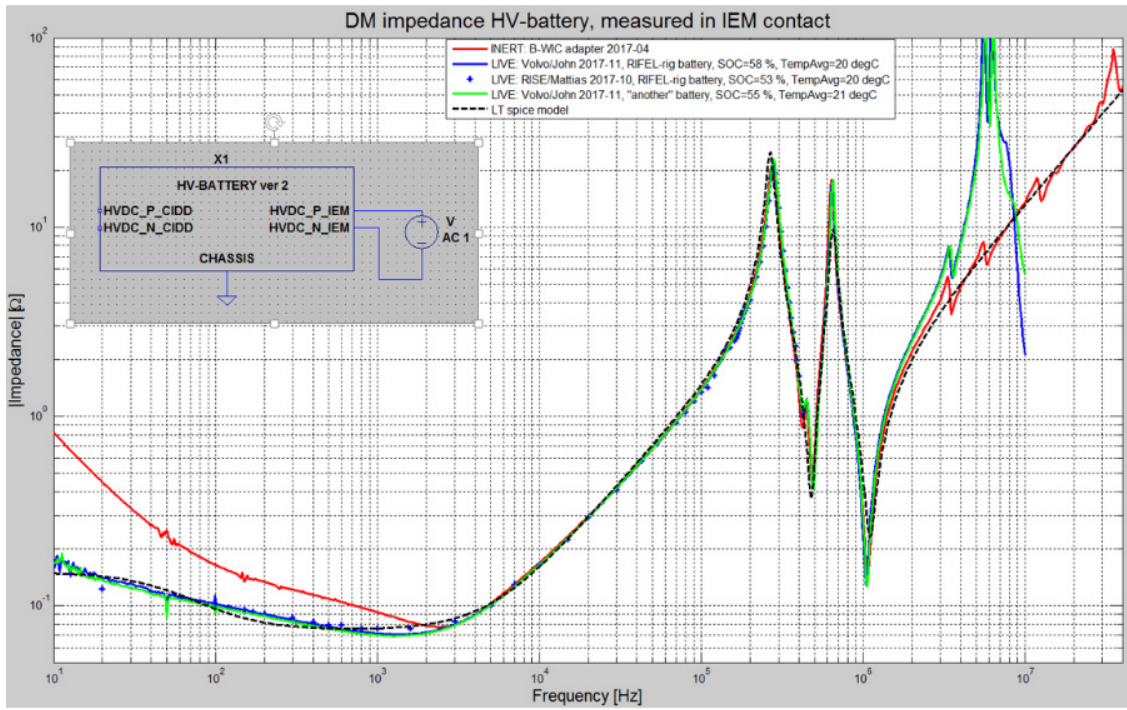
Figure 9.23 - Differential mode impedance measurements on live and inert batteries compared with model results
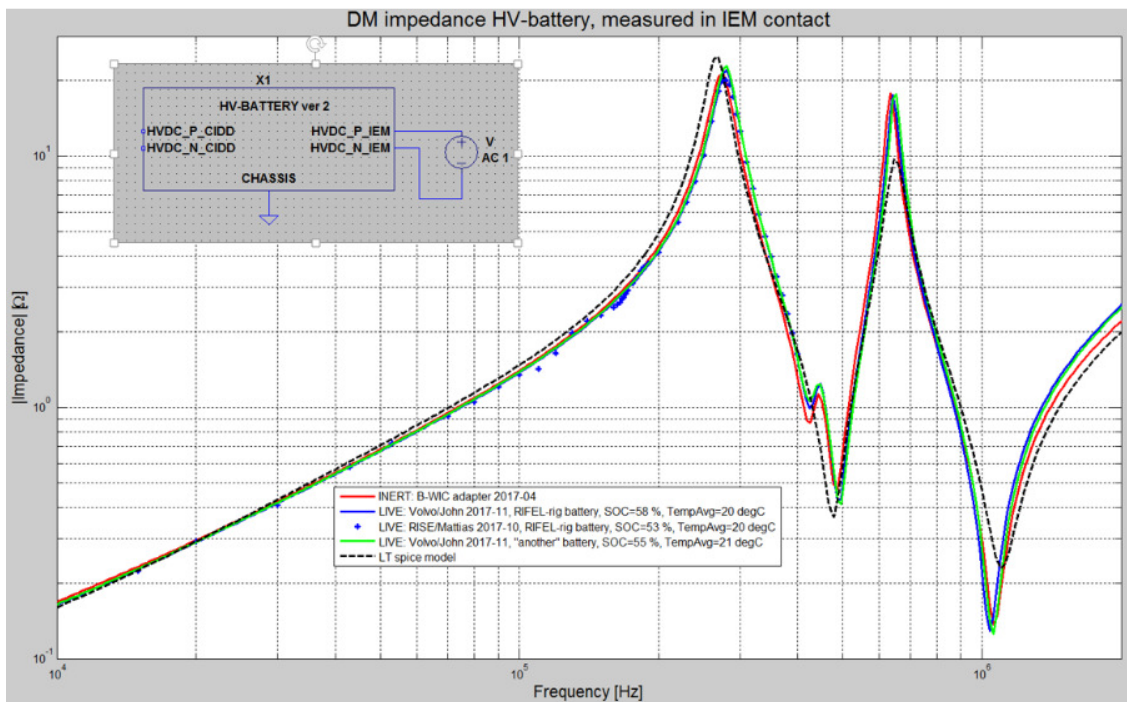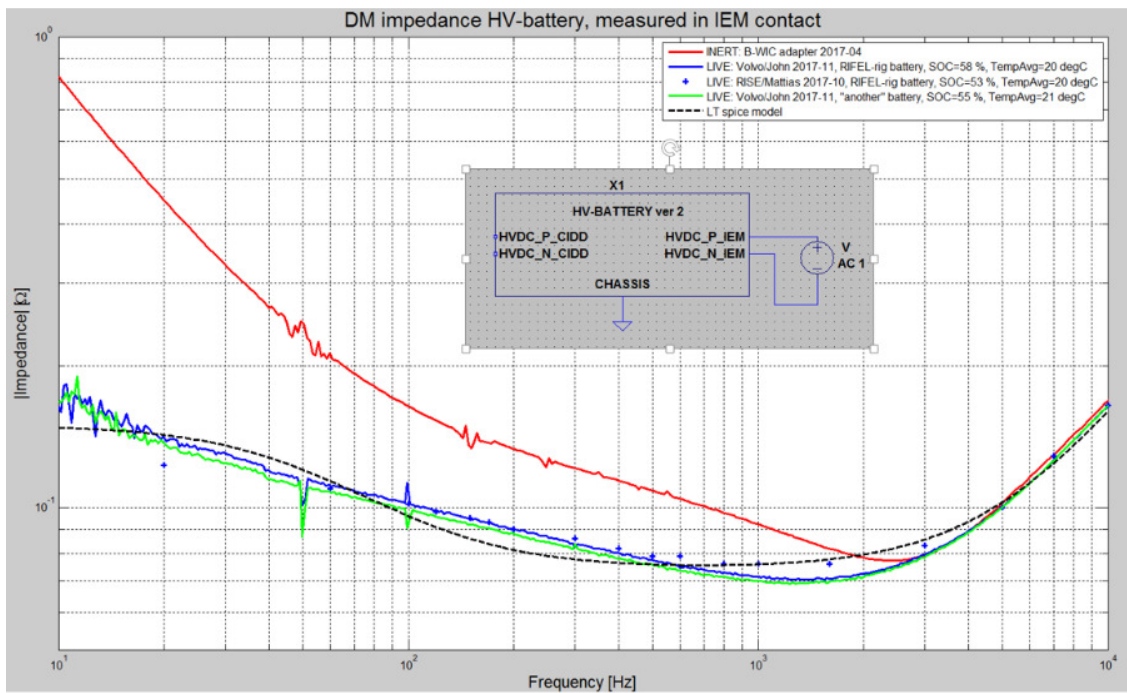
Figure 9.24 - Differential mode impedance measurements on live and inert batteries compared with model results. Zoom in on different frequency ranges of Figure 9.23
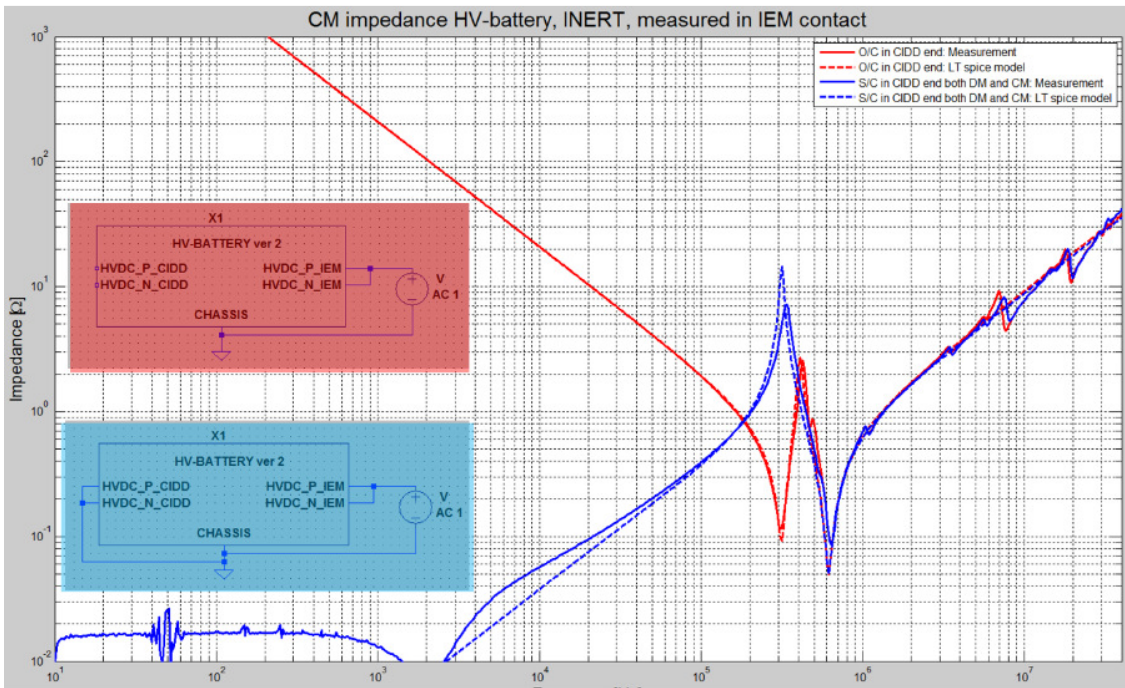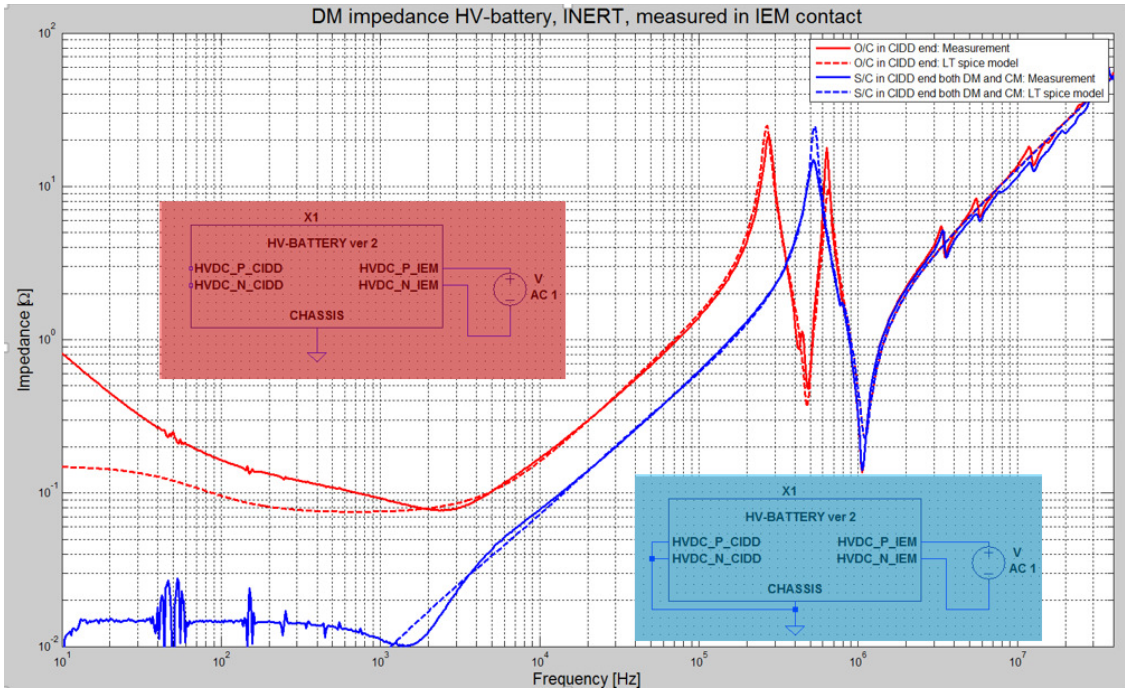
Figure 9.25 - Measurements on the inert battery vs model results
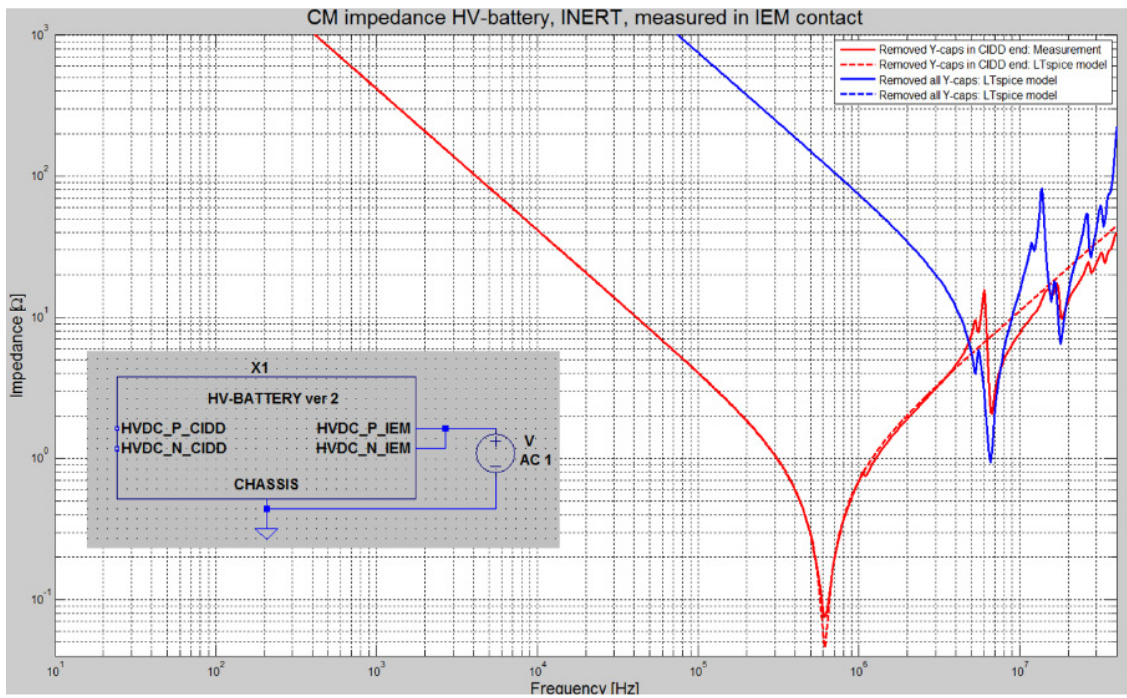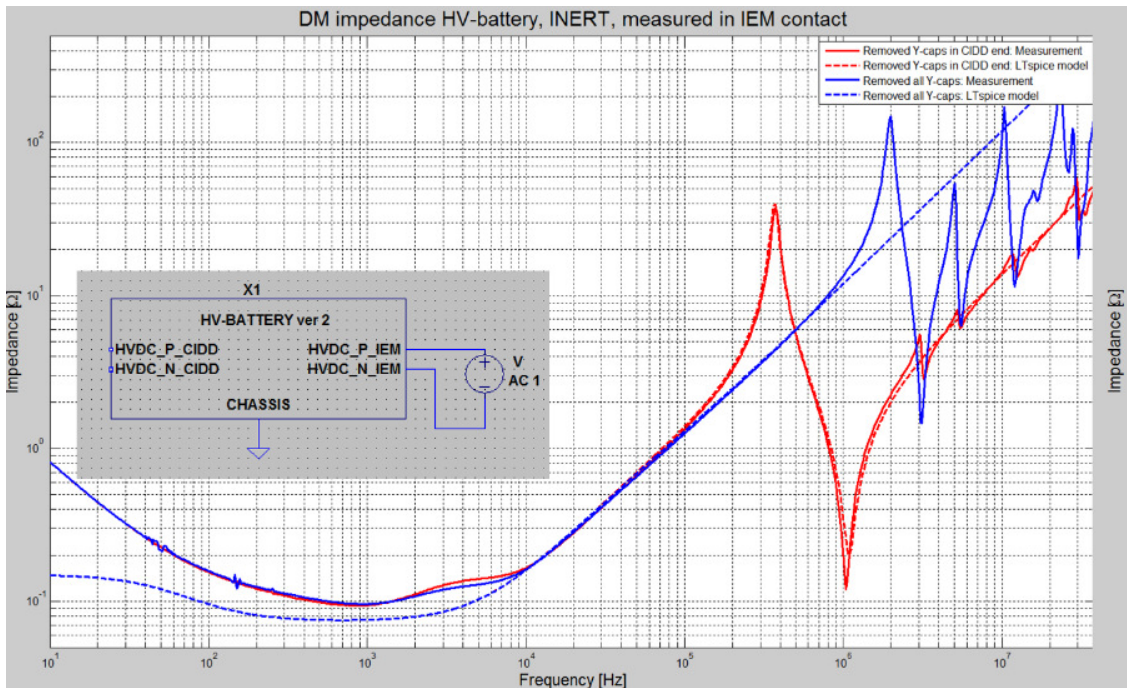
Figure 9.26 - Measurements on the inert battery vs model results when removing Y-capacitors

9.3.2.3 *"Sub-system" model predictions vs measurements results*

In Figure 9.27 the effect of the cable between IEM and the HV-battery on the differential mode impedance can be seen. Tests with "original" cabling and cabling with integrated Break-out-Boxes have been performed. When performing ripple measurements in a test rig cables with these type of Break-out-Boxes has been used in order to be able to access nodes inside the shielded cables. The model seems to take care of the cable and Break-out-Boxes influence on the differential mode impedance in a good way.

In Figure 9.28 the effect of adding two other units in the system, the CIDD and the OBC and the associated cabling can be seen. It is the CIDD, the other inverter in the Volvo SPA platform that has the biggest effect on the differential impedance. The model takes care also of this case in a good way via models of CIDD, OBC and the cables.
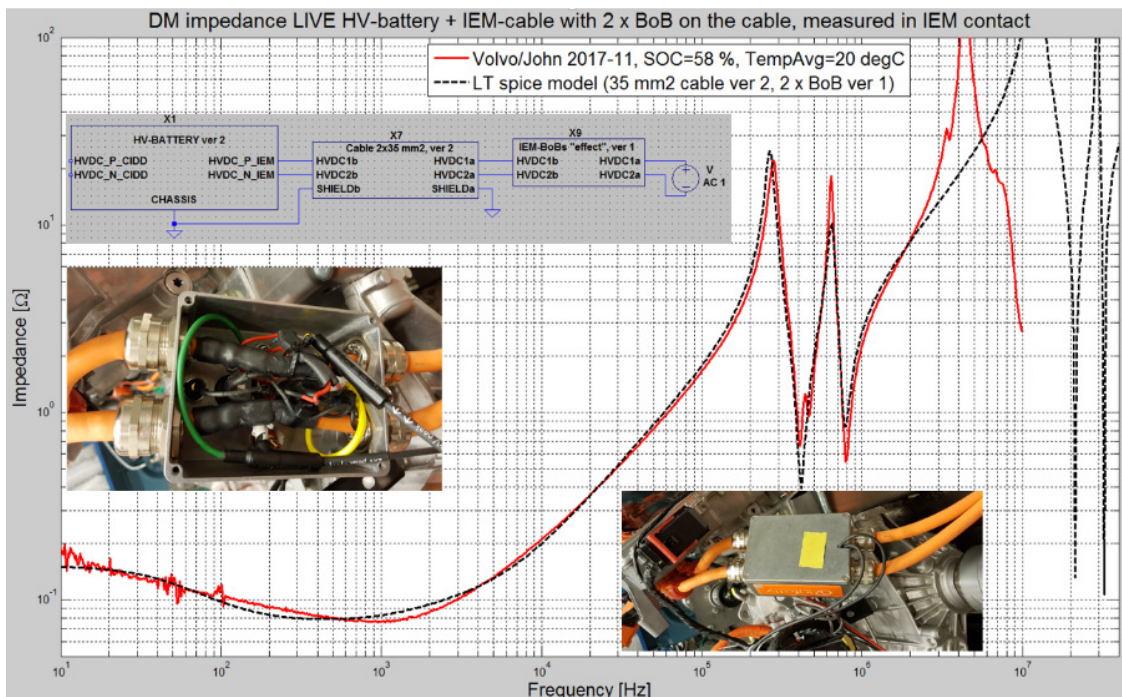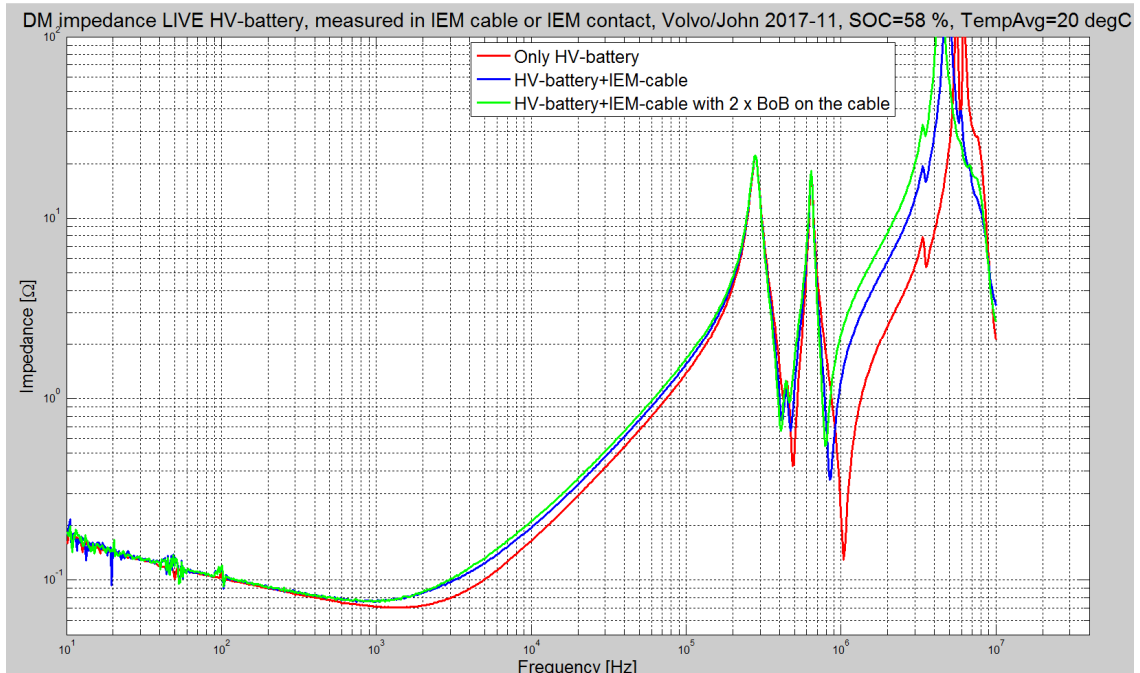
Figure 9.27 - Measurements on the "sub-system" consisting of a HV-battery and an IEM-HV-battery cable that is 1.9 m long with or without 2 Break-Out-Boxes on the cable. Model vs measurement in the lower plot. The effect of the cables can be seen in the upper plot
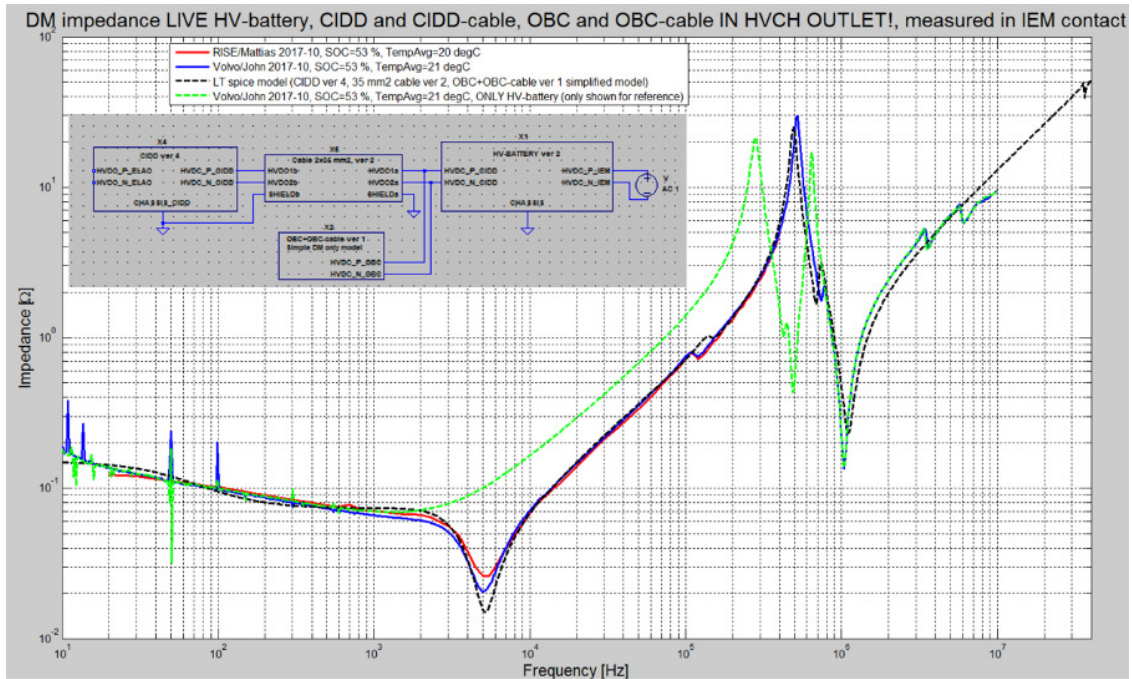
Figure 9.28 - Measurements on the "sub-system" consisting of HV-battery, CIDD, OBC and the associated cabling. Model vs measurement in the lower plot. One plot is included with measurements on only the HV-battery to show the effect of connecting the other two units

10 Inverter and Machine model

10.1 General Inverter Modeling

The Inverter can be modeled in three different levels of detail. The more details that are included in the simulation model, the longer it takes to simulate the total drive system

10.1.1 Ideal IGBT Models

If the inverter is considered as an ideal component, no losses are accounted for in the components. The IGBTs and diodes are modeled as ideal switches, see Figure 10.1. Also, no parasitic components (e.g. inductances and capacitances) are present in the circuit.
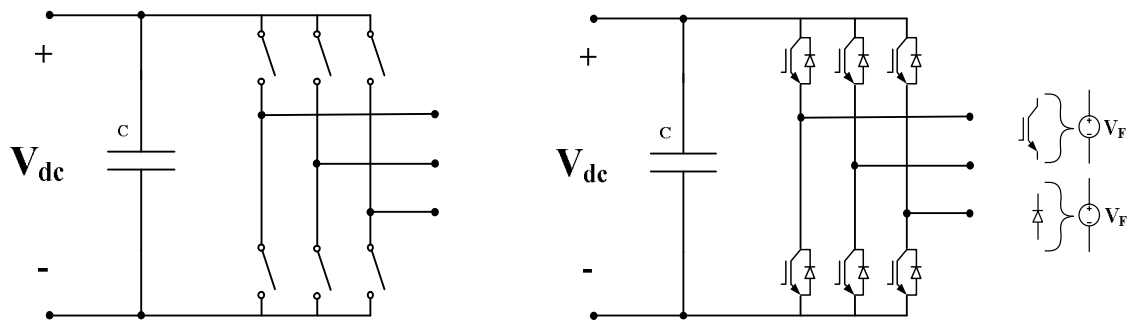
Figure 10.1 - Schematic of a three-phase inverter with ideal switches (left) or switches with forward voltage drop (right)

10.1.2 IGBTs with Switching Events

In order to increase the details in the IGBT model, several different approaches can be used to model both the actual switching events in the circuit as well as the component losses. The model in Figure 10.2 shows an overview of the Average IGBT model that accounts for the losses in the component. The parameter extraction is done by a step-by-step wizard based on datasheet values. Note that the switching events are not accurately described since the focus of the model is to predict component losses.
The IGBT model with most details is the Basic Dynamic IGBT, see Figure 10.3. As for the average IGBT model, the parameter extraction procedure is done in a step-by-step guide where datasheet graphs and data is used for input. In addition to the losses, the parasitic capacitance and inductance of the component is accounted for in the model. The purpose of the model is to both determine the actual switching events as well as the losses in the component.
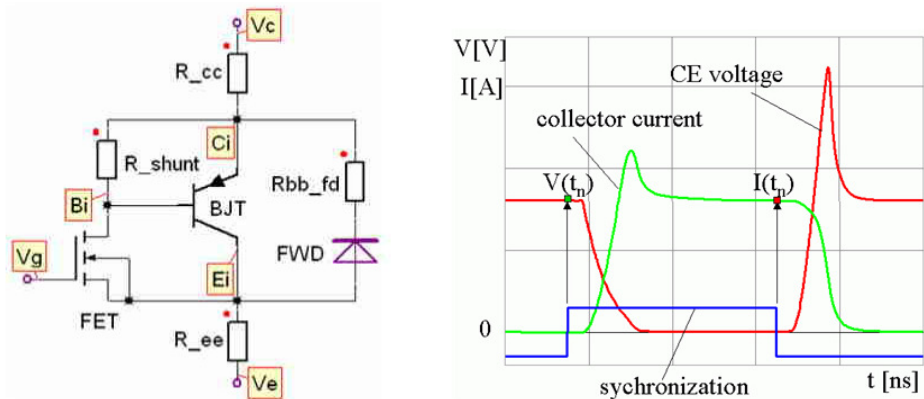
Figure 10.2 - Average IGBT Model that accounts for both conduction and switching losses in Ansys Simplorer.
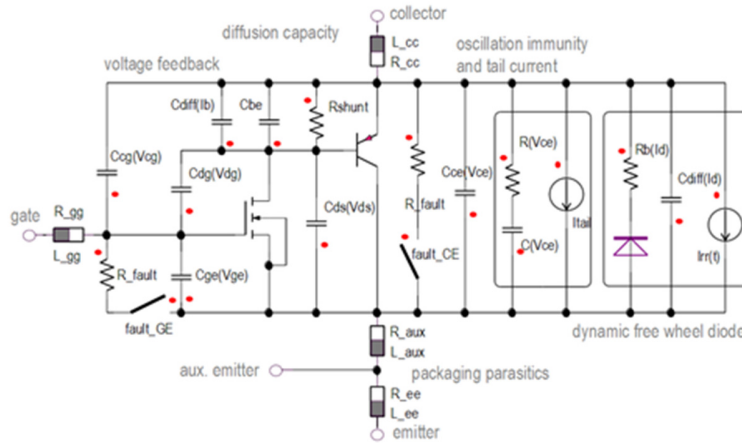
Figure 10.3 - Basic Dynamic IGBT Model in Ansys Simplorer that accounts for actual switching events.

10.2 IGBT Model Impact on the DC-Link

In order to investigate the needed degree of details within the inverter, the IGBT models in section 10.1 were implemented in the System Simulation Model. It is noted that in order to predict the correct average value of the battery current, the models of the IGBTs and the diodes needs to account for the correct *iv*-characteristics.

It is concluded that the IGBT model with correct *iv*-characteristics will give the largest deviation in the resulting DC-Link current ripple, see Figure 10.4 and Figure 10.5. The reason for this is not analysed further in this report. Also, the simulation times are strongly dependent on which model that is used, see Table 10.1. Depending on the purpose of the simulation, it is recommended to use either an ideal switch or the Average IGBT model.

Table 10.1 – Simulation times for the different IGBT models

	Ideal	*iv*-Char	AVG	Basic
Simulation Time	31min	33min	47min	1h38min
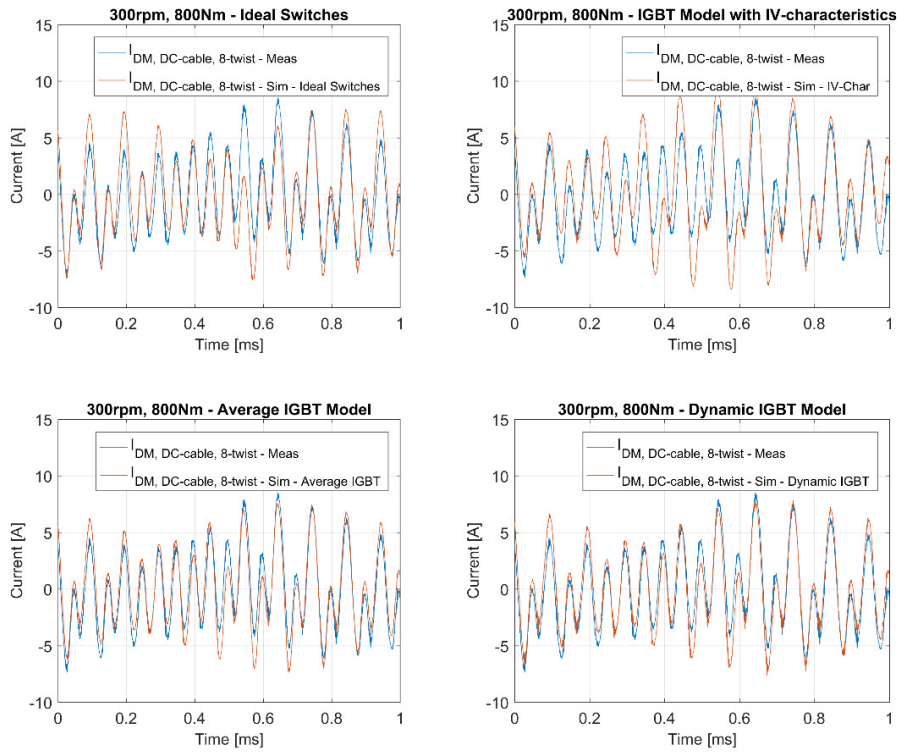
Figure 10.4 – Resulting DC-Link DM current ripple for different switch simulation models
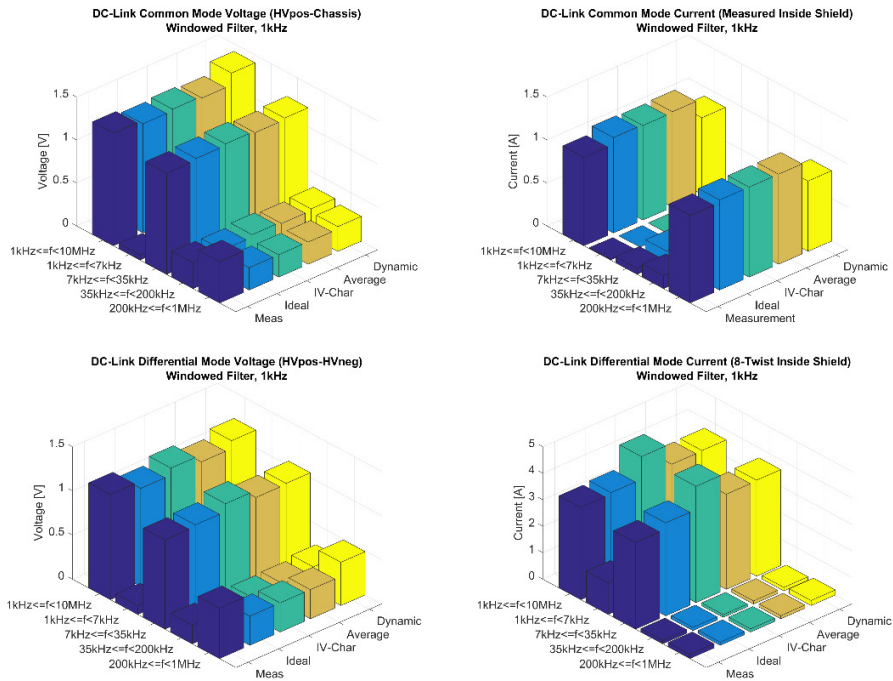
Figure 10.5 - Resulting RMS values for the DC-Link DM current ripple for different switch simulation models.

10.3 General PMSM Machine Modeling

A 20 kW interior permanent magnet (IPM) motor is used in the analyzed traction system. The motor parameters that used in simulations are summarized in Table 10.2.

Table 10.2 - Parameters of the ERAD IPM motor.

Power	28kW continuous
Max phase current	410A$_{RMS}$
Maximum speed	13 000rpm
Rated torque (Continuous)	90Nm
Rated torque (Peak)	240Nm
No of poles, P	8
Stator resistance	10.7mΩ @ 20°C (measured)
d-axis inductance	200µH (measured)
q-axis inductance	420µH (measured)
Permanent magnet flux	0.054Vs (calculated)
Max power in 20s	~70kW

The mathematical model of a PMSM in the rotor reference frame can be written as

$$v_d = R_s i_d + L_d \frac{di_d}{dt} - \omega_r L_q i_q$$

$$v_q = R_s i_q + L_q \frac{di_q}{dt} + \omega_r (\psi_{PM} + L_d i_d)$$

where v_d, v_q, i_d and i_q are the voltages and currents in d- and q axis respectively. Moreover, R_s, L_d, L_q, Ψ_{PM}, and ω_r are the stator resistance, the dq stator inductances, the permanent magnet flux and the rotor electrical speed, respectively. The developed electromechanical torque can be written as

$$T_e = \frac{3}{2} \frac{P}{2} (\psi_{PM} i_q + (L_d - L_q) i_d i_q)$$

where T_e is the torque and P is the number of poles in the machine.

10.4 Model Implementation

The general equations for a PMSM machine can be implemented in several different software tools. In this project, both Mathworks SimScape and Ansys Simplorer has been evaluated where the model implementation is similar in both tools. Due to reasons of compatibility, the decision was taken to use Ansys Simplorer for all further simulations, see Figure 10.6 for screenshot of the implementation.

Note that the input parameters of the PMSM (L_d, L_q and Ψ_m) are dependent on the current flowing in the machine, therefore are all machine parameters implemented by look-up-tables where the dq-currents are used as inputs.
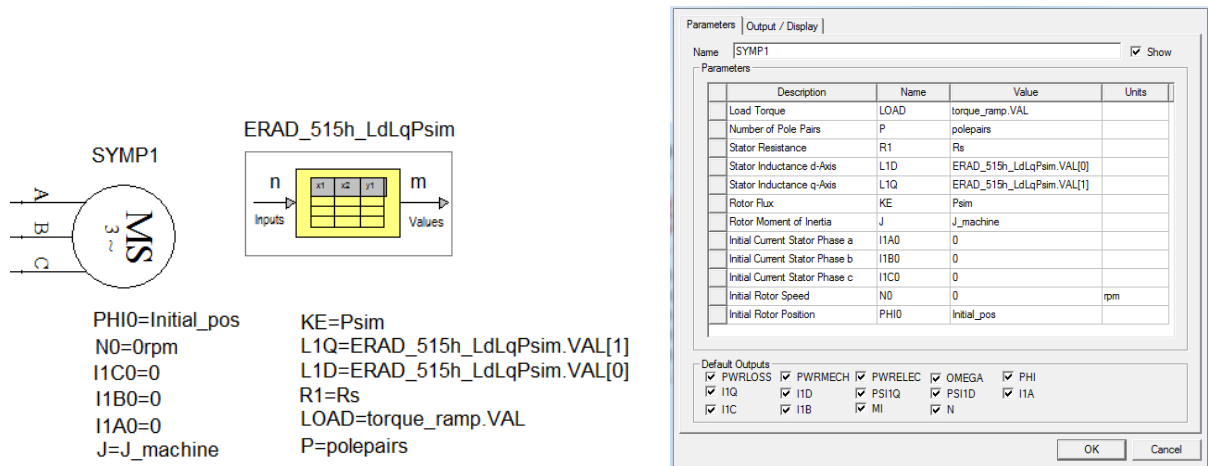
Figure 10.6 – The standard permanent magnet machine model (SYMP) in Ansys Simplorer

10.4.1 Ansys Maxwell and Reduced Order Models

The equation based model described in Section 10.3 is and idealized model and does not include e.g. cogging torque and loss analysis. If more detailed models are needed, the PMSM can be implemented in a FEM software e.g. Ansys Maxwell, seeFigure 10.7.
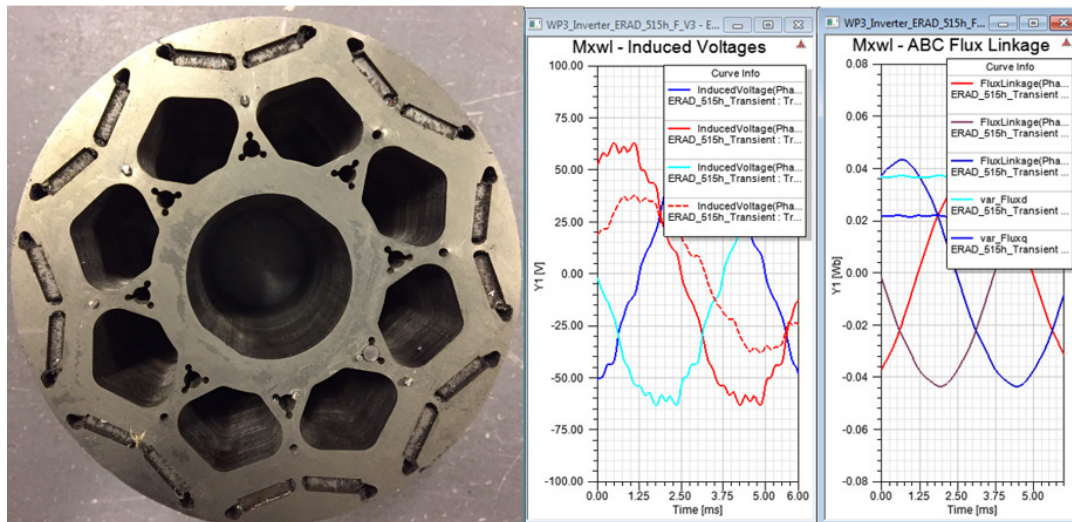

Figure 10.7 – 2D FEM model of the ERAD in Ansys Maxwell

The FEM model in Ansys Maxwell can also be co-simulated with the electric circuit in Ansys Simplorer. The magnetic circuit is then solved for each time step in the electric simulator. Since a complete FEM-calculation is done at each time step, the simulation time will be very long, a comparative simulation was performed and the total simulation time was several days. Therefore, this method is not recommended for the current simulation model. If co-simulations are to be used, a steady state operating point shall be analyzed but due to the controller implementation it is not possible to obtain this in the current system

simulation model. Based on the FEM-simulations in Ansys Maxwell, a Reduced Order Model (ROM) can be extracted automatically, see Figure 10.8. The purpose with this approach is to automatically obtain the machine parameters (L_d, L_q and Ψ_m) based on a FEM-model. The method is automatic and the extraction process is fairly quick (~3h). When the equivalent circuit is derived, solving the electric circuit will run fairly fast (~1h). The method was found to be working but no further evaluations of the model performance on the DC-Link were made.
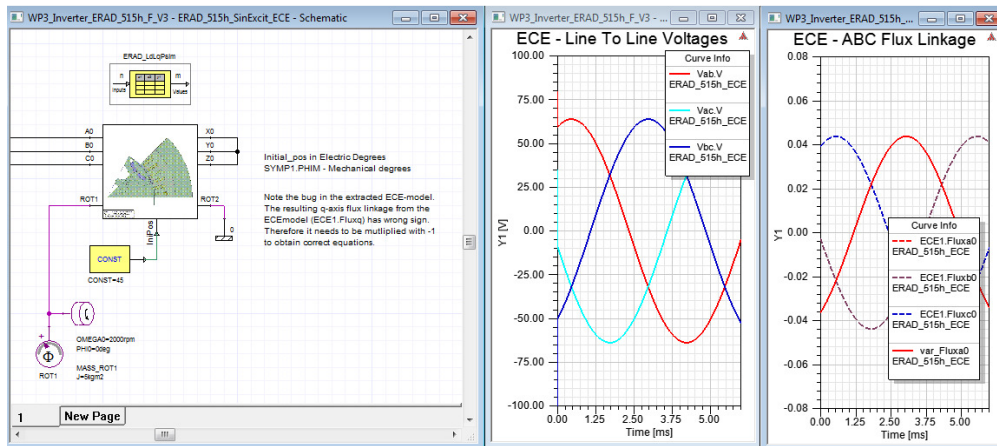
Figure 10.8 – Reduced order model based on FEM-simulations implemented in Ansys Simplorer

10.4.2 VHDL-AMS Model in Ansys Simplorer

To increase the level of detail in the simulation model and to be able to use input data from the supplier for the machine parameters, an improved PMSM model was implemented in VHDL-AMS see Figure 10.9. The model includes a sinusoidal varying cogging torque and access to the neutral point so that the CM-impedance of the machine can be accounted for.
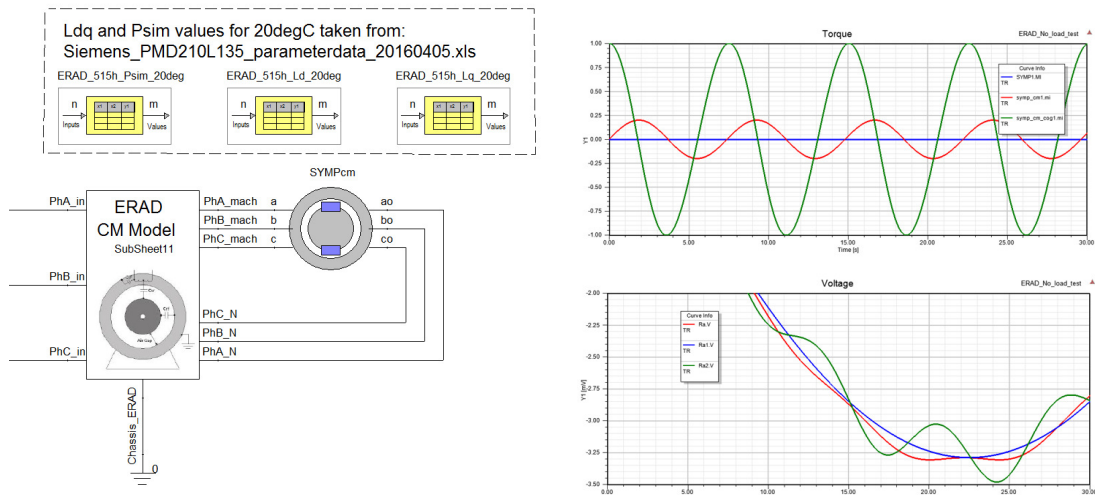
Figure 10.9 – VHDL-AMS PMSM model in Ansys Simplorer

As for the standard SYMP-model, the input parameters (L_d, L_q and Ψ_m) are dependent on the *dq*-currents which means that they are implemented by look-up-tables where the *dq*-currents are used as inputs. In the VHDL-AMS model, the cogging torque varies sinusoidally and can be adjusted by coefficients, see Figure 10.10. The cogging torque will mainly affect the AC-side quantities where the switching ripple will differ, see Figure 10.11.
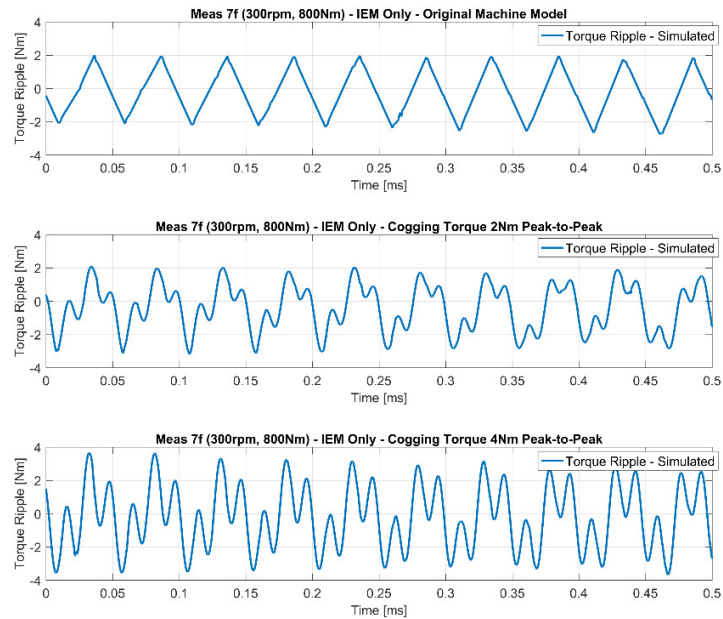
Figure 10.10 – Examples of simulated cogging torque for the improved VHDL-AMS PMSM model
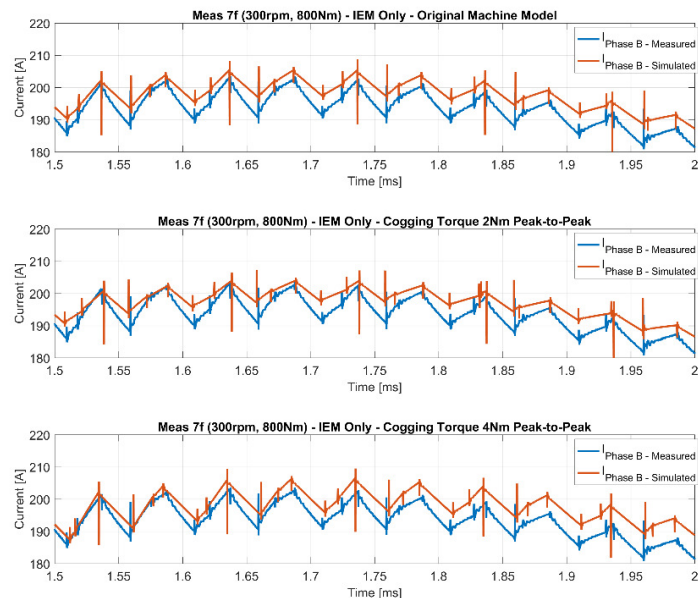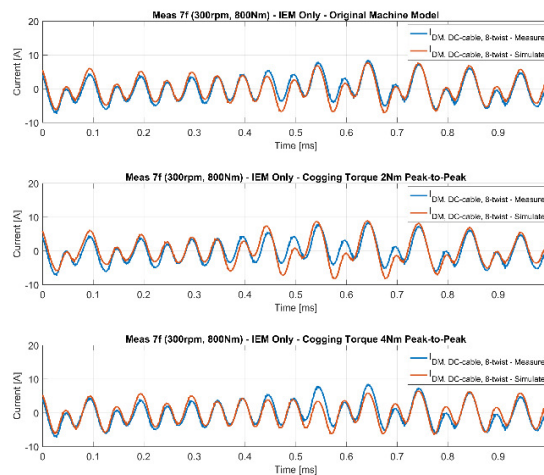

Figure 10.11 – Simulated AC-side current with different cogging torques in the PMSM VHDL-AMS model. Comparison with measurements in the Rifel-rig with 515h components

10.5 Cogging Torque Impact on the DC-Link

Depending on the frequency and the amplitude of the cogging torque in the VHDL-AMS PMSM model, the resulting DC-side current ripple will also vary, see Figure 10.12. If the frequency components of the cogging torque is poorly positioned with respect to the switching of the inverter, the resulting DM current ripple may even increase. How this is handled by the IEM is not known since the controller implementation is done by the supplier. The effect of changed cogging torque is also seen if the RMS-values of all DC-side quantities are studied, see Figure 10.13. It is noted that the cogging torque will mainly affect the common mode voltage and the differential mode current. The exact reason why it mainly affect these two quantities is not investigated in detail but one reasonable explanation might be that it originates from small changes in the switching pattern due to changes in the measured AC-side reference currents fed into the controller.

Figure 10.12 Simulated DC-side current with different cogging torques in the PMSM VHDL-AMS model. Comparison with measurements in the Rifel-rig with 515h components.
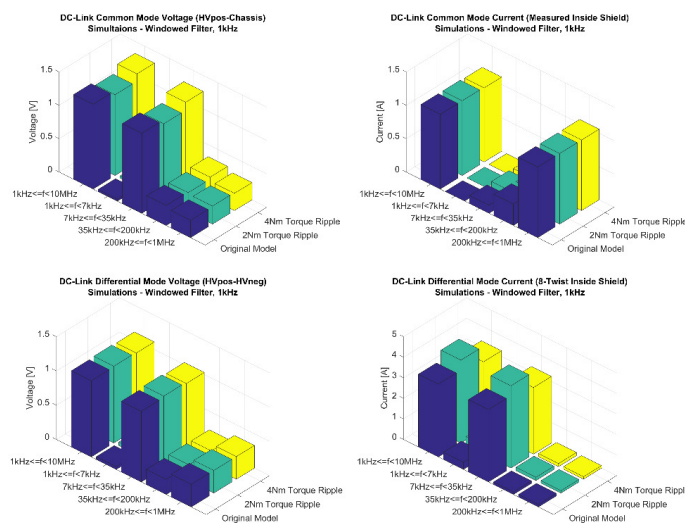
Figure 10.13 - Simulated DC-side RMS-values with different cogging torques in the PMSM VHDL-AMS model.

10.6 Parameter variations and temperature dependence

The machine parameters will change with temperature and the variations can be in the range of 15-20% in a temperature interval from 20°C to 120°C. This change in will affect the resulting current and voltage ripple on the AC-side, see Figure 10.14. A lower *dq*-inductance will give higher current ripple and vice versa. The DC-side is also affected, see Figure 10.15 and Figure 10.16.
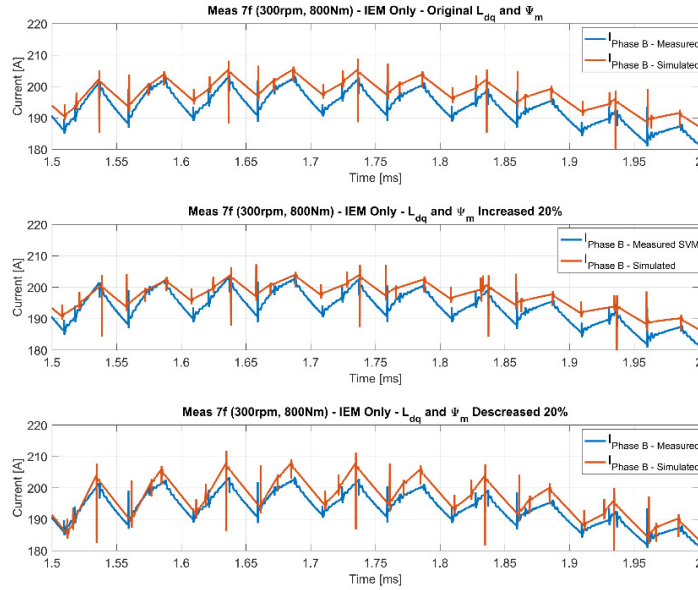

Figure 10.14 - Simulated AC-side current with varying machine parameters (L_d, L_q and Ψ_m).
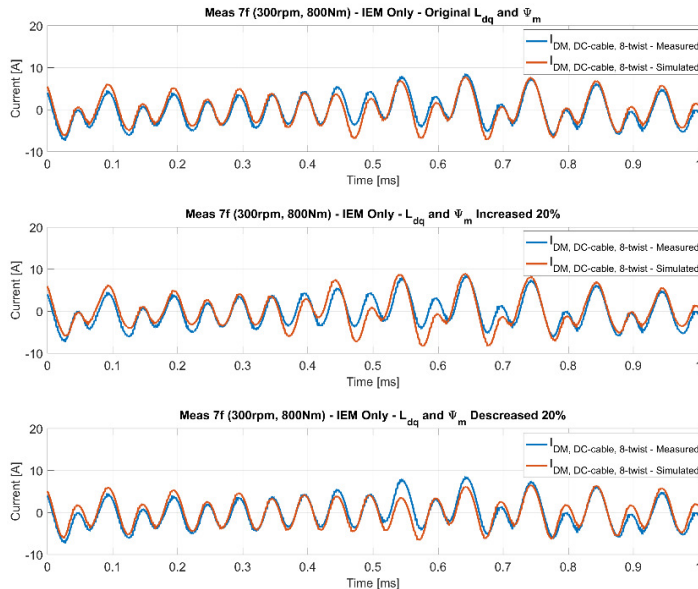
Figure 10.15 - Simulated DC-side DM current with varying machine parameters (L_d, L_q and Ψ_m).
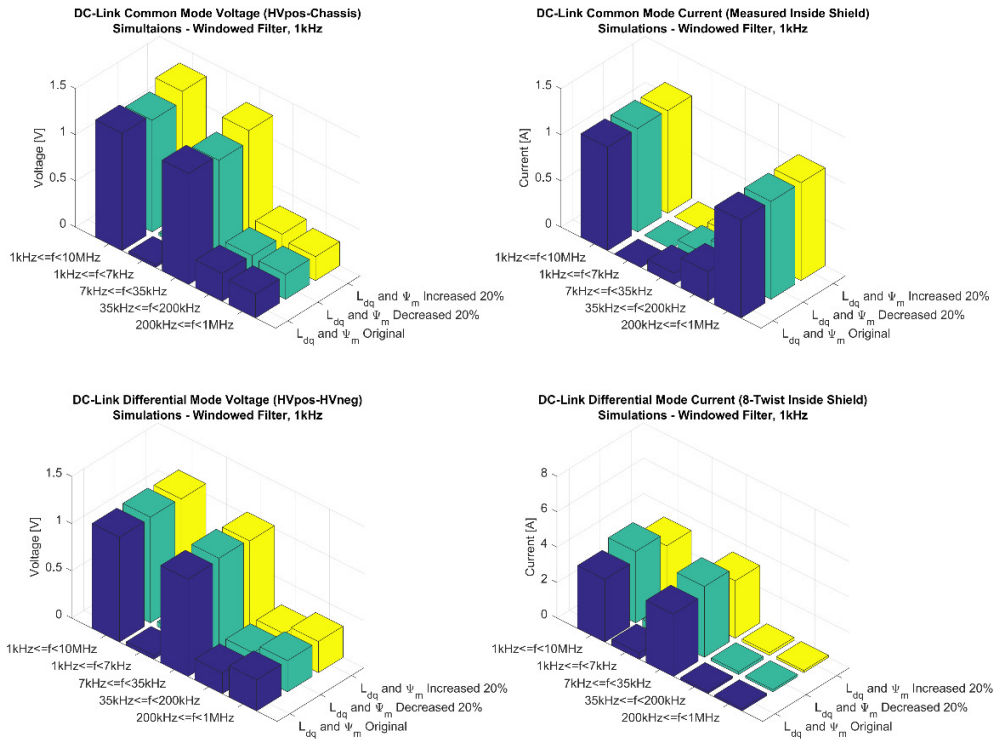
Figure 10.16 - Simulated DC-side RMS-values with varying machine parameters (L_d, L_q and Ψ_m).

10.7 Common Mode Model of a PMSM Machine

An important feature with the improved VHDL-AMS PMSM model is the access to the machine neutral point. Since the stator capacitance is the most important pathway of common mode currents in the machine, a RLC-network is connected at the y-point in order to create a CM-model of the machine, see Figure 10.17.
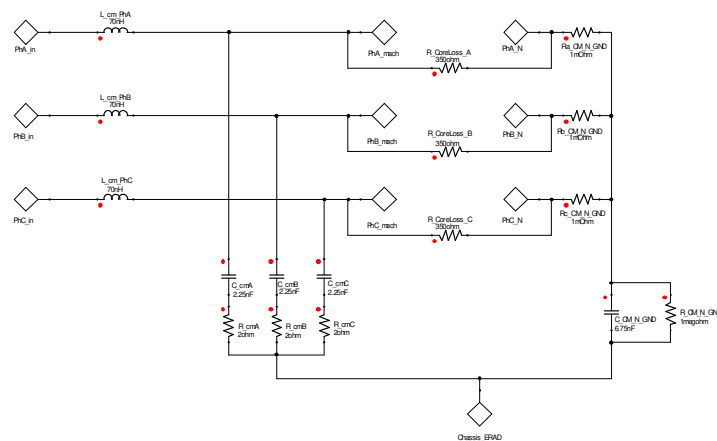

Figure 10.17 – Common mode (CM) impedance model of the electric machine

On the input of each winding is an RC-network connected to emulate the input winding capacitance. On the *y*-point is a stator capacitance connected to the surrounding ground. This component is perhaps the most important component in the network in order to determine correct CM currents. In parallel with each winding is a resistor connected to emulate the losses and the impedance resonance damping of the machine. This component does not affect the overall DC-side quantities to a significant extent. Since a constant resistance is used in the model, it is assumed that it will represent the eddy current losses in the machine since these losses are proportional to the speed squared. If even more accurate loss are needed, the hysteresis losses needs to be accounted for as well. This can be done with another parallel resistor where the resistance is inversely proportional with the speed of the machine.

10.8 PMSM Machine Controller

Field-oriented *dq*-control is a widely used control scheme for traction applications. There is no detailed information regarding the control algorithm of the ERAD system, so it is assumed that the system is based on Space Vector Modulation (SVM). The controller structure implemented in the system simulation model is seen in Figure 10.18.

The generated control signals in the ABC-domain in the system model can be set to either standard pulse width modulation (PWM), space vector modulation (SVM) or third harmonic injection. The impact of different switching strategies is analyzed in Section 10.9.
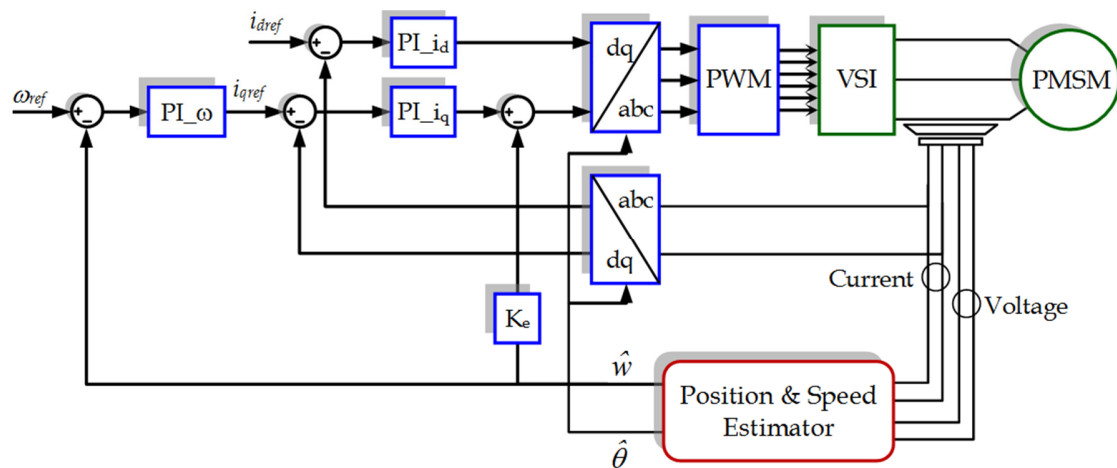

Figure 10.18 – Block diagram of the IEM controller structure

The optimal trajectory which would produce maximum torque per Ampere as a function of the *dq*-currents is referred to the MTPA-Algorithm. The algorithm is implemented by the supplier and solved based on the machine parameters. The values are stored in a look up table in the controller circuit of the IEM. This data is not known due to proprietary reasons and therefore an approximation based on the machine parameters is implemented in the system simulation model, see Figure 10.19.
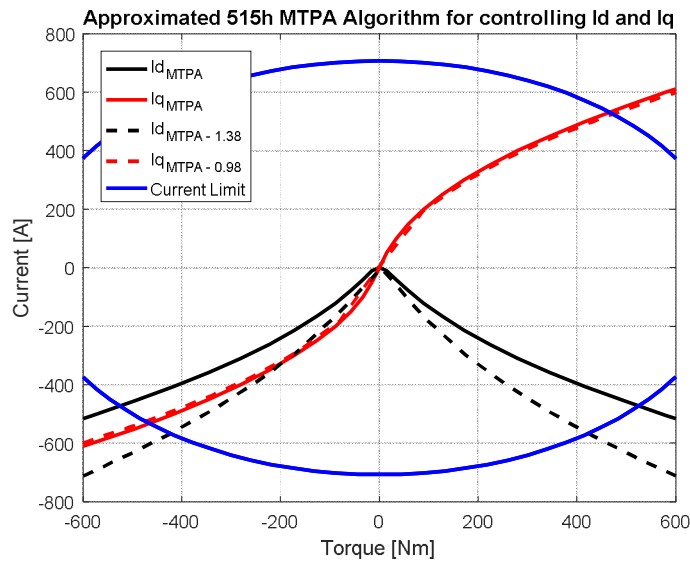
Figure 10.19 – Approximated MTPA algorithm to control I_d and I_q

To verify the switching scheme of the IEM, a measurement of the internal phase leg currents was performed, see Figure 10.20. This measurement was performed by inserting Rogowski coils directly on the DC-link capacitor connectors. The result of the current measurements were found to be accurate and therefore it could be concluded that the IEM is switching with a SVM scheme.
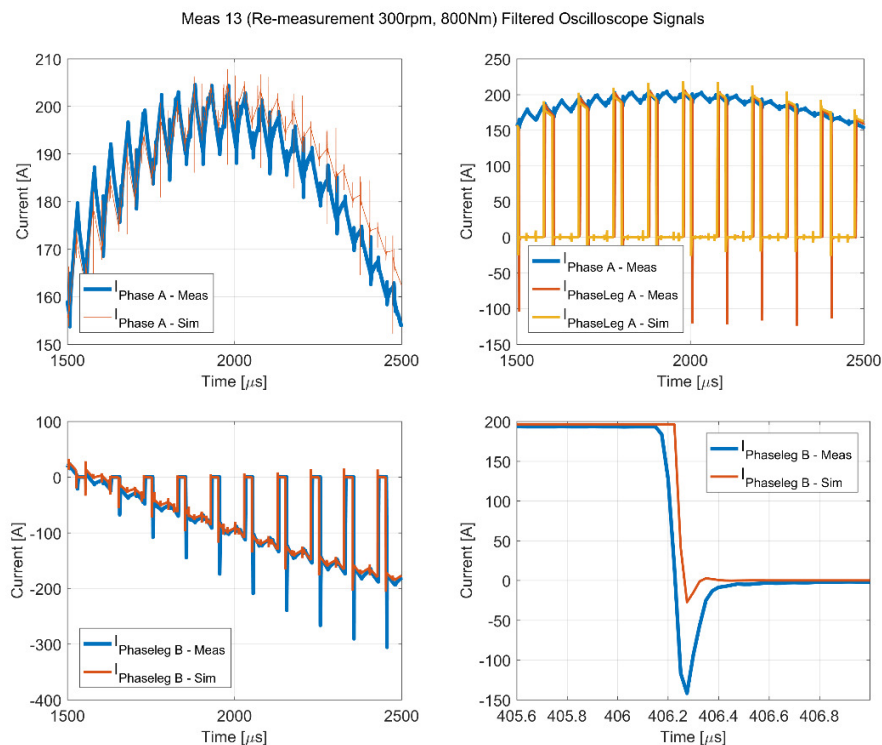

Figure 10.20 – Measurements and simulations of the phase leg currents internally in the IEM.

10.9 Controller Impact on the DC-Link

The switching scheme will affect the DC-link differential mode current ripple as seen in Figure 10.21. It is well known that SVM will generate the lowest current ripple, third harmonic injection will generate almost similar reference voltages which means that the harmonic content will be almost the same. Also, the differential mode voltage on the DC-link will be affected, see Figure 10.22.
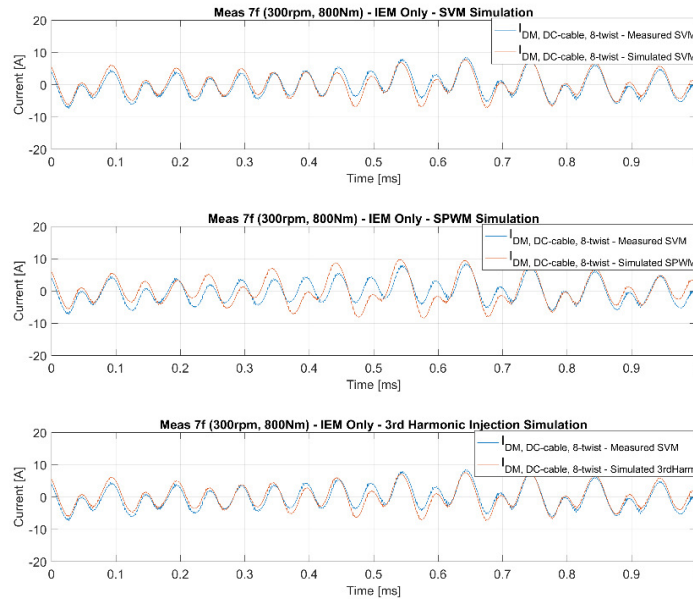

Figure 10.21 - Simulated DC-side DM current with different switching schemes
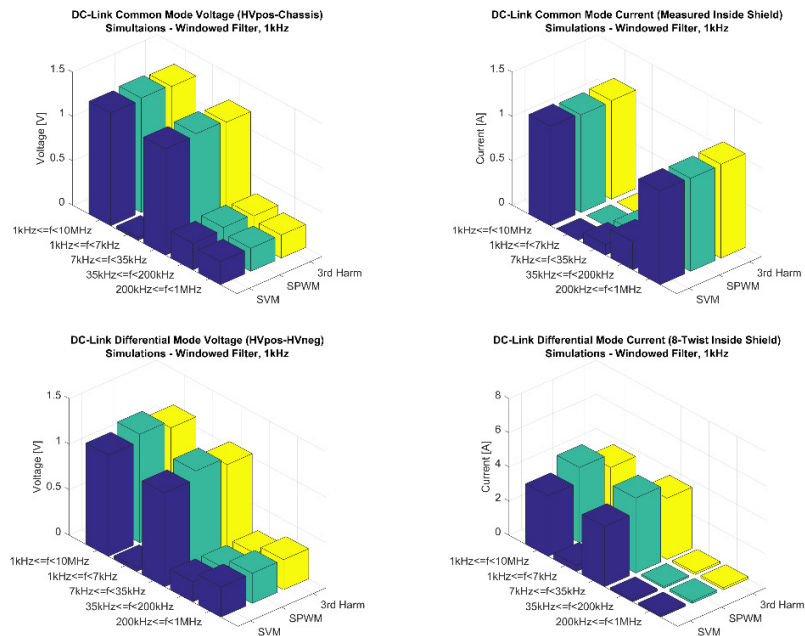
Figure 10.22 - Simulated DC-side RMS-values with different switching schemes

10.10 Inverter Modeling – Input Filter

In order to capture all effects in the IEM input filter, all capacitors, inductors and capacitors needs to be accounted for. The input consist of a bus bar with low inductance, two smaller y-caps (500nF), a smaller x-cap (880nF), a ferrite CM-choke mounted directly on the bus bar (8uH) and a large DC-link x-cap (~520uF).

The largest and perhaps most important component is the main x-cap which means that its impedance needs to be thoroughly characterized. Two different models are proposed with the purpose to represent the physical structure of the capacitor in the equivalent circuit design, see Figure 10.23 and Figure 10.24.

In addition to these physical components, the parasitic coupling between the IGBT module and the chassis is also accounted for in the IEM input filter model.
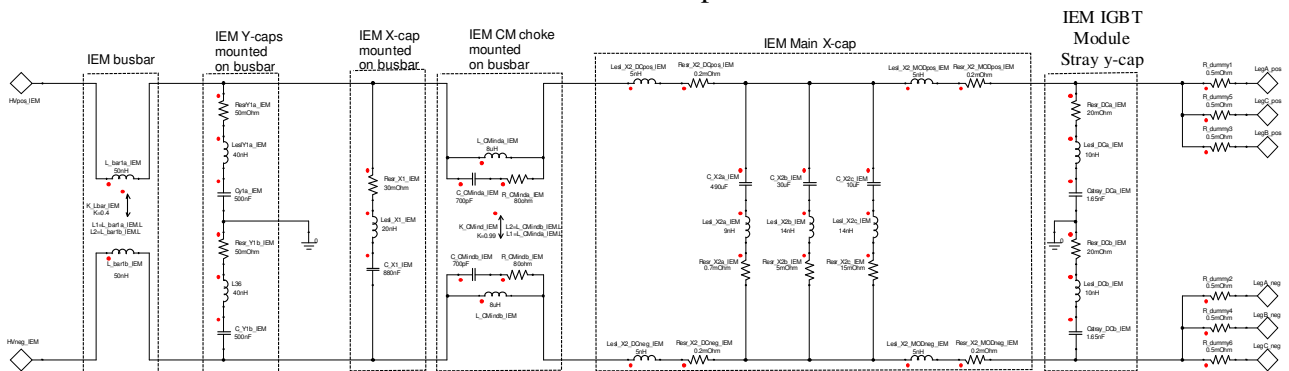
Figure 10.23 – Implementation of the IEM input filter in Ansys Simplorer, DC-link cap circuit suggested by John Simonsson
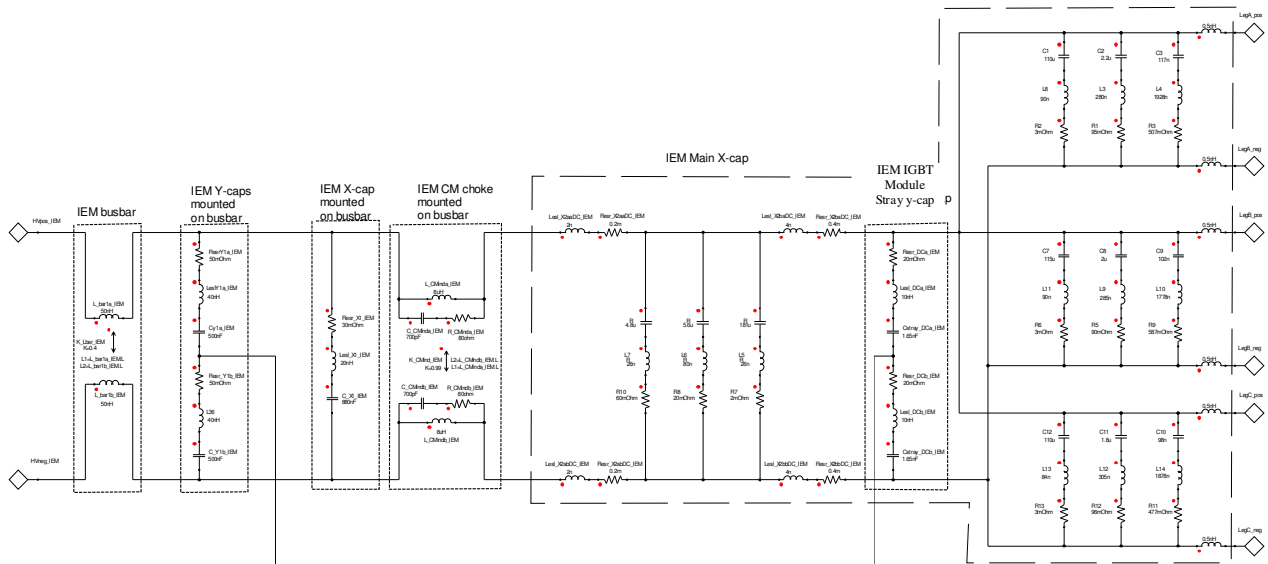
Figure 10.24 - Implementation of the IEM input filter in Ansys Simplorer, DC-link cap circuit suggested by Andreas Henriksson

10.11 Input Filter Modeling and Measurements

The derived impedance model is based on measurements of DC-link capacitor impedance and also of its transfer impedance. The model accounts for the impedance(s) of the bus bar package with CM-ferrite, y-capacitors and small x-capacitor, the IGBT module impedance vs chassis and the transfer impedance from the phase legs of the DC-link capacitor to the HVDC-connector. A simple measurement setup and the resulting transfer impedances can be seen in Figure 10.25. As noted, this denomination of DC-link capacitor impedance will give a slightly different impedance compared to traditional measurements. This is necessary to account for since it is the inverter that is the main source of disturbance.
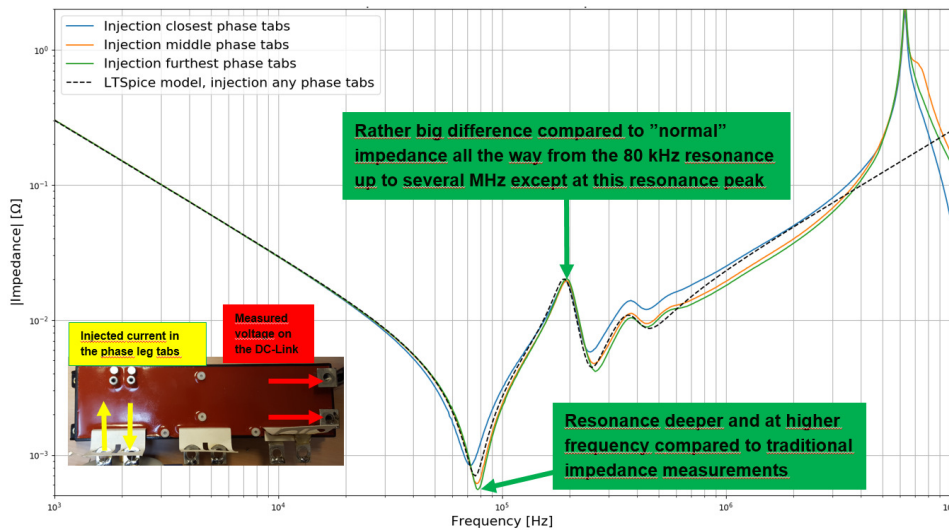

Figure 10.25 – Transfer impedance from the phase leg tabs to the DC-link tabs of the IEM DC-link capacitor

The rest of the input filter (CM-choke, small x-caps and y-caps) is also characterized by measurements, see Figure 10.26. The resulting RLC-model will show good agreement with the measurements.
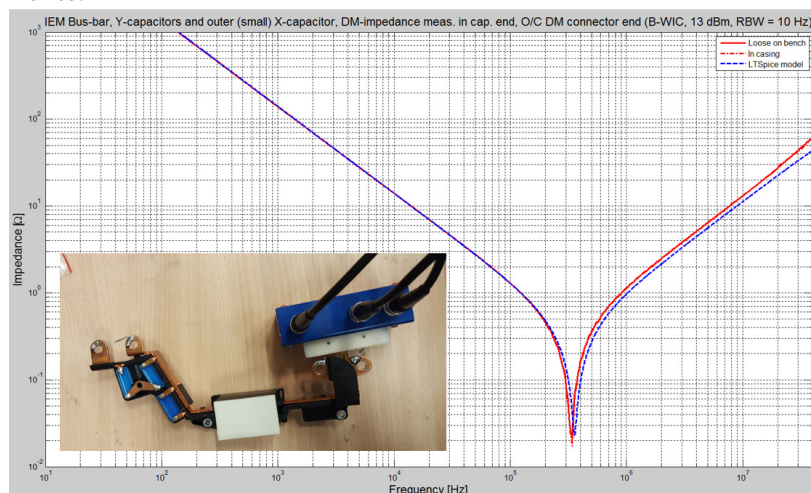

Figure 10.26 – Simulated and measured IEM input filter impedance. Measured in DC-link-cap end with removed DC-link-cap and IGBT module. Differential mode impedance with open connection in DC-Link end.

10.12 Input Filter Impact on the DC-Link

It is clearly seen in the simulations that a simple RLC-representation of the DC-link capacitor is not sufficiently accurate, see Figure 10.27.This is primarily seen as a significant increase of high frequency oscillations on all DC-link quantities.

The general performance of the two different DC-link x-cap equivalent circuits are in general similar, see Figure 10.28. Depending on which quantity that is analysed, the different models perform slightly different. For general simulations, it is recommend to use the version proposed by John Simonsson due to its lower complexity.
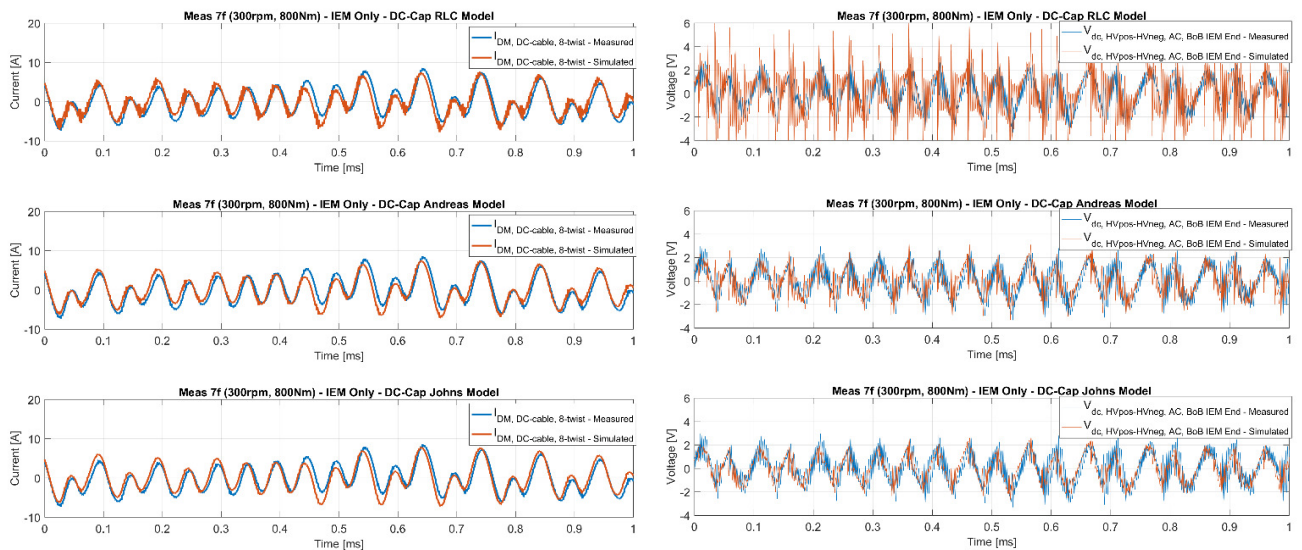

Figure 10.27 - Simulated DC-side DM current and voltage with different IEM input filters.
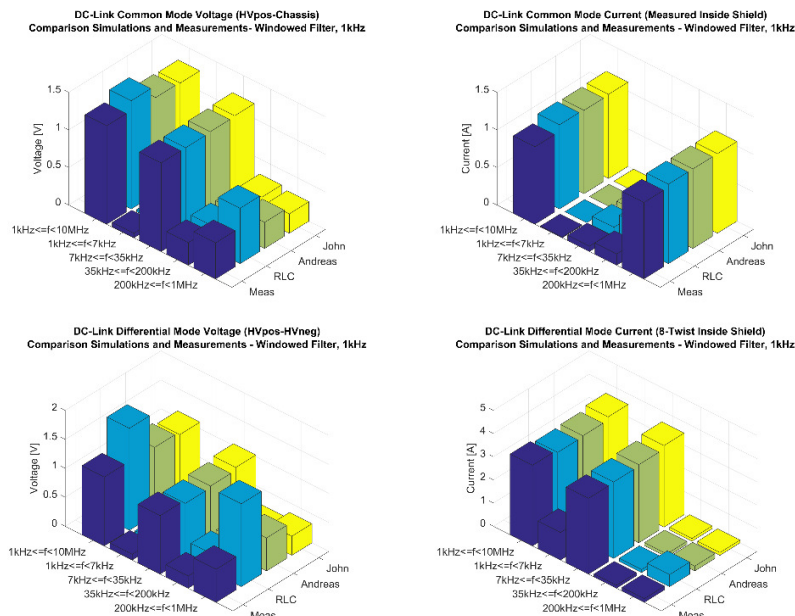

Figure 10.28 - Simulated DC-side RMS values with different IEM input filters..

10.13 Busbar and CM-Choke

If the impedance of the input filter is to be simulated, one option would be to implement it in a 3D analysis software. Ansys Q3D is a method of moments solver designed to produce electric equivalent circuits of metallic structures such as busbars or via connectors. However, this is not possible in this case since there is a ferrite mounted directly on the busbar; Ansys Q3D cannot handle permeable materials which gives faulty results, see Figure 10.29.

If the IEM input filter is implemented as proposed in Section 10.10, the simulated results will correspond well to the measurements. In order to verify the performance of the common mode choke and the smaller x-cap, the DC-link current and voltage was measured directly on busbar connection to the main x-cap. A comparison of simulations and measurements can be seen in Figure 10.30 which once again show good agreement.
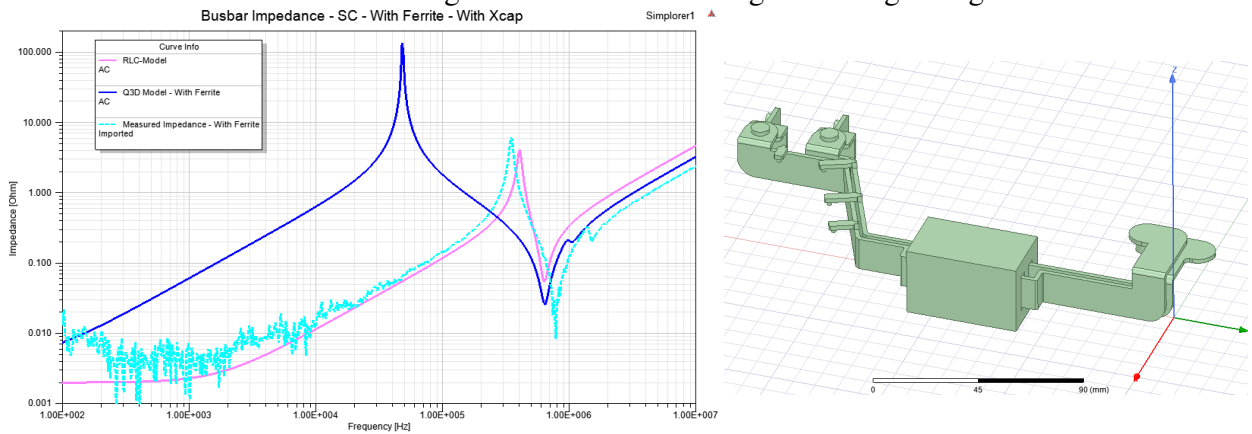

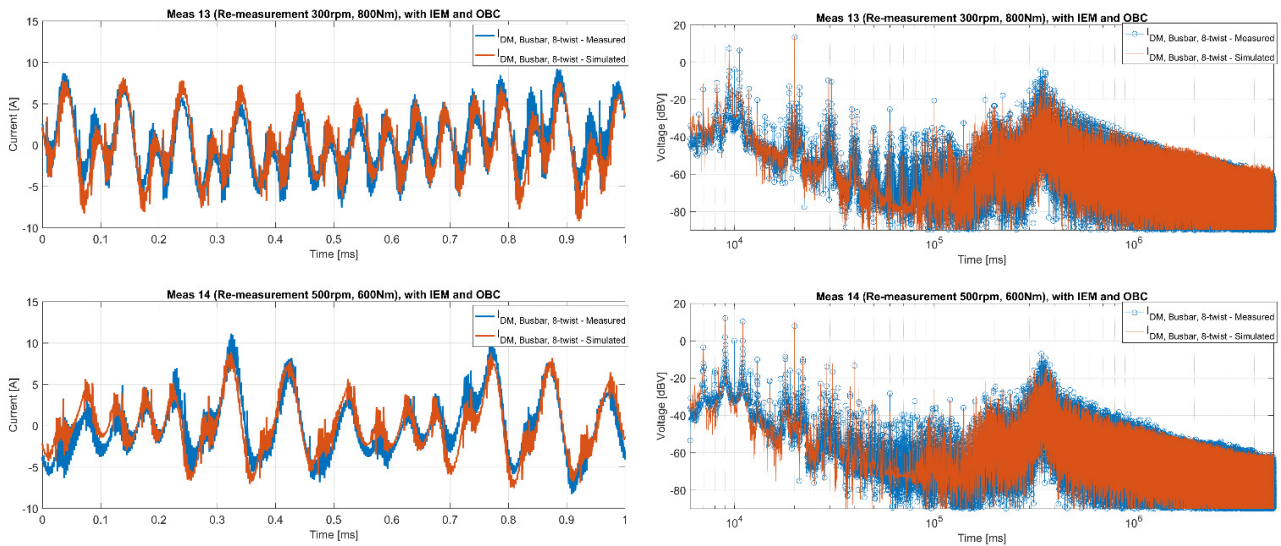Figure 10.29 – Implementation of the IEM busbar in Ansys Q3D

Figure 10.30 – Implementation of the IEM busbar in Ansys Q3D

11 System level verification

In this chapter, the full system model is described. Models for all the component models discussed in previous chapters have been assembled and connected. To verify the full model, simulations results have been compared to experimental measurements performed at different combinations of speed and torque.

11.1 System model

The overall system model implementation in ANSYS Simplorer is shown in Figure 11.1. Although alternative models have been developed for some individual components such as battery and cables, the overall structure is in all cases as displayed here, except for some variation due to whether shielding is explicitly represented. Each component in turn consists of some subsystem which can be of different types. For instance the cable models consist of RLC networks while the electric machine model is implemented as equations expressed in VHDL-AMS. All components are developed in pure Simplorer except the controller for which a Simulink model was created and linked to Simplorer.
Component models were stored in a Simplorer library, making it possible to select models of various fidelity in a reasonably simple manner.
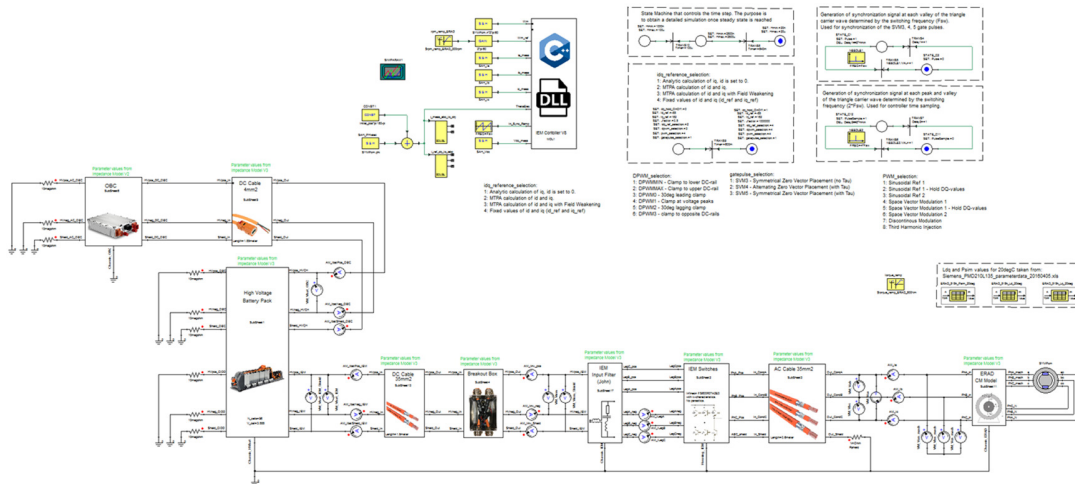

Figure 11.1 - Complete system model in Simplorer.

11.2 Measurement system

An experimental rig was set up at Chalmers University. A schematic layout is shown in Figure 11.2 and the physical system in Fig.11.3. It features the battery, inverter, motor, and

cables used in a real car. The drive shaft is connected to a DC machine by which a given torque load can be applied, representing the impact of factors such as inertia of the car, wheel and air friction, braking, etc. A target motor speed can be specified, making it possible to emulate arbitrary driving conditions.
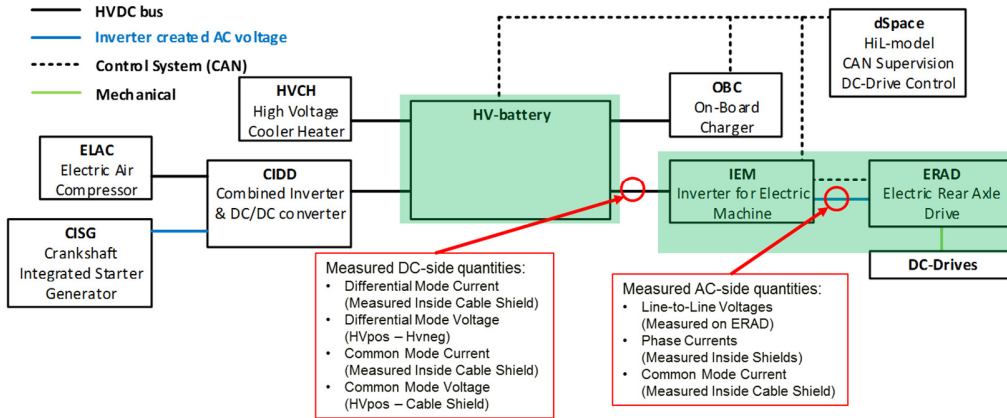

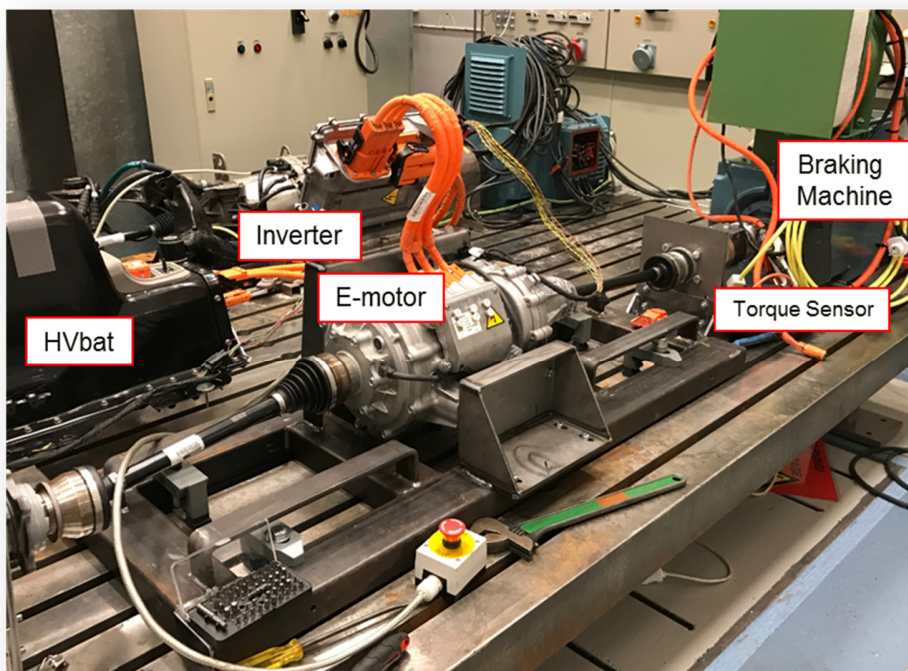Figure 11.2 - Schematic of experimental rig.

Figure 11.3 - Experimental rig.

A number of probes and sensors monitor currents and voltages at different locations. Results in cables depend on whether measurements are performed inside the shield, in which case only signals for the inner conductor are picked up, or outside the shield, in which case net results for inner conductor and shield are detected. Breakout boxes are used to access voltages and currents for inner conductors are shown in Figure 11.4.
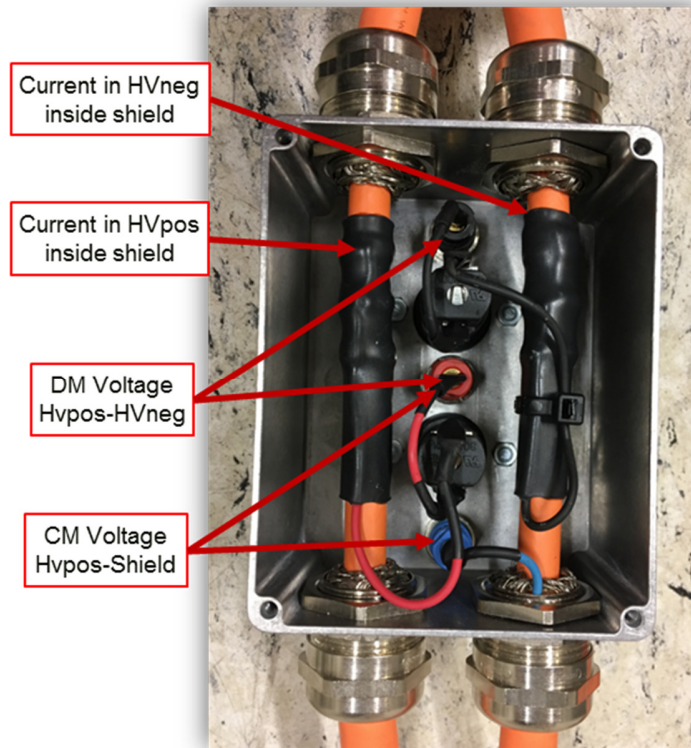

Figure 11.4 - Breakout box (with lid removed) for accessing currents and voltages inside cable shielding.

Common mode and differential mode currents on the DC link are of great interest. While they could be found from measurements of the respective currents on the positive and negative connection individually which are then appropriately summed or subtracted, such a method is prone to error since it becomes important that the measured signals are exactly synced. Therefore probes were positioned so that CM and DM currents were instead directly measured, see Figure 11.5.
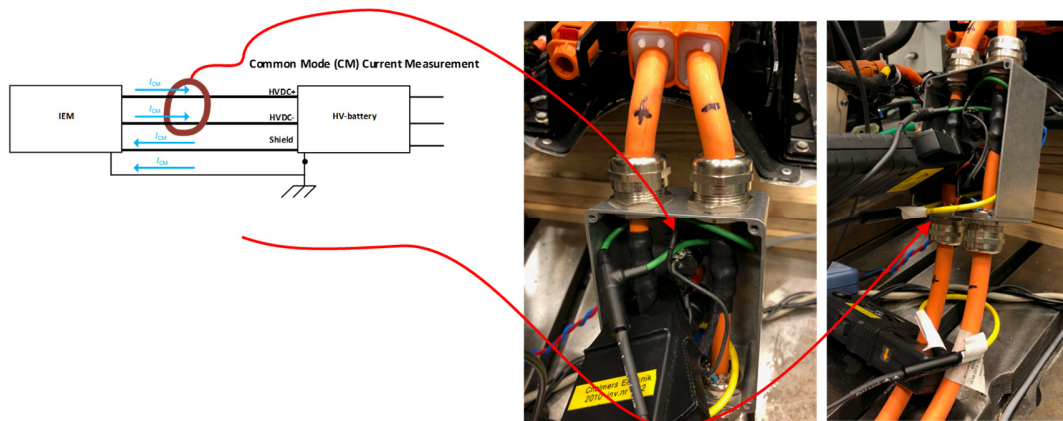
Figure 11.5 - Measurement of CM current using a common probe for positive and negative directions.

Certain measurement artifacts will appear. In particular, Rogowski coils pick up low frequency signals from the environment, often 50Hz, which are unrelated to the electric drive. They are eliminated here using software high pass filters.

11.3 Verification of time domain model

The system model has been verified by comparing simulations to measurements done in the experimental rig. The procedure follows these steps:
- Run system in rig with certain speed and load torque until steady state has been achieved. Store measurements of various currents and voltages. Do this for a few load cases, i.e. speed and torque combinations.
- Set up simulation model such that the speed and torque reference values match those of experiments. Run the simulation for a time long enough that a steady state is achieved. Extract currents and voltages in positions matching those of measurement probes.
- Compare measurements and simulations according to various criteria such as visual display of time domain and frequency domain signals and rms values within selected frequency bands.

11.3.1 Standstill

In the first loadcase studied, the machine was standing still without any load. In such a case, no useful differential mode current is produced, however higher harmonics due to inverter switching are still present. Agreement is generally good except that the DC link DM current is overestimated at intermediate frequencies.
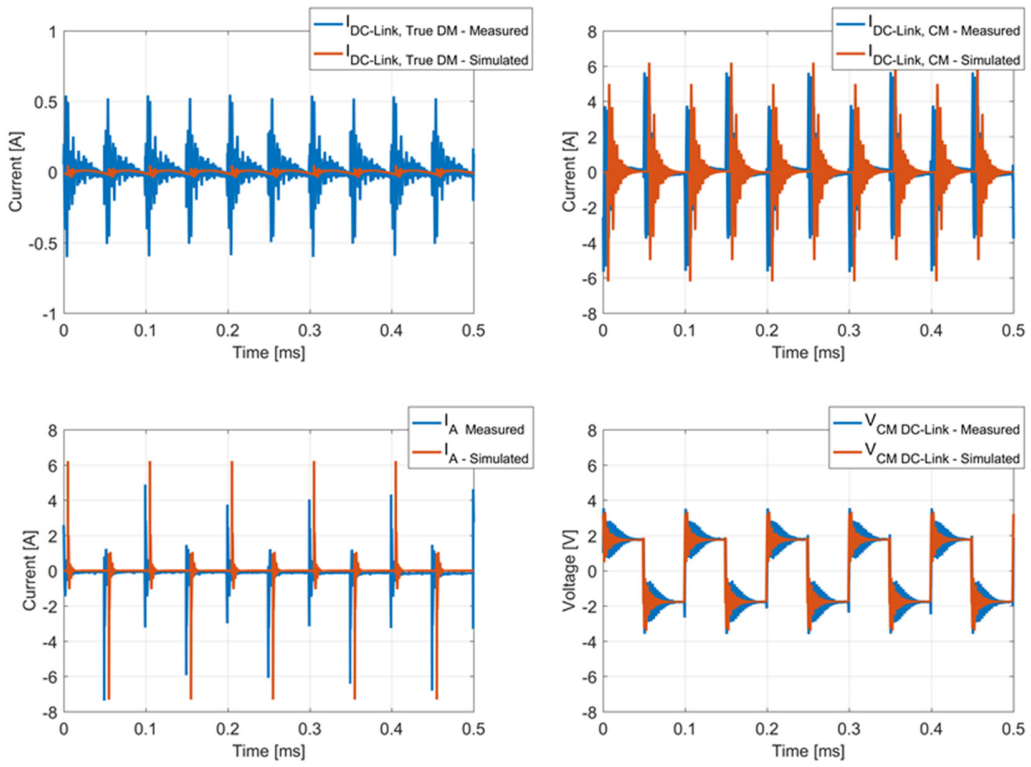
Figure 11.6 - Comparison between DC link measurements and simulations at standstill in time domain.
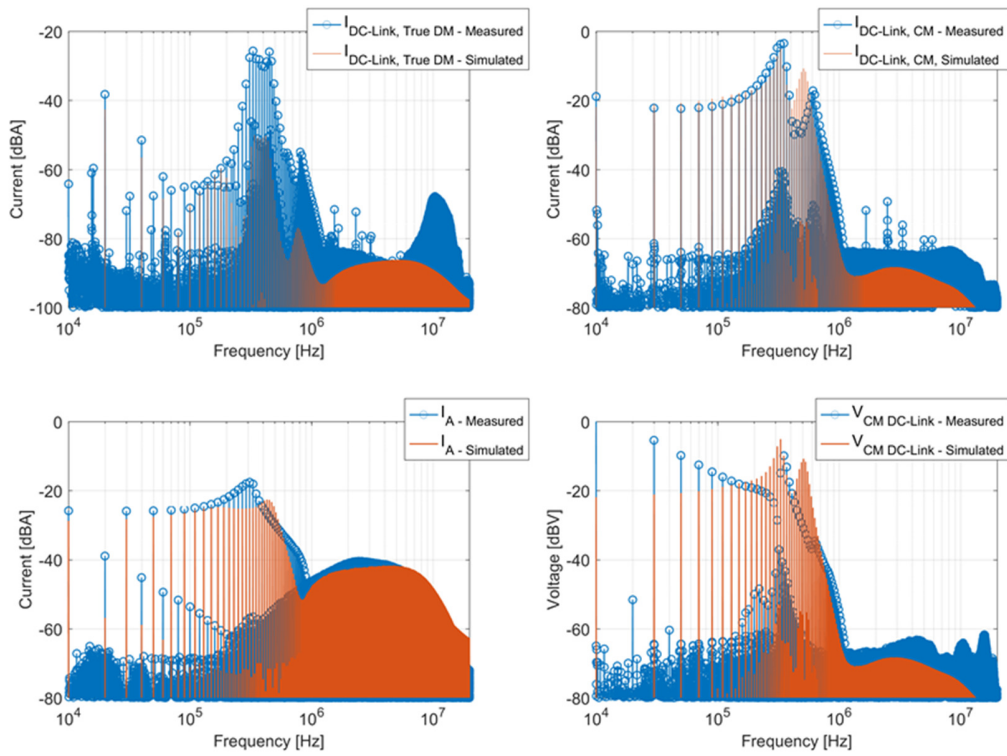
Figure 11.7 - Comparison between DC link measurements and simulations at standstill in frequency domain.
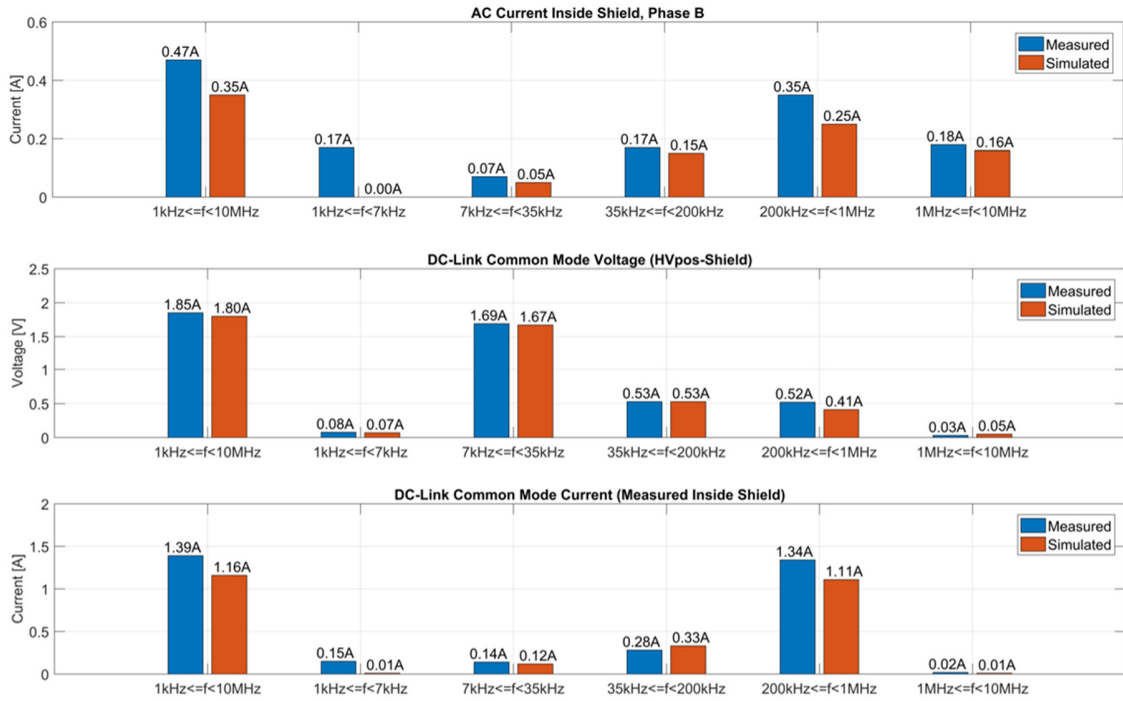

Figure 11.8 - Comparison between DC link measurements and simulations at standstill using rms values within frequency bands.
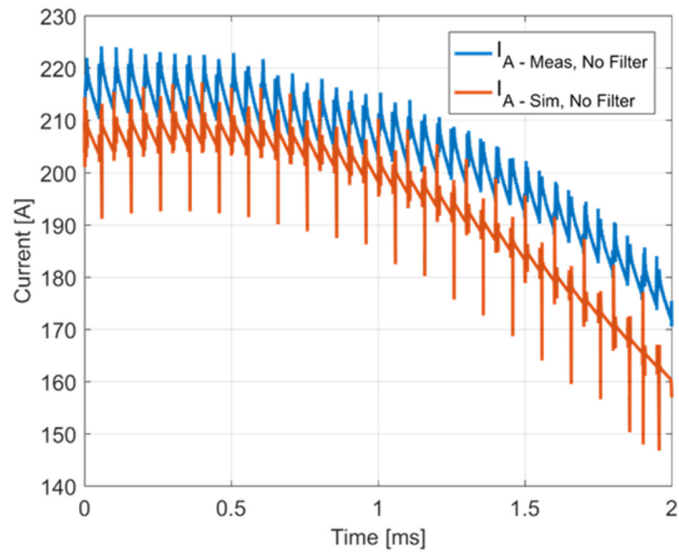
Figure 11.9 - Comparison of measured and simulated AC current at standstill in the time domain.
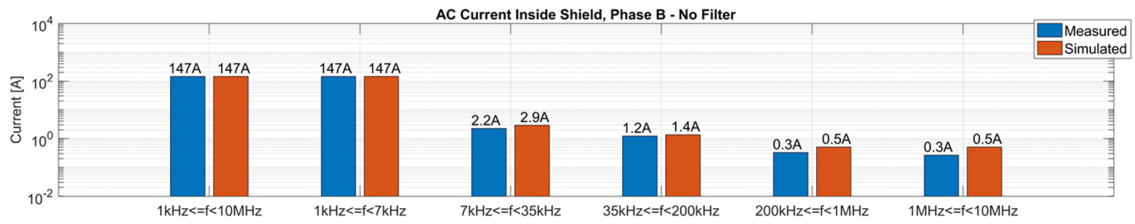
Figure 11.10 - Comparison of measured and simulated AC current at standstill using rms values within frequency bands.

11.3.2 Under load

Comparisons were also done for the load case speed = 100 rpm, torque = 800 Nm. The agreement is found to be very good across the frequency range and for all signals.

Figure 11.11 - DC link DM and CM results in time domain.
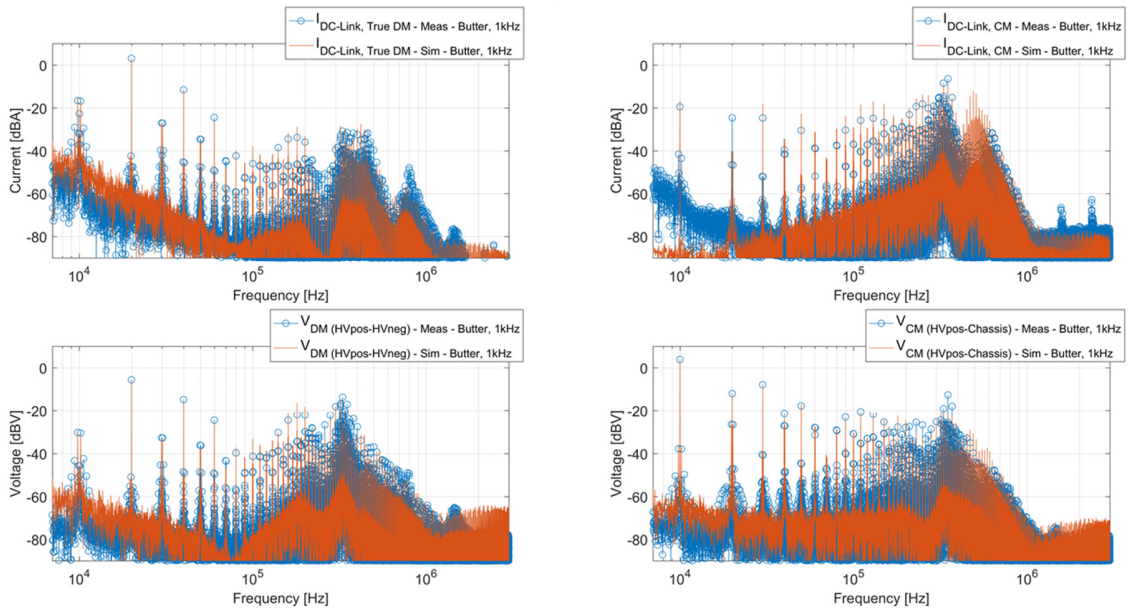
Figure 11.12 - DC link DM and CM results in frequency domain.

Figure 11.13 - DC link results using rms values in frequency bands.

11.3.3 Different system configurations

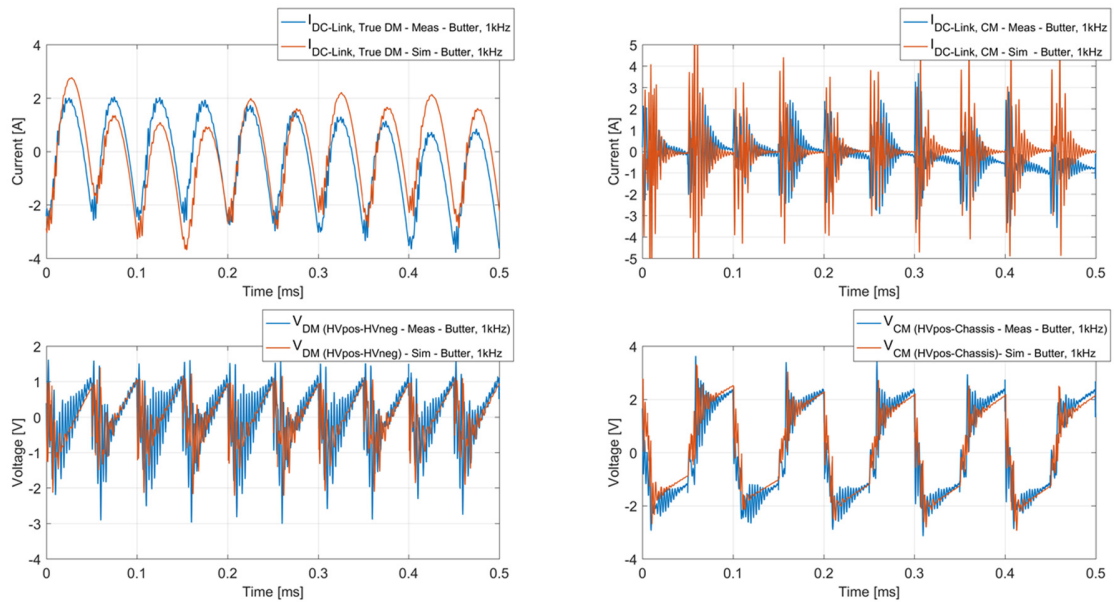The system also contains an OBC and a CIDD that can be connected or disconnected. Tests were done to investigate to what extent their presence affects the results. Results are presented for common mode signals in Figure 11.14 and differential mode signals in Figure 11.15. The impact of the OBC on the ripple is generally small for all signals. The CIDD on the other hand significantly decreases the CM voltage and increases the CM current at high frequencies. These effects are very well captured by the simulations.
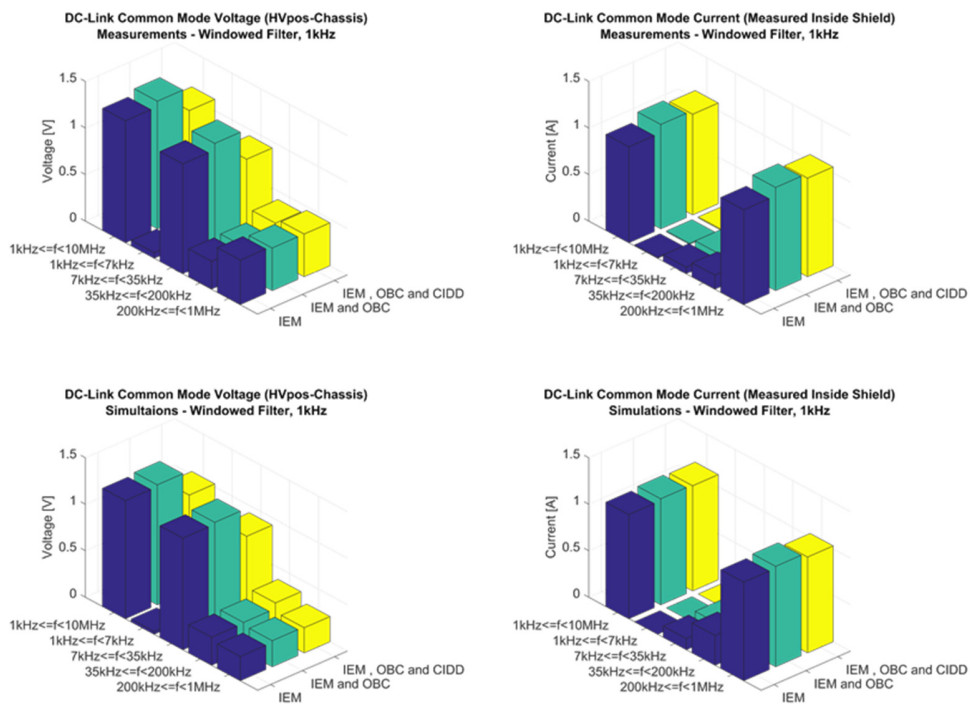
Figure 11.14 - DC link CM currents and voltages with OBC and CIDD connected, OBC connected, and both disconnected.
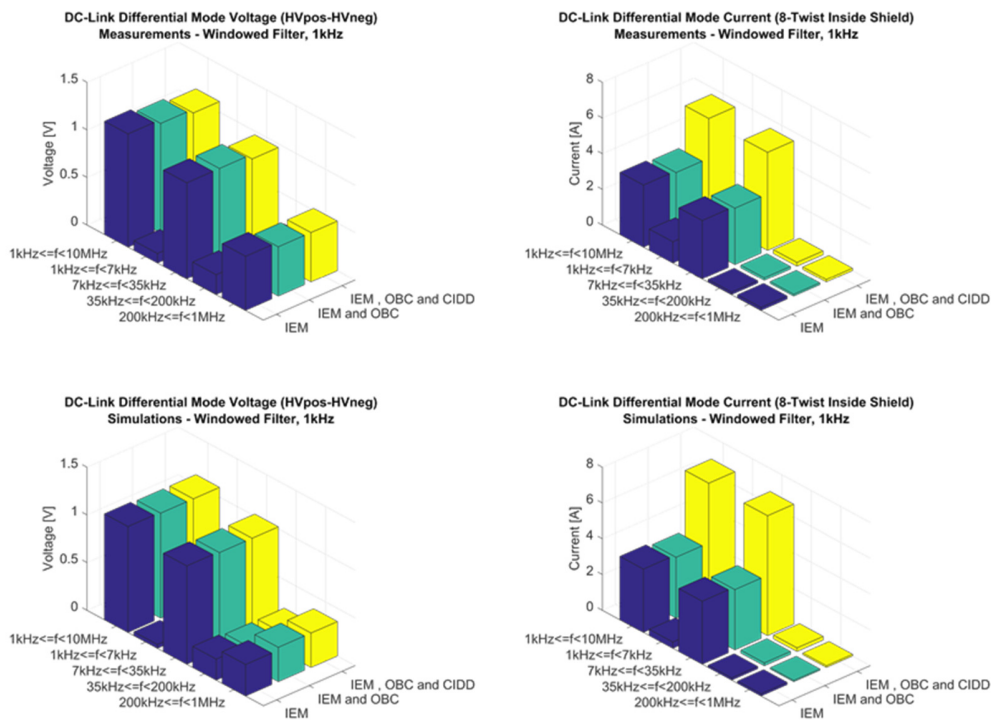
Figure 11.15 - DC link DM currents and voltages with OBC and CIDD connected, OBC connected, and both disconnected.

11.3.4 Different DC cable lengths

Comparisons between simulations and measurements were also made for different lengths of the DC cable. Four different lengths were used: 1.6m, 3.6m, 5.6m, and 8.6m. The most notable effect in measurements is that DM voltage and current decrease at intermediate frequencies as the cable length increases. As shown in Figure 11.16 and Figure 11.17, this effect is well predicted by the model for the current, less so for the voltage.
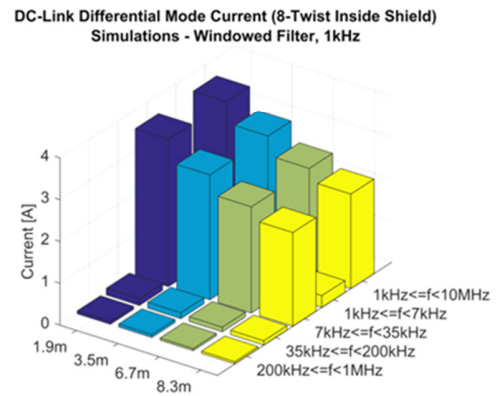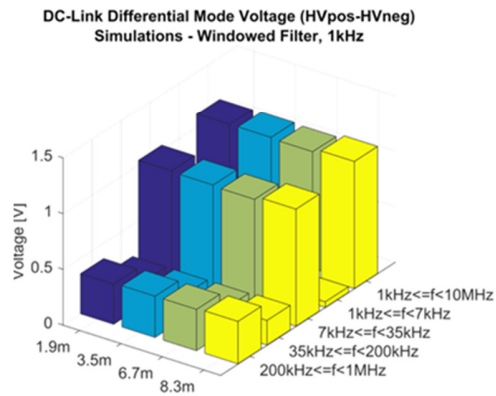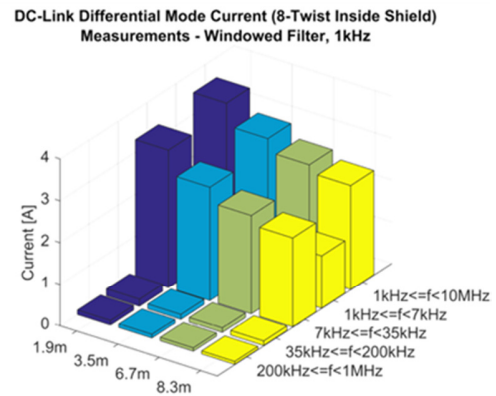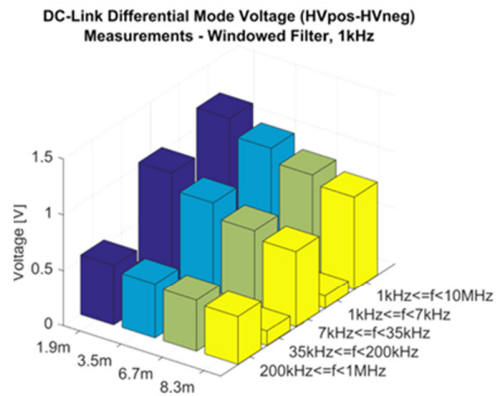
Figure 11.16 - DC link DM currents and voltages for different cable lengths.
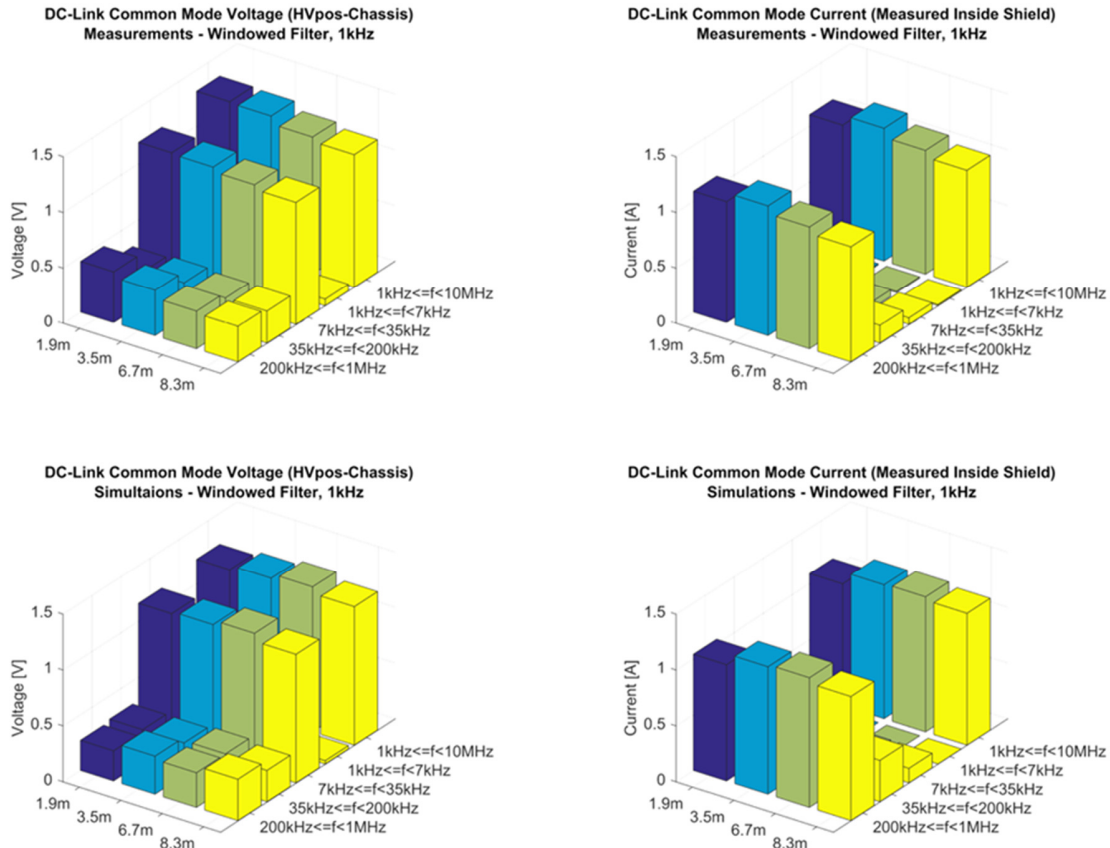
Figure 11.17 - DC link CM currents and voltages for different cable lengths.

11.4 Comparison with measurements in car

Comparisons have also been made with measurements of voltage and current ripple on the DC side in an actual XC90 car. Experiments are obviously more challenging to make in a running vehicle due to the difficulty of placing sensors and exactly controlling the torque and speed. Also, measurements need to be done with an MSD outlet which can affect the result. Figure 11.18 - Figure 11.19 show that results in the car were very similar to results in the rig. Figure 11.20 shows a comparison between car measurements and simulations with very good agreement at the speed 295 rpm and torque 410 Nm. This indicates that while the model verifications have mainly been done with use of the rig, the results are also valid for a real vehicle.
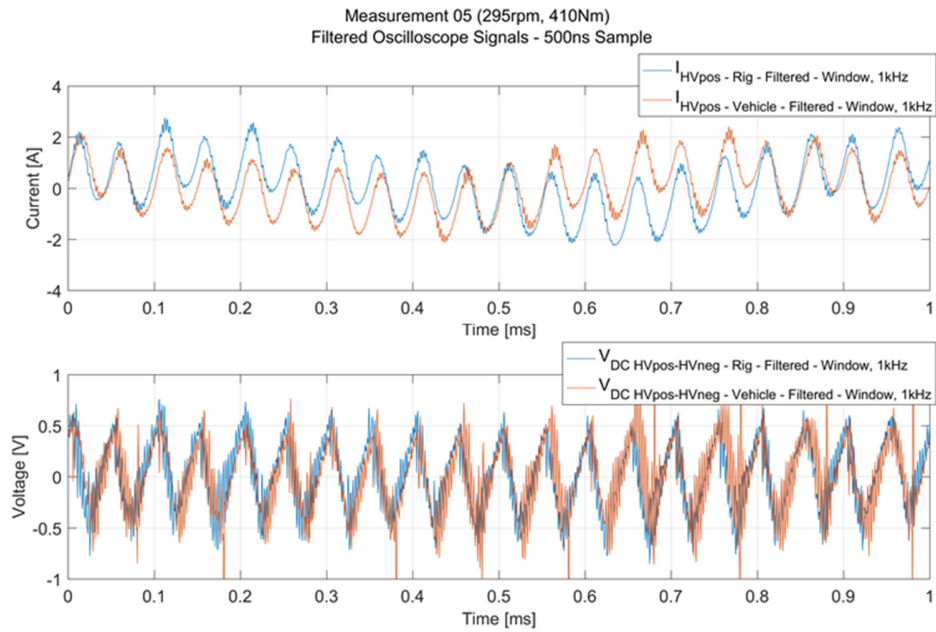
Figure 11.18 - Comparison between measurements in car and in rig in time domain.
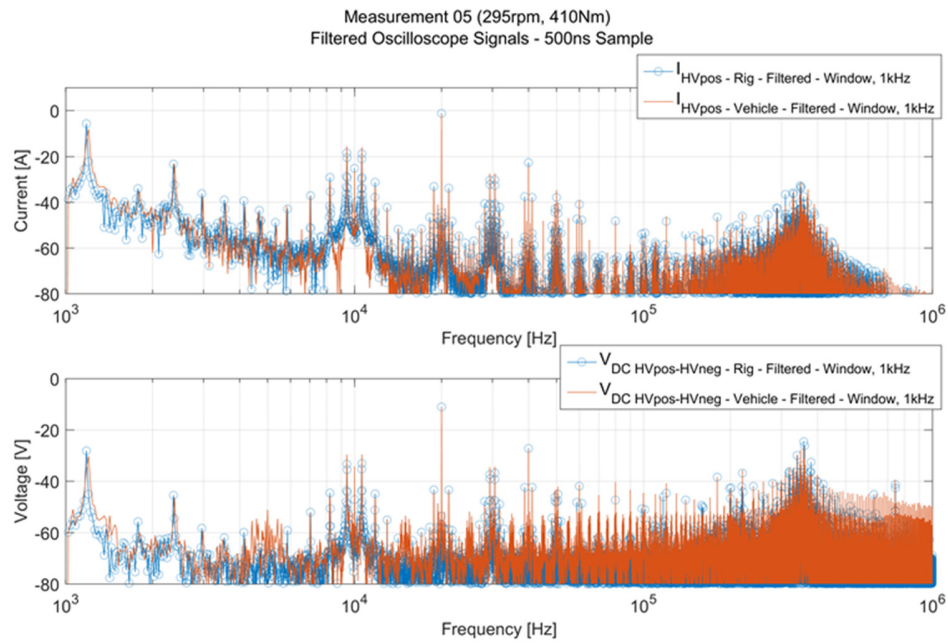
Figure 11.19 - Comparison between measurements in car and in rig in frequency domain.
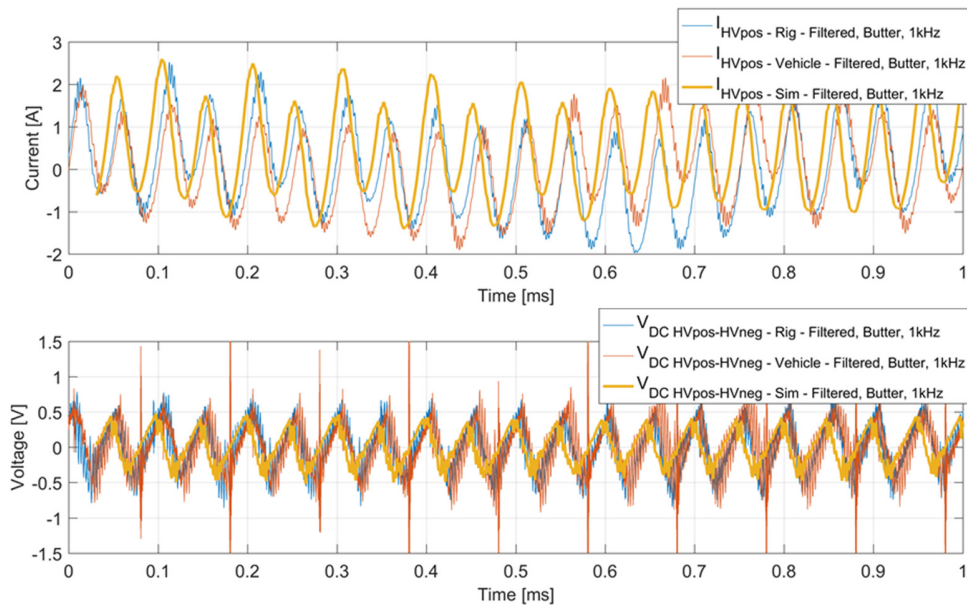
Figure 11.20 - Comparisons between simulations and measurements in real car.

11.5 Sensitivity analysis

Apart from predicting currents and voltages in the system, the model can be used to investigate which components and parameters that affect various results the most. Some parameters, for instance related to filters, can to a certain extent be chosen and the model provides a way to select appropriate parameter values when dimensioning the system for optimal performance. Other parameters, such as cable length can be difficult to change but are well known. Finally some parameters, such as stator capacitance, may be difficult to know and next to impossible to control but might still have a significant effect on the results. In such a case it is of interest to see if it is important to spend the effort to find these parameters or if they can be neglected. Finally, it might be of interest to have a simplified version of the model that will still give results that are good enough. This requires determining what simplifications will not impact the results too much.

These issues can be investigated by performing simulations where certain parameters are varied and their impact on various outputs is studied. Some examples of parameters that have been varied are:
- Y and X capacitance in inverter input filter
- Main battery inductance
- DC cable length
- Presence of AC common mode choke inductance
- Electric motor core loss and winding capacitance

Their impact on the following signals has been investigated:
- Common mode and differential mode current on DC side
- Common mode and differential mode current on AC side

The following sections show some results from these investigations.

11.5.1 Y capacitance

The IEM filter Y capacitance is intended to reduce common mode ripple on the DC side. This is also observed in simulations when its value is varied from 50 nF to 5000 nF. Figure 11.21 shows results in the time domain and the reduction in current spikes when capacitance is increased is obvious. Figure 11.22 shows RMS values within certain frequency bands for common mode and differential mode currents on both the DC side and the AC side. are shown in Figure 11.22. It is seen that the other signals are far less affected.
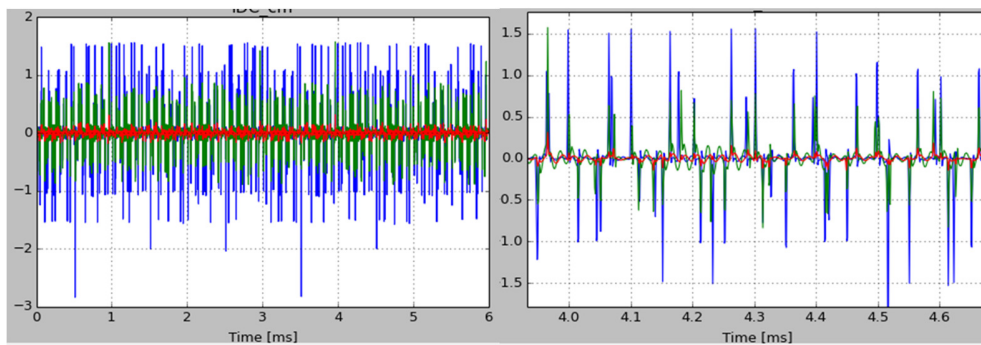
Figure 11.21 - Time domain results for common mode current on DC side for capacitance 50nF (blue curve), 500nF (green) and 5000 nF (red). The right figure enlarges the time scale.
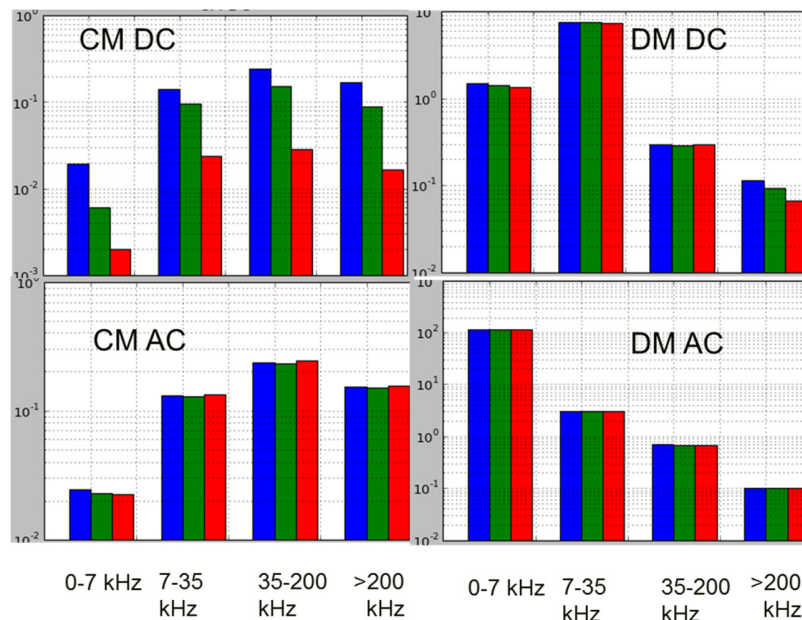
Figure 11.22 - RMS values of different current signals in frequency bands for different Y capacitance values. Blue=50 nF, green=500nF, red=5000nF.

11.5.2 X capacitance

The X capacitance in the IEM filter is on the other hand intended to reduce the differential mode ripple on the DC side. This is clearly seen in Figure 11.23 with the capacitance varied from 48 nF to 4800 nF. The effect on other signals is much smaller.
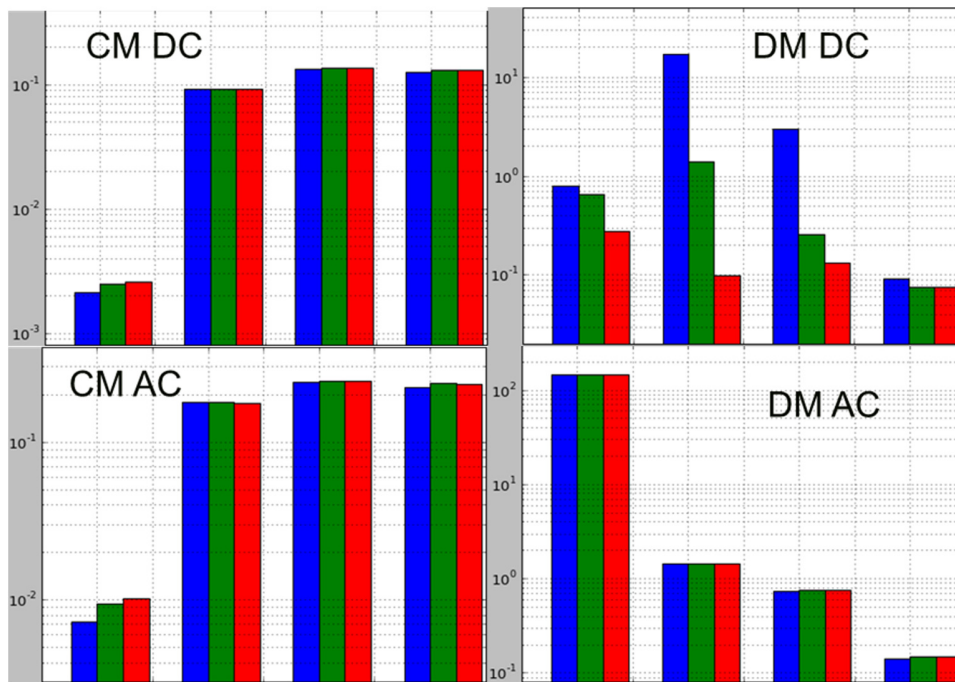
Figure 11.23 - RMS values of different current signals in frequency bands for different X capacitance values. Blue=48 nF, green=480nF, red=4800nF.

11.5.3 Battery inductance

While the battery model incorporates many impedance elements, there is one main inductance that depends on how cells and modules are arranged and, importantly, the routing of busbars and cables connecting modules. This routing may be subject to late design changes. Finding it through simulations is possible through finite element simulations but requires a considerable effort due to the complexity of the CAD models involved. Figure 11.24 shows the RMS currents for inductances in the range 0.15 µH to 15 µH. The impact on the differential mode current on the DC side is quite significant, meaning that the battery inductance must be known reasonably well to get accurate system results.
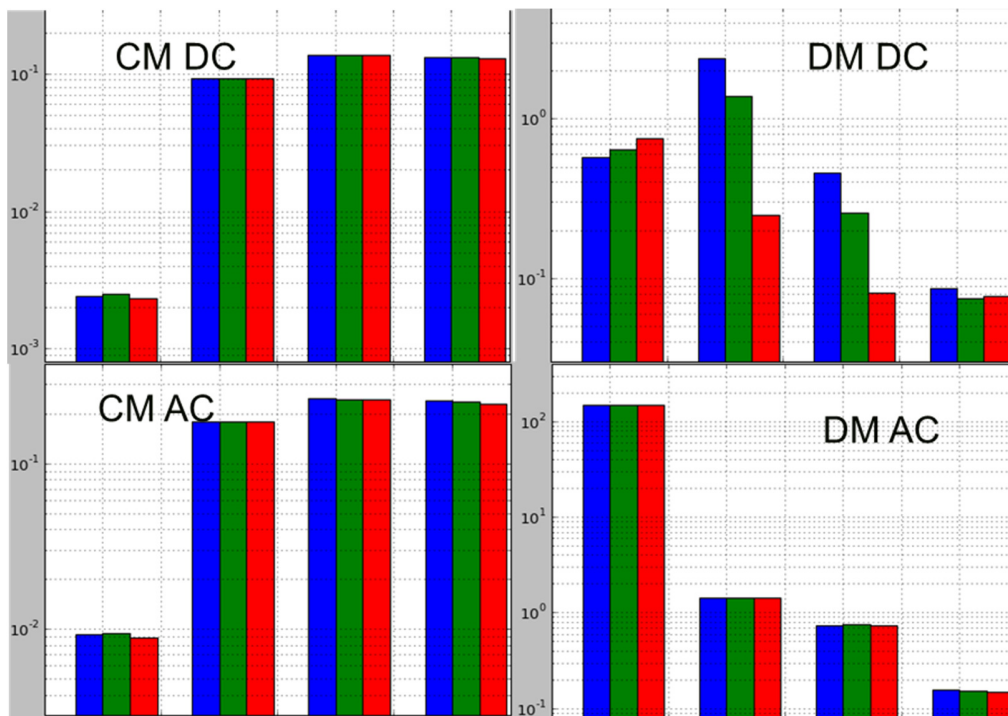
Figure 11.24 - RMS values of different current signals in frequency bands for different battery inductance values. Blue=0.15 µH, green=1.5 µH, red=15 µH.

11.5.4 Stator winding capacitance

The parasitic winding capacitance on the other hand does not affect the main functionality of a motor. Furthermore, it is very hard to accurately find through simulations since it depends on the specific details of how the windings are bundled, information that is typically hard to get. Figure 11.25 shows that increasing it has a very significant effect on common mode current on both AC and DC sides. This is expected since this is the main path for the common mode current ripple to ground. Thus it is important to have a fairly accurate value for this capacitance, which can be a challenge if no physical prototype of a motor yet exists.
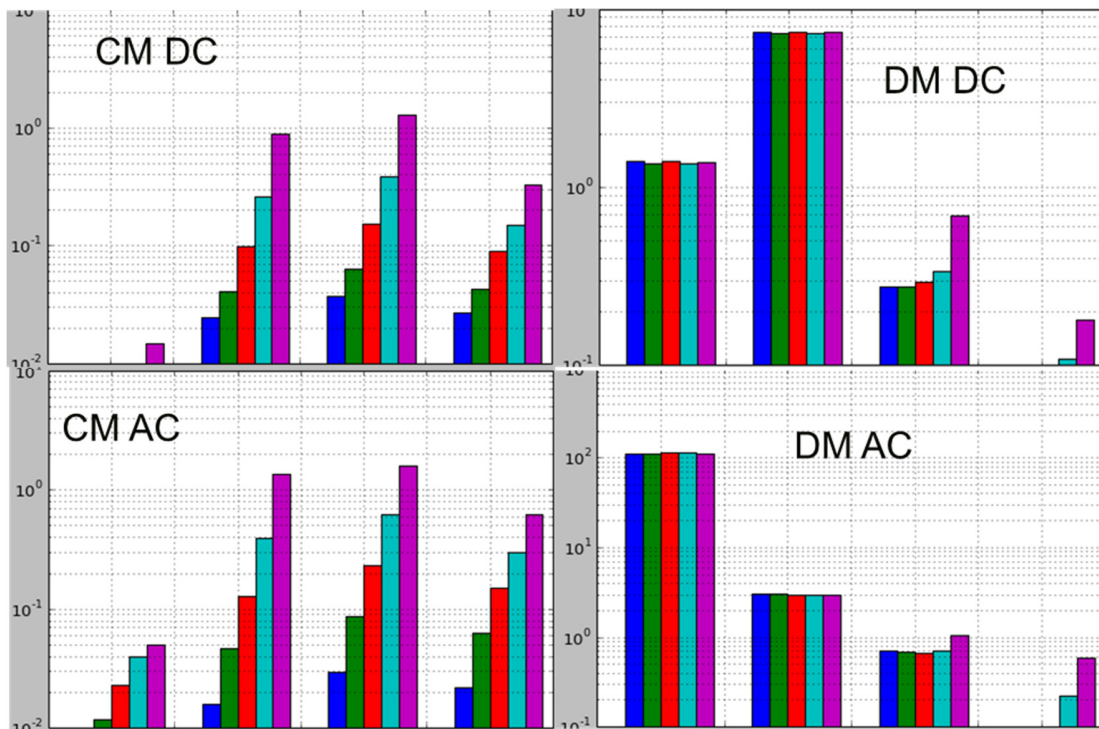
Figure 11.25 - Result for stator winding capacitance values 1.35nF, 4.05 nF, 13.5 nF, 40.5 nF and 135 nF.

11.5.5 Summary

The main observations are summed in Table 11.1. In addition to the parameters described above, variation of core loss resistance and common mode choke on the AC side are listed.

Component	DC DM	DC CM	AC DM	AC CM
DC link Y caps	HF	*LF,MF,HF*	-	*LF,MF,HF*
DC link X cap	LF, *MF*, HF	LF	-	-
Battery inductance	LF, *MF*, HF	LF	-	-
Winding capacitance	-	*LF,MF,HF*	HF	*LF,MF,HF*
Core loss	-	-	-	-
AC side CM choke	-	LF,MF,HF	-	LF,MF,HF

Table 11.1 - Overview of impact of different components on common and different mode currents on DC and AC sides, for low (LF), medium (MF) and high (HF) frequencies.

11.6 Alternative frequency domain approach

An alternative approach to using time domain simulations in ANSYS Simplorer has been developed in LTspice/Python.

- LTspice is a free spice simulator from Linear Technology
- Python is also freeware. It is used here for doing data handling, generating a current into the DC-link capacitor in the inverter, FFT, plotting, e.g. similar to what can be done in MATLAB.

Here it is investigated how good this approach is by combining LTspice results with Python data handling to give "simulated" results. These "simulated" results are then compared with the measurement results in the RIFEL rig for a few different electric machine operating points and three different system configurations.

It will be shown that this approach works rather well, although better for differential mode than for common mode. This allows very quick sensitivity analyses, i.e. if and how much some current or voltage will increase or decrease in the frequency domain due to a parameter change, in LTspice.

Both differential mode (DM) and common mode (CM) performance has been investigated, one mode at a time.

The top level of the simulation model in LTspice is shown in Figure 11.26. The different system configurations used have been

- Always connected
    - X2: ERAD (Electric Machine)
    - X6: Cables between ERAD and IEM
    - X13: IEM (Inverter for ERAD)
- Connected in all tests except one
    - X9: The effect of 2xBoB:s (Break-out-Boxes) on the IEM to HV-battery cables
    - X3: A cable between the IEM and the HV-battery without BoB:s
    - X1: HV-battery
- Connected in a few cases, always together with X1, X3 and X9
    - X5: Cables between the HV-battery and the CIDD (Combined Inverter and DC/DC converter)
    - X4: CIDD
    - X14: Cable to the OBC (On-Board Charger)
    - X8: OBC

In Figure 11.26 the current source, Idm, is connected when investigating differential mode behaviour in the system. If common mode behaviour is investigated the current source,

Idm, is short circuited between nodes CURSRC_P_IEM and CURSRC_N_IEM. Thereafter the loose end of the voltage source, Vcm, is connected to e.g. CURSRC_N_IEM.

It should be noted that all models, e.g. electric motor and inverter, only contain passive components such as resistors, capacitors, inductors and inductor couplings. The inverter model has however been developed so that six switches (e.g. IGBTs or ideal switches) can be connected, on the top level drawing seen in Figure 11.26, to the 5 nodes CURSRC_P_IEM, CURSRC_N_IEM, VOLSRC_PH1_IEM, VOLSRC_PH2_IEM and VOLSRC_PH3_IEM if a time domain analyses is to be performed. Here an alternative approach is however utilized where we only work in the frequency domain in LTspice so no switches are needed.
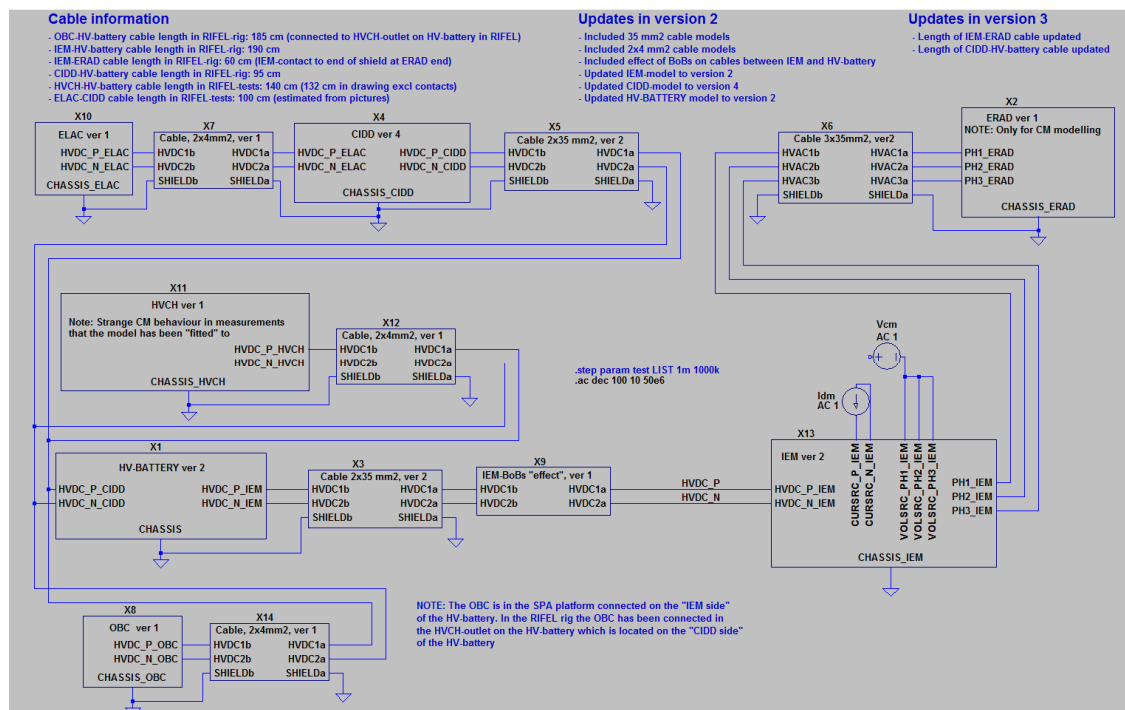
Figure 11.26 - The top level drawing of the complete SPA platform model developed. Only parts of it has been used in the verification of this alternative approach

11.6.1 Differential Mode (DM)

In this mode, the following is done:

1. The transfer functions from injected current in the IEM DC-link capacitor, Idm, to differential mode voltage and "true" differential current is obtained in LTspice

2. The ideal current generated to the IEM DC-link capacitor by the switching of the IGBTs for different machine operating points assuming SVPWM (Space Vector PWM) modulation is calculated

3. The simulated result(s) are obtained by multiplying the transfer function(s) with an FFT of the ideal current and compared with the measurement results.

Measurements have been compared with simulations in two configurations. In one of the configurations tests were performed in three different EM operating points.

- Only HV-battery connected to IEM on the HVDC bus
    - Measurement 04: 100 rpm, 800 Nm, 374 V, 11 kW
    - Measurement 07: 300 rpm, 800 Nm, 352 V, 28 kW
    - Measurement 10: 500 rpm, 600 Nm, 330 V, 35 kW

- HV-battery, CIDD and OBC connected to the HVDC bus
    - Measurement 15: 100 rpm, 800 Nm, 346 V, 11 kW

Note: The ERAD (electric machine) temperature during the tests was 28-37 °C

11.6.1.1 The transfer functions

The transfer functions were obtained in LTspice from an applied current source, Idm, connected as in the circuit diagram in Figure 11.27 to

- DC differential voltage, i.e. HVDC_P_IEM – HVDC_N_IEM

- DC "true" differential current, taken as half the sum of current out of HVDC_P_IEM andf current into HVDC_N_IEM. Note that we could equially well have used current into HVDC_P_IEM and current out of HVDC_N_IEM.
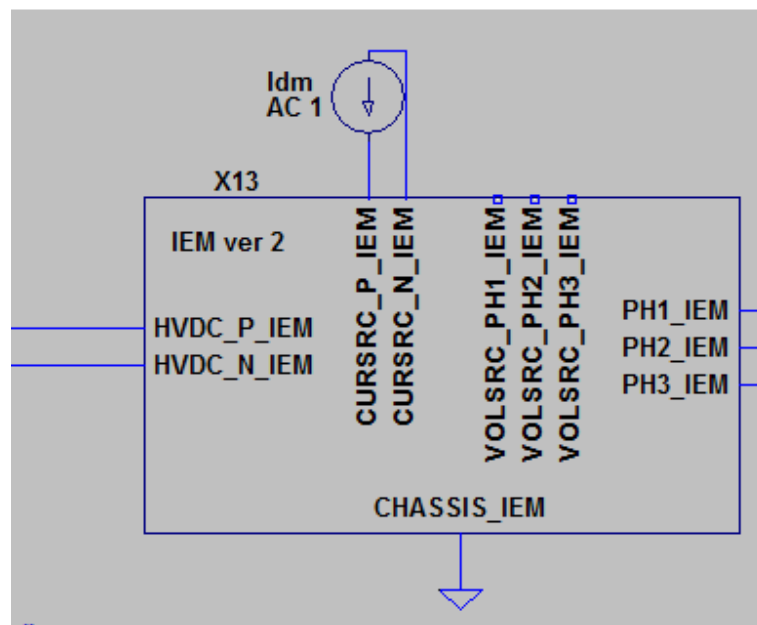
Figure 11.27 - The current source is applied between the nodes CURSRC_P_IEM and CURSRC_N_IEM which are connected directly over the DC-link capacitor where the IGBTs/switches can be connected in the LTspice model

The obtained transfer functions can be seen in Figure 11.28 below.

In the transfer function to differential voltage it can be seen that basically no voltage change is expected due to addition of typical loads on the HVDC bus above 10 kHz. Since the switching frequency is 10 kHz, the expectation is to **not** see any effect on the measured ripple voltage when adding the CIDD and OBC, i.e. no difference is expected between measurement 04 and 15.

Adding the CIDD and the OBC should however significantly increase the DM current in the frequency range ~4 kHz to 300 kHz when comparing measurements 04 and 15.
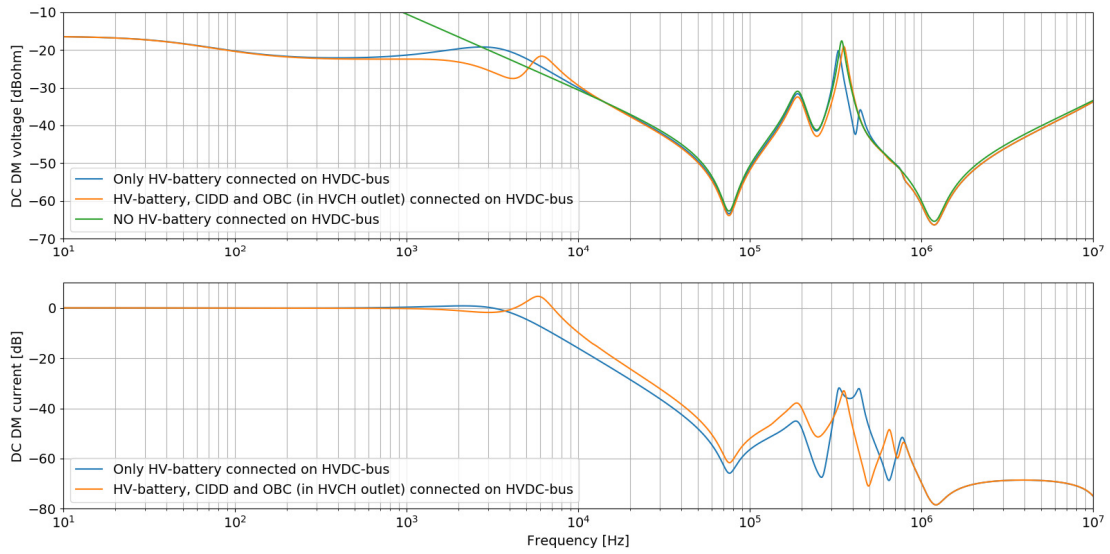
Figure 11.28 - The transfer functions from injected current, I_{dm}, in Figure 11.27 to differential voltage and current

11.6.1.2 The ideal current to the DC-link capacitor

The following steps should be performed here:

- First decide what electric machine operating point that is of interest, i.e. torque, rpm and machine temperature

- The above is used as input together with the HVDC voltage to a function/script that implements a large lookup table originating from the electric machine manufacturer. The output from this script is the inverter operating point, i.e. phase current, phase voltage and power factor

- The inverter operating point (incl. HVDC voltage) is then used as input to a script that calculates the ideal currents generated by the IGBT switching into the inverter DC-link capacitor. It is here assumed Space Vector PWM is used to control the IGBT switches but the script also supports SPWM and third harmonic injection

The function/script has been used to generate the inverter working point for a machine (magnets and windings) temperature of 35 °C. This has then been compared with the measured inverter operating point, see Table 11-2 below. It seems that the measured currents are slightly lower those than obtained from the script, voltages are slightly higher and the power factor is higher.

Parameter	Measurement 04		Measurement 15		Measurement 07		Measurement 10	
	Script.	Meas.	Script.	Meas.	Script.	Meas.	Script.	Meas.
[1,3]RPM [1/min]	100		100		300		500	
[1,3]Torque [Nm]	800		800		800		600	
[1]Udc [V]	374		346		352		330	
[2]Iphase [A_{rms}]	147	143	147	144	147	138	116	111
[2,4]Vphase [V_{rms}]	25	27	25	27	72	76	106	114
[2,5]Power factor	0.825	0.966	0.825	0.940	0.810	0.899	0.867	0.913

Note 1: Input parameter
Note 2: Output parameter
Note 3: Parameters valid at the drive axle. The gear ratio ~10
Note 4: Measured is phase-phase voltage divided by sqrt(3)
Note 5: A bit challenging to measure the power factor very accurately

Table 111.2 - The inverter operating point for a few electric machine operating points. Comparison of predictions from the script with measurements results.
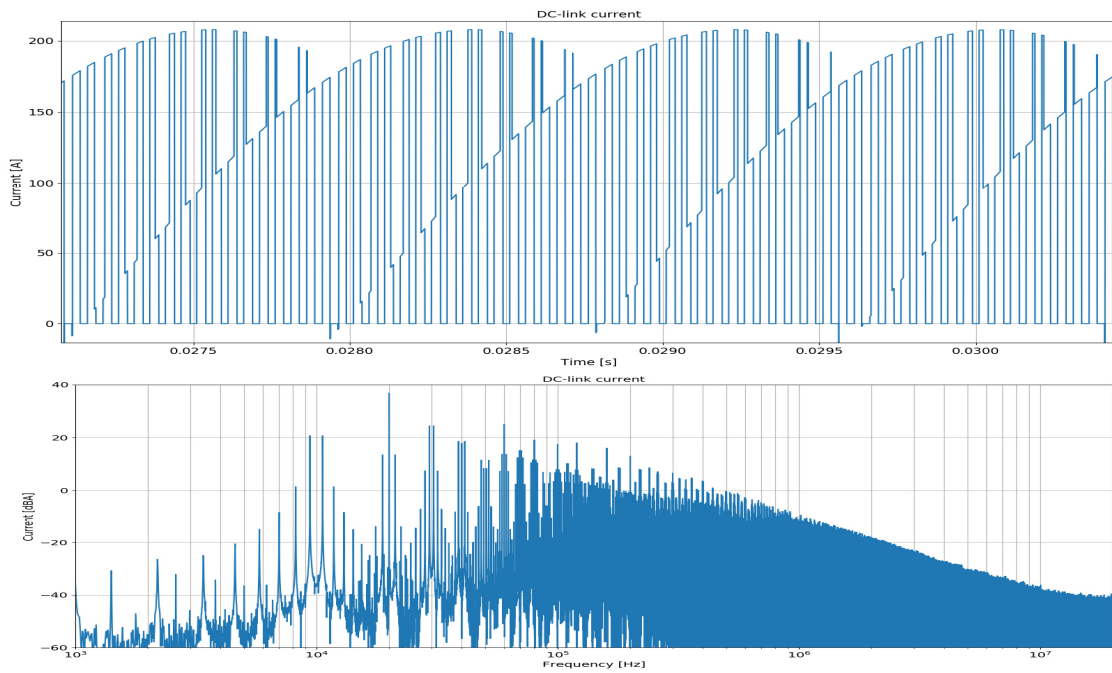
Figure 11.29 - The current injected into the DC-link capacitor, Idm, obtained from the script for measurement 07. Time domain (top) and frequency domain (bottom)

11.6.1.3 Compare the simulation results with the measurement results

A comparison of simulation and measurement results can be seen for measurement 07 in Figure 11.30– Figure 11.33.

The results show that the simulations match the measurement results rather well. The match was even better when the measured inverter operating point was used instead of the inverter operating point generated by the script, i.e. when generating the DC-link capacitor current. This means that there seems to be room for improvement in the script/lookup table from the electric machine manufacturer.

In Figure 11.34 the current and voltage RMS values, from simulations and measurements, are compared for all measurements. The match is generally quite good.
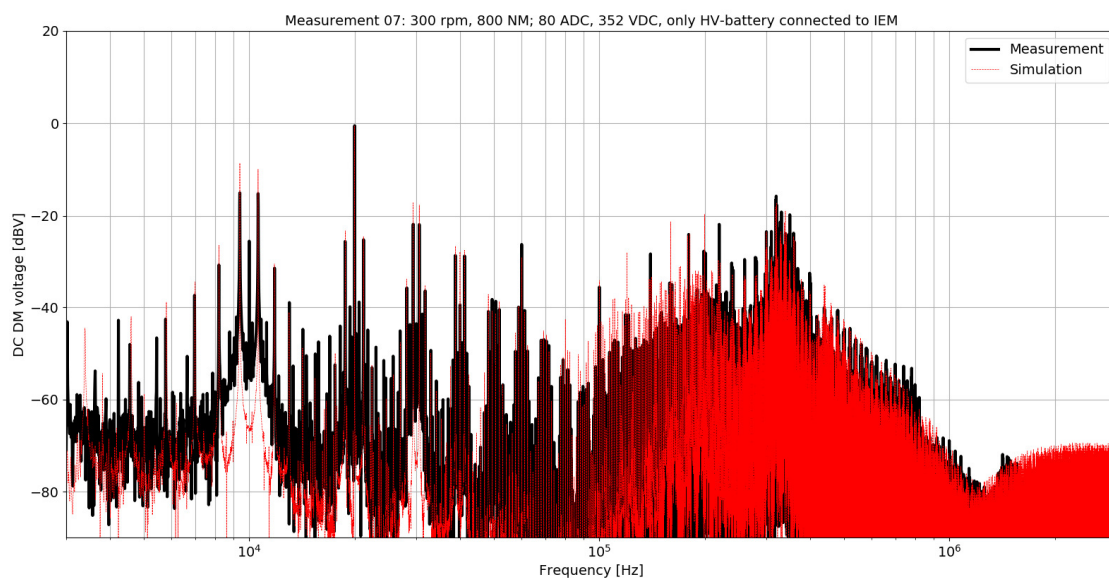
Figure 11.30 - Measurement vs simulation for measurement 07, differential voltage in the frequency domain
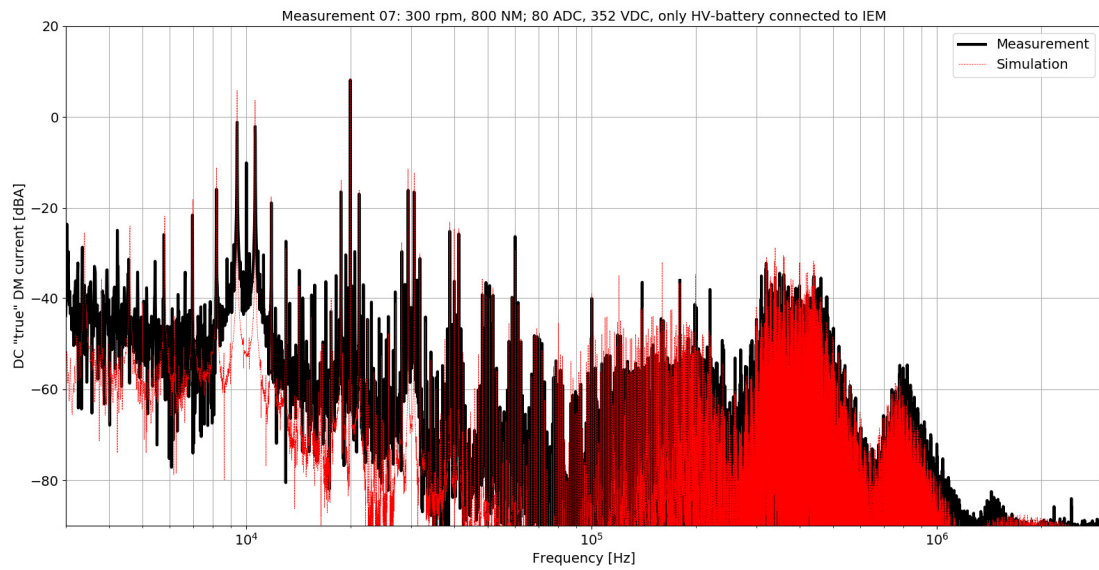
Figure 11.31 - Measurement vs simulation for measurement 07, "true" differential current in the frequency domain
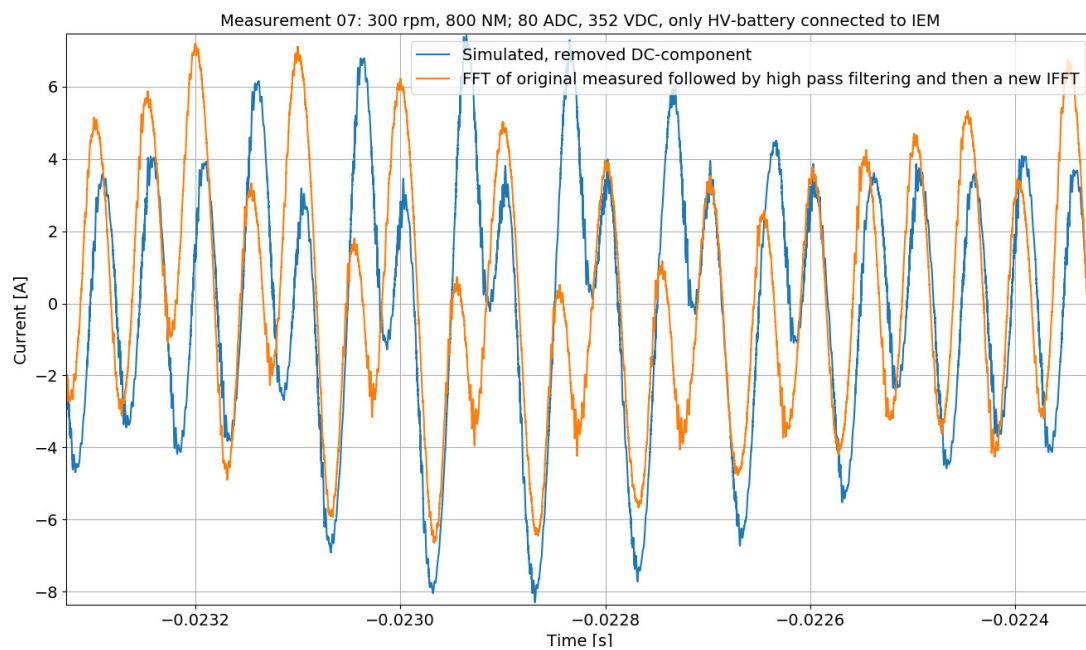
Figure 11.32 - Measurement vs simulation for measurement 07, "true" differential current in the time domain. An inverted FFT was performed on the simulation data. All content below 1 kHz was filtered out, mainly due to low frequency oscillations in measurement data that was obtained with a Rogowski current probe. Note that no "time synchronisation" has been performed between simulation and measurement data

Measurement 07: 300 rpm, 800 NM; 80 ADC, 352 VDC, only HV-battery connected to IEM
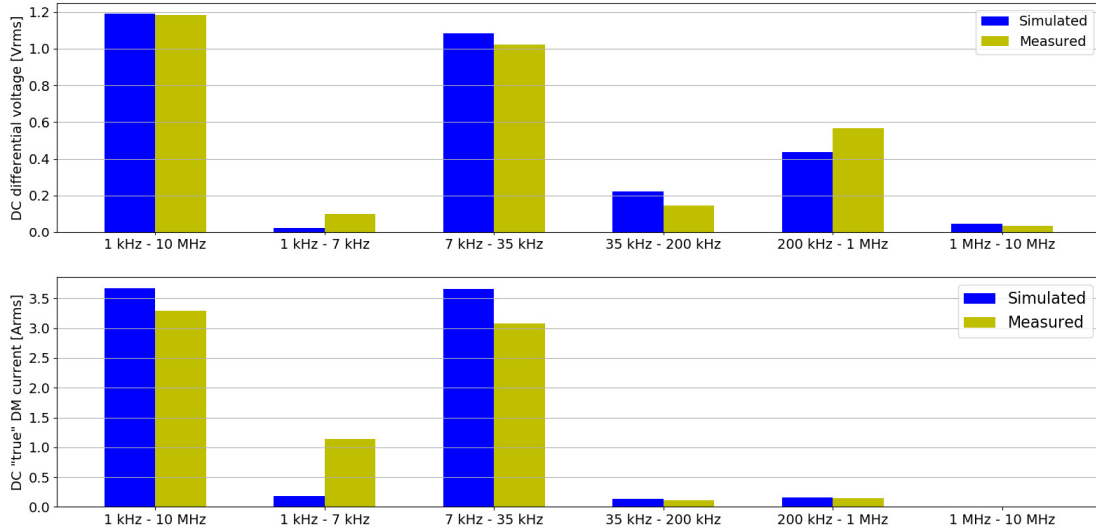
Figure 11.33 - Measurement vs simulation for measurement 07, rms values of voltage and current in different frequency ranges

Measurement 04: 100 rpm, 800 Nm, 11 kW
Measurement 15: 100 rpm, 800 Nm, 11 kW (CIDD+OBC added)
Measurement 07: 300 rpm, 800 Nm, 28 kW
Measurement 10: 500 rpm, 600 Nm, 35 kW
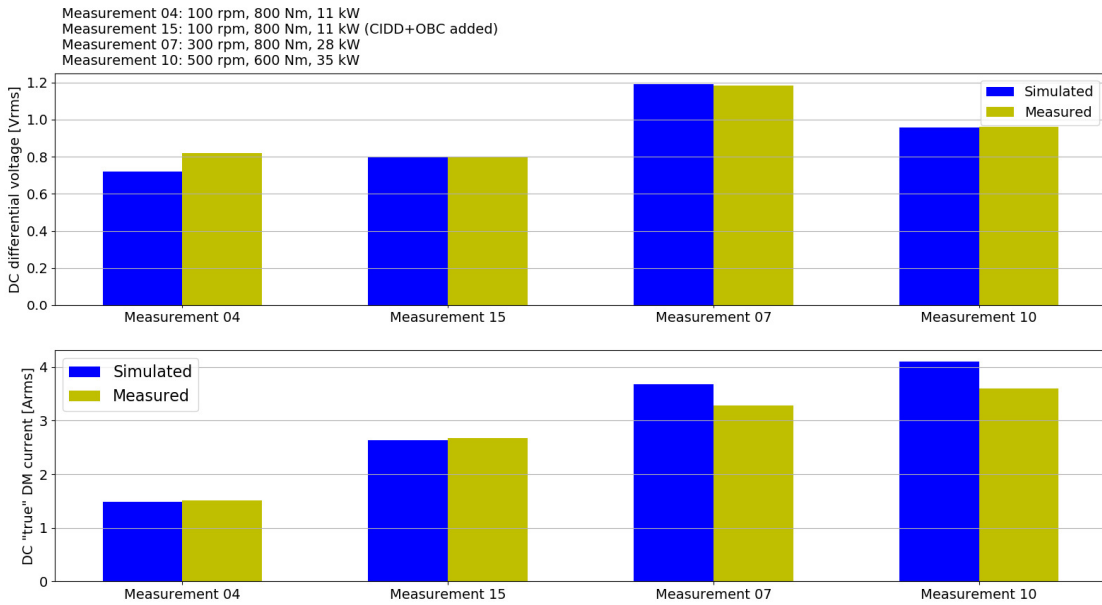
Figure 11.34 - Measurement vs simulation for all measurements, rms values of voltage and current in the frequency range 1 kHz – 10 MHz

11.6.2 Common Mode (CM)

Here the following is done:

1. The transfer functions from applied voltage between the DC-link capacitor nodes tied together and all phase outputs tied together, Vcm, to HVpos vs chassis voltage, common mode current and a phase current are obtained in LTspice.

2. The simulated result(s) are obtained by multiplying the transfer function(s) with an FFT of an ideal square wave and compared with the measurement results.

Measurements have been compared with simulations in two"configurations". Both measurements were performed when the electric machine was at standstill and with no applied torque. In this state the inverter (IEM) is still in Torque Control mode and all three phases are pulled high and low approximately simultaneously with a duty cycle of 50 %.

- Only HV-battery connected to IEM on HVDC bus
  - Measurement 01: 0 rpm, 0 Nm, 386 V

- HV-battery, CIDD and OBC connected to HVDC bus
  - Measurement 14: 0 rpm, 0 Nm, 356 V

11.6.2.1 The transfer functions
The transfer functions from an applied voltage source, Vcm, connected as in the circuit diagram in Figure 11.35 to

- DC positive voltage vs chassis voltage, i.e. HVDC_P_IEM – CHASSIS_IEM

- DC common mode current, i.e. current into HVDC_P_IEM plus current into HVDC_N_IEM

- AC phase current, e.g. current out of PH1_IEM
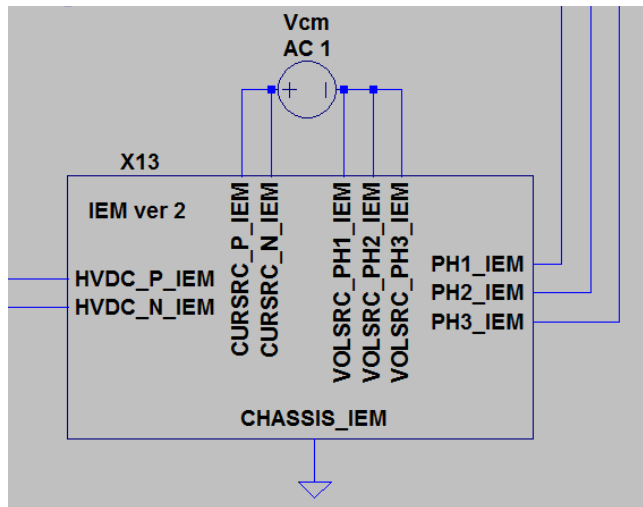
Figure 11.35 - The voltage source is applied between the nodes CURSRC_P_IEM/CURSRC_N_IEM on one side and VOLSRC_PH1_IEM/VOLSRC_PH2/IEM VOLSRC_PH3_IEM on the other side

The obtained transfer functions can be seen in Figure 11.36 below.

In the transfer functions to DC+ vs chassis voltage and to DC common mode current it can be seen that there is basically no change above 100 kHz between the two configurations.

In the transfer function to AC phase current it can be seen that no change at all is expected between the two configurations.
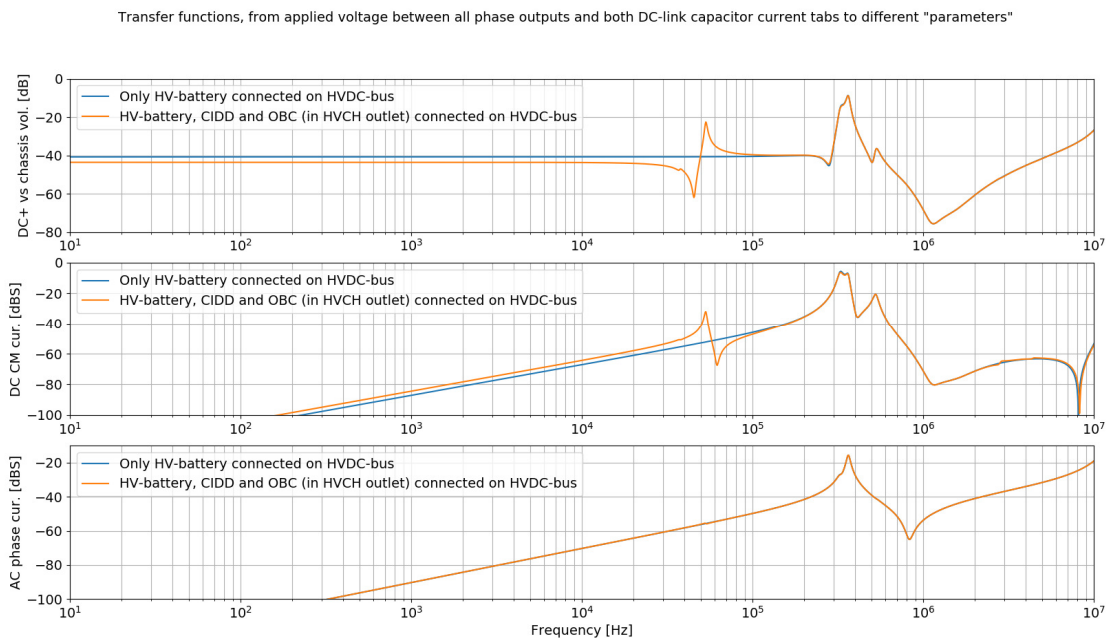
Figure 11.36 - The transfer functions from applied voltage, Vcm, in Figure 11.35 to voltage and current(s)

11.6.2.2 Compare the simulation results with the measurement results

In Figure 11.37 the square wave used in the simulations in measurement 01 is shown.

A comparison of simulations results and measurements results can be seen for measurement 01 in Figure 11.38 - Figure 11.41.

The results show, that the "general behaviour" of the simulations match the measurement results rather well. Around the resonance at ~350 kHz there are significant differences though. The simulation results are so high here that this leads to a somewhat less good match of the rms values in the frequency range 200 kHz – 1 MHz which is the frequency range with the highest rms/energy content, see Figure 11.41.

In Figure 11.42, rms values, from simulations and measurements, in different frequency ranges are shown for measurement 14. The overall match is similar to the match for measurement 01 in Figure 11.39.
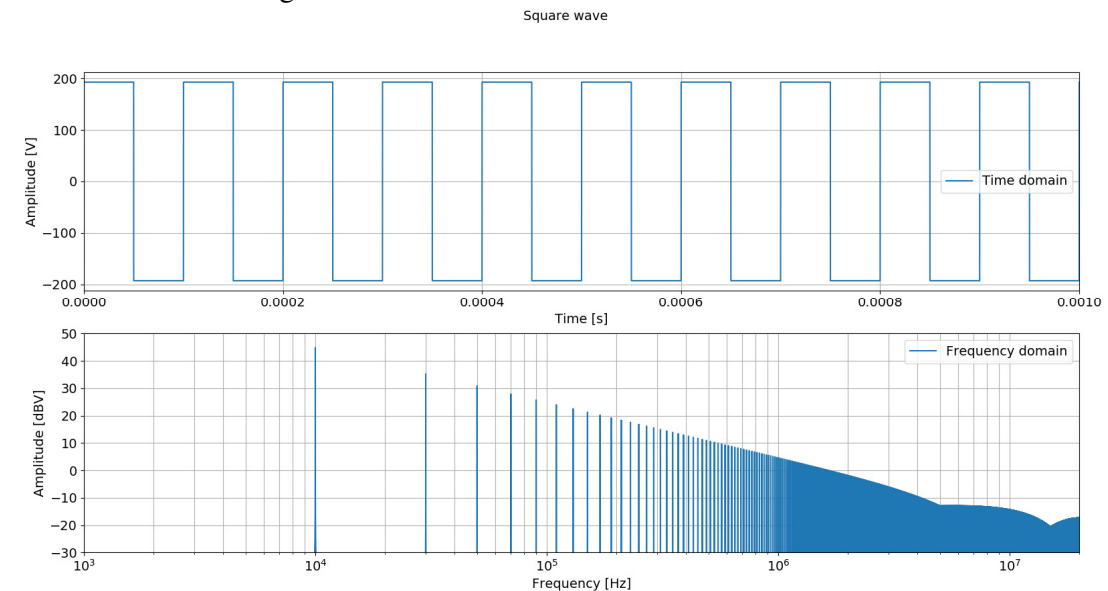
Figure 11.37 - The square wave used for measurement 01 both in time and frequency domain.
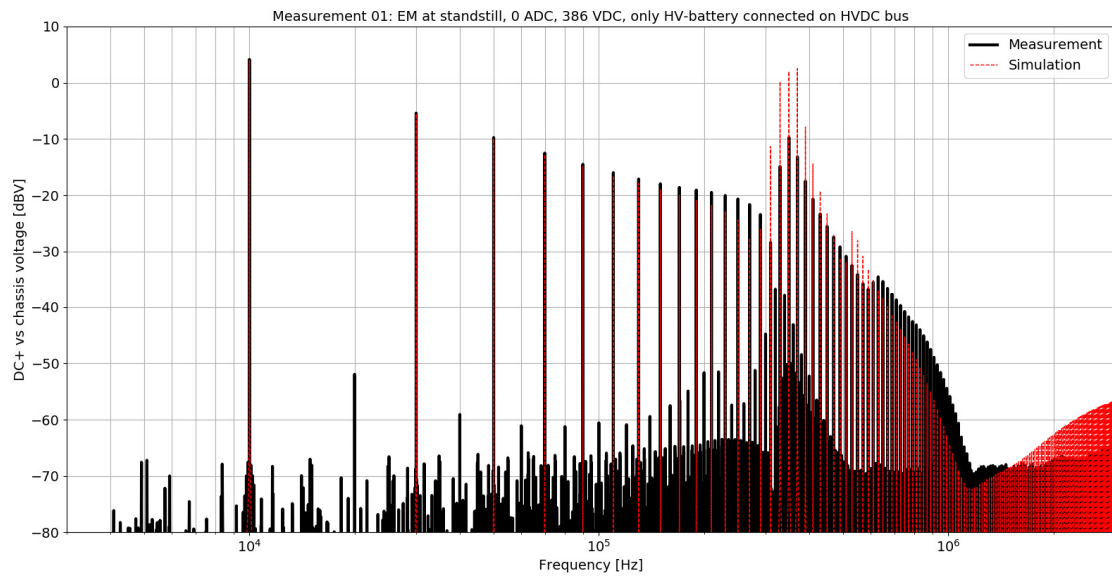
Figure 11.38 - Measurement vs simulation for measurement 01, DC+ vs chassis in the frequency domain
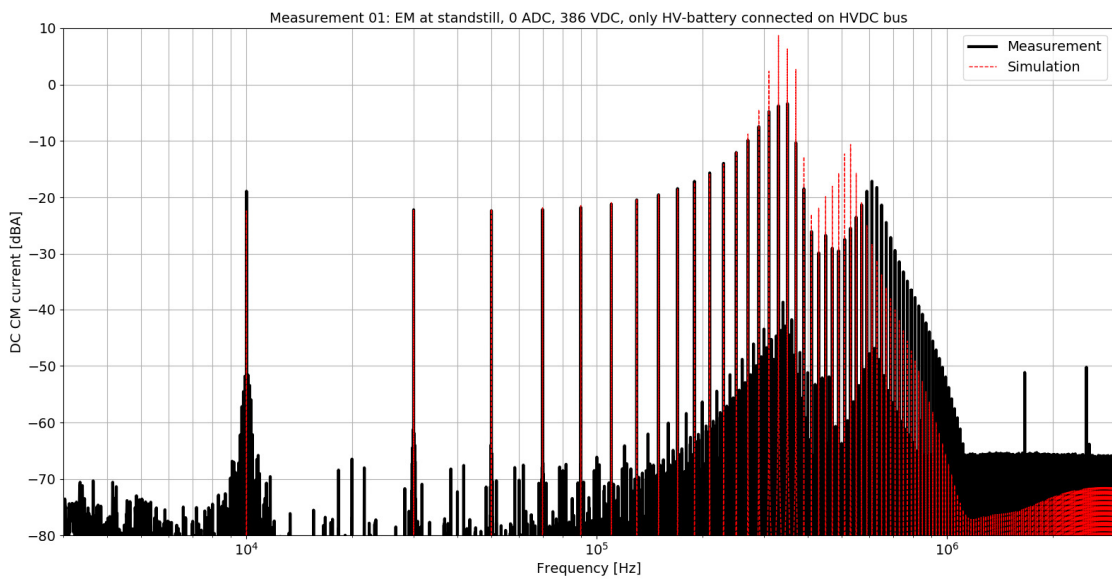
Figure 11.39 - Measurement vs simulation for measurement 01, DC common mode current in the frequency domain
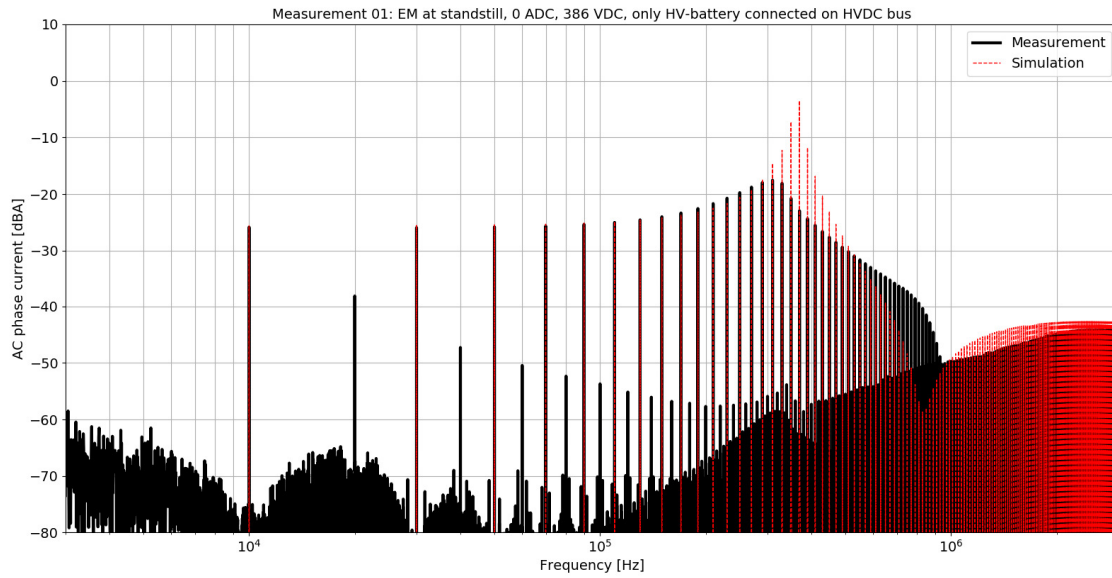
Figure 11.40 - Measurement vs simulation for measurement 01, AC phase current in the frequency domain
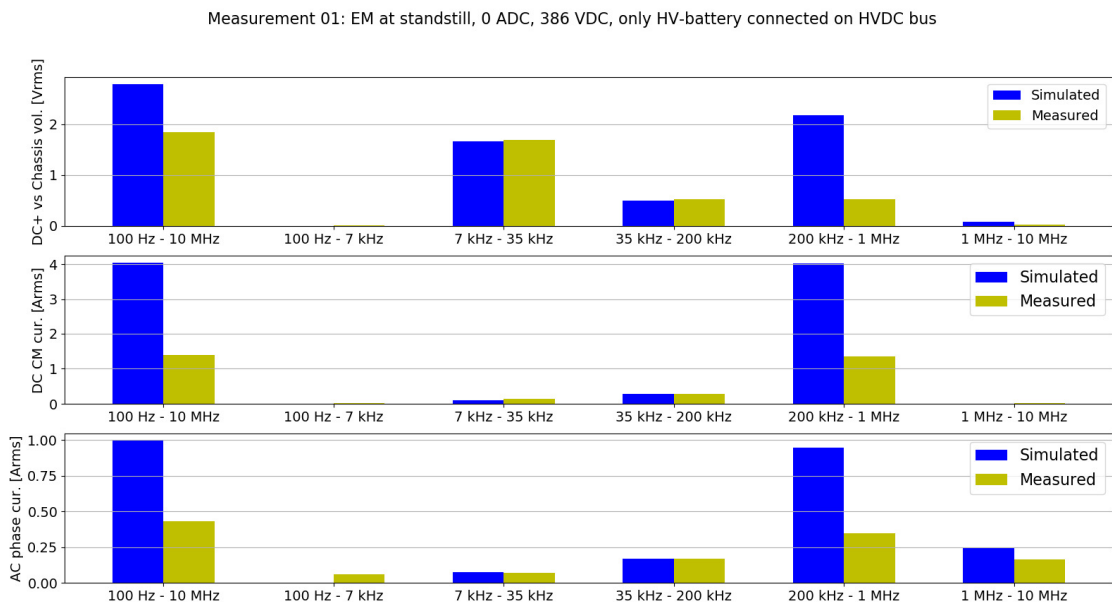
Figure 11.41 - Measurement vs simulation for measurement 01, rms values of voltage and current(s) in different frequency ranges

Measurement 14: EM at standstill, 0 ADC, 356 VDC, measured with HV-battery connected to IEM,CIDD and OBC (OBC connected in HVCH battery outlet)
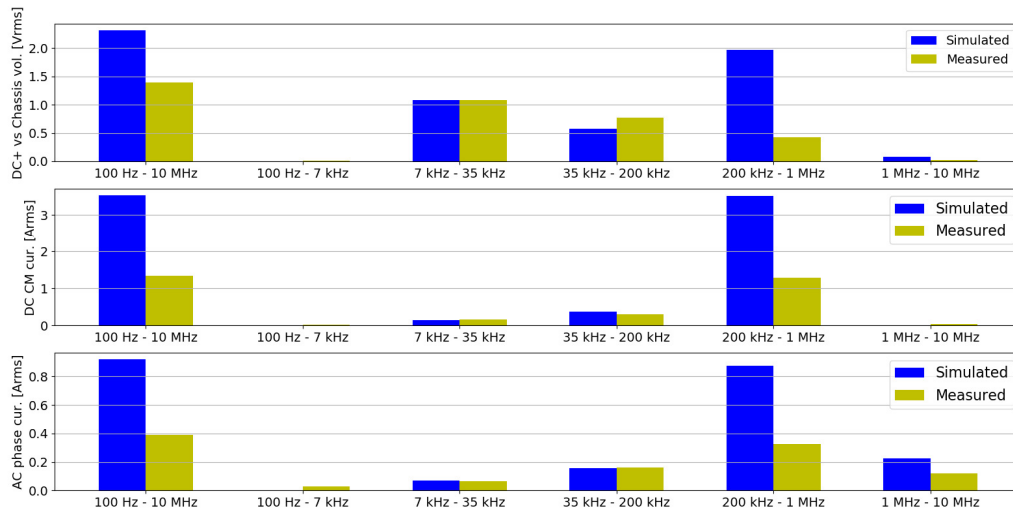
Figure 11.42 - Measurement vs simulation for measurement 14, rms values of voltage and current(s) in different frequency ranges

11.7 System model conclusions

- The system model is found to match measurements well up to 1 MHz with regards to both currents and voltages at the DC and AC sides.
- Some aspects of the model are ad hoc, for instance the actual implementation of the control system is not known and it could have a significant impact on the results.
- Some component parameter values are found from component measurements and there are many cases where it would be desirable to know these properties without access to physical hardware.
- In some cases, equivalent circuits are reconstructed from frequency domain measurements. If the circuit elements do not represent physical objects, a more compact and convenient approach might be to use state space models rather than equivalent circuits.
- In some cases, the frequency domain approach may be more convenient tool than the time domain approach.

12 Magnetic field simulations and measurements

In this chapter magnetic field simulations are performed and compared to measurements in the electric powertrain rig at Chalmers. The field depends on parameters such as 3D geometry, material properties and electric currents. An outcome of this project is the ability to predict magnetic fields by providing the electric currents in the powertrain. The magnetic field inside and outside a vehicle should meet various requirements and as an introduction a short presentation of measured magnitude fields in previous projects and literature is shown. Due to the difficulty to measure the magnetic field close to the powertrain's AC and DC cables in a real car (you have to cut away part of the chassis), the measurements are done at the powertrain rig at Chalmers.

12.1 Measurement of magnetic field in previous projects and literature

Low emission levels of electromagnetic fields (EMF) for avoiding harmful biological effects is a legal requirement since June 2016. Since currents are the sources of EMF it is especially important to consider this aspect in electrical vehicles. In this chapter we present an overview of what has been done in previous projects and what has been published concerning EMF in electrical vehicles.

12.1.1 Measured magnetic fields in electric vehicles in previous projects

Measurements of the magnetic field inside the compartment of a hybrid vehicle when driving at a speed of 50 km/h have been done by VCC. The magnetic field was measured with a magnetic field meter (Radians Innova BMM-3000) covering the frequency interval 5 – 2000 Hz. From the measurements a weighted "Body average" magnetic field value was calculated for different areas. For the driver and almost all passenger areas the Body average value was approximately 0.25 µT. An exception was at the left rear passenger area where the Body average value was 0.34 µT. This area is right over the cables between the inverter and electrical motor. High currents on these cables are most probably the source of the high measured magnetic field.

12.1.1.1 Safe Hybrid Project
H-field measurements were done in the project, among them on a Volvo V60 Hybrid driving at a speed of 40 km/h. These measurements were done for the frequency range 9 kHz to 30 MHz with a loop antenna in x-, y- and z-directions. The antenna was positioned on the right side of the car at a distance of 3 m and a height of 1 m. The recorded peak values in all three directions were close to or less than 20 dBµA/m in the frequency interval 9 kHz to 1 MHz and close to or less than -10 dBµA/m above 1 MHz. In the frequency range 15 MHz to 30 MHz peaks were found with level close to -10 dBµA/m. Also, measurements of common mode current on cables between battery and inverter located in the car trunk were done. When the car was driving with a speed of 20 km/h current peaks

of -30 dBA (90 dBμA) were found between 10 kHz and 1 MHz. The levels decreased to less than -60 dBA (60 dBμA) at 10 MHz.

12.1.1.2 Deliver Project

In this project, common mode currents were measured in an electric delivery vehicle. Measurements were done on the cables between battery and inverter. Peak values of 100 dBμA at 1 kHz and 93 dBμA at 20 kHz were recorded. Levels close to 60 dBμA were recorded up to 500 kHz. In the frequency interval 500 kHz to 10 MHz the common mode current peak value was less than 50 dBμA. Besides measurements, numerical simulations were done in the project. As a result, magnetic field with a level of 0.74 μT at 20 kHz was found.

12.1.2 Field levels from literature

To get an understanding of which levels of magnetic field strengths that can be expected near high current cables in a hybrid car, a search for publications where such information can be found was done. The results of this survey are presented in the following.

In a work [8] looking at EMC performance of an electric car powertrain before integration into the car body radiated and conducted emissions from the powertrain are studied by measurements. The inverter/converter and electric motor are placed on a table with a ground plane in a semi anechoic chamber for EMC tests. Common mode currents (I_{cm}) were measured at cables between the DC power supply (600 V) and the inverter and between inverter and motor. The test was performed with a very small load on the motor corresponding to 0%, 0.9%, 1.5% and 3% of maximum torque. Between the DC supply and the inverter, the I_{cm} peak value was 100 dBμA at 20 Hz and dropping to about 50 dBμA at 1 kHz. The difference in current for different torque was only visible above 1 kHz. Between inverter and motor the I_{cm} peak value was 120 dBμA at 20 Hz and dropping to about 80 dBμA at 1 kHz. The magnetic field was measured in the frequency range 150 kHz to 30 MHz with a loop antenna at a distance of 1 m. Different grounding configurations for cable shields were evaluated. The configurations showing highest levels of magnetic field strength gave about 30 dBμA/m for the frequency interval 150 kHz to 1 MHz and a peak (resonance) at 1.5 MHz with a level about 47 dBμA/m. A comparison of measurements shows similarities between common mode current and radiated magnetic field. The different grounding configurations affect the I_{cm} and radiated field strength more than 25 dB, and even more at frequencies where resonances occur.

In another study similar measurements are performed with different load conditions for the motor, including dynamic operation [9]. Measurement of common mode currents (I_{cm}) were done on the three phase cables between inverter and motor. The measurements were done in a motor test rig. I_{cm} peaks of more than 80 dBμA between 10 kHz and 300 kHz were found. I_{cm} data up to 200 MHz for different loading scenarios are presented in the article.

A work looking at electromagnetic reliability in electric vehicles [10] is examining shielding, cable routing and variations during real driving conditions. Common mode current (I_{cm}) on three phase cables between inverter and motor is measured for three different prototype/demonstrator vehicles. Peak levels close to 60 dBμA between 150 kHz and 1 MHz were found for two prototypes, while the third prototype shows lower levels after introducing a common mode toroidal core choke. Currents are compared with measured near field E-field strength for the prototypes.

In a paper from 2010 [11], the average of minimum and maximum magnetic field from measurements in hybrid cars are presented. The result is shown in the table below.

Location	Minimum (μT)	Maximum (μT)
Rear left floor	0.2	3.5
Rear left seat	0.09	1.32
Rear right floor	0.09	1.43
Rear right seat	0.15	0.84
Driver head	0.03	0.56
Front left floor	0.15	0.75
Front left seat	0.1	2.39
Front right floor	0.05	1.31
Front right seat	0.05	1.79
Resting rear right floor	0.12	0.43
Resting front left seat	0.1	0.4

To summarize this study some results from the different sources can be compared for a better understanding of typical levels of common mode currents and magnetic field levels.

	Safe Hybrid	Deliver	Ref.[8]	Ref.[9]	Ref.[10]	Ref.[11]
Icm Battery [dBμA]	90	100	100			
Icm Motor [dBμA]			120	80	60	
LF B-field [μT]		0.74				3.5
LF H-field [dBμA/m]	20		30			

12.2 Generation of magnetic field

Magnetic fields generated by current loops in vacuum can be calculated semi-analytically. For example, the formula for the field far from a planar current loop can be calculated according to Figure 12.1.

Metallic materials (such as the car body) affect the magnetic field, calling for techniques such as finite elements.
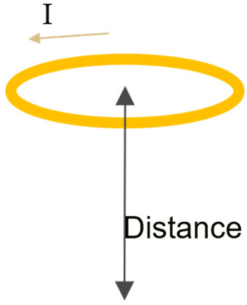
$$B \approx \frac{\mu_0 \times \text{Current} \times \text{Loop area}}{2\pi \times \text{Distance}^3}$$

Figure 12.1 - Far field magnetic field generated by a planar current loop in vacuum.

12.2.1.1 Shielding from metals

Metals can shield magnetic fields in two distinctly different ways: magnetically and conductively. We see, in Figure 12.2, an illustration of how the field is repelled by conductive shielding. The repelling depends on the material's conductivity, thickness and frequency. In Figure 12.3, simulations of conductive shielding effect using a copper plate with varying frequencies are shown. We see that the higher the frequency, the higher shielding.
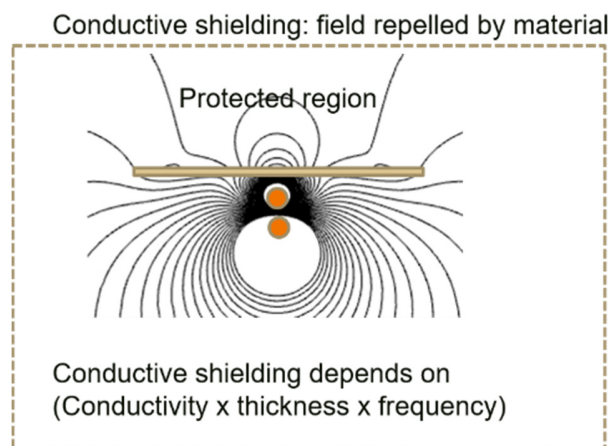
Figure 12.2 - Illustration of conductive shielding.
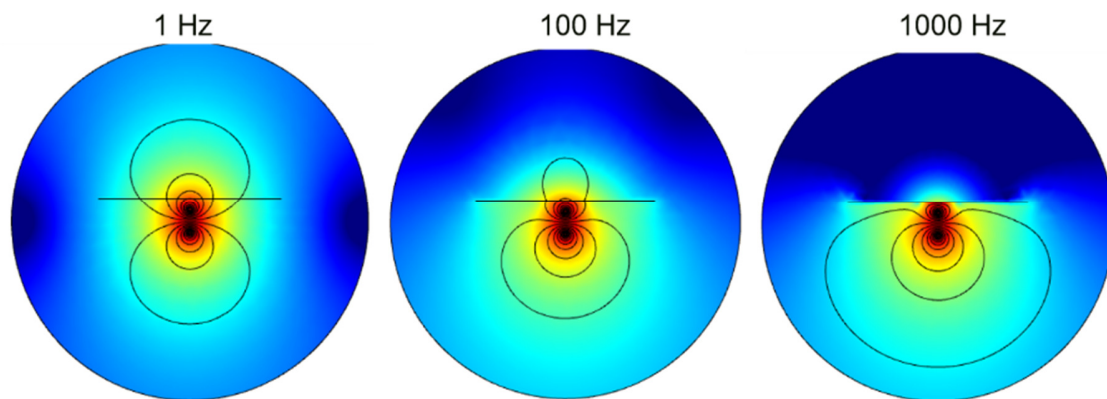
Figure 12.3 - Simulation showing conductive shielding effect.

An illustration of how field is attracted by magnetic shielding can be seen in Figure 12.4. The attraction depends on the material's permeability and thickness. In Figure 12.5, simulations of magnetic shielding effect from a steel plate with varying permeability μ is shown. We see that the higher the permeability, the higher the shielding.

Figure 12.4 - Illustration of magnetic shielding.
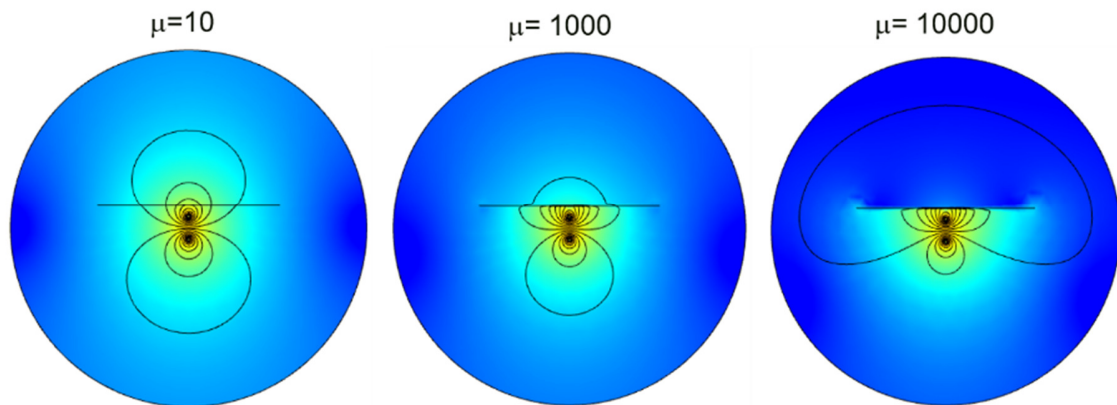
Figure 12.5 - Simulation showing magnetic shielding effect.

The steel used in car bodies is usually both magnetic and conducting. The two shielding effects will interact in sometimes nontrivial ways.

12.3 Measurement of magnetic field in electric powertrain rig

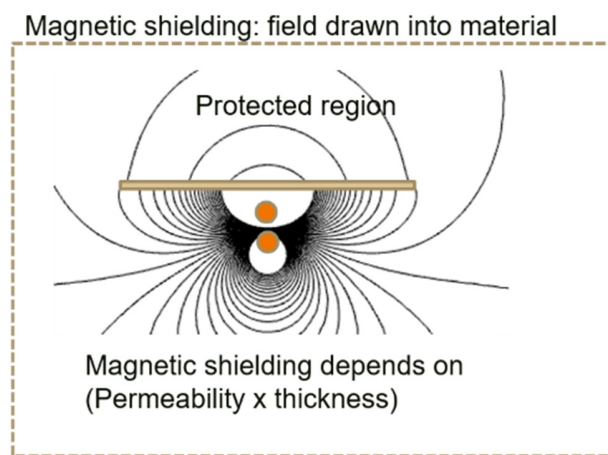Due to the difficulty to measure the magnetic field close to the powertrain's AC and DC cables in a real car (you have to cut away part of the chassis), the measurements were done at the powertrain rig at Chalmers.

To measure the magnetic field, a compact field analyzer/probe (NARDA EHP-50F), together with a PC software (EHP-TS) was used. The magnetic field measurements were performed with and without the presence of a steel plate, approximate 5 cm from the AC cables (half way between the inverter and electric machine). A photo of the set-up is shown in Figure 12.6. The currents in the AC cables were measured with Rogowski coils. Similar measurements were also done for the DC cables (half way between battery and inverter) but are not shown in this report.

The drive axle speed and torque were set to 100 rpm and 300 Nm, respectively, and the magnetic field and currents were recorded. This was also done for the combinations 100 rpm and 700 Nm, 500 rpm and 300 Nm. The gear ratio between the drive axle and the electric machine is about 10, so 100 rpm at drive axle corresponds to about 1000 rpm at electric machine.

To give a hint of the car chassis effect on the magnetic field about 5 cm away from the AC and DC cables, the magnetic field is measured at frequencies 10 Hz-100 kHz with and without the presence of a steel plate (material properties as used in cars). The steel plate has the dimension 800x270x0.7 mm and an approximate permeability of $\mu_r \approx 150$ and conductivity $\sigma \approx 6e6$ S/m.
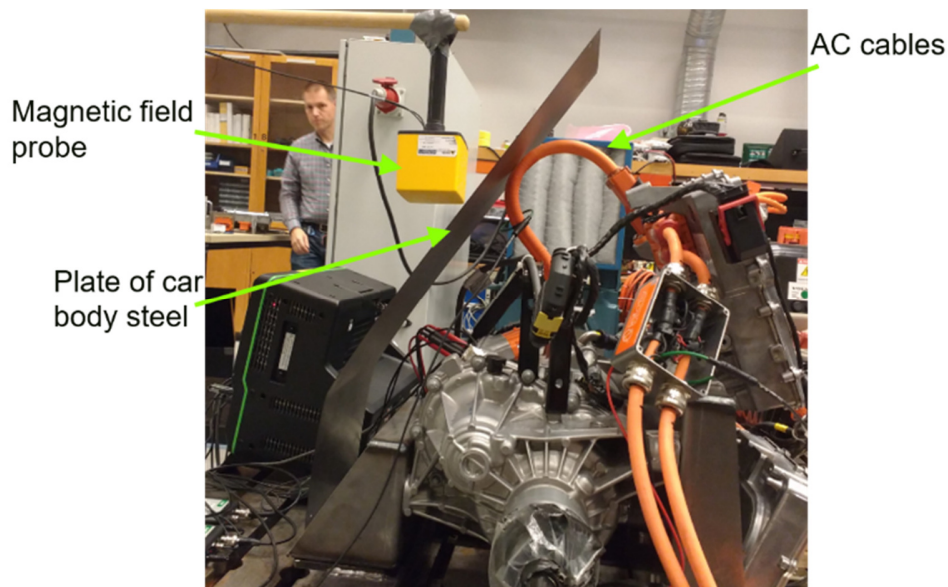
Figure 12.6 - Measurement of magnetic field with a probe close to the AC cables with a steel plate in between, on the powertrain rig at Chalmers.

12.3.1 Magnetic field without steel plate for several torques and speeds:

In Figure 12.7 the measured magnetic field in the frequency range 0-500 Hz is shown approximate 5 cm from the AC cables, without a steel plate. As can be seen there are two peaks at about 65 Hz corresponding to an electric machine speed of 1000 rpm (drive axle about 100 rpm). At 65 Hz we also see that that a higher torque (700 Nm) gives higher magnetic field. For an increase in speed of 5 times to 5000 rpm the peak is shifted to a frequency 5 times higher, i.e. to about 325 Hz. At higher frequencies up till 100 kHz, we can see peaks at 10 kHz, 20 kHz and so on, coming from the inverter switching frequency at 10 kHz, see Figure 12.8.

Figure 12.7 - Measured magnetic field 0-500 Hz, approximate 5 cm from AC cable without steel plate on powertrain rig at Chalmers.
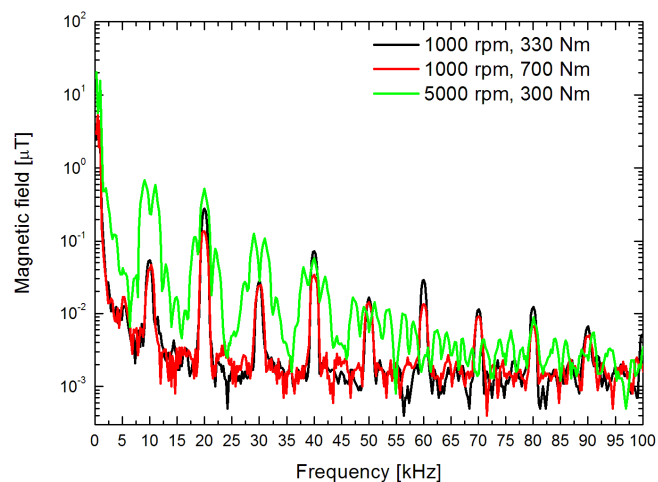
Figure 12.8 - Measured magnetic field 0-100 kHz, approximate 5 cm from AC cable without steel plate on powertrain rig at Chalmers.

12.3.2 Magnetic field with and without steel plate at a fixed torque and speed:

The magnetic field measurements were performed with and without the presence of a steel plate, approximate 5 cm from the AC cables. The frequency interval is 10Hz-100kHz and in Figure 12.9. is shown the whole frequency interval, and enlargements at low and high frequencies.

The influence of the steel plate is found to be significant:
- About 60% damping at low frequencies (magnetic shielding)
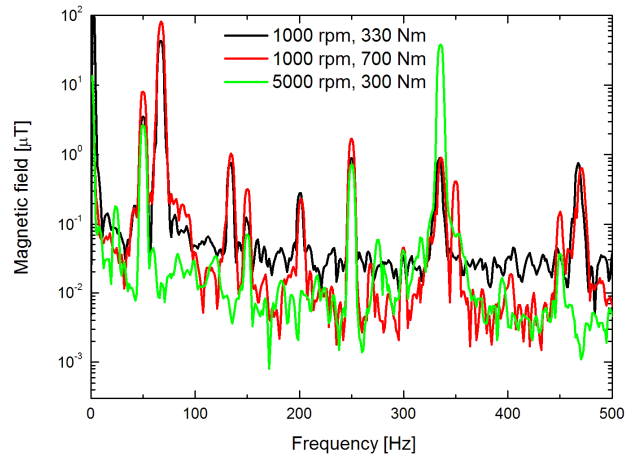- About 90% damping at high frequencies (conductive shielding)

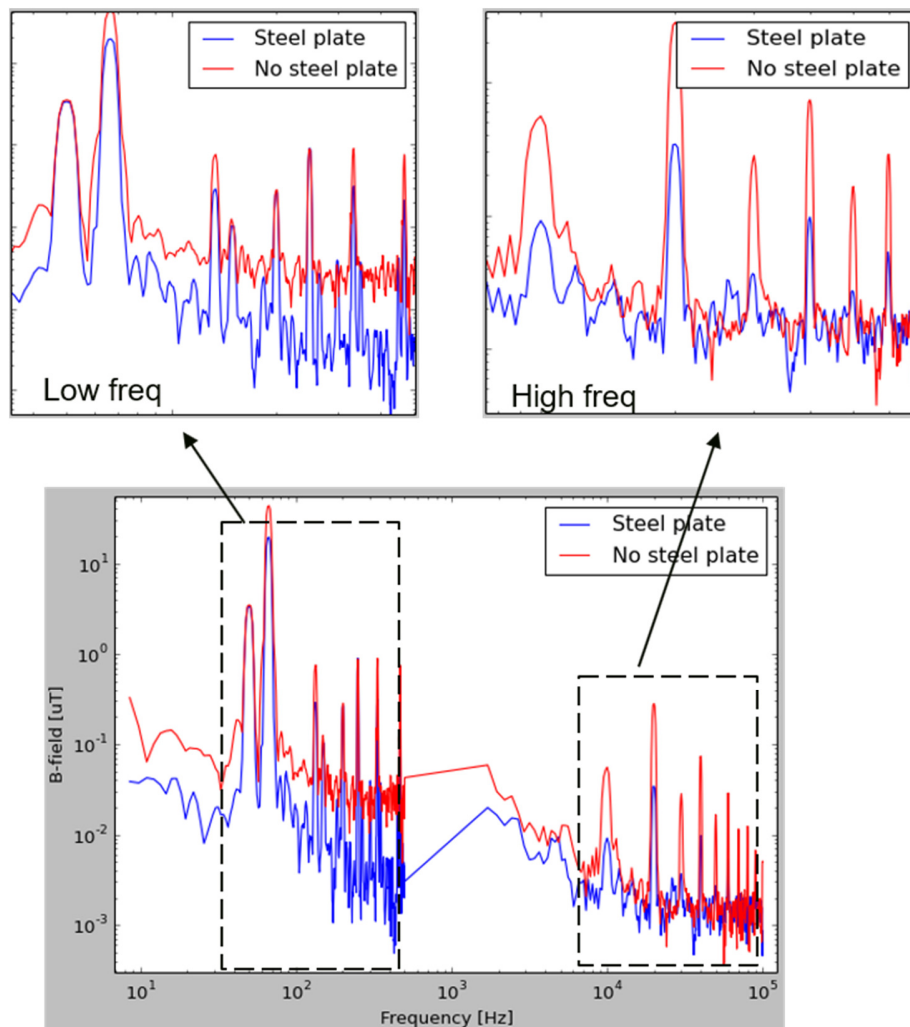Figure 12.9 - Measured magnetic field approximate 5 cm from AC cables, with and without steel plate on powertrain rig at Chalmers. Lower - frequency interval 10 – 100 kHz. Upper – enlargement for lower and higher frequencies.

12.4 Magnetic field simulation

The electromagnetic simulations shown in this report are done in COMSOL [12], using Finite Element (FE) meshing. Mainly because of its shell mesh formulation for thin sheets which is very useful when considering magnetic shielding.

Another electromagnetic simulation software CST [13], also using FE mesh, has a Low Frequency solver and a High Frequency solver. For both solvers, we have spent much effort to get accurate results for thin sheets magnetic shielding in this project. However, none of these two CST solvers give good enough results and will not be shown here.

12.4.1 Procedure for magnetic field simulations:

In general, the procedure for magnetic field simulations using the AC cables can be:
- Use system model to find currents in AC cables.
- Use 3D finite element model to find magnetic field for those currents.

Note that the simulated currents in the AC cables are found by running the system simulator for the system model, including powertrain components such as battery and cables. Thereafter, we could take the simulated currents for all frequencies and feed into FE simulations. However, a FE simulation for a single frequency takes a few minutes and solving for ~10^4 frequencies would take weeks. So instead we can:
a) Perform a system simulation to get currents for all frequencies.
b) Perform FE simulations for a small (20-30) number of frequencies with nominal currents.
c) Use external scripts (Python/MATLAB) and linear algebra to combine results from a) and b).

A field is linear with respect to the current, so for each frequency (the current) x (field at nominal current at 1A) = (field at the actual current) as shown in Figure 12.10. However, the nominal field varies smoothly with frequency, so we can use a small number of FEM simulations and interpolate.
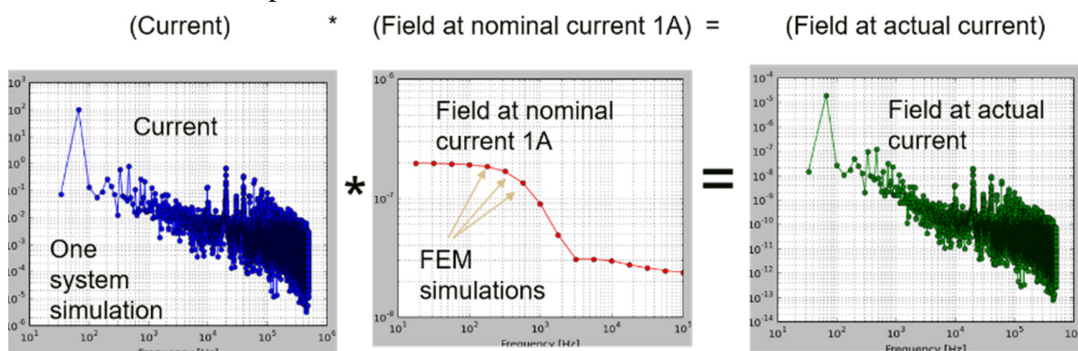
Figure 12.10 - Simulation procedure for magnetic field simulations for AC cables using currents from system model as sources.

To be more precise we must also
- Keep track of contributions from different phase currents.
- Keep separate track of x, y, z components of B-field.

The nominal field is therefore calculated when applying a unit current 1A for each of the three phases a, b and c and storing the resulting field vectors $\mathbf{B}_{\text{nom,a}}(f)$, $\mathbf{B}_{\text{nom,b}}(f)$, $\mathbf{B}_{\text{nom,c}}(f)$ separately. Then the total field is:

$$\mathbf{B}_{tot}(f) = I_a(f) \cdot \mathbf{B}_{\text{nom,a}}(f_k) + I_b(f) \cdot \mathbf{B}_{\text{nom},b}(f) + I_c(f) \cdot \mathbf{B}_{\text{nom},c}(f)$$

12.4.2 FE modeling and simulation results

The FE simulations are done in COMSOL. We started by making a simplified CAD geometry of the rig, recreated from photographs, see Figure 12.11. The most critical dimensions are distances between cables and distance from cables to probe.
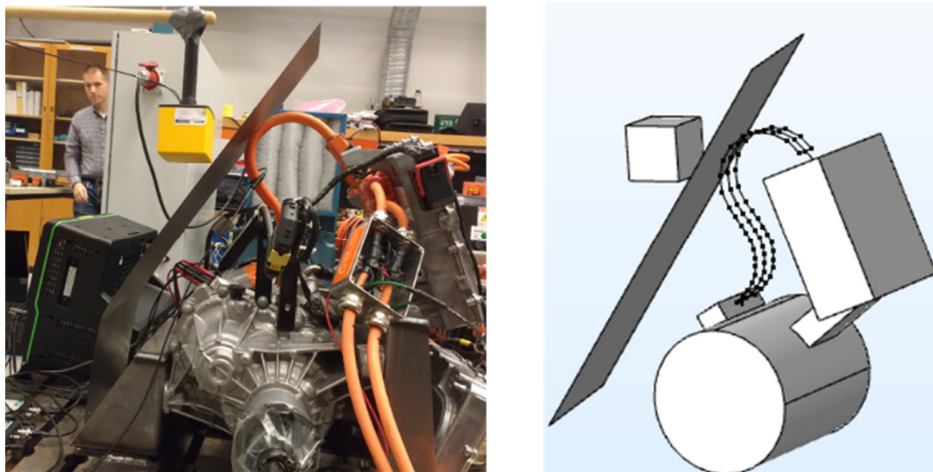
Figure 12.11 - Left – Photo of measurement magnetic field at powertrain rig. Right - Simplified CAD geometry of rig recreated from photographs.

12.4.2.1 Magnetic field profile for differential mode
Simulations of the magnetic flux density (B-field) for the differential mode case, i.e. when the 3 phase currents balance each other, has been done with and without steel plate. In Figure 12.12, we see the B-field profile without steel plate at 50 Hz. In Figure 12.13 the B-field profile with steel plate also at 50 Hz is shown and as can be seen the B-field is reduced, due to magnetic shielding. At even higher frequency (10 kHz) the B-field is even more reduced, due to both magnetic and conductive shielding.
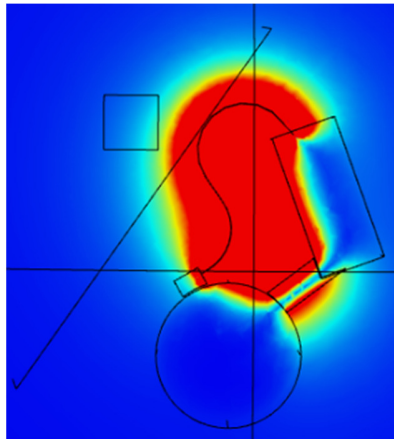
Figure 12.12 - Simulated magnetic flux density profile for 50 Hz without steel plate for 50 Hz. Differential mode.
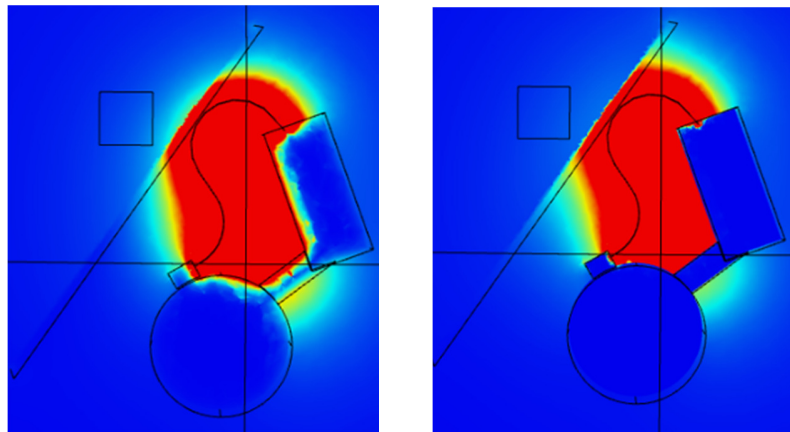
Figure 12.13 - Simulated magnetic flux density profile for 50 Hz with steel plate for 50 Hz (left) and 10 kHz (right), respectively. Differential mode.

12.4.2.2 Magnetic field profile for common mode

Simulations of the magnetic flux density (B-field) for the common mode case, i.e. the same current is applied in all 3 phases, has been done with and without steel plate. We can see the B field profile without steel plate at 50 Hz in Figure 12.14. The B field profile with steel plate at 50 Hz the B-field is reduced due to magnetic shielding, as can be seen in Figure 12.15. At 10 kHz the B-field is even more reduced, due to both magnetic and electric shielding.
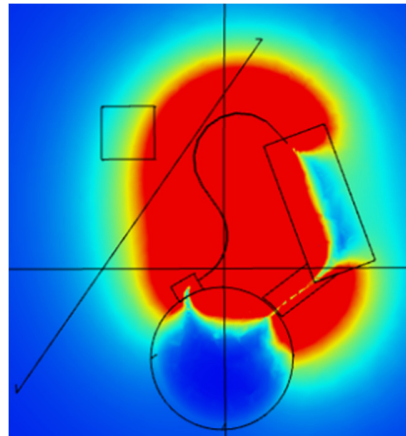
Figure 12.14 - Simulated magnetic flux density profile for 50 Hz without steel plate for 50 Hz. Common mode.
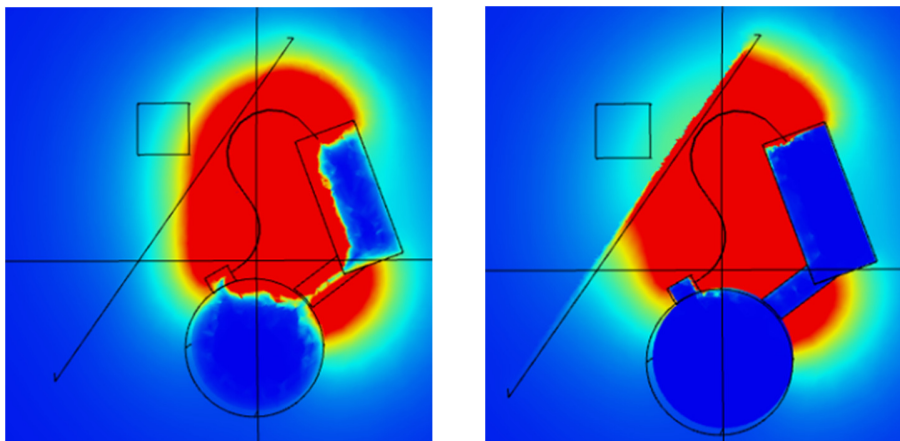
Figure 12.15 - Simulated magnetic flux density profile for 50 Hz with steel plate for 50 Hz (left) and 10 kHz (right), respectively. Common mode.

For the centre of the probe position, the field as function of frequency for an excitation current of 1 A can be seen in Figure 12.16. We see that the B-field without a steel sheet is constant in the frequency interval 10 Hz – 100 kHz, for both differential and common mode. For differential mode, with a steel sheet, the B-field is decreasing for higher frequencies. The common mode case also has a B-field decreasing behavior for a metal sheet, except at around 20 kHz where a local minimum can be seen.
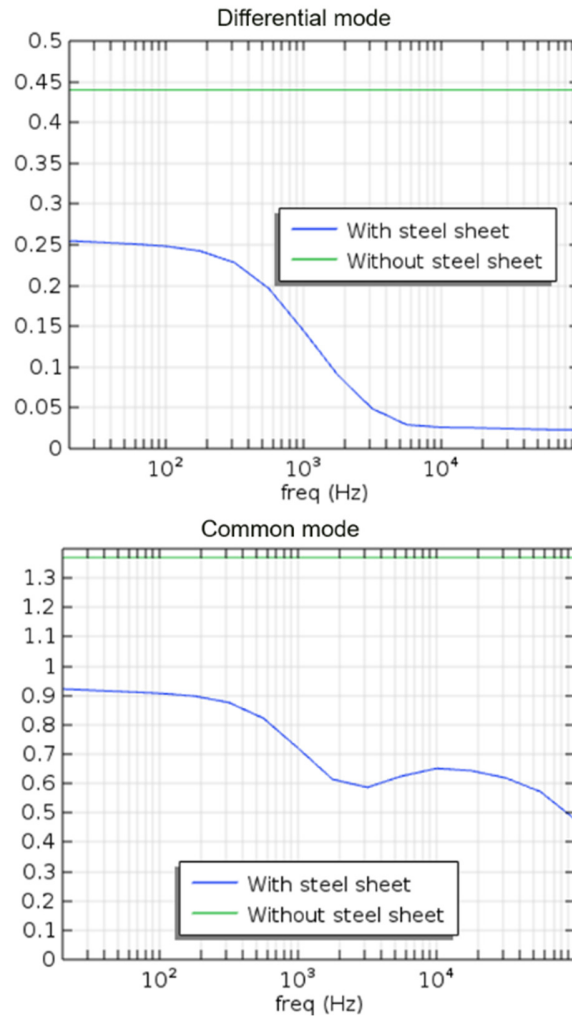
Figure 12.16 - Simulated magnetic field B(µT) for differential mode and common mode as function of frequency with and without steel sheet, respectively.

12.5 Magnetic field simulation vs measurement

12.5.1.1 Without steel plate - simulation vs measurements

The simplified geometry of the rig without steel plate can be seen Figure 12.17. The B-field as function of frequency in Figure 12.18, has been calculated at a few discrete frequencies. The agreement between measurements and simulations are quite good.
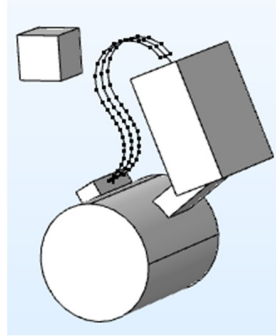
Figure 12.17 - Simplified CAD geometry of rig without metal plate.
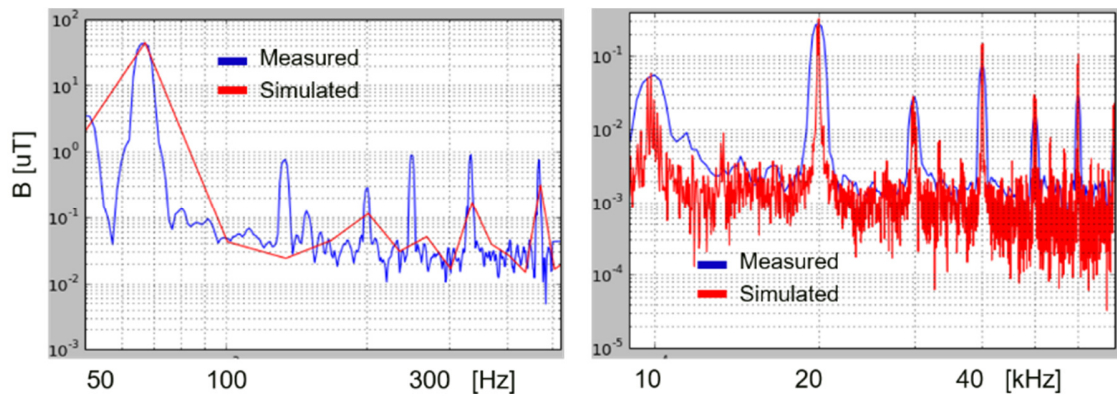
Figure 12.18 - Simulated and measured B-field vs frequency without steel plate in rig. Left - low frequencies. Right - high frequencies.

12.5.1.2 With steel plate - simulation vs measurements

The simplified geometry of the rig with metal plate between AC cables and probes can be seen in Figure 12.19. The B-field as function of frequency in Figure 12.20 has been calculated at a few discrete frequencies. We see that the magnetic shielding from a steel plate reduces B-field about 20 dB (60%) in both measurements and simulations (at 65Hz). Magnetic and conductive shielding from a steel plate reduces a B-field about 50 dB (90%) in both measurements and simulations (at 10 and 20 kHz). The conclusion is that the shielding effect is well predicted.
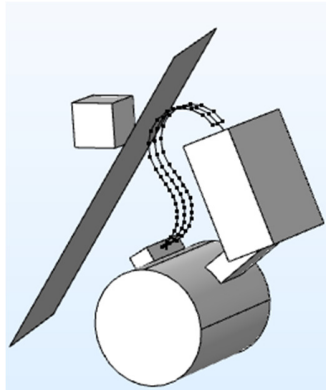
Figure 12.19 - Simplified CAD geometry of rig with metal plate.
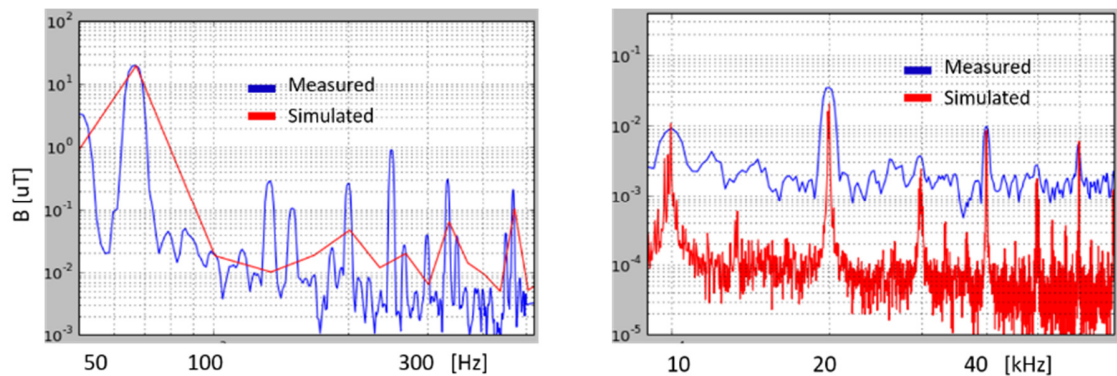
Figure 12.20 - Simulated and measured B-field vs frequency with steel plate in rig. Left - low frequencies. Right - high frequencies.

12.6 Conclusions

Magnetic field simulations have been calculated and compared to measurements in rig.
- The system model provides currents.
- The FE model provide fields at nominal currents, taking into account 3D CAD and shielding effects of metals.
- Actual field found by combining system and FE results.
- Good match with measurements across frequency range.
- This means the same method can be used to simulate magnetic fields inside and outside a car.

13 Dissemination and publications

13.1 Dissemination

How are the project results planned to be used and disseminated?	Mark with X	Comment
Increase knowledge in the field	X	
Be passed on to other advanced technological development projects	X	Will be continued in research project Virtual Electric Propulsion System
Be passed on to product development projects		
Introduced on the market		N/A
Used in investigations / regulatory / licensing / political decisions	X	

13.2 Publications

Below is a list of publications and conference presentations associated with the project:

[1] Alexandra Nafari, Robert Eriksson, Continued High Voltage System Development, EEHE – Electric & Electronic Systems in Hybrid and Electric Vehicles and Electrical Energy Management, 8-9 June 2016, Wiesloch, Germany

[2] Virtual methods for investigating system-level ripple and EMC in electrified vehicles, Per Jacobsson, Anders Bergqvist, John Simonsson, EEHE – Electric & Electronic Systems in Hybrid and Electric Vehicles and Electrical Energy Management, 12-13 June 2018, Würzburg, Germany

[3] Peter Ankarson, Urban Lundgren, Modelling and Simulation of a High Voltage Car Electric Drive Line to See Ripple on HV DC and AC cables for Different Cable Routings – Measurements vs Simulations, EMC Europe 2018 Workshop Automotive AMC, August 27-30 August, Amsterdam, Netherlands

[4] Andreas Henriksson, Impedance Modeling for Accurate Estimation of DC-Link Current and Voltage Ripple in Electric Vehicles, International Electric Vehicle Symposium, Sep 30-Oct 3, 2018, Kobe, Japan.

14 Conclusions and future research

Regarding the impedance modelling of the battery cells and the validity of this impedance to module and pack level, clear results were found. The electrical characteristics up to a frequency of ca 1000 Hz was well determined using an impedance spectroscopy instrument, Gamry Reference 3000. This means that the influence of temperature and SOC level on a battery can be determined using a single cell and just add the cells together. Regarding the impedance behaviour for frequencies above 1000 Hz, the determination must be done on the battery pack level. The reason is that the inductance in a battery cell is extremely low, so it makes it impossible to determine it on the cell level. In addition, internal bus bars in the battery will be the ones that are important for the determination of the inductance. Also the resistance for frequencies above some kHz, needs to be determined for the whole package, results obtained using a cell measurements are not very accurate. Very satisfying was that the Gamry measurements were compared with results using the Bode 100 instrument, and the results in the frequency range 100-1000 Hz agreed very well between the two instruments.

When dealing with the inverter and the electric machine there are many different aspects that need to be taken into account. For the actual switching events in the inverter, an idealized simulation model of the IGBT is sufficient. Actual switching events will only increase the simulation time drastically. The control of the inverter is very important for the overall behaviour and in this project SVM was used which has been shown to give the lowest current and voltage ripple of the traditional switching schemes. Also, no data of the control structure was given which required a great deal of reverse engineering. For future projects, more details about the inverter control loop is needed.

For the machine model, the temperature variations must be taken into account since the machine parameters has been found to vary with ~20% over the specified temperature range. Also, the traditional PMSM-machine model is not enough since is does not give access to the y-point of the machine and does not account for the stator and rotor CM impedance. This impedance is one of the most important components for the CM-currents and must be accounted for in the system simulation model. Therefore a more detailed machine model is necessary, and in this project it was realized in VHDL-AMS. This model also includes a simple implementation of cogging torque which has been shown to affect the current and voltage ripple on the DC-link.

The system model is found to agree well with rig measurements up to 1 MHz with regards to both currents and voltages at the DC and AC sides. Furthermore, measurements in a real car match those in the rig. Some aspects of the model are ad hoc, for instance the actual implementation of the control system is not known and it could have an impact on the results. When it comes to components, some parameter values are found from component measurements and there are many cases where it would be desirable to know these properties without access to physical hardware. In some cases, equivalent circuits are reconstructed from frequency domain measurements. If the circuit elements do not represent physical objects, a more compact and convenient approach might be to use state space models rather than equivalent circuits. Furthermore, the frequency domain approach may be a more convenient tool than the time domain approach in some cases.

The selection of simulation tools in this project were mainly based on the functionality of circuit simulations for the inverter and the electric machine. Another important aspect was the possibility to co-simulate different simulation domains and the possibility to link the selected tool to other simulation tools within Volvo. For time domain simulations, it was decided to use Ansys Simplorer since it can handle these requirements very well. In addition to this, it is easy to use, gives fast simulation time, support multiple simulation domains, supports FMU, and has previously been used within Volvo. The main drawbacks are the cost, installation, licensing, and poor control handling capabilities. For frequency domain simulations, it was decided to use LTspice since it is freeware, has support for AC-sweeps, improved switching compared to other SPICE-simulators, and is easy to use. The main drawbacks are poor control handling capabilities, no official support since it is freeware, and no electric machine modelling.

For shielded cables, such as high voltage cables in vehicles, the problem has to be divided into two parts, one inner problem and one outer. The reference for the inner problem is the shield, and for the outer the chassis of the vehicle. From measurements of differential mode impedance it is found that it is important that the mutual inductance between centre conductor and shield is included in the model to describe cable impedance below 10 kHz properly. The induced current in the cable shield can be quite large if the shield loop impedance is small and depending mainly on contact resistances for the shield connection in the cable ends. The resistive losses in the cable shield will give the cable a low pass filter characteristic for ripple currents. The potential high shield currents are because forward and return currents are shielded separately. A configuration with forward and return current conductors with a common shield, the shield current magnitude can be much smaller.

Magnetic field simulations have been calculated and compared to measurements in the driveline rig at Chalmers. It was a good match across the investigated frequency range 10 Hz to 100 kHz. The procedure for magnetic field simulations can shortly be summarized as follows. The system model of the driveline is used to provide currents on the cables. The electromagnetic simulation model provides actual magnetic fields, taking into account 3D CAD and shielding effects of metals. This means the same method can be used to simulate magnetic fields inside and outside a car. To get correct simulated magnetic fields at low frequencies it is important to choose an electromagnetic simulation software that can handle thin steel plate (permeability and conductivity), as is used in the car chassis. One such electromagnetic simulation software is e.g. COMSOL [12].

When it comes to the model architecture, it is important that the chosen solution supports flexibility in terms of component variants and fidelity level. Even for a specific system as was the case in the RIFEL project, the number of possible system model configurations grows rapidly when component model variants are introduced. In order to be able to switch between different component models easily as well as to keep track of combinations used in the system model, it is preferable if these features are available in the software tool. This is very important for traceability and confidence level for the system models.

In this project, only internally developed component models were considered. To expand the functionality of the system modelling tool, international interface standards such as the Functional Mockup Interface (FMI) need to be investigated. Consequently, it would be a good idea to include additional automotive OEMs as well as suppliers and software vendors in future research collaborations. Another important focus for future research projects

could be flexibility and usability. With a simulation tool that is flexible in terms of component fidelity, the tool could be used throughout the product development process and updated in an agile manner. This would allow the tool to be used in early phases for concept studies as well as in late stages as a high-fidelity digital twin. Flexibility in terms of system configuration is also important for using the tool for new designs. In the RIFEL project, a system model validated both on component and system level for a specific vehicle platform has been created. The next step is to use the existing framework to set up new system configurations and use them for system performance predictions.

Another aspect of the system model that needs to be explored further, is the use of currents in the system model as sources for an external electromagnetic field simulation. Building on preliminary investigations, an aim for future projects could be to create reduced order models for radiated electromagnetic fields based on 3D or 2D field simulations.

14.1 Deliveries to FFI Goals

This project contributes to the goal of the FFI program by:

14.1.1 Technologies that make it possible to reduce fossil dependency

This project has focused on electrified vehicles and their improvement in design and time to market. By decreasing the development cost and increasing the design, the usage of electric vehicles will increase hence reducing the CO_2 emissions within the vehicle fleet. This project will also make earlier verification possible hence reducing the lead times and development cost.

14.1.2 Promote the competitiveness of the Swedish automotive industry

Shorten lead times is a key factor in maintaining as well as increasing the Swedish competiveness within the vehicle industry. This project has enabled such competiveness by offer validated virtual system models in early phases hence shortening the lead times.

14.1.3 Strengthen research and innovation capacity in Sweden

The developed system models and the increased competence will be important tools for both the industry (Volvo) and the academy (Chalmers and RI.SE) after the project end. The knowledge how to develop and execute system models will strengthen research and innovation by giving feedback on new concepts before HW is available.

14.1.4 Promote collaboration between industry and academia

The project was performed in collaboration with Chalmers and RI.SE. Knowledge gained within the project was spread at 3 different seminaries with participants from varying

companies such as Volvo AB, Scania, BorgWarner, CEVT but also from the academic side. Based on previous experiences it is known that collaboration between industry and academia will increase the knowledge at national level as well.

This project supports the "Electronic, Software and communication" goals through creating and building new competences and tools. The vision to "Develop necessary base technology to realise functions…" and "Establish world leading methods and tools to the automotive industry" are described below.

Develop the necessary base technology for the realization of "green functions" includes to study the frequency range between 1kHz and 1MHz thoughtfully since different physical phenomenon will be dominating at different frequency which makes these models quite complex. The project sought to investigate these phenomenon and clarify the somewhat diffuse knowledge in this area. Even though the models first should be validated up to 100kHz it has been shown that they can perform effective results in a higher frequency range as well.

The project also supports the Verification/Validation within the programme through increased virtual availability to include the HV DC systems electrical environment with focus on ripple. These virtual methods can be used for analysing new or changed concepts in the early phases of a project which will lead to shorter development times and higher quality.

15 Participating parties and contact persons

Contact persons	Email	Contributions / Role/ Involvement
Dr. Anders Bergqvist	anders.bergqvist.3@volvocars.com	WP5
Dr. Andreas Henriksson	andreas.henriksson.2@volvocars.com	WP3, WP5
Jan Welinder	jan.welinder@ri.se	WP2
Johan Lektenius	johan.lektenius@volvocars.com	Project leader
John Simonsson	john.simonsson@simtech.se	WP2, WP3, WP4, WP5
Peter Ankarson	peter.ankarson@ri.se	WP4
Dr. Per Jacobsson	per.jacobsson@volvocars.com	WP5
Dr. Shemsedin Nursebo Salih	shemsedin.nursebo.salih@volvocars.com	WP2
Prof. Torbjörn Thiringer	torbjorn.thiringer@chalmers.se	WP2
Urban Lundgren	urban.lundgren@ri.se	WP4
Dr. Alexandra Nafari	anafari@borgwarner.com	WP1
Dr Astrid Lundgren	N/A	WP5
Dr. Svetla Chakarova Käck	N/A	WP2

16 Abbreviations

ABC	Phase current domain
AC	Alternating Current
AP	ArbetsPaket
AVG	Average
CAD	Computer Aided Design
CEVT	China Euro Vehicle Technology
CIDD	Combined Inverter DC/DC
CM	Common Mode
DC	Direct Current

DC/DC	Direct Current to Direct Current Converter
DM	Differential Mode
EIS	Electrochemical Impedance Spectroscopy
EMC	Electromagnetic Compatibility
EMF	Electromagnetic Fields
EMI	Electromagnetic Interference
ERAD	Electric Rear Axle Drive
FE	Finite Element
FEM	Finite Element Method
FFI	Fordonsstrategist Forskning och Innovation
FFT	Fast Fourier Transform
FMI	Functional Muck-up Interface
FMU	Functional Mock-up
GND	Ground
GUI	Graphical User Interface
HF	High Frequency
HV	High Voltage
HVCH	High Voltage Coolant Heater
HVDC	High Voltage Direct Current
ICE	Internal Combustion Engine
IEM	Inverter Electrical Machine
IGBT	Insulated Gate Bipolar Transistor
IPM	Interior Permanent Magnet
LC	Inductance Capacitance
LF	Low Frequency
MF	Medium frequency
MSD	Manual Service Disconnect
MTL	Multi-wire Transmission line
OBC	On Board Charger
OEM	Original Equipment Manufacturer
PC	Personal Computer
PMSM	Permanent Magnet Synchronous Machine
PWM	Pulse Width Modulation
RC	Resistor Capacitor
RISE	Research Institute of Sweden

RLC	Resistor Inductor Capacitor
RMS	Root Mean Square
ROM	Reduced Order Model
SOC	State Of Charge
SP	Statens Provningsanstalt
SPA	Scalable Product Architecture
SPWM	Sinusoidal Pulse Width Modulation
SVM	Space Vector Modulation
TL	Transmission Line
VCC	Volvo Cars Corporation
VHDL	Very high speed Hardware Description Language
WP	Work Package

17 References

[1] Wei et al., "Multiconductor Transmission Lines in Multilayered Dielectric Media", *IEEE Transactions on Microwave Theory and Techniques*, Vol. 32, No. 4, April 1984, pp. 439-450.

[2] J. Carlsson, "Crosstalk on Printed Circuit Boards", SP Report 1994:14, ISBN 91-7848-721-8, 1998.

[3] J. Carlsson, P.-S. Kildal, "A Simple Method to Compute Crosstalk on Printed Circuit Boards", *Microwave and Optical Technology Letters*, vol. 19, no. 2, pp. 87-94, Oct. 1998.

[4] R.F. Harrington, "Time-harmonic electromagnetic fields", McGraw-Hill, inc., 1961.

[5] J. Carlsson, L. Hasselgren, D. Nunez, U. Lundgren, J. Delsing, M. Hörlin, "A Systematic Methodology for the Generation of SPICE Models Feasible for EMC Analysis", SP Report 2000:07, ISBN 91-7848-804-4, 1999.

[6] Computer code LTspice for Windows, http://www.linear.com/solutions/ltspice

[7] Computer code Simscape for Windows, http://www.mathworks.com

[8] M. Iglesias, I. Echeverria, F. Arteche, J. Piedrafita, A. Pradas and J. De Clercq, "EMC mapping of a power train for fully electric 4-wheel drive vehicle", EMC Europe 2014.

[9] S. Jeschke, H. Hirsch, " Investigations on the EMI of an Electric Vehicle Traction System in Dynamic Operation", EMC Europe 2014.

[10] J. Leopold, M. Kuhn, H. Feng, D. Krause, T. Enzinger, C. Lippert, K. Friedrich, "Electromagnetic Reliability (EMR) of Electronic Systems for Electro Mobility", Poster, EMC Europe 2014.

[11] M. N. Halgamuge, C. D. Abeyrathne, P. Mendis, "Measurement and Analysis of Electromagnetic Fields from Trams, Trains and Hybrid Cars", *Radiation Protection Dosimetry* (2010), Vol. 141, No. 3, pp. 255–268.

[12] https://www.comsol.co/acdc-module

[13] https://www.cst.com/Products/CSTMWS

[14] Jih-Sheng Lai, Xudong Huang, E. Pepa, Shaotang Chen and T. W. Nehl, "Inverter EMI modeling and simulation methodologies," in *IEEE Transactions on Industrial Electronics*, vol. 53, no. 3, pp. 736-744, June 2006.

[15] L. Ran, S. Gokani, J. Clare, K. J. Bradley and C. Christopoulos, "Conducted electromagnetic emissions in induction motor drive systems. I. Time domain analysis and identification of dominant modes," in *IEEE Transactions on Power Electronics*, vol. 13, no. 4, pp. 757-767, Jul 1998.

[16] L. Ran, S. Gokani, J. Clare, K. J. Bradley and C. Christopoulos, "Conducted electromagnetic emissions in induction motor drive systems. II. Frequency domain models," in *IEEE Transactions on Power Electronics*, vol. 13, no. 4, pp. 768-776, Jul 1998.

[17] S. Guttowski, S. Weber, E. Hoene, W. John and H. Reichl, "EMC issues in cars with electric drives", 2003 *IEEE Symposium on Electromagnetic Compatibility*. Symposium Record (Cat. No.03CH37446), 2003, pp. 777-782 vol.2.

[18] D. Gonzalez, J. Gago, J. Balcells, "Analysis and simulation of conducted EMI generated by switched power converters: application to a voltage source inverter," Industrial Electronics, 2002. ISIE 2002. *Proceedings of the 2002 IEEE International Symposium on*, 2002, pp. 801-806 vol.3.

[19] Xudong Huang, E. Pepa, Jih-Sheng Lai, Shaotang Chen and T. W. Nehl, "Three-phase inverter differential mode EMI modeling and prediction in frequency domain," *38th IAS Annual Meeting on Conference Record of the Industry Applications Conference*, 2003, pp. 2048-2055 vol.3.

[20] W. Luo, C. Lv, L. Wang, and C. Liu, "Study on impedance model of Li-ion battery," in *2011 6th IEEE Conference on Industrial Electronics and Applications*, 2011, pp. 1943–1947.

[21] U. Westerhoff, K. Kurbach, F. Lienesch, and M. Kurrat, "Analysis of Lithium-Ion Battery Models Based on Electrochemical Impedance Spectroscopy," *Energy Technol.*, vol. 4, no. 12, pp. 1620–1630, Dec. 2016.

[22] H. Dai, B. Jiang, and X. Wei, "Impedance Characterization and Modeling of Lithium-Ion Batteries Considering the Internal Temperature Gradient," *Energies*, vol. 11, no. 1, p. 220, Jan. 2018.

[23] F. Saidani, F. X. Hutter, R.-G. Scurtu, W. Braunwarth, and J. N. Burghartz, "Lithium-ion battery models: a comparative study and a model-based powerline communication," *Adv. Radio Sci.*, vol. 15, pp. 83–91, Sep. 2017.

[24] V. Ramadesigan, P. W. C. Northrop, S. De, S. Santhanagopalan, R. D. Braatz, and V. R. Subramanian, "Modeling and Simulation of Lithium-Ion Batteries from a Systems Engineering Perspective," *J. Electrochem. Soc.*, vol. 159, no. 3, pp. R31–R45, Jan. 2012.

[25] R. Xiong, H. He, H. Guo, and Y. Ding, "Modeling for Lithium-Ion Battery used in Electric Vehicles," *Procedia Eng.*, vol. 15, pp. 2869–2874, Jan. 2011.

[26] E. Hoene, S. Guttowski, R. Saikly, W. John, and H. Reichl, "Rf-properties of automotive traction batteries," in *2003 IEEE International Symposium on Electromagnetic Compatibility, 2003. EMC '03*, 2003, vol. 1, pp. 425-428 Vol.1.

[27] T. Doersam, S. Schoerle, E. Hoene, K. D. Lang, C. Spieker, and T. Waldmann, "High frequency impedance of Li-ion batteries," in *2015 IEEE International Symposium on Electromagnetic Compatibility (EMC)*, 2015, pp. 714–719.